

AD-A244 900



ESL-TR-89-45

2

# NUMERICAL ANALYSIS OF DYNAMIC SPLITTING-TENSILE AND DIRECT TENSION TESTS

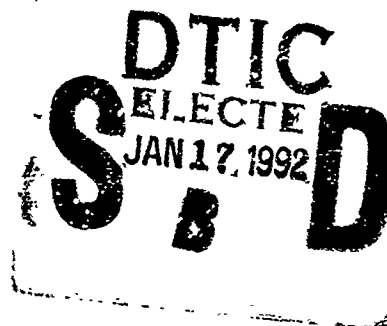
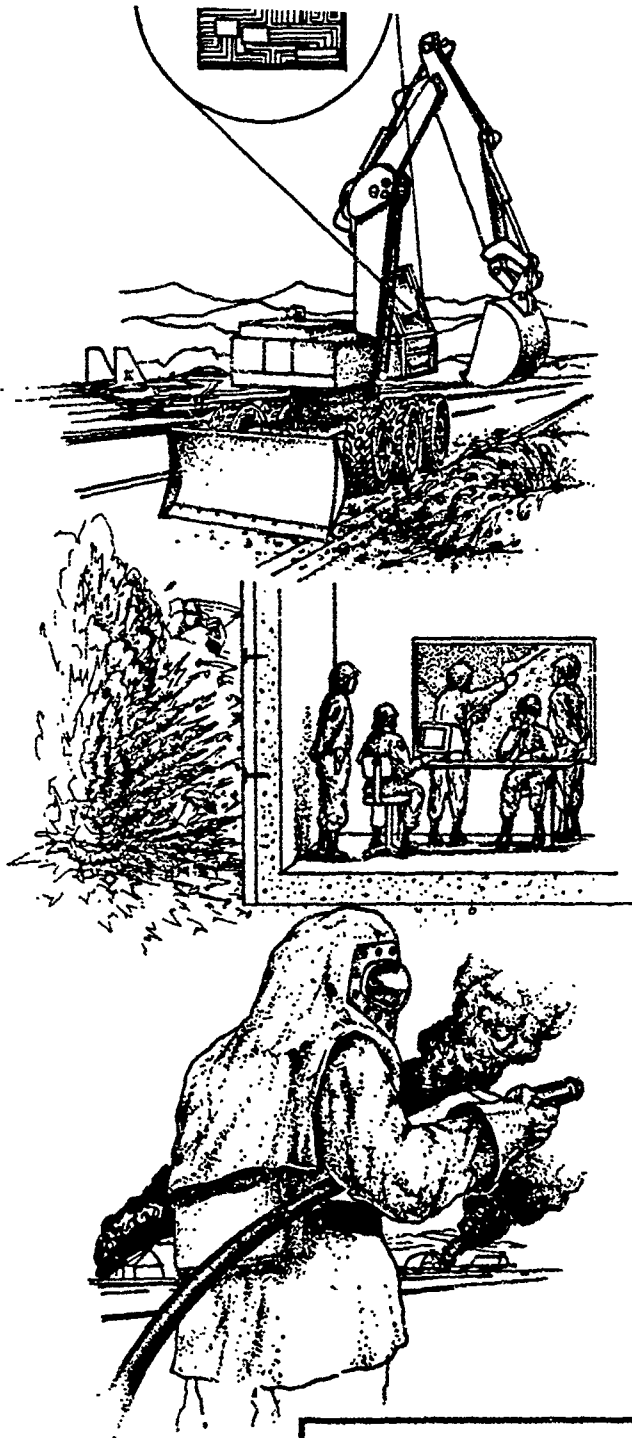
J.W. TEDESCO

AUBURN UNIVERSITY  
DEPARTMENT OF CIVIL ENGINEERING  
AUBURN AL 36849

SEPTEMBER 1990

FINAL REPORT

JULY 1988 — SEPTEMBER 1989



92-01472



APPROVED FOR PUBLIC RELEASE: DISTRIBUTION UNLIMITED



**ENGINEERING RESEARCH DIVISION**  
Air Force Engineering & Services Center  
**ENGINEERING & SERVICES LABORATORY**  
Tyndall Air Force Base, Florida 32403



92 1 16 056

NOTICE

PLEASE DO NOT REQUEST COPIES OF THIS REPORT FROM  
HQ AFESC/RD (ENGINEERING AND SERVICES LABORATORY).  
ADDITIONAL COPIES MAY BE PURCHASED FROM:

NATIONAL TECHNICAL INFORMATION SERVICE  
5285 PORT ROYAL ROAD  
SPRINGFIELD, VIRGINIA 22161

FEDERAL GOVERNMENT AGENCIES AND THEIR CONTRACTORS  
REGISTERED WITH DEFENSE TECHNICAL INFORMATION CENTER  
SHOULD DIRECT REQUESTS FOR COPIES OF THIS REPORT TO:

DEFENSE TECHNICAL INFORMATION CENTER  
CAMERON STATION  
ALEXANDRIA, VIRGINIA 22314

UNCLASSIFIED

SECURITY CLASSIFICATION OF THIS PAGE

## REPORT DOCUMENTATION PAGE

Form Approved  
OMB No 0704-0188

1a REPORT SECURITY CLASSIFICATION Unclassified			1b RESTRICTIVE MARKINGS	
2a SECURITY CLASSIFICATION AUTHORITY			3 DISTRIBUTION / AVAILABILITY OF REPORT Approved for public release. Distribution Unlimited.	
2b DECLASSIFICATION / DOWNGRADING SCHEDULE				
4 PERFORMING ORGANIZATION REPORT NUMBER(S)			5 MONITORING ORGANIZATION REPORT NUMBER(S) ESL-TR-89-45	
6a NAME OF PERFORMING ORGANIZATION Auburn University	6b OFFICE SYMBOL (If applicable)	7a NAME OF MONITORING ORGANIZATION Air Force Engineering and Services Center		
6c ADDRESS (City, State, and ZIP Code) Auburn University Department of Civil Engineering Auburn, AL 36849		7b ADDRESS (City, State, and ZIP Code) HQ AFESC/RDCM Tyndall AFB, FL 32403-6001		
8a NAME OF FUNDING / SPONSORING ORGANIZATION Air Force Engi- neering and Services Center	8b OFFICE SYMBOL (If applicable) RDCM	9 PROCUREMENT INSTRUMENT IDENTIFICATION NUMBER Contract #F08635-88-C-0195		
8c ADDRESS (City, State, and ZIP Code) HQ AFESC/RDCM Tyndall AFB, FL 32403-6001		10 SOURCE OF FUNDING NUMBERS		
		PROGRAM ELEMENT NO 6.2	PROJECT NO 2673	TASK NO 0086 WORK UNIT ACCESSION NO N/A
11 TITLE (Include Security Classification) Numerical Analysis of Dynamic Splitting-Tensile and Direct Tension Tests				
12 PERSONAL AUTHOR(S) Joseph W. Tedesco				
13a TYPE OF REPORT Final	13b TIME COVERED FROM 7/88 TO 9/89	14. DATE OF REPORT (Year, Month, Day) September 1990	15 PAGE COUNT 202	
16 SUPPLEMENTARY NOTATION Availability of this report is specified on reverse of front cover.				
17. COSATI CODES			18 SUBJECT TERMS (Continue on reverse if necessary and identify by block number)	
FIELD	GROUP	SUB-GROUP	Split Hopkinson Pressure Bar Finite Element Analysis	
			Splitting-Tensile Test Impulse Loading	
			Direct Tension Test Concrete Tensile Strength	
19 ABSTRACT (Continue on reverse if necessary and identify by block number)				
<p>This report summarizes the results of a comprehensive numerical analysis of splitting-tensile and direct tension tests of plain concrete performed at strain rates between 1 and <math>10^2</math> on a Split Hopkinson Pressure Bar (SHPB). The objective of the study was to gain some insight into failure mechanisms of concrete at strain rates associated with high intensity loadings from conventional explosives.</p> <p>Both an elastic and an inelastic concrete model were employed in all numerical analyses. The modes of failure predicted by the numerical analyses are consistent with those observed in experimental studies. A definite pattern between load rate and mode of failure was established.</p>				
20 DISTRIBUTION / AVAILABILITY OF ABSTRACT <input checked="" type="checkbox"/> UNCLASSIFIED/UNLIMITED <input type="checkbox"/> SAME AS RPT <input type="checkbox"/> DTIC USERS			21 ABSTRACT SECURITY CLASSIFICATION Unclassified	
22 NAME OF RESPONSIBLE INDIVIDUAL Capt. Steven T. Kuennen			22b TELEPHONE (Include Area Code) 904-283-4932	22c OFFICE SYMBOL HQ AFESC/RDCM

DD Form 1473, JUN 86

Previous editions are obsolete

SECURITY CLASSIFICATION OF THIS PAGE

i

(the reverse of this page is blank.)

## EXECUTIVE SUMMARY

### A. OBJECTIVE

The objective of this study was to gain some insight into failure mechanisms of concrete at strain rates associated with high intensity loadings from conventional explosives. To this end, a comprehensive numerical analysis of splitting-tensile and direct tension tests of plain concrete, performed at strain rates between 1 and  $10^2$  per second on a Split Hopkinson Pressure Bar (SHPB), was conducted.

### B. BACKGROUND

The understanding of material response to high amplitude, short-duration, impulse loads generated in a weapons environment is an important problem in protective construction design and analysis. To model the response in the laboratory requires that the environment must reflect the type of confinement, magnitude of stress change, and the time scale of loading anticipated in the field. The Split Hopkinson Pressure Bar (SHPB) technique can produce the required environments in the laboratory.

However, several significant shortcomings are associated with SHPB experiments. First, it is not possible to accurately determine the stress condition in the specimen at failure from the available data, and second, it is frequently not possible to ascertain the mode of failure in the specimen. Therefore, a comprehensive numerical analysis was conducted on various SHPB experiments to gain some insight into those phenomena.

### C. SCOPE

Two different types of SHPB experiments were simulated in the numerical analyses: (1) splitting-tensile tests and (2) direct tension tests. In the splitting-tensile analyses, the numerical model included the 2-inch (51 mm) diameter cylindrical specimen and a 10-inch (25.4 cm) length of the transmitter bar. Three different load cases were investigated. In the direct tension study, both a square notch and saddle notch specimen were analyzed. The numerical model included the entire lengths of the incident and transmitter bars, in addition to the 2-inch (51 mm) diameter specimen. One load case for each specimen type was investigated.

#### D. METHODOLOGY

Because of the dynamic nature of the impulse loading associated with the SHPB experiments, and the highly nonlinear behavior of the concrete test specimens, the finite element method (FEM) of analysis was employed in the research effort through implementation of the ADINA computer programs. The analyses were conducted on two-dimensional, axisymmetric models comprised of nine-node isoparametric finite elements. Both linear and nonlinear analyses were performed.

#### E. TEST DESCRIPTION

The high strain rate SHPB experiments were performed using the Air Force Engineering and Services Center (AFESC) 50.8 mm diameter SHPB by AFESC personnel. All numerical analyses were conducted on the Alabama Supercomputer Network (ASN) Cray X-MP/24 Supercomputer by Auburn University personnel.

#### F. RESULTS

Both an elastic and an inelastic concrete material model were employed in all numerical analyses. For the splitting-tensile study, the results of the linear analyses indicate that the dynamic stress distribution in the cylinder behind the initial stress wave is identical to that exhibited in static analyses. The linear results also indicate that the maximum tensile stress always occurs at the center of the cylinder. This observation is likewise consistent with the results of the static analysis.

The mode of failure predicted by the nonlinear analysis differs from that suggested by the results of the linear analysis. In all three load cases, the initiation of first cracking is not at the center of the cylinder (as the results of the linear analysis indicate), but at an approximate distance of  $0.2D$  from the top of the cylinder. The sequence of failure for all load cases is essentially the same: initiation of first cracking at location  $0.2D$  from the top, and subsequent propagation of the cracks in both directions along the vertical centerline of the cylinder toward the top and bottom surfaces. Some mid-diameter crack bifurcation occurs as the load rate is increased. This prediction has been verified by observation of experimental results using high speed photography.

For the direct tension study, the results of the linear analyses indicate the development of high stress concentrations at the root of the notch in the square-notch specimens, and at the apex of the notch in the saddle-notch specimens. These results suggest that first cracking will begin at these locations of high stress concentration factors and that failure will occur on vertical planes passing through these locations.

The mode of failure predicted by the nonlinear analysis differs from that suggested by the results of the linear analysis. In the square-notch specimen, first cracking occurs at the root of the notch. This is consistent with the stress concentration predictions from the linear analysis. However, eventual failure of the specimen occurs on a vertical plane adjacent to the face of the incident bar. In the saddle-notch specimen, first cracking occurs at a transverse section in the specimen next to the incident bar. Almost simultaneously, cracks develop in the apex of the notch. Eventual failure is along the transverse section adjacent to the incident bar.

#### G. CONCLUSIONS

In the case of the splitting-tensile tests, it can be concluded that the nature of the failure mode is directly affected by the rate of loading. For a relatively low load rate, the failure mode manifests itself as a single crack propagating along the vertical centerline of the cylinder. However, for increasingly higher load rates, the mode of failure is characterized by several bifurcations in the primary crack pattern. The higher the load rate, the more pronounced are the bifurcations.

In the case of the direct-tension tests, the results of the linear analyses indicate high stress concentration factors in the vicinity of the notches. These results suggest a failure in a transverse plane passing through the notches. The nonlinear analyses, however, predict failure in a transverse plane near the end of the specimen next to the incident bar. The reason for this is that the load rate is so high, that the tensile limit of the material is reached at the end of the specimen (adjacent to the incident bar) before any significant stresses can develop on the transverse plane passing through the notch.

#### H. RECOMMENDATIONS

The failures predicted in both the splitting-tensile tests and the direct tension tests are highly sensitive to the rate of loading. Therefore it is recommended that additional analyses be conducted at a wide range of load rates to quantify the relationship of load rate to mode of failure. It is also apparent from the results of the analyses that material strain rate effects will delay the time of failure, allowing the specimen to be subjected to a higher load, thus possibly affecting the failure mode. Therefore, it is further recommended that additional numerical analyses be conducted to investigate material strain rate effects on the mode of failure.

Finally, the notches in the direct tension specimens analyzed in this study were relatively shallow. It is recommended that specimens with deeper notches be analyzed, both experimentally and numerically, to quantify the effect of notch depth on the mode of failure.



<b>Accession For</b>	
NTIS GRA&I	<input checked="checked" type="checkbox"/>
DTIC TAB	<input type="checkbox"/>
Unannounced	<input type="checkbox"/>
Justification	
By	
Distribution/	
Availability Codes	
Dist	Avail and/or Special
A-1	

## PREFACE

This report was prepared by the Department of Civil Engineering, Auburn University, Auburn, Alabama, under Contract No. F08635-88-C-0195 for Engineering and Services Laboratory, Headquarters, Air Force Engineering and Services Center (HQ AFESC/RDCM), Tyndall AFB, Florida.

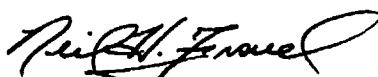
This report summarizes the results of work to simulate several types of experiments conducted on a split-Hopkinson pressure bar through a comprehensive numerical analysis. The work was initiated in July 1988 and completed in September 1989. Dr Joseph W. Tedesco served as principal investigator at Auburn University. Capt S. T. Kuennen served as the project officer for HQ AFESC/RDCM.

This report has been reviewed by the Public Affairs Office and is releasable to the National Information Service (NTIS). At NTIS it will be available to the general public, including foreign nationals.

This report has been reviewed and is approved for publication.



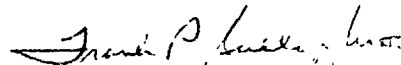
STEVEN T. KUENNEN, Capt, USAF  
Project Officer



NEIL H. FRAVEL, Lt Col, USAF  
Chief, Engineering  
Research Division



LOREN M. WOMACK, GM-14  
Chief, Air Base Structural  
Materials Branch



FRANK P. GALLAGHER III, Col, USAF  
Director, Engineering and  
Services Laboratory



## TABLE OF CONTENTS

Section	Title	Page
I	INTRODUCTION.....	1
	A. OBJECTIVE.....	1
	B. BACKGROUND.....	1
	1. Split Hopkinson Pressure Bar (SHPB).....	1
	2. Numerical Analysis.....	5
	C. SCOPE.....	6
II	SPLITTING-TENSILE TESTS.....	7
	A. INTRODUCTION.....	7
	B. LINEAR ANALYSES.....	14
	1. The FEM Model.....	14
	2. Static Analysis.....	14
	3. Dynamic Analysis.....	16
	C. NONLINEAR ANALYSIS.....	59
	1. Background.....	59
	2. Results of Nonlinear Analysis (Load Case 1)....	64
	3. Results of Nonlinear Analysis (Load Case 2)....	78
	4. Results of Nonlinear Analysis (Load Case 3)....	127

## TABLE OF CONTENTS (CONTINUED)

III	DIRECT TENSION TESTS.....	144
	A. INTRODUCTION.....	144
	B. LINEAR ANALYSIS.....	149
	1. The FEM Model.....	149
	2. Calibration of FEM Model.....	149
	3. Square Notch Test.....	149
	4. Saddle Notch Test.....	160
	C. NONLINEAR ANALYSIS.....	160
	1. Introduction.....	160
	2. Square Notch Test.....	160
	3. Saddle Notch Test.....	180
IV	DISCUSSION OF RESULTS.....	194
	A. SPLITTING-CYLINDER ANALYSIS.....	194
	1. Linear Analysis.....	194
	2. Nonlinear Analysis.....	194
	B. DIRECT TENSION TESTS.....	196
	1. Linear Analysis.....	196
	2. Nonlinear Analysis.....	196

## TABLE OF CONTENTS (CONTINUED)

V	CONCLUSIONS AND RECOMMENDATIONS.....	198
	A. CONCLUSIONS.....	198
	1. Splitting-Tensile Tests.....	198
	2. Direct Tension Tests.....	198
	B. RECOMMENDATIONS.....	199
	REFERENCES.....	200

## LIST OF FIGURES

Figure	Title	Page
1	Illustration of AFESC 2-in. diameter Split Hopkinson Pressure Bar.....	3
2	Schematic of Split Hopkinson Pressure Bar.....	4
3	Illustration of static split cylinder test.....	8
4	Distribution of horizontal stress ( $\sigma_y$ ) on the vertical diameter for a static split cylinder test.....	8
5	Splitting-tensile test arrangement in the SHPB.....	9
6	Splitting-tensile test data trace for Load Case 1.....	11
7	Splitting-tensile test data trace for Load Case 2.....	12
8	Splitting-tensile test data trace for Load Case 3.....	13
9	FEM model of cylinder and portion of transmitter bar.....	15
10	Horizontal stress distribution along the vertical diameter.....	17
11	Vertical stress distribution along the vertical diameter.....	18
12	Horizontal stress distribution along the horizontal diameter.....	19
13	Vertical stress distribution along the horizontal diameter.....	20
14	Corrected SHPB data for Load Case 1.....	22
15	Corrected SHPB data for Load Case 2.....	23
16	Corrected SHPB data for Load Case 3.....	24
17	Typical ramp loading function used in FEM analyses.....	25
18	Time history for horizontal stress at $z = .125D$ , Load Case 1.....	28
19	Time history for horizontal stress at $z = 0.30D$ , Load Case 1.....	29
20	Time history for horizontal stress at $z = 0.50D$ , Load Case 1.....	30
21	Time history for horizontal stress at $z = 0.715D$ , Load Case 1.....	31
22	Time history for horizontal stress at $z = 0.915D$ , Load Case 1.....	32
23	Time history for vertical stress at $z = .125D$ , Load Case 2.....	33
24	Time history for vertical stress at $z = 0.30D$ , Load Case 2.....	34
25	Time history for vertical stress at $z = 0.50D$ , Load Case 2.....	35
26	Time history for vertical stress at $z = 0.715D$ , Load Case 2.....	36
27	Time history for vertical stress at $z = 0.915D$ , Load Case 2.....	37
28	Time history for vertical stress at $z = 0.125D$ , Load Case 3.....	38
29	Time history for vertical stress at $z = 0.30D$ , Load Case 3.....	39

30	Time history for vertical stress at $z = 0.50D$ , Load Case 3.....	40
31	Time history for vertical stress at $z = 0.715D$ , Load Case 3.....	41
32	Time history for vertical stress at $z = 0.915D$ , Load Case 3.....	42
33	Time history for vertical stress in the transmitter bar, Load Case 1.....	43
34	Time history for vertical stress in the transmitter bar, Load Case 2.....	44
35	Time history for vertical stress in the transmitter bar, Load Case 3.....	45
36	Profiles for the horizontal stress along the vertical diameter, Load Case 1 ( $t_1, t_2, t_3, t_4, t_5$ ).....	47
37	Profiles for the horizontal stress along the vertical diameter, Load Case 1 ( $t_6, t_7, t_8, t_9, t_{10}$ ).....	48
38	Profiles for the horizontal stress along the horizontal diameter, Load Case 1 ( $t_1, t_2, t_3, t_4, t_5$ ).....	49
39	Profiles for the horizontal stress along the horizontal diameter, Load Case 1 ( $t_6, t_7, t_8, t_9, t_{10}$ ).....	50
40	Profiles for the horizontal stress along the vertical diameter, Load Case 2, ( $t_1, t_2, t_3, t_4, t_5$ ).....	51
41	Profiles for the horizontal stress along the vertical diameter, Load Case 2, ( $t_6, t_7, t_8, t_9, t_{10}$ ).....	52
42	Profiles for the horizontal stress along the vertical diameter, Load Case 3 ( $t_1, t_2, t_3, t_4, t_5$ ).....	53
43	Profiles for the horizontal stress along the vertical diameter, Load Case 3 ( $t_6, t_7, t_8, t_9, t_{10}$ ).....	54
44	Profiles for the horizontal stress along the horizontal diameter, Load Case 2 ( $t_1, t_2, t_3, t_4, t_5$ ).....	55
45	Profiles for the horizontal stress along the horizontal diameter, Load Case 2 ( $t_6, t_7, t_8, t_9, t_{10}$ ).....	56
46	Profiles for the horizontal stress along the horizontal diameter, Load Case 3 ( $t_1, t_2, t_3, t_4, t_5$ ).....	57
47	Profiles for the horizontal stress along the horizontal diameter, Load Case 3 ( $t_6, t_7, t_8, t_9, t_{10}$ ).....	58
48	Uniaxial stress-strain relation used in concrete model.....	60

49	Three dimensional tensile failure envelope of concrete model.....	61
50	Time histories for (a) horizontal stress and (b) horizontal strain at $z = 0.1D$ , Load Case 1, nonlinear analysis.....	65
51	Time histories for (a) horizontal stress and (b) horizontal strain at $z = 0.3D$ , Load Case 1, nonlinear analysis.....	66
52	Time histories for (a) horizontal stress and (b) horizontal strain at $z = 0.5D$ , Load Case 1, nonlinear analysis.....	67
53	Time histories for (a) vertical stress and (b) vertical strain at $z = 0.1D$ , Load Case 1, nonlinear analysis.....	68
54	Time histories for (a) vertical stress and (b) vertical strain at $z = 0.3D$ , Load Case 1, nonlinear analysis.....	69
55	Time histories for (a) vertical stress and (b) vertical strain at $z = 0.5D$ , Load Case 1, nonlinear analysis.....	70
56	Time histories for (a) horizontal stress and (b) horizontal strain at $y = 0.25D$ , Load Case 1, nonlinear analysis.....	71
57	Time histories for (a) horizontal stress and (b) horizontal strain at $y = 0.38D$ , Load Case 1, nonlinear analysis.....	72
58	Time histories for (a) horizontal stress and (b) horizontal strain at $y = 0.50D$ , Load Case 1, nonlinear analysis.....	73
59	Time histories for (a) vertical stress and (b) vertical strain at $y = 0.25D$ , Load Case 1, nonlinear analysis.....	74
60	Time histories for (a) vertical stress and (b) vertical strain at $y = 0.38D$ , Load Case 1, nonlinear analysis.....	75
61	Time histories for (a) vertical stress and (b) vertical strain at $y = 0.50D$ , Load Case 1, nonlinear analysis.....	76
62	Time histories for (a) vertical stress and (b) vertical strain in the transmitter bar, Load Case 1, nonlinear analysis.....	77
63	Profiles for (a) horizontal stress and (b) horizontal strain along the vertical diameter, Load Case 1, nonlinear analysis, $t = 56.1 \mu\text{sec}$ .....	79
64	Profiles for (a) horizontal stress and (b) horizontal strain along the vertical diameter, Load Case 1, nonlinear analysis, $t = 56.3 \mu\text{sec}$ .....	80
65	Profiles for (a) horizontal stress and (b) horizontal strain along the vertical diameter, Load Case 1, nonlinear analysis, $t = 58.0 \mu\text{sec}$ .....	81

66	Profiles for (a) horizontal stress and (b) horizontal strain along the vertical diameter, Load Case 1, nonlinear analysis, t = 66.0 $\mu$ sec.....	82
67	Profiles for (a) horizontal stress and (b) horizontal strain along the vertical diameter, Load Case 1, nonlinear analysis, t = 85.0 $\mu$ sec.....	83
68	Profiles for (a) horizontal stress and (b) horizontal strain along the horizontal diameter, Load Case 1, nonlinear analysis, t = 56.1 $\mu$ sec.....	84
69	Profiles for (a) horizontal stress and (b) horizontal strain along the horizontal diameter, Load Case 1, nonlinear analysis, t = 56.3 $\mu$ sec.....	85
70	Profiles for (a) horizontal stress and (b) horizontal strain along the horizontal diameter, Load Case 1, nonlinear analysis, t = 58.0 $\mu$ sec.....	86
71	Profiles for (a) horizontal stress and (b) horizontal strain along the horizontal diameter, Load Case 1, nonlinear analysis, t = 66.0 $\mu$ sec.....	87
72	Profiles for (a) horizontal stress and (b) horizontal strain along the horizontal diameter, Load Case 1, nonlinear analysis, t = 85.0 $\mu$ sec.....	88
73	Profiles for (a) vertical stress and (b) vertical strain along the horizontal diameter, Load Case 1, nonlinear analysis, t = 56.1 $\mu$ sec.....	89
74	Profiles for (a) vertical stress and (b) vertical strain along the horizontal diameter, Load Case 1, nonlinear analysis, t = 56.3 $\mu$ sec.....	90
75	Profiles for (a) vertical stress and (b) vertical strain along the horizontal diameter, Load Case 1, nonlinear analysis, t = 58.0 $\mu$ sec.....	91
76	Profiles for (a) vertical stress and (b) vertical strain along the horizontal diameter, Load Case 1, nonlinear analysis, t = 66.0 $\mu$ sec.....	92
77	Profiles for (a) vertical stress and (b) vertical strain along the horizontal diameter, Load Case 1, nonlinear analysis, t = 85.0 $\mu$ sec.....	93

78	Failure pattern for splitting-tensile specimen, Load Case 1, nonlinear analysis.....	94
79	Time histories for (a) horizontal stress and (b) horizontal strain at $z = 0.1D$ , Load Case 2, nonlinear analysis.....	95
80	Time histories for (a) horizontal stress and (b) horizontal strain at $z = 0.3D$ , Load Case 2, nonlinear analysis.....	96
81	Time histories for (a) horizontal stress and (b) horizontal strain at $z = 0.5D$ , Load Case 2, nonlinear analysis.....	97
82	Time histories for (a) vertical stress and (b) vertical strain at $z = 0.1D$ , Load Case 2, nonlinear analysis.....	98
83	Time histories for (a) vertical stress and (b) vertical strain at $z = 0.3D$ , Load Case 2, nonlinear analysis.....	99
84	Time histories for (a) vertical stress and (b) vertical strain at $z = 0.5D$ , Load Case 2, nonlinear analysis.....	100
85	Time histories for (a) horizontal stress and (b) horizontal strain at $y = 0.25D$ , Load Case 2, nonlinear analysis.....	101
86	Time histories for (a) horizontal stress and (b) horizontal strain at $y = 0.38D$ , Load Case 2, nonlinear analysis.....	102
87	Time histories for (a) horizontal stress and (b) horizontal strain at $y = 0.5D$ , Load Case 2, nonlinear analysis.....	103
88	Time histories for (a) vertical stress and (b) vertical strain at $y = 0.25D$ , Load Case 2, nonlinear analysis.....	104
89	Time histories for (a) vertical stress and (b) vertical strain at $y = 0.38D$ , Load Case 2, nonlinear analysis.....	105
90	Time histories for (a) vertical stress and (b) vertical strain at $y = 0.5D$ , Load Case 2, nonlinear analysis.....	106
91	Time histories for (a) vertical stress and (b) vertical strain in the transmitter bar, Load Case 2, nonlinear analysis.....	108
92	Profiles for (a) horizontal stress and (b) horizontal strain along the vertical diameter, Load Case 2, nonlinear analysis, $t = 29.2 \mu\text{sec}$ .....	109
93	Profiles for (a) horizontal stress and (b) horizontal strain along the vertical diameter, Load Case 2, nonlinear analysis, $t = 31.2 \mu\text{sec}$ .....	110



94	Profiles for (a) horizontal stress and (b) horizontal strain along the vertical diameter, Load Case 2, nonlinear analysis, $t = 35 \mu\text{sec}$ .....	111
95	Profiles for (a) horizontal stress and (b) horizontal strain along the vertical diameter, Load Case 2, nonlinear analysis, $t = 45 \mu\text{sec}$ .....	112
96	Profiles for (a) horizontal stress and (b) horizontal strain along the horizontal diameter, Load Case 2, nonlinear analysis, $t = 29.2 \mu\text{sec}$ .....	113
97	Profiles for (a) horizontal stress and (b) horizontal strain along the horizontal diameter, Load Case 2, nonlinear analysis, $t = 31.2 \mu\text{sec}$ .....	114
98	Profiles for (a) horizontal stress and (b) horizontal strain along the horizontal diameter, Load Case 2, nonlinear analysis, $t = 35 \mu\text{sec}$ .....	115
99	Profiles for (a) horizontal stress and (b) horizontal strain along the horizontal diameter, Load Case 2, nonlinear analysis, $t = 45 \mu\text{sec}$ .....	116
100	Profiles for (a) vertical stress and (b) vertical strain along the horizontal diameter, Load Case 2, nonlinear analysis, $t = 29.2 \mu\text{sec}$ .....	118
101	Profiles for (a) vertical stress and (b) vertical strain along the horizontal diameter, Load Case 2, nonlinear analysis, $t = 31.2 \mu\text{sec}$ .....	119
102	Profiles for (a) vertical stress and (b) vertical strain along the horizontal diameter, Load Case 2, nonlinear analysis, $t = 35 \mu\text{sec}$ .....	120
103	Profiles for (a) vertical stress and (b) vertical strain along the horizontal diameter, Load Case 2, nonlinear analysis, $t = 45 \mu\text{sec}$ .....	121
104	Failure pattern for splitting-tensile specimen, Load Case 2, nonlinear analysis.....	122
105	Time histories for (a) horizontal stress and (b) horizontal strain at root of bifurcation at top of cylinder, Load Case 2, nonlinear analysis.....	123

106	Time histories for (a) vertical stress and (b) vertical strain at root of bifurcation at top of cylinder, Load Case 2, nonlinear analysis.....	124
107	Time histories for (a) horizontal stress and (b) horizontal strain at root of bifurcation at bottom of cylinder, Load Case 2, nonlinear analysis.....	125
108	Time histories for (a) vertical stress and (b) vertical strain at root of bifurcation at bottom of cylinder, Load Case 2, nonlinear analysis.....	126
109	Time history for horizontal stress at $z = 0.1D$ , Load Case 3, nonlinear analysis.....	128
110	Time history for horizontal stress at $z = 0.3D$ , Load Case 3, nonlinear analysis.....	129
111	Time history for horizontal stress at $z = 0.5D$ , Load Case 3, nonlinear analysis.....	130
112	Time history for vertical stress at $z = 0.2D$ , Load Case 3, nonlinear analysis.....	131
113	Time history for vertical stress at $z = 0.5D$ , Load Case 3, nonlinear analysis.....	132
114	Profile for horizontal stress along the vertical diameter, Load Case 3, nonlinear analysis, $t = 27.1 \mu\text{sec}$ .....	133
115	Profile for horizontal stress along the vertical diameter, Load Case 3, nonlinear analysis, $t = 28.1 \mu\text{sec}$ .....	134
116	Profile for horizontal stress along the vertical diameter, Load Case 3, nonlinear analysis, $t = 28.9 \mu\text{sec}$ .....	135
117	Profile for horizontal stress along the vertical diameter, Load Case 3, nonlinear analysis, $t = 30.5 \mu\text{sec}$ .....	136
118	Profile for horizontal stress along the vertical diameter, Load Case 3, nonlinear analysis, $t = 35.0 \mu\text{sec}$ .....	137
119	Profile for horizontal stress along the horizontal diameter, Load Case 3, nonlinear analysis, $t = 27.1 \mu\text{sec}$ .....	138
120	Profile for horizontal stress along the horizontal diameter, Load Case 3, nonlinear analysis, $t = 28.1 \mu\text{sec}$ .....	139
121	Profile for horizontal stress along the horizontal diameter, Load Case 3, nonlinear analysis, $t = 28.9 \mu\text{sec}$ .....	140

122	Profile for horizontal stress along the horizontal diameter, Load Case 3, nonlinear analysis, $t = 30.5 \mu\text{sec}$ .....	141
123	Profile for horizontal stress along the horizontal diameter, Load Case 3, nonlinear analysis, $t = 35.0 \mu\text{sec}$ .....	142
124	Failure pattern for splitting-tensile specimen, Load Case 3, nonlinear analysis.....	143
125	Direct tension specimens: (a) square notch, (b) saddle notch.....	145
126	Schematic of direct tension SHPB.....	146
127	Square notch test data trace.....	147
128	Saddle notch test data trace.....	148
129	FEM model of incident bar.....	150
130	FEM model of transmitter bar.....	151
131	FEM model of square notch specimen.....	152
132	FEM model of saddle notch specimen.....	153
133	Time history for longitudinal stress at $z = 1.0$ in.....	154
134	Time history for longitudinal stress at $z = 12.0$ in.....	155
135	Time history for longitudinal stress at $z = 26.0$ in.....	156
136	Time history for longitudinal stress at $z = 51$ in.....	157
137	Modified ramp loading function used in FEM analysis.....	158
138	Time histories for longitudinal stress along longitudinal centerline, square notch test.....	159
139	Time histories for longitudinal stress at the notch roots, square notch test.....	161
140	Profiles of longitudinal stress along a transverse plane through the notch root.....	162
141	Profiles of longitudinal stress along a transverse plane through the notch root.....	163
142	Time histories for longitudinal stress along the longitudinal centerline, saddle notch test.....	164
143	Time histories for longitudinal stress in the vicinity of the notch, saddle notch test.....	165
144	Profiles of the longitudinal stress along a transverse plane through the notch.....	166

145	Time histories for (a) longitudinal stress and (b) longitudinal strain along the exterior surface, nonlinear analysis, square notch, $z = 0$ .....	167
146	Time histories for (a) longitudinal stress and (b) longitudinal strain along the exterior surface, nonlinear analysis, square notch, $z = L/2$ .....	168
147	Time histories for (a) longitudinal stress and (b) longitudinal strain along the exterior surface, nonlinear analysis, square notch, $z = L$ .....	169
148	Time histories for (a) longitudinal stress and (b) longitudinal strain along the axis of symmetry, nonlinear analysis, square notch, $z = 0$ .....	170
149	Time histories for (a) longitudinal stress and (b) longitudinal strain along the axis of symmetry, nonlinear analysis, square notch, $z = L/2$ .....	172
150	Time histories for (a) longitudinal stress and (b) longitudinal strain along the axis of symmetry, nonlinear analysis, square notch, $z = L$ .....	173
151	Profiles for longitudinal stress transverse to the longitudinal axis, nonlinear analysis, square notch, $z = 0$ .....	174
152	Profiles for longitudinal stress transverse to the longitudinal axis, nonlinear analysis, square notch, $z = L/2$ .....	175
153	Profiles for longitudinal stress transverse to the longitudinal axis, nonlinear analysis, square notch, $z = L$ .....	176
154	Cracking in square notch specimen at time $t = 270.0 \mu\text{sec}$ .....	177
155	Cracking in square notch specimen at time $t = 274.0 \mu\text{sec}$ .....	178
156	Cracking in square notch specimen at time $t = 275.0 \mu\text{sec}$ .....	179
157	Time histories for (a) longitudinal stress and (b) longitudinal strain along the exterior surface, nonlinear analysis, saddle notch, $z = 0$ .....	181
158	Time histories for (a) longitudinal stress and (b) longitudinal strain along the exterior surface, nonlinear analysis, saddle notch, $z = L/2$ .....	182

159	Time histories for (a) longitudinal stress and (b) longitudinal strain along the exterior surface, nonlinear analysis, saddle notch, $z = L$ .....	183
160	Time histories for (a) longitudinal stress and (b) longitudinal strain along the axis of symmetry, nonlinear analysis, saddle notch, $z = 0$ .....	184
161	Time histories for (a) longitudinal stress and (b) longitudinal strain along the axis of symmetry, nonlinear analysis, saddle notch, $z = L/2$ .....	185
162	Time histories for (a) longitudinal stress and (b) longitudinal strain along the axis of symmetry, nonlinear analysis, saddle notch, $z = L$ .....	186
163	Profiles for longitudinal stress transverse to the longitudinal axis, nonlinear analysis, saddle notch, $z = 0$ .....	187
164	Profiles for longitudinal stress transverse to the longitudinal axis, nonlinear analysis, saddle notch, $z = L/2$ .....	188
165	Profiles for longitudinal stress transverse to the longitudinal axis, nonlinear analysis, saddle notch, $z = L$ .....	189
166	Cracking in saddle notch specimen at time $t = 256.0 \mu\text{sec}$ .....	190
167	Cracking in saddle notch specimen at time $t = 257.0 \mu\text{sec}$ .....	191
168	Cracking in saddle notch specimen at time $t = 258.0 \mu\text{sec}$ .....	192

## LIST OF TABLES

Number	Title	Page
1	Summary of SHPB Results.....	14
2	Static Stresses at Center of Cylinder.....	16
3	Parameters for Ramp Load Function.....	21
4	Selected Times for Stress Profiles (Linear Analysis).....	46
5	Dynamic Stresses at Center of Cylinder.....	59
6	Concrete Model Parameters.....	62
7	Maximum Stresses and Strain Rates at Selected Locations (Load Case 1).....	64
8	Maximum Stresses and Strain Rates at Selected Locations (Load Case 2).....	107
9	Maximum Stresses and Strain Rates at Selected Locations (Square Notch Test).....	171
10	Maximum Stresses and Strain Rates at Selected Locations (Saddle Notch Test).....	193

## SECTION I

### INTRODUCTION

#### A. OBJECTIVE

A comprehensive numerical analysis of splitting-tensile and direct tension tests of plain concrete, performed at strain rates between 1 and  $10^2$  on a Split Hopkinson Pressure Bar (SHPB), was conducted to ascertain the states of stress in the concrete specimens at failure and to identify the modes of failure.

#### B. BACKGROUND

##### 1. Split Hopkinson Pressure Bar (SHPB)

The understanding of material response to high-amplitude, short-duration, impulse loads generated in a weapons environment is an important problem in protective construction design and analysis (Reference 1). To model the response in the laboratory requires that the environment must reflect the type of confinement, magnitude of stress change, and the time scale of loading anticipated in the field (Reference 2). The Split Hopkinson Pressure Bar (SHPB) technique (Reference 3) can produce the required environments in the laboratory.

During the past several years researchers have demonstrated that the SHPB technique can determine the dynamic, high stress and strain rate of soil (References 4, 5, 6, 7, and 8) and concrete (References 9, 10, 11, and 12). Although the conditions of the experiment have been restrictive (e.g., conditions of uniaxial strain), this technique has significantly extended the stress and strain-rate regimes over which dynamic material properties can be investigated.

Hopkinson (Reference 13) introduced the concept of using a cylindrical bar for evaluating material response to impulse loads. The apparatus consisted of a long cylindrical bar with a time piece of the same diameter and material attached by magnetic attraction to one end. By propagating a compressive wave down the bar and capturing the momentum transferred to time pieces of different lengths, an approximate stress-time curve could be constructed. Davies (Reference 14) improved the experimental technique by introducing electrical condenser units to measure the displacement at the surface of the bar caused by the propagating wave. In addition, Davies developed a

theoretical foundation of dispersion phenomenon and established the accuracy of the technique when assuming one-dimensional wave propagation in the bar. Using this framework, Kolsky (Reference 15) modified the technique to permit the dynamic response of a material to be measured indirectly by placing a specimen between two bars fitted with condenser microphones for data recording. Assuming that a uniform distribution of stress existed along the longitudinal axis of the specimen, Kolsky developed relationships to compute the average stress, strain, and strain-rate response of the specimen. This technique is now known as the Kolsky technique or Split Hopkinson Pressure Bar technique.

An illustration of the SHPB device is shown in Figure 1. The device is operated by the Engineering and Services Laboratory, Air Force Engineering and Services Center, Tyndall AFB, Florida. The pressure bars are constructed of PH 13-8 MO stainless steel. Each pressure bar is 2.0 inches (51 mm) in diameter. The lengths of the incident and striker bars are 12 and 11 feet (3.66 and 3.35 m), respectively. Striker bar lengths of 4, 6, and 8 inches (102, 153, and 203 mm), are available. The loading compressive stress wave is initiated by the impact of the striker bar (which is propelled by the gas gun) on the incident bar (Figure 2). The amplitude of the incident stress pulse is determined by the impact velocity and material properties of the striker bar, while the duration of the pulse depends on the length and wave speed of the striker bar (Reference 16).

The incident stress wave ( $\sigma_I$ ) generated in the incident bar travels down the bar and is recorded at Strain Gage A (Figure 2), is partially reflected at the incident bar/specimen interface, and partially reflected at the specimen/transmitter bar interface. Strain Gage B (Figure 2) on the transmitter bar records the portion of the wave that has transmitted the specimen ( $\sigma_T$ ), while Strain Gage A on the incident bar records that portion of the wave reflected at the incident bar/specimen interface ( $\sigma_R$ ). From these strain gage measurements, the stress and strain in the specimen, which is sandwiched between the two pressure bars, can be computed as a function of time using simple wave mechanics.

From one-dimensional theory of wave analysis, the particle velocity ( $V$ ) and stress ( $\sigma$ ) in the bars are related through the impedance (i.e.,  $\rho C_0$  where  $\rho$  is the mass density of the bars and  $C_0$  is the rod wave velocity):



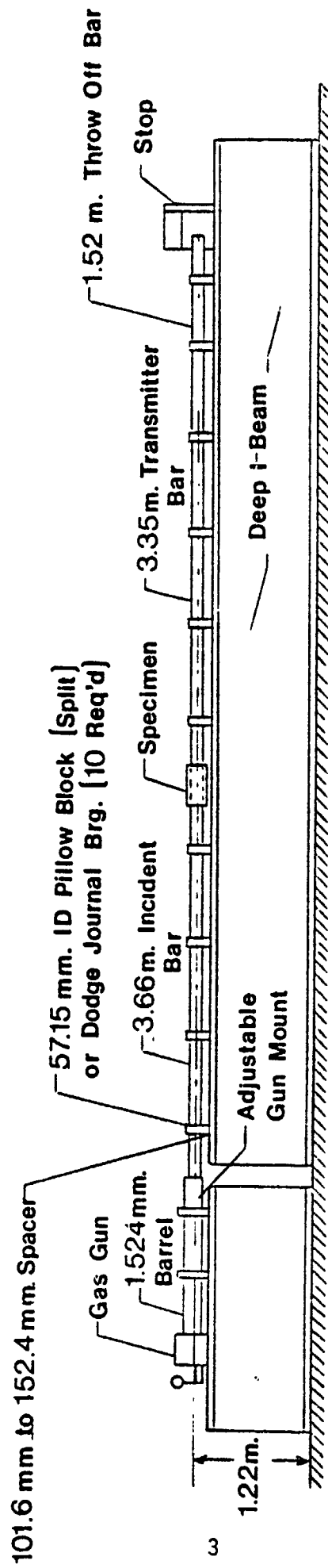


Figure 1. Illustration of AFESC 2-in. Diameter Split Hopkinson Pressure Bar.

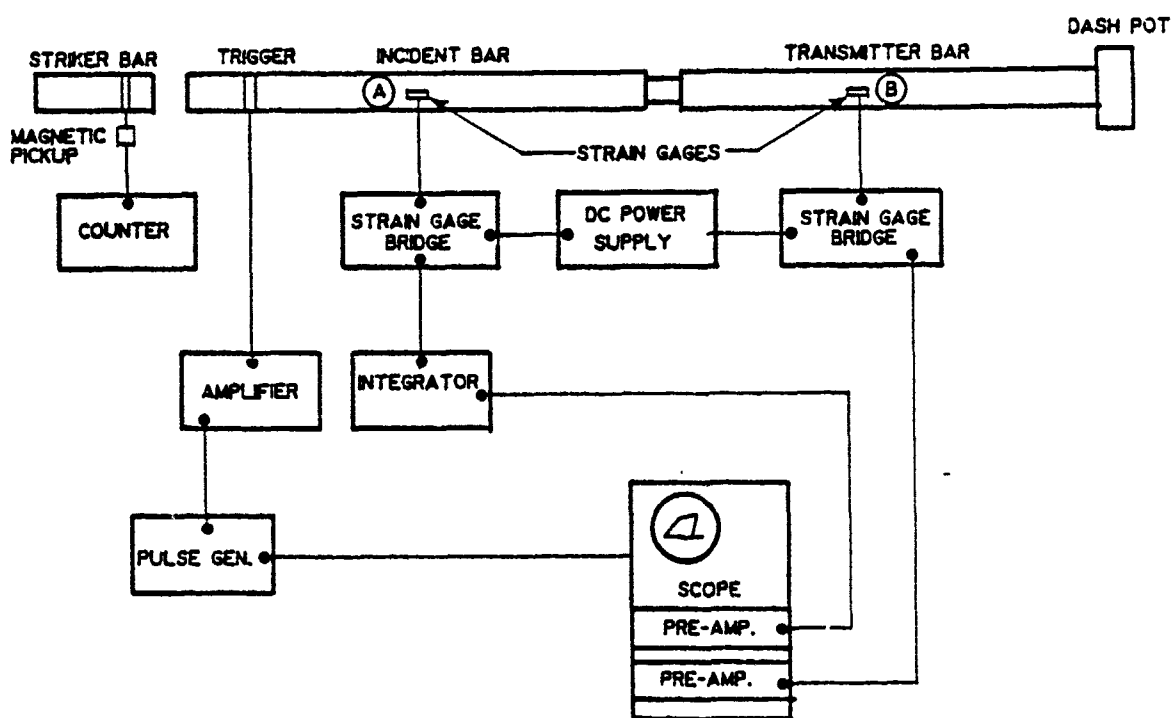


Figure 2. Schematic of Split Hopkinson Pressure Bar

$$V = \frac{\sigma}{\rho C_0} \quad (1)$$

The net particle velocity of the incident bar-specimen interface is the result of both the incident and reflected wave,

$$V_1 = \frac{\sigma_T - \sigma_R}{\rho C_0} \quad (2)$$

Note that the sign of  $\sigma_R$  is opposite that of  $\sigma_I$  and  $\sigma_T$ . The particle velocity of the transmitter bar-specimen interface is

$$V_2 = \frac{\sigma_T}{\rho C_0} \quad (3)$$

By averaging the particle velocities at the specimen-bar interfaces, the average stress and strain-rate in the specimen can be determined from

$$\sigma_{AVG} = \frac{(\sigma_I + \sigma_R + \sigma_T)A_1}{2A_2} \quad (4)$$

and

$$\dot{\epsilon}_{AVG} = \frac{V_1 - V_2}{L_0} \quad (5)$$

where  $A_1$  and  $A_2$  are the areas of the pressure bars and specimen respectively, and  $L_0$  is the initial length of the specimen. The average specimen strain is computed by integrating Equation (5).

## 2. Numerical Analysis

High strain-rate mechanical testing is complicated by the effects of stress wave propagation. At strain rates above  $10^3 \text{ s}^{-1}$  it is difficult to achieve uniform loading conditions over the gage length of a standard tensile specimen because there may be insufficient time to dampen the often complex stress waves generated during the test. The complex geometry associated with grips, specimen design, screw threads, etc., makes analysis of stress wave propagation in such a test virtually intractable.

The SHPB has evolved into a useful high-rate test apparatus because the stress waves generated in long cylinders are relatively simple and are

capable of precise analysis. In addition, specimen dimensions have been reduced significantly to minimize delays associated with stress wave propagation. However, several significant shortcomings are associated with SHPB experiments. First, it is not possible to accurately determine the stress condition in the specimen at failure from the available data, and second, it is frequently not possible to ascertain the mode of failure in the specimen. A comprehensive numerical analysis was conducted on various SHPB experiments to gain some insight into those phenomena.

Because of the dynamic nature of the impulse loading associated with the SHPB experiments, and the highly nonlinear behavior of the concrete test specimens, the finite element method (FEM) of analysis was employed in the research effort through the implementation of the ADINA (Reference 17) computer programs. The analyses were conducted on two-dimensional, axisymmetric models comprised of nine-node isoparametric finite elements (Reference 18). Both linear and nonlinear analyses were performed.

#### C. SCOPE

Two different types of SHPB experiments were simulated in the FEM analyses: (1) Splitting-tensile tests and (2) direct tension tests. In the splitting tension analyses, the FEM model included the 2-inch (51 mm) diameter cylinder and a 10-inch (254 mm) length of the transmitter bar. Three different load cases were investigated. In the direct tension study, both a square notch and saddle notch specimen were analyzed. The FEM model included the entire lengths of the incident and transmitter bars, in addition to the 2-inch (51 mm) diameter specimen. One load case for each specimen type was investigated.

## SECTION II

### SPLITTING-TENSILE TESTS

#### A. INTRODUCTION

The splitting-tensile test has recently established itself as a measure of the tensile strength of concrete (Reference 19). In a standard (static) splitting-tensile test, a concrete cylinder of diameter  $D$  and length  $L$  is placed with its longitudinal axis horizontal between the platens of a testing machine as illustrated in Figure 3. The load is increased until failure by splitting along the vertical diameter takes place. For any compressive load  $P$  on the cylinder, an element near the center on the vertical diameter of the cylinder is subjected to a vertical compressive stress of

$$\sigma_z = \frac{2P}{\pi LD} \left[ \frac{D^2}{z(D-z)} - 1 \right] \quad (6)$$

and a horizontal tensile stress of

$$\sigma_y = \frac{2P}{\pi LD} \quad (7)$$

The horizontal stress,  $\sigma_y$ , on a section through the vertical diameter is shown in Figure 4 (Reference 20). The stress is expressed in terms of  $2P/\pi LD$ . It is observed that a high horizontal compressive stress exists in the vicinity of the loads. However, since this is accompanied by a vertical compressive stress of comparable magnitude, a state of biaxial stress is produced. Therefore, failure in compression does not occur.

To investigate the effects of strain rate on the tensile strength of concrete, splitting-tensile tests of plain concrete specimens were conducted on a Split Hopkinson Pressure Bar, which is illustrated in Figure 1. The specimen arrangement for the splitting-tensile tests is illustrated in Figure 5. The cylindrical specimens were 2 inches (51 mm) in diameter and 2 inches (51 mm) in length. The static, linear material properties for the specimens were calculated as follows: The static compressive strength,  $f'_{cs} = 7000$  psi (48.3 MPa); the static tensile strength  $f_{ts} = 560$  psi (3.86 MPa); Young's Modulus,  $E = 5.5 \times 10^6$  psi (37.9 GPa); and mass density,  $\rho = .0006747$  lb-sec<sup>2</sup>/in<sup>4</sup> (2.4 kg/m<sup>3</sup>).

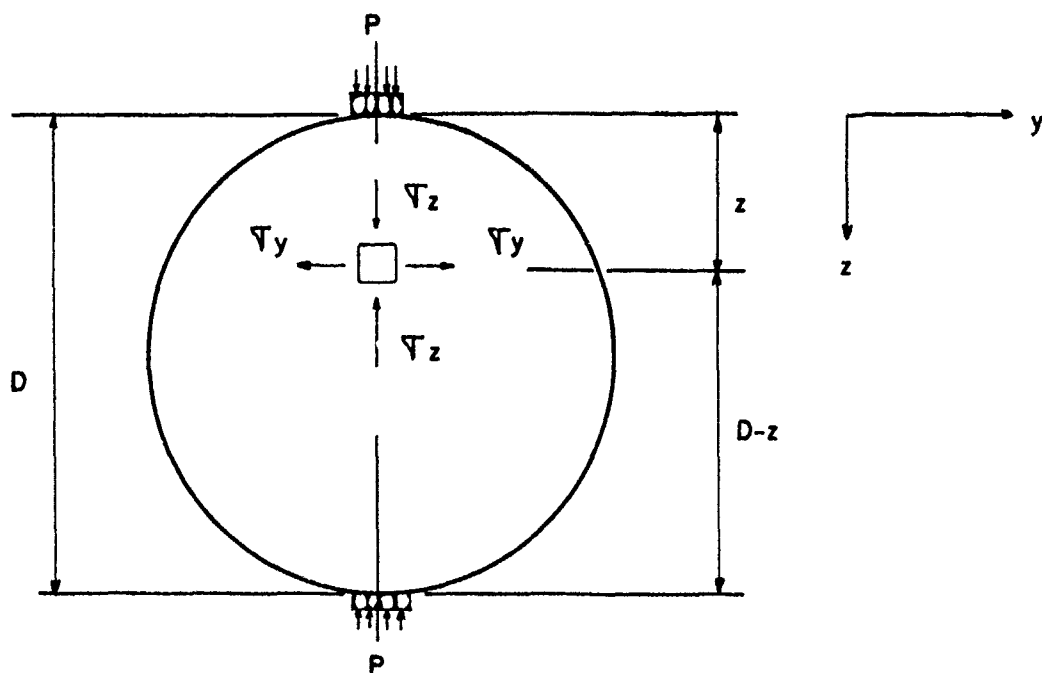


Figure 3. Illustration of Static Split Cylinder Test

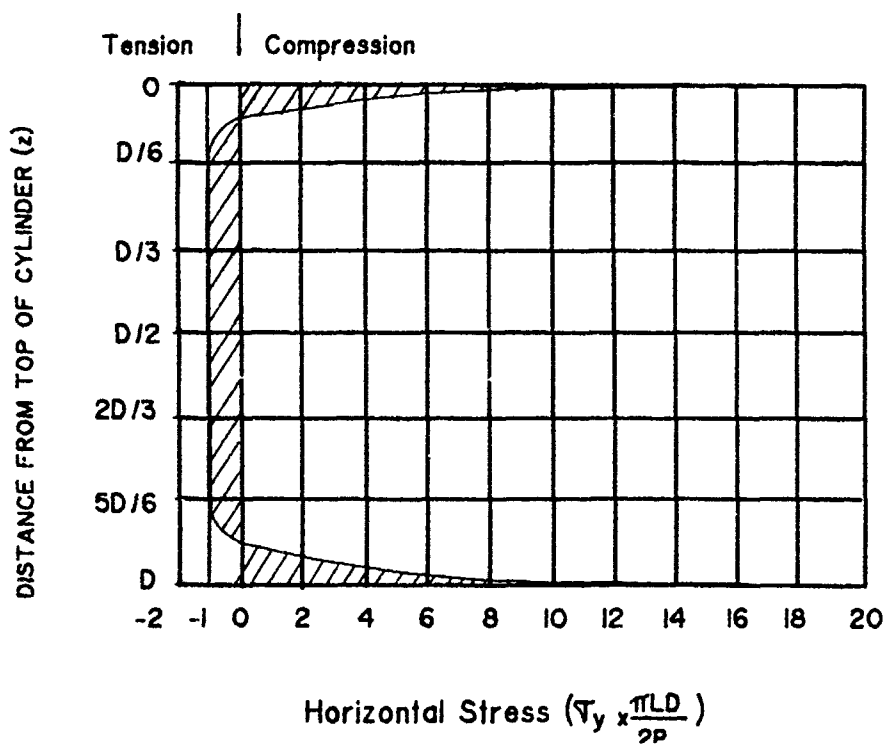
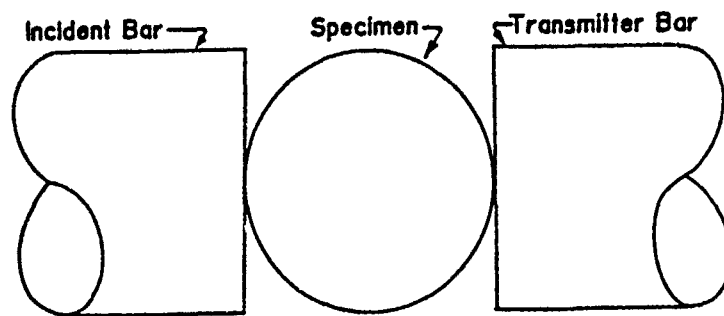
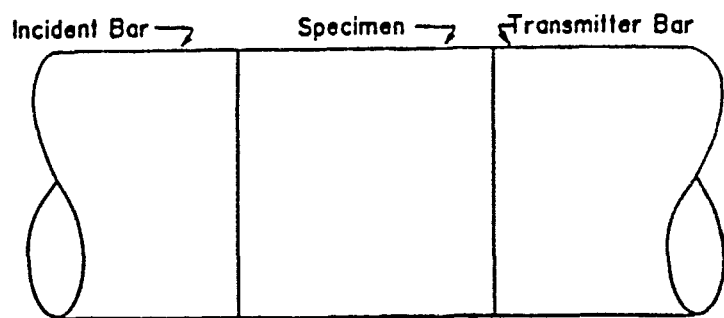


Figure 4. Distribution of Horizontal Stress ( $\sigma_y$ ) on the Vertical Diameter for a Static Split Cylinder Test.



PLAN VIEW



SIDE VIEW

Figure 5. Splitting-Tensile Test Arrangement in the SHPB.

SHPB tests were conducted for three different loading conditions. The stress vs. time histories for these cases are illustrated in Figures 6, 7, and 8. It is assumed that the peak dynamic tensile stress,  $f_{td}$ , of the split cylinder is proportional to the peak transmitted stress,  $\sigma_T$ , through the closed form solution of Neville (Reference 20):

$$f_{td} = \frac{2P}{\pi LD} \quad (8)$$

in which

$$P = \pi R^2 \sigma_T \quad (9)$$

where  $L$  is the specimen length,  $D$  is the specimen diameter, and  $R$  is the radius of the SHPB.

Additionally, the loading rate,  $\dot{\sigma}$ , and the strain rate,  $\dot{\epsilon}$ , in the specimen can be estimated from the expressions

$$\dot{\sigma} = \frac{f_{td}}{\tau} \quad (10)$$

and

$$\dot{\epsilon} = \frac{\dot{\sigma}}{E} \quad (11)$$

where  $\tau$  is the time lag between the start of the transmitted stress wave and the maximum transmitted stress (which is determined from the stress histories presented in Figures 6, 7, and 8). Table 1 summarizes the results obtained from the SHPB tests.

To ascertain the stress condition in the material specimens at failure, a comprehensive finite element method (FEM) study was conducted on the SHPB experiments. Both linear and nonlinear analyses were performed. From the results of the numerical analyses, the dynamic states of stress occurring in the splitting-tensile specimens prior to failure were researched, as well as the modes of failure.



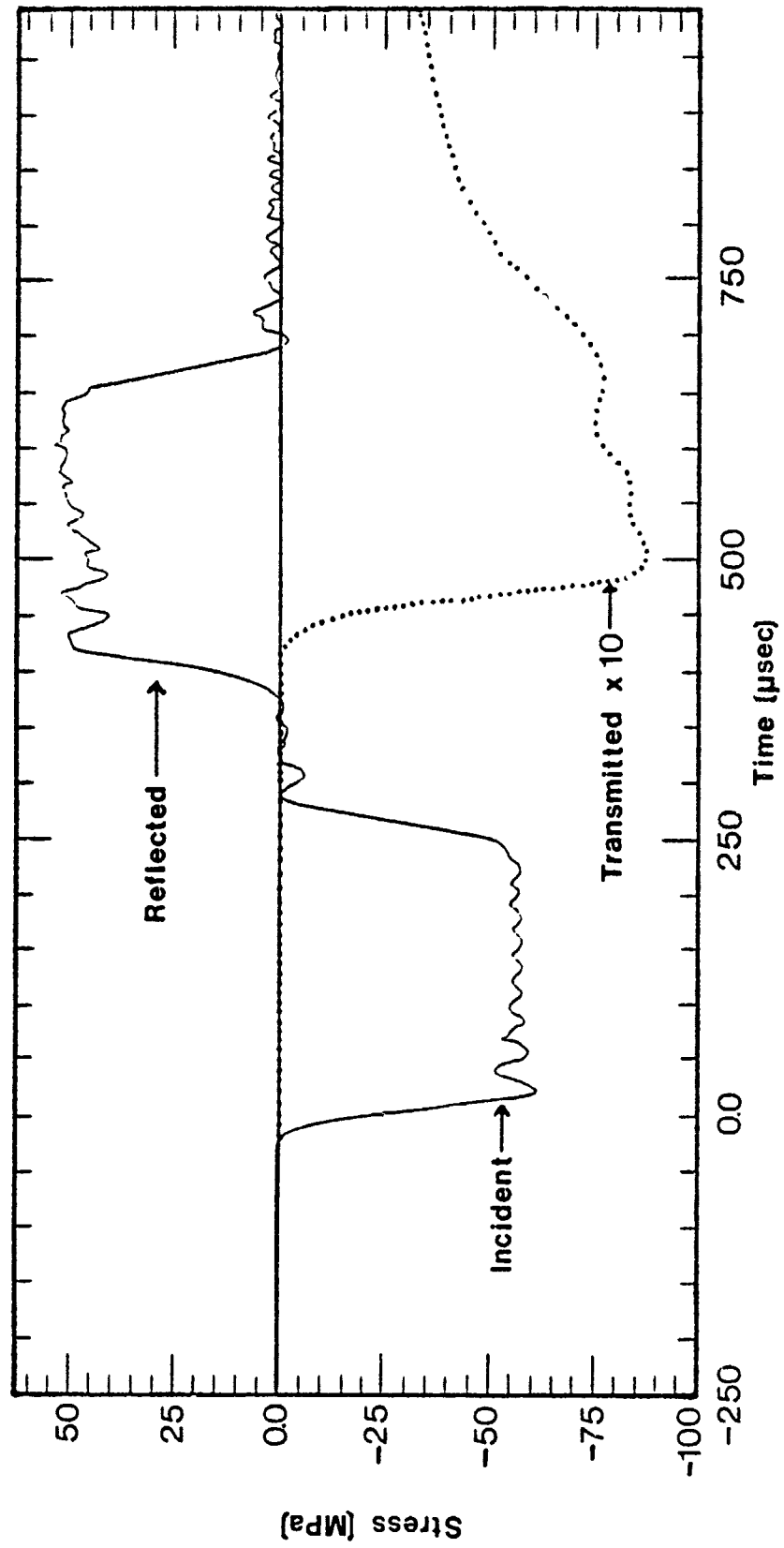


Figure 6. Splitting-Tensile Test Data Trace for Load Case 1.

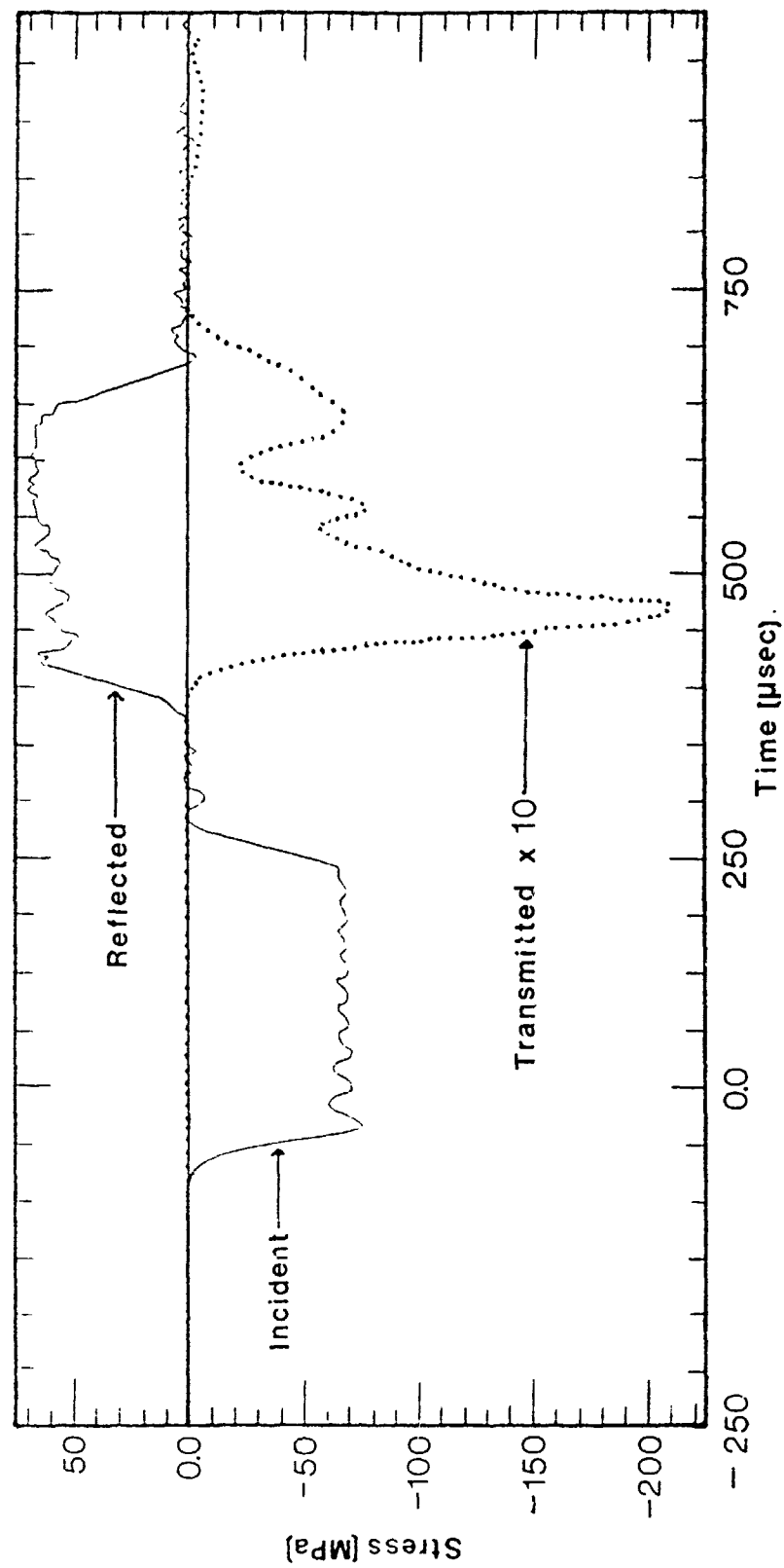


Figure 7. Splitting-Tensile Test Data Trace for Load Case 2.

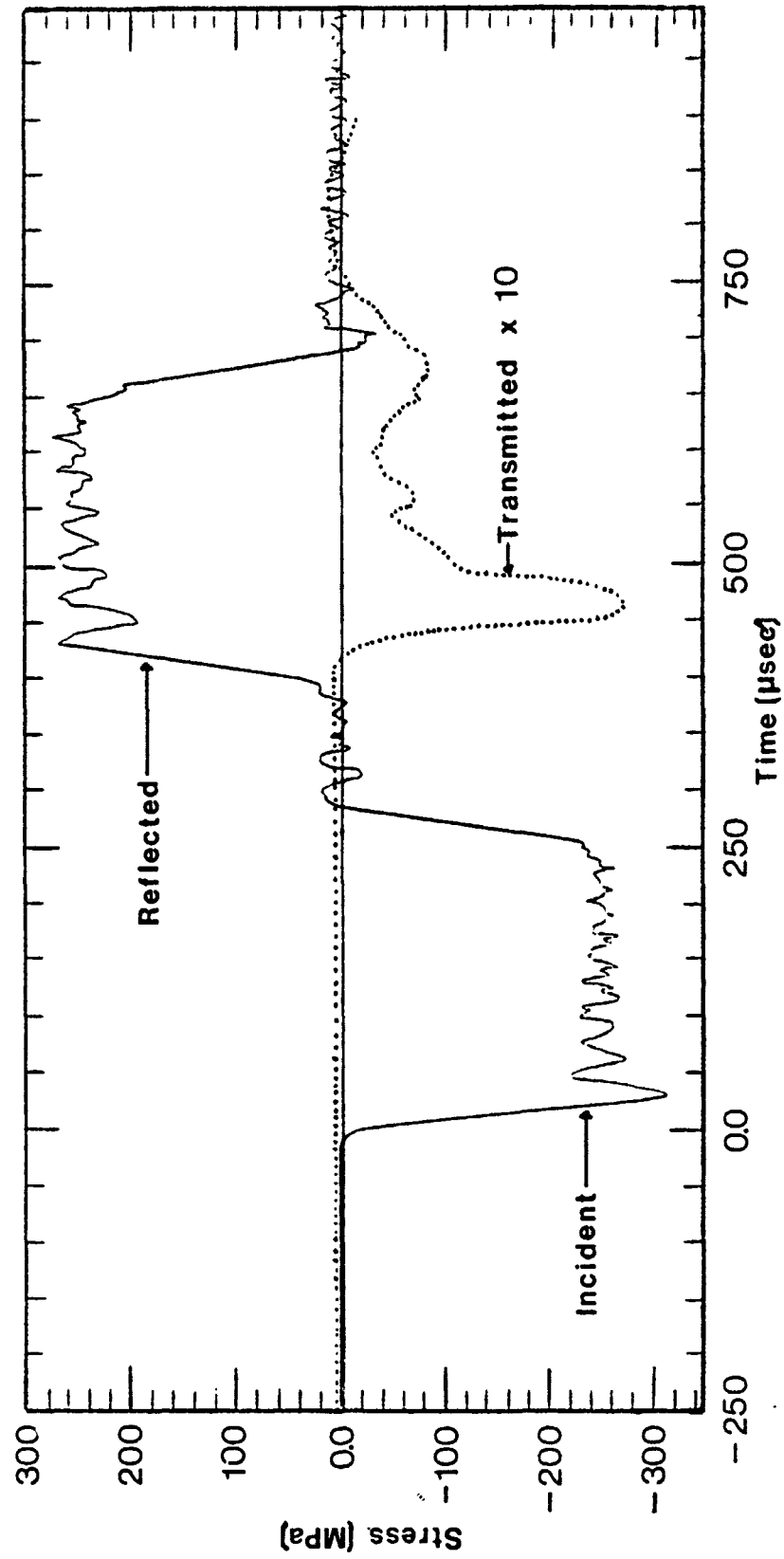


Figure 8. Splitting-Tensile Test Data Trace for Load Case 3.

TABLE 1. SUMMARY OF SHPB RESULTS.

Load Case No.	Incident Stress	Transmitted Stress	Dynamic Tensile Stress	Loading Rate	Strain Rate	Experimental Dynamic Increase Factor
	$\sigma_I$ (psi)	$\sigma_T$ (psi)	$f_{td}$ (psi)	$\dot{\sigma}$ ( $\frac{\text{psi}}{\text{sec}}$ )	( $\text{sec}^{-1}$ )	$\frac{f_{td}}{f_{ts}}$
	(MPa)	(MPa)	(MPa)	( $\frac{\text{GPa}}{\text{sec}}$ )		
1	-8740 -(60.22)	-1270 -(8.76)	635 (4.38)	$9.6 \times 10^6$ (66.25)	1.7	1.14
2	-10550 -(72.76)	-3040 -(20.97)	1520 (10.48)	$2.1 \times 10^7$ (144.83)	3.8	2.71
3	-38320 -(264.27)	-4080 -(28.14)	2040 (14.07)	$4.2 \times 10^7$ (289.66)	7.7	3.64

## B. LINEAR ANALYSES

### 1. The FEM Model

An illustration of the FEM model employed in the study is depicted in Figure 9. The cylinder is comprised of 1200 eight-node, two-dimensional finite elements. To avoid the development of artificial reflected stresses at the interface between the cylinder and the transmitter bar by the imposition of a rigid boundary, a 10-inch (254 mm) length of the transmitter bar was incorporated into the FEM model. This portion of the model is comprised of 200 eight-node, two-dimensional finite elements. The loading on the split cylinder is applied at the boundary of the cylinder and the incident bar, which is designated as the top of the cylinder.

### 2. Static Analysis

To calibrate the FEM model and verify its accuracy, static analyses of the cylinder portion of the model were conducted for the three load cases summarized in Table 1. The statically applied load was taken as the product

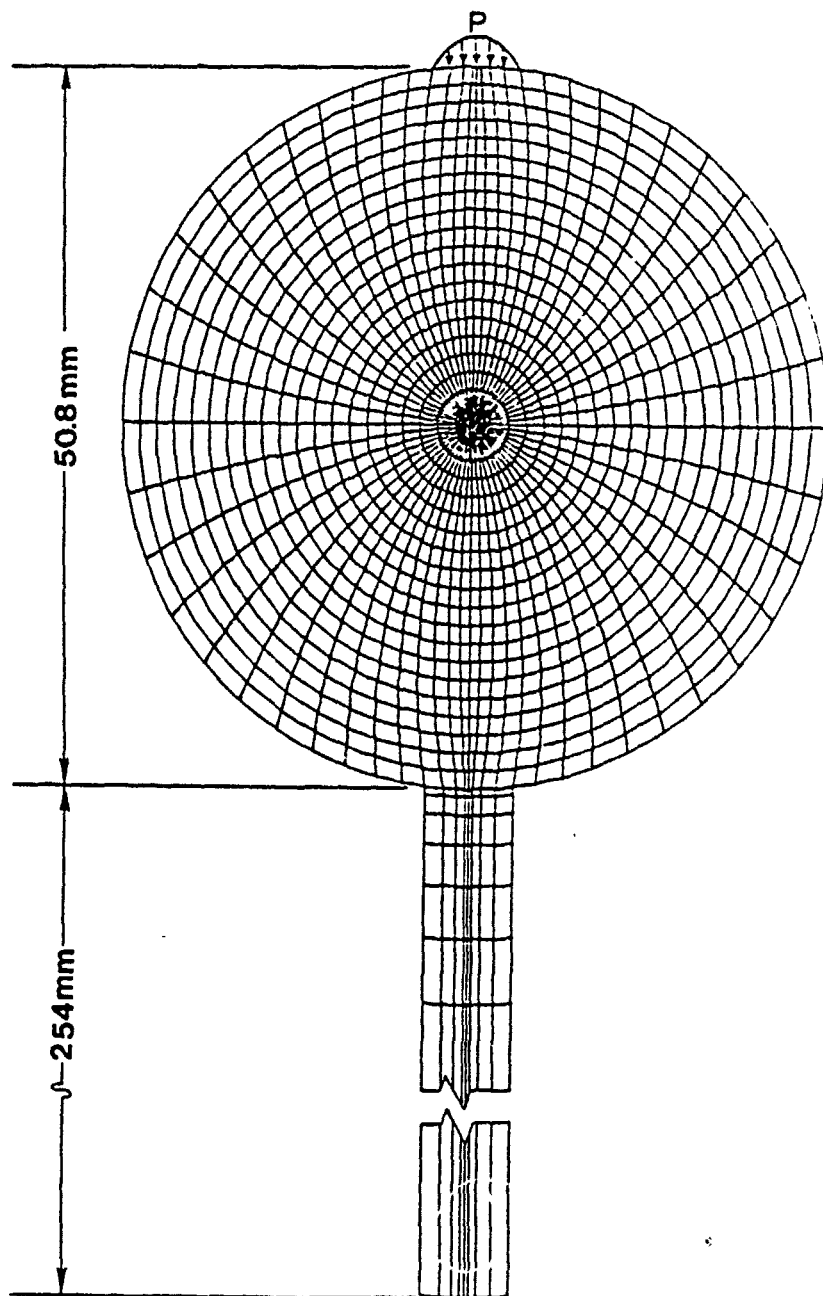


Figure 9. FEM Model of Cylinder and Portion of Transmitter Ban

of the incident stress and the cross-sectional area of the incident bar. The numerical results were compared with a closed-form analytical solution (Reference 20).

The distribution of the horizontal and vertical stresses along the vertical diameter, obtained from the FEM analysis for Load Case 1, are presented in Figures 10 and 11, respectively. Similar plots for the horizontal and vertical stress distributions along the horizontal diameter are presented in Figures 12 and 13. The numerical results for the horizontal and vertical stresses occurring at the center of the cylinder for all three load cases are presented in Table 2. Excellent correlation with the closed-form solutions is noted.

TABLE 2. STATIC STRESSES AT CENTER OF CYLINDER.

Load Case No.	Vertical Stress, $\sigma_z$ (psi) (MPa)		Horizontal Stress, $\sigma_y$ (psi) (MPa)	
	FEM Analysis	Eq. (5)	FEM Analysis	Eq. (6)
1	-1861	-1905	613	635
	-(12.83)	-(12.14)	(4.23)	(4.38)
2	-4456	-4560	1468	1520
	-(30.73)	-(31.45)	(10.12)	10.48)
3	-5980	-6120	1970	2040
	-(4.124)	-(42.21)	(13.39)	(14.07)

### 3. Dynamic Analysis

Dynamic analyses were conducted on the SHPB splitting-tensile specimens described in the previous section. The loading conditions for the dynamic analyses were determined from the SHPB data curves of the incident, reflected, and transmitted strain gage traces presented in Figures 6, 7, and 8. These curves were corrected for dispersion and phase change. The stress on the

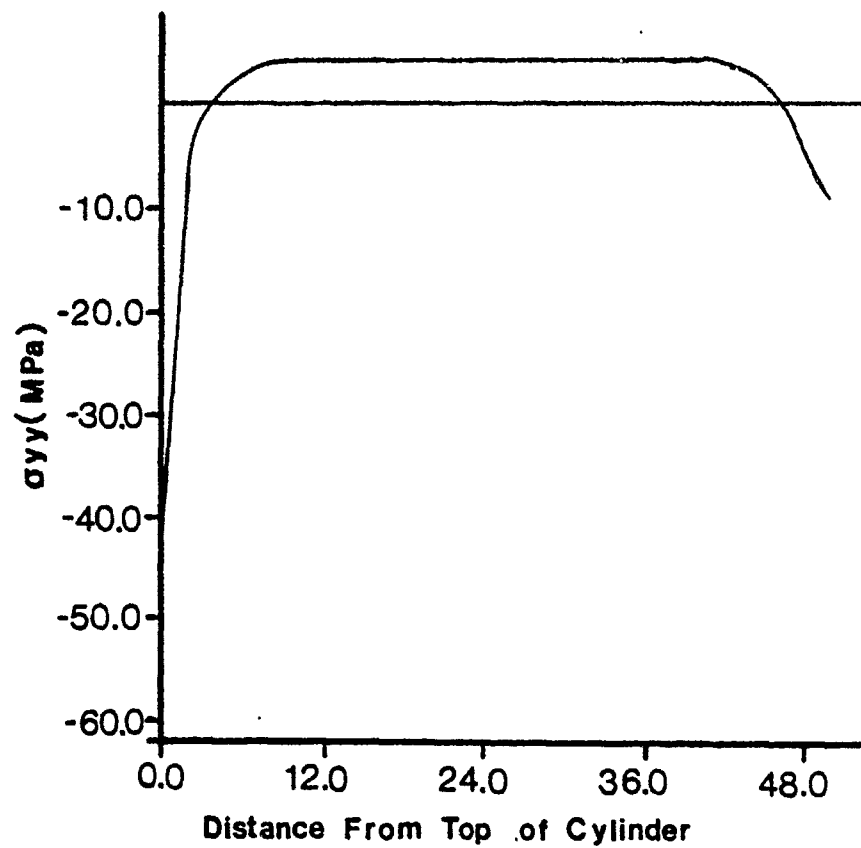


Figure 10. Horizontal Stress Distribution along the Vertical Diameter

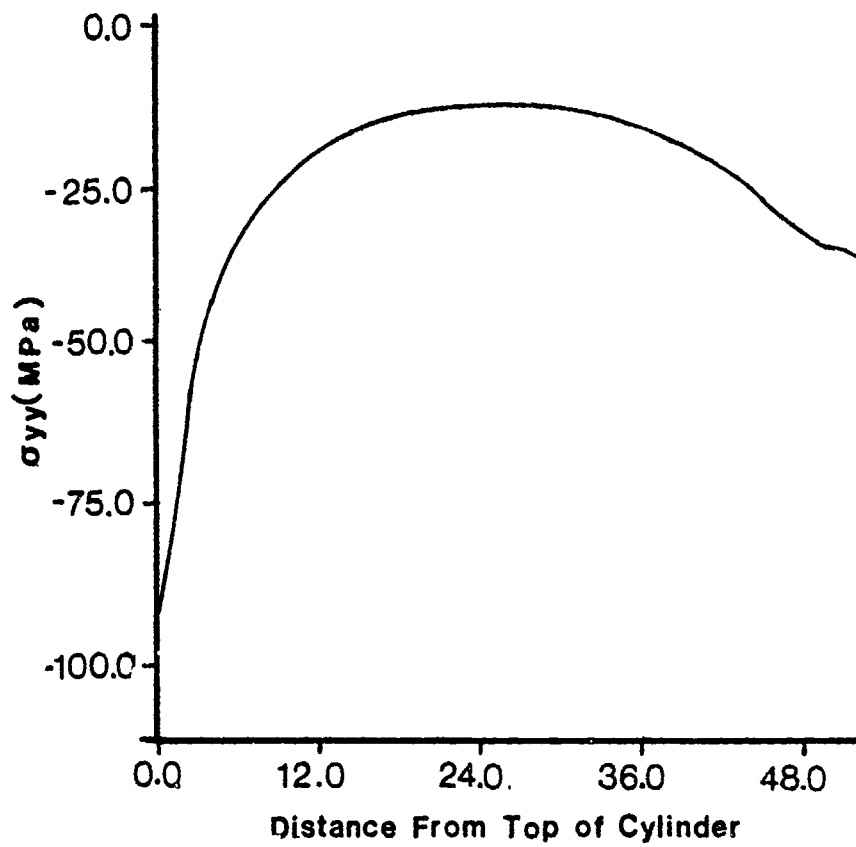


Figure 11. Vertical Stress Distribution along the Vertical Diameter



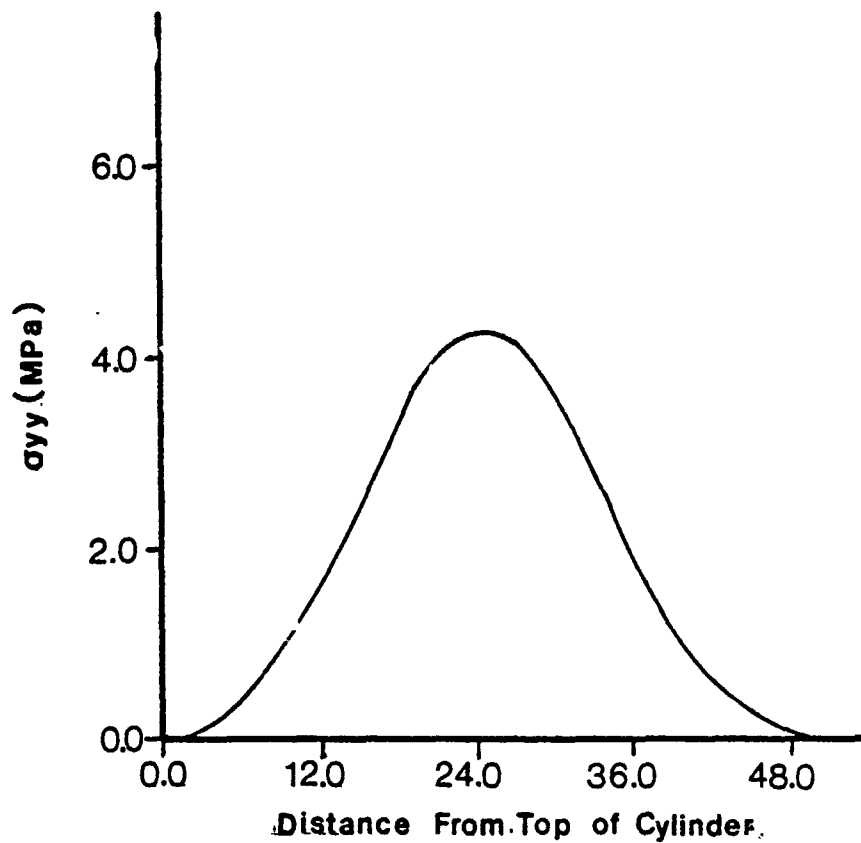


Figure 12. Horizontal Stress Distribution along the Horizontal Diameter

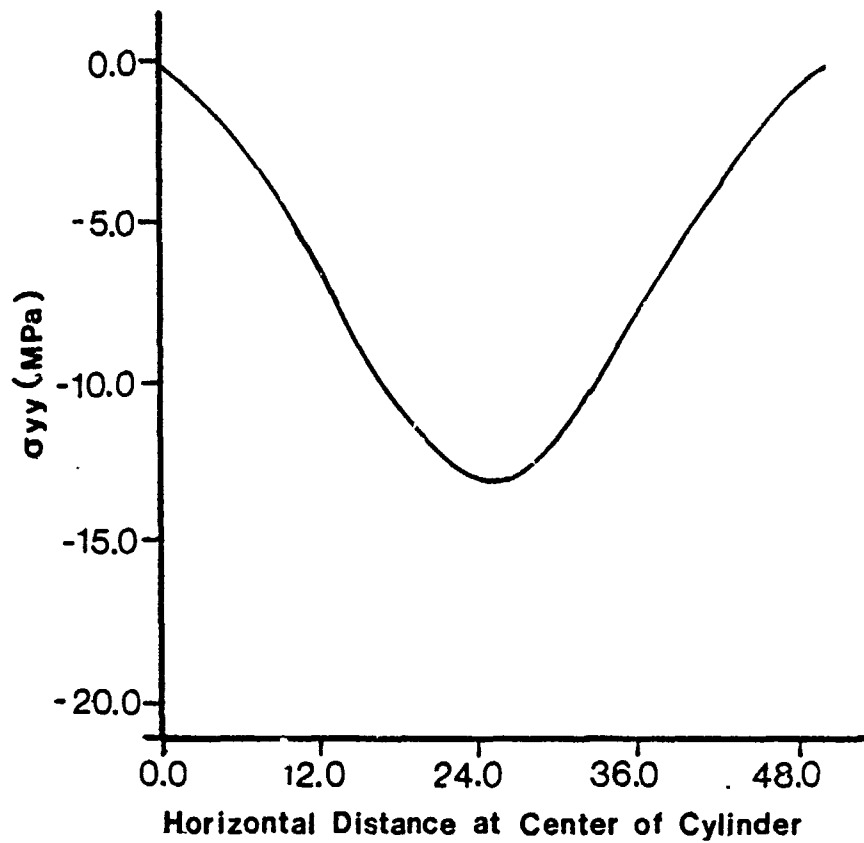


Figure 13. Vertical Stress Distribution along the Horizontal Diameter

incident face, STRESS 1, the stress on the transmitted face, STRESS 2, and the average of these two stresses, AVE STRESS, are shown in Figures 14, 15, and 16, for Load Cases 1, 2, and 3, respectively.

Experience with SHPB experiments (References 10, 11) suggests that the STRESS 2 curve is indicative of the load transmitted to the specimen. In the numerical analyses, the load functions were simulated with the ramp loading depicted in Figure 17. The rise time,  $t_r$ , the stress level,  $P_0$ , and the time of duration,  $t_d$ , for the three load cases are summarized in Table 3.

TABLE 3. PARAMETERS FOR RAMP LOAD FUNCTION

Load Case No.	Rise Time $t_r$ ( $\mu$ sec)	Stress Level $P_0$ (psi) (MPa)	Time of Duration $t_d$ ( $\mu$ sec)
1	66	-1270 -(8.76)	100
2	72	-3040 -(20.97)	100
3	48	-4080 -(28.14)	100

For problems in which an elastic body is subjected to a short-duration impulse loading, the propagation of stress/strain waves through the body must be considered in formulating the solution. Modal analyses generally do not yield cost-effective, accurate results for wave propagation problems, therefore, a direct numerical integration procedure must be utilized.

In the present study, the Newmark method of implicit time integration with a consistent mass formulation is employed. The dynamic equilibrium equations for the system are expressed as

$$[M]\{\ddot{U}(t)\} + [C]\{\dot{U}(t)\} + [K]\{U(t)\} = \{R(t)\} \quad (12)$$

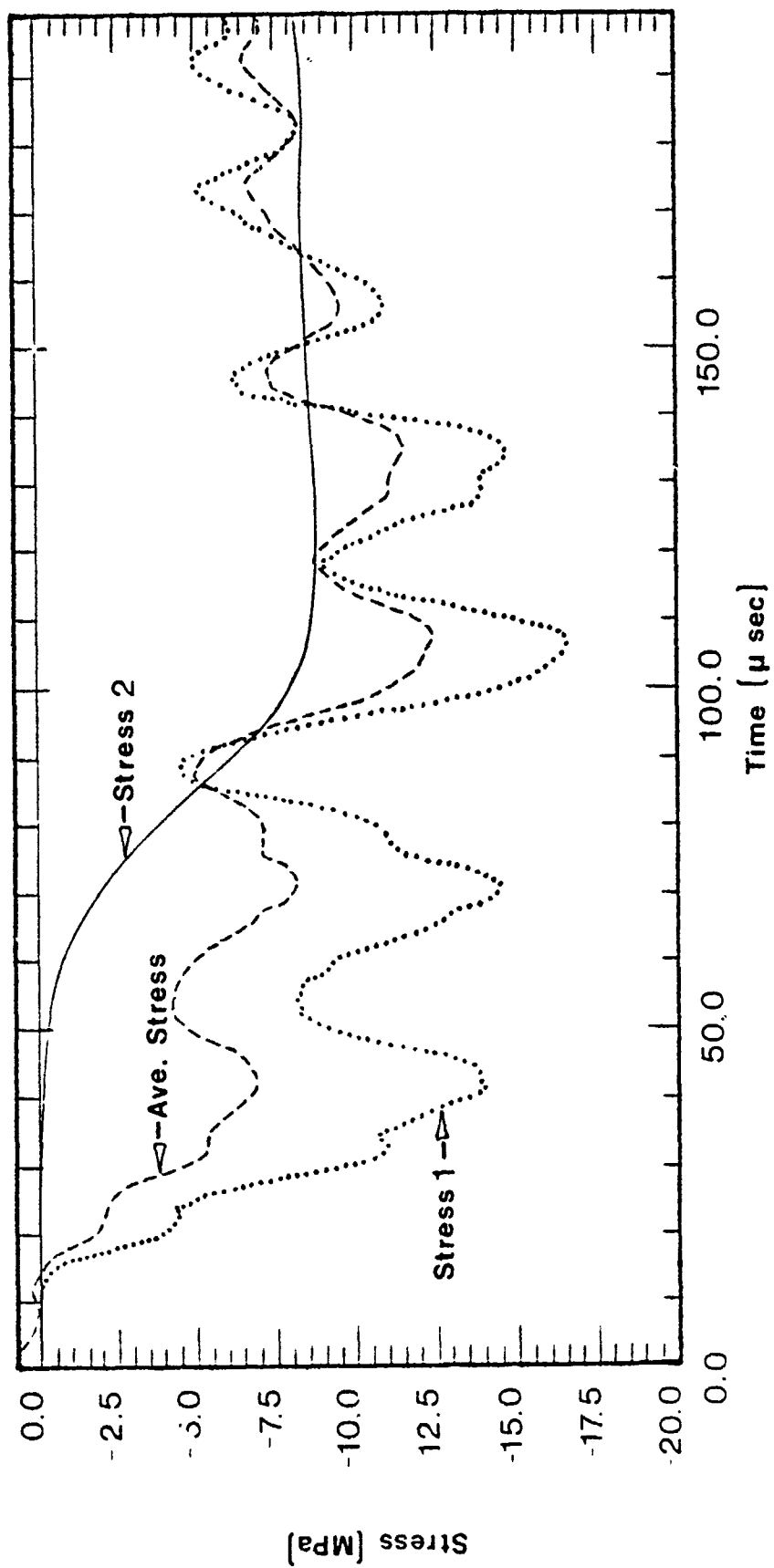


Figure 14. Corrected SHPB Data for Load Case 1.

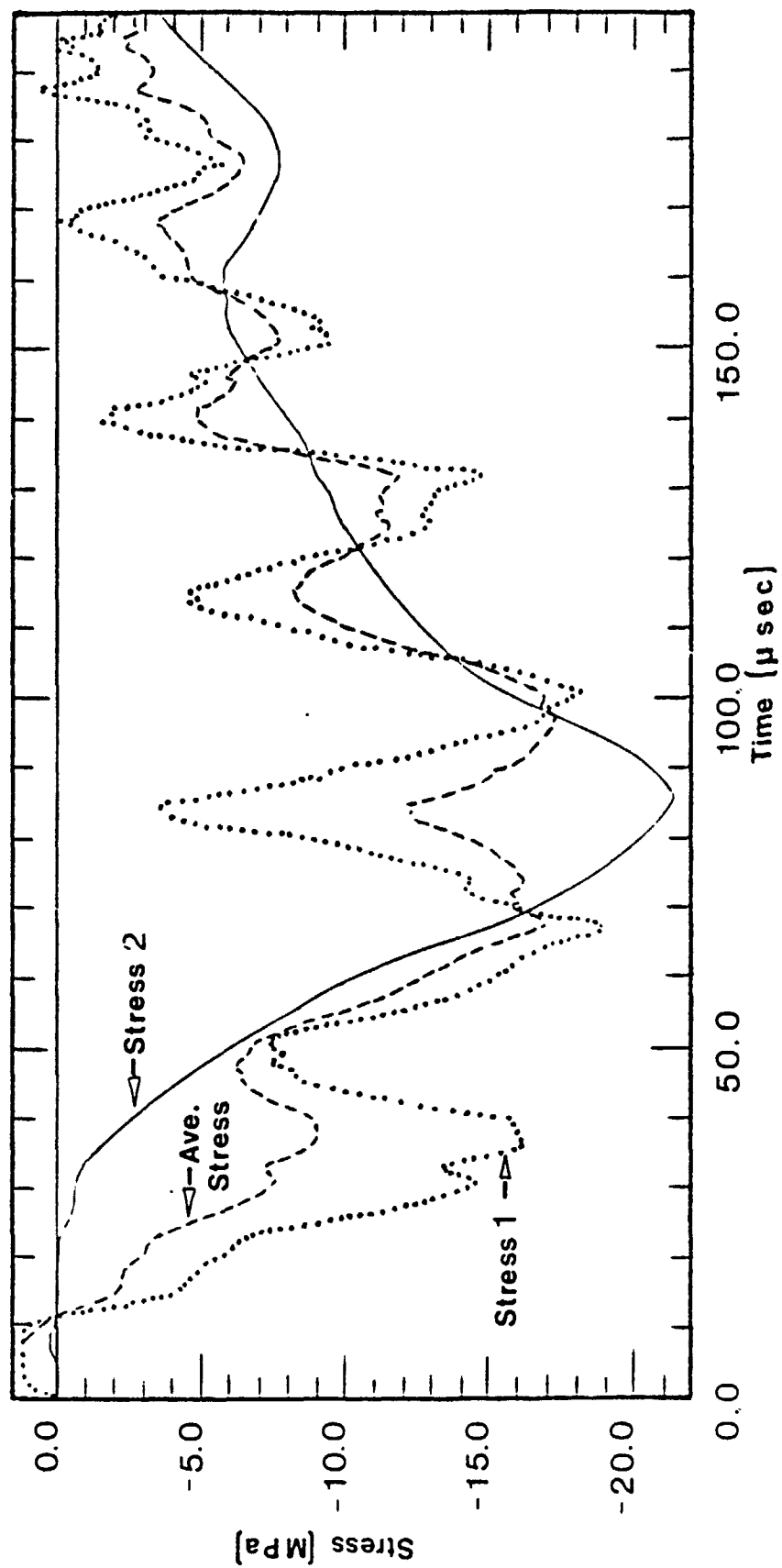


Figure 15. Corrected SHPB data for Load Case 2.

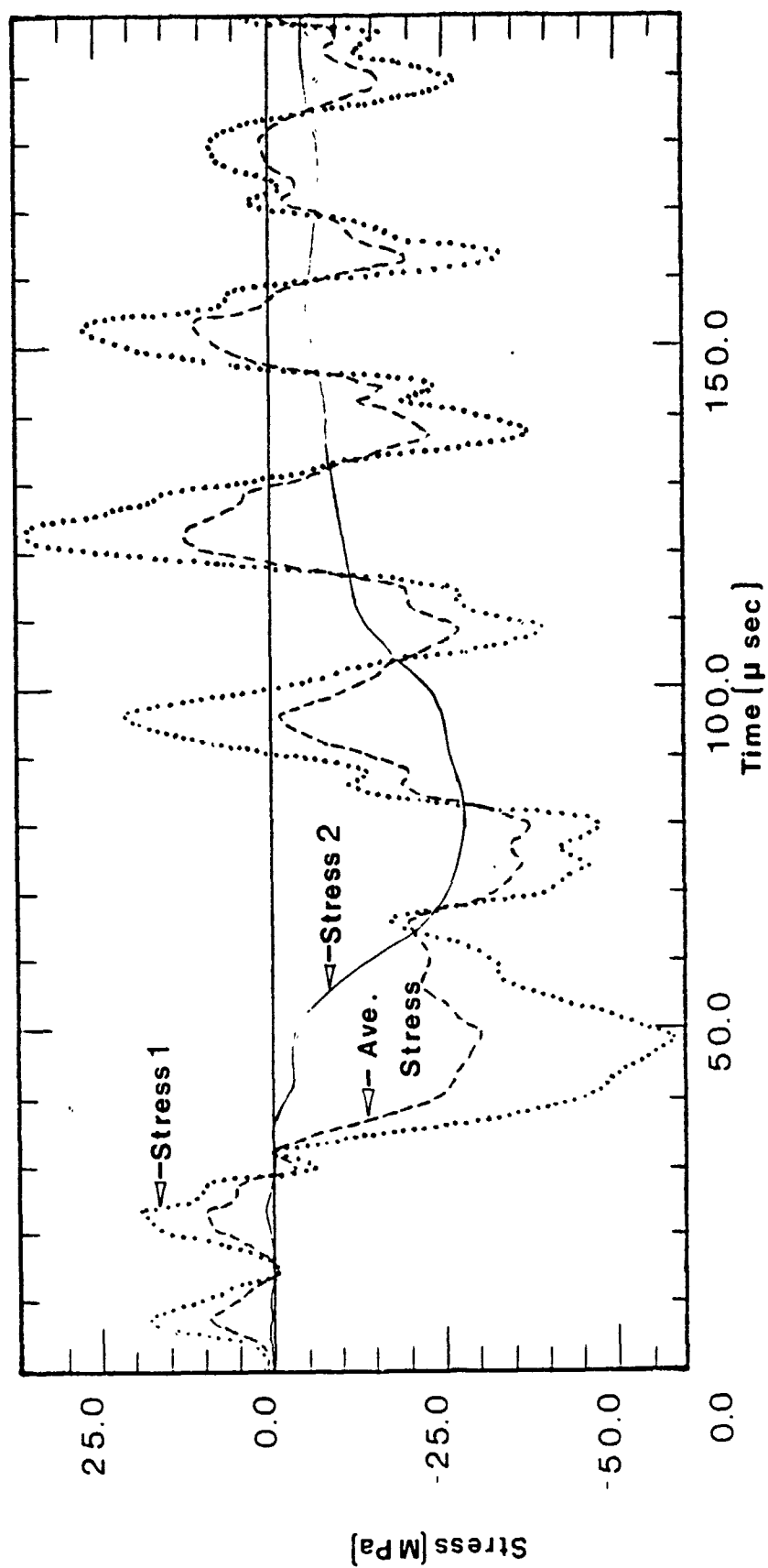


Figure 16. Corrected SHPB Data for Load Case 3.

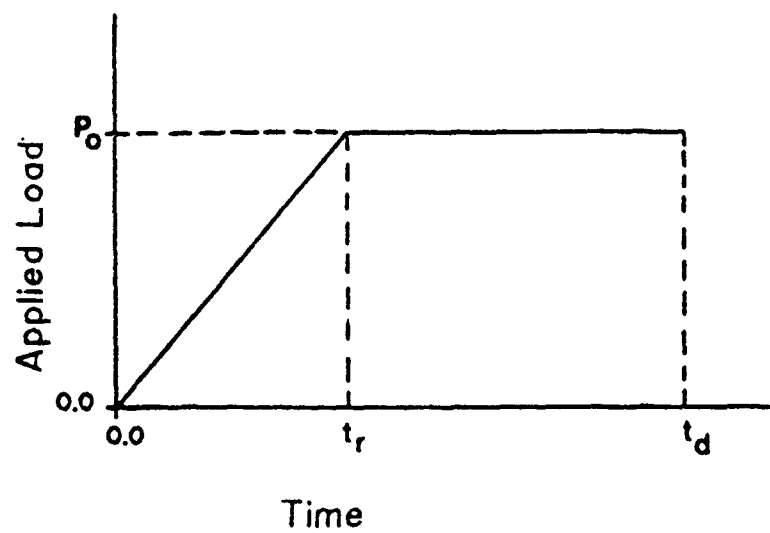


Figure 17. Typical Ramp Loading Function used in FEM Analysis.

when  $[M]$ ,  $[C]$ ,  $[K]$  are the mass, damping, and stiffness matrices;  $\{R\}$  is the external load vector; and  $\{U\}$ ,  $\{\dot{U}\}$ , and  $\{\ddot{U}\}$  are the displacement, velocity, and acceleration vectors of the finite element assemblage. In the Newmark method, the following assumptions are used (Reference 21):

$${}^{t+\Delta t}\{U\} = {}^t\{U\} + \frac{\Delta t}{2} ({}^t\{\dot{U}\} + {}^{t+\Delta t}\{\dot{U}\}) \quad (13)$$

$${}^{t+\Delta t}\{\dot{U}\} = {}^t\{\dot{U}\} + \frac{\Delta t}{2} ({}^t\{\ddot{U}\} + {}^{t+\Delta t}\{\ddot{U}\}) \quad (14)$$

In addition to Equations (13) and (14), for solution of the displacements, velocities, and accelerations at time  $t + \Delta t$ , the equilibrium equations (Equation (12)) at time  $t + \Delta t$  are also considered:

$$[M] {}^{t+\Delta t}\{\ddot{U}\} + [C] {}^{t+\Delta t}\{\dot{U}\} + [K] {}^{t+\Delta t}\{U\} = {}^{t+\Delta t}\{R\} \quad (15)$$

Solving from Equation (14) for  ${}^{t+\Delta t}\{\ddot{U}\}$  in terms of  ${}^{t+\Delta t}\{U\}$ , and then substituting for  ${}^{t+\Delta t}\{\ddot{U}\}$  into Equation (13), the equations for  ${}^{t+\Delta t}\{\ddot{U}\}$  and  ${}^{t+\Delta t}\{\dot{U}\}$  are obtained, each in terms of the unknown displacements  ${}^{t+\Delta t}\{U\}$  only. These two relations for  ${}^{t+\Delta t}\{\dot{U}\}$  and  ${}^{t+\Delta t}\{\ddot{U}\}$  are substituted into Equation (15) to solve for  ${}^{t+\Delta t}\{U\}$ , after which, using Equation (13) and Equation (14),  ${}^{t+\Delta t}\{\ddot{U}\}$  and  ${}^{t+\Delta t}\{\dot{U}\}$  can also be calculated.

The time step selected for temporal integration in a wave propagation problem is critical to the accuracy and stability of the solution. Since the Newmark method is unconditionally stable, selection of the time step can be based entirely upon accuracy. In a wave propagation problem, the maximum time step is related to wave speed in the material and element size. The maximum time step is selected so that the stress wave propagates the distance between element integration points within that time increment. The maximum time step is defined by

$$(\Delta t)_{\max} = \frac{L_e/2}{c} \quad (16)$$

where  $L_e$  is the length of an element in the direction of wave propagation, and  $c$  is the velocity of wave propagation, given by



$$c = \frac{E}{\rho} \quad (17)$$

It has been determined from experience (Reference 22) that a time step of

$$\Delta t \leq \frac{1}{3}(\Delta t)_{\max} \quad (18)$$

yields accurate results. In the present study a time step of  $\Delta t = 50$  nano-seconds was used for all dynamic analyses.

Time histories for the horizontal stress,  $\sigma_y$ , for Load Case 1 at five locations along the vertical diameter are illustrated in Figures 18, 19, 20, 21, and 22 for  $z$  equal to 0.125D, 0.30D, 0.50D, 0.715D, and 0.915D, respectively. Similar time histories for Load Case 2 are presented in Figures 23 through 27, and for Load Case 3 are presented in Figures 28 through 32. These time histories indicate that the maximum horizontal stress,  $(\sigma_y)_{\max}$ , occurs in the vicinity of the center of the cylinder ( $z = 0.50D$ ). The values for  $(\sigma_y)_{\max}$ , for the three load cases, are 690 psi (4.76 MPa), 1650 psi (11.38 MPa), and 2450 psi (16.90 MPa), as illustrated in Figures 20, 25, and 30, respectively. This observation suggests that, under dynamic loading, the cylinder would initiate cracking somewhere in its interior between the loading face and middepth. The crack would then propagate along the vertical diameter toward the outer boundaries of the cylinder and eventually perpetuate failure.

Time histories for the vertical stress,  $\sigma_z$ , in the transmitter bar are illustrated in Figures 33, 34, and 35 for Load Cases 1, 2, and 3, respectively. The computed maximum vertical stress,  $(\sigma_z)_{\max}$ , for the three load cases are 1540 psi (10.62 MPa), 3400 psi (23.45 MPa), and 5750 psi (34.66 MPa), respectively. The experimentally measured transmitted stresses are illustrated in Figures 6, 7, and 8 for Load Cases 1, 2, and 3, respectively. The corresponding values for  $(\sigma_z)_{\max}$  for the three load cases are 1300 psi (8.97 MPa), 3200 psi (22.07 MPa), and 4000 psi (27.59 MPa), respectively. For each case the measured transmitted stress is higher than the calculated stress. However, this is to be expected in a linear analysis where no cracking of the specimens is considered. Results for the same computed stress based upon a nonlinear analysis are in closer agreement with the experimentally measured transmitted

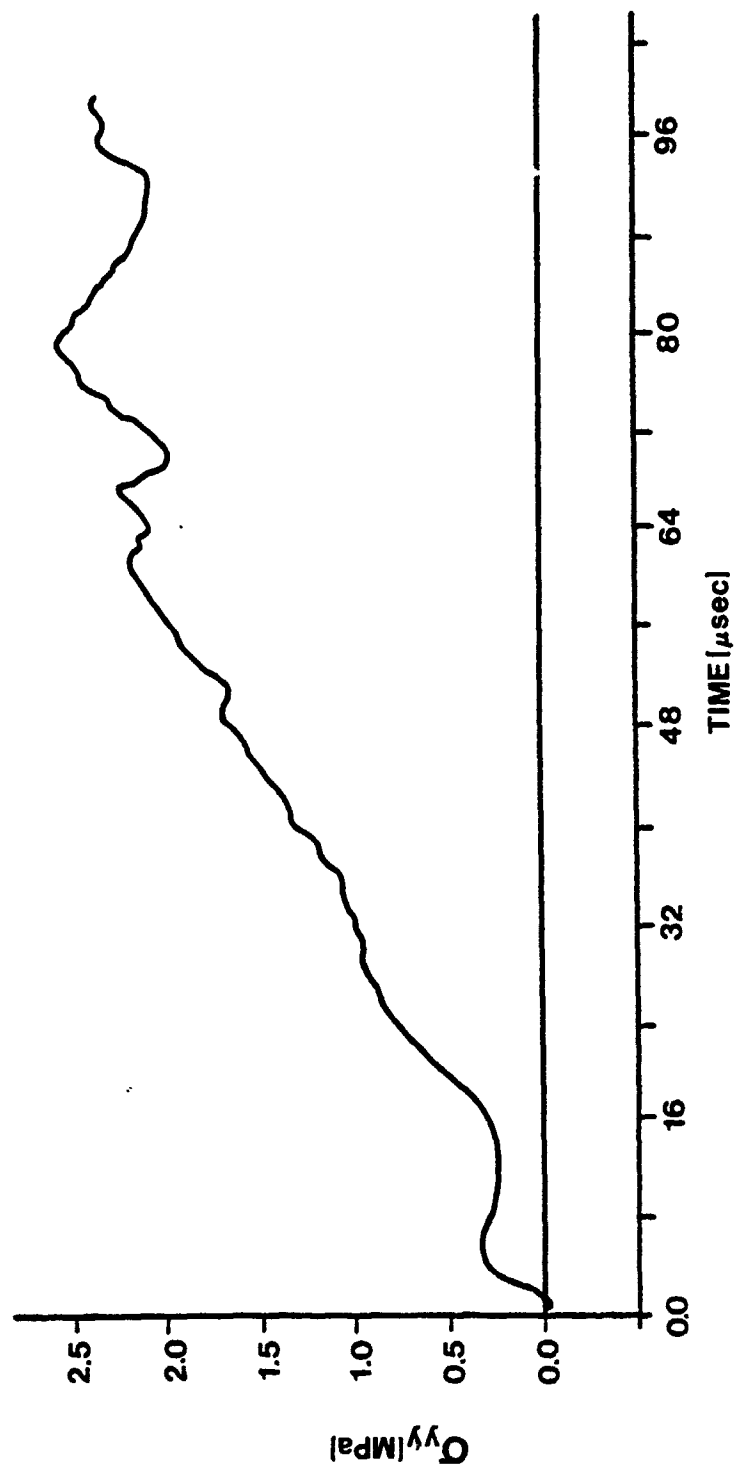


Figure 18. Time History for Horizontal Stress at  $z = .125D$ , Load Case 1.

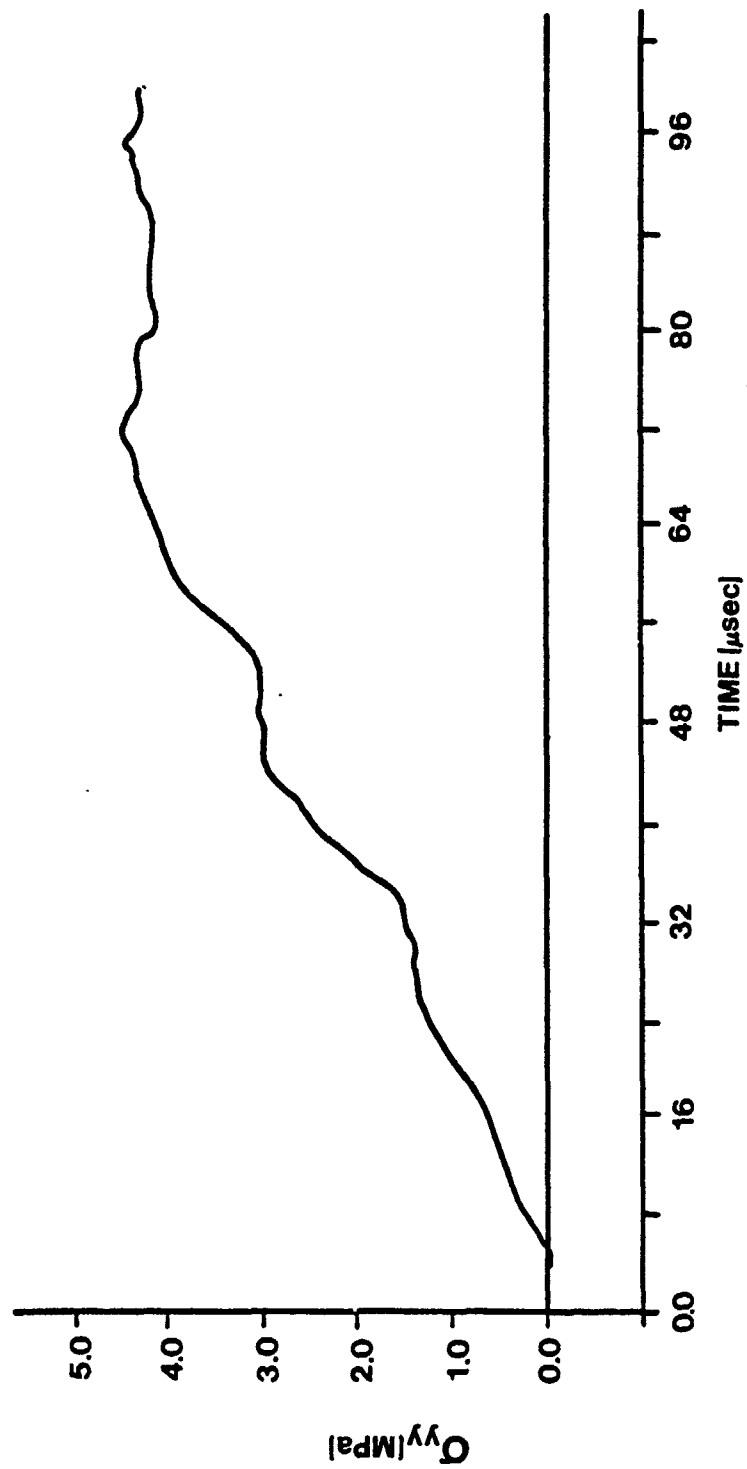


Figure 19. Time History for Horizontal Stress at  $z = 0.30D$ , Load Case 1.

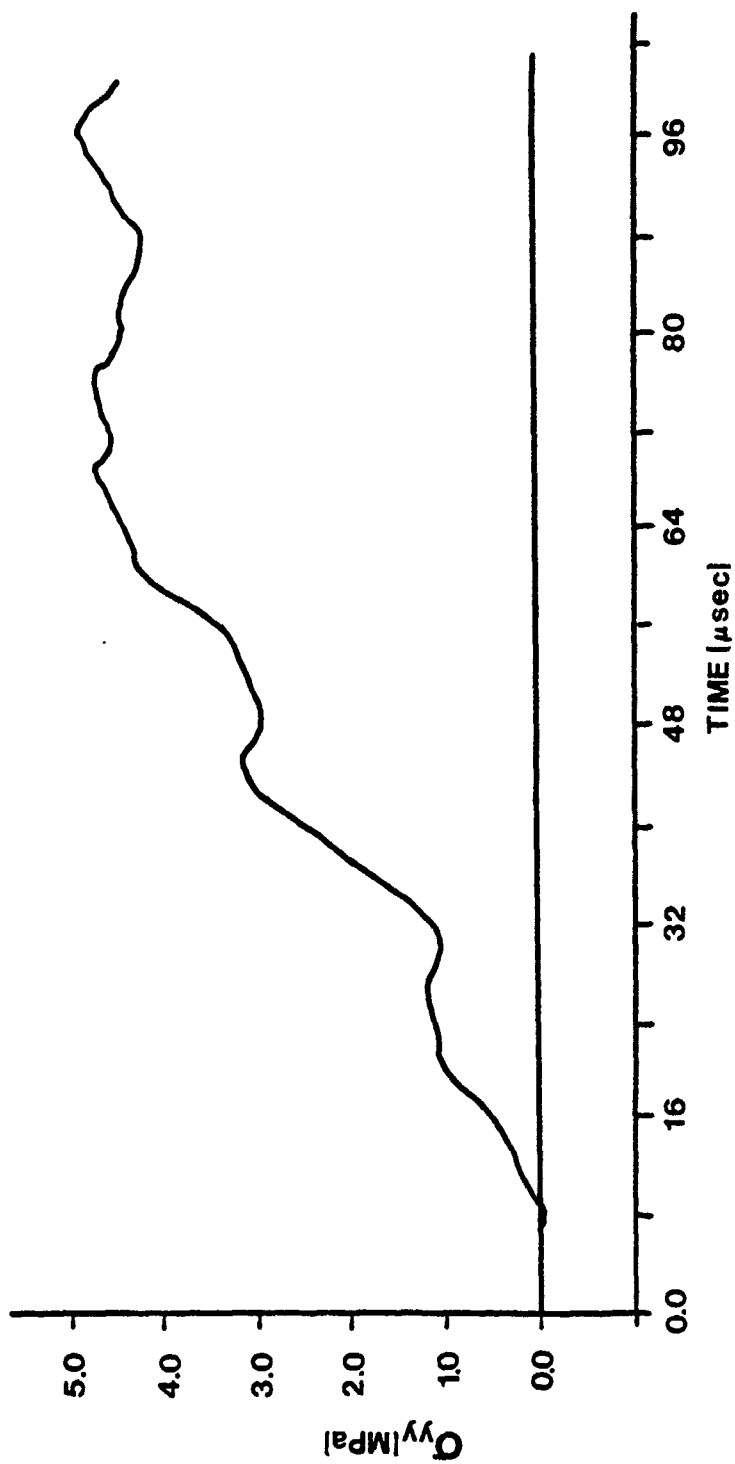


Figure 20. Time History for Horizontal Stress at  $z = 0.50D$ , Load Case 1.

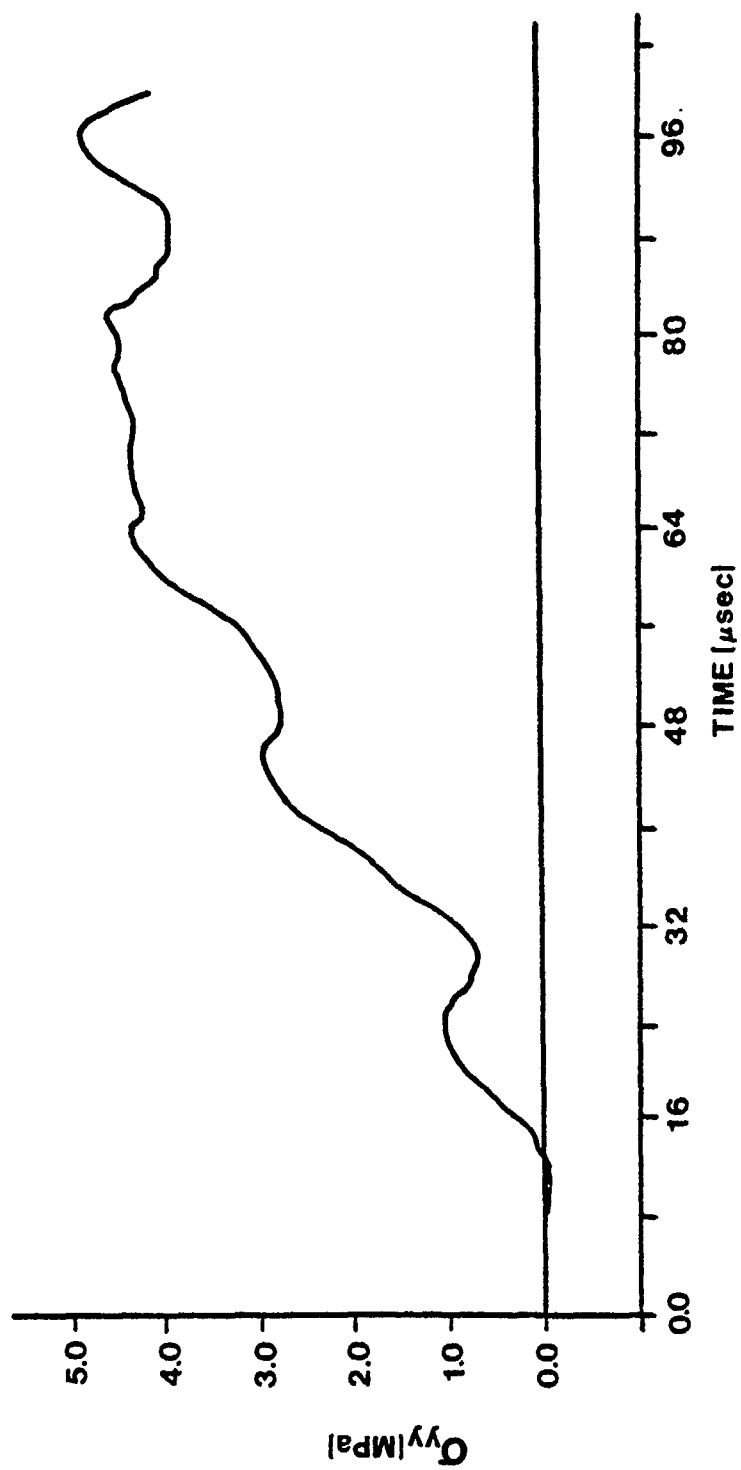


Figure 21. Time History for Horizontal Stress at  $z = 0.715D$ , Load Case 1.

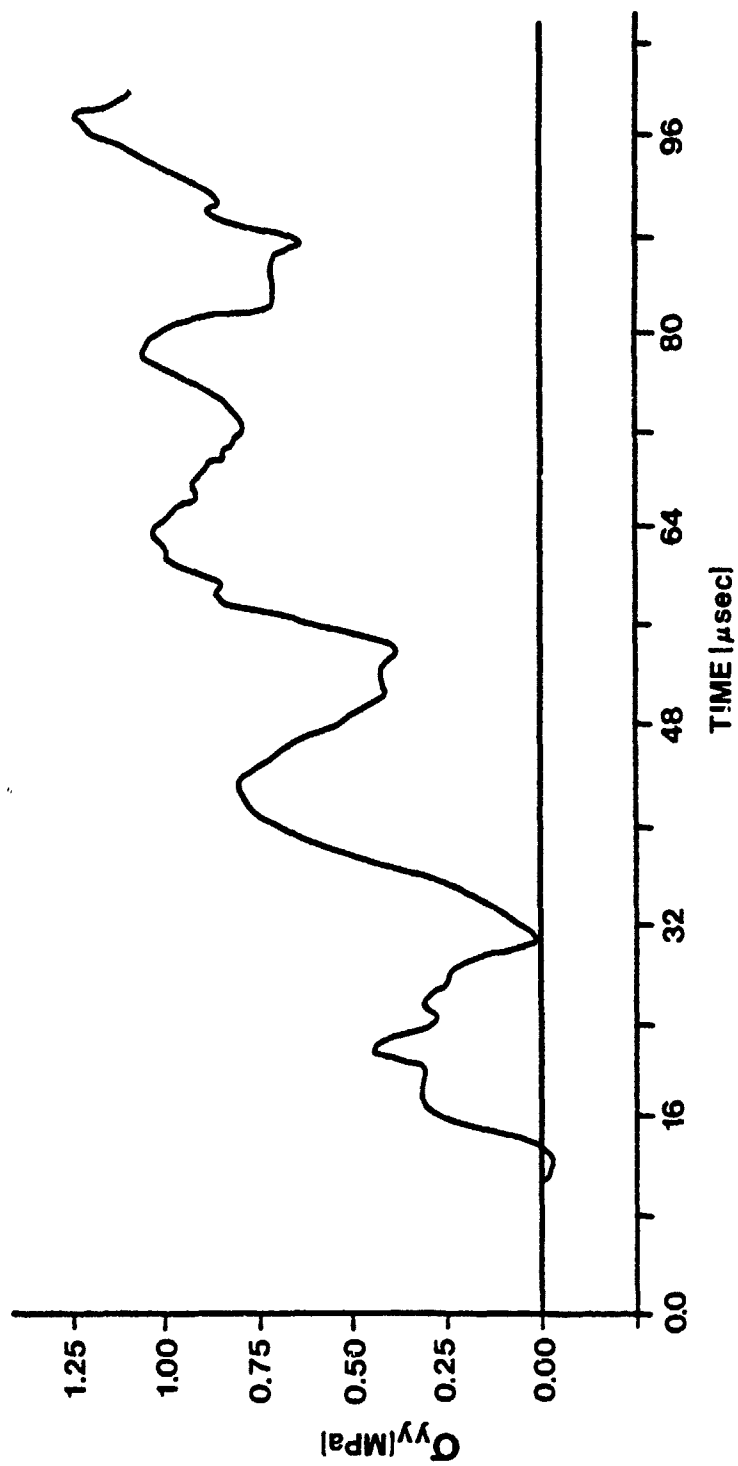


Figure 22. Time History for Horizontal Stress at  $z = 0.915D$ , Load Case 1.

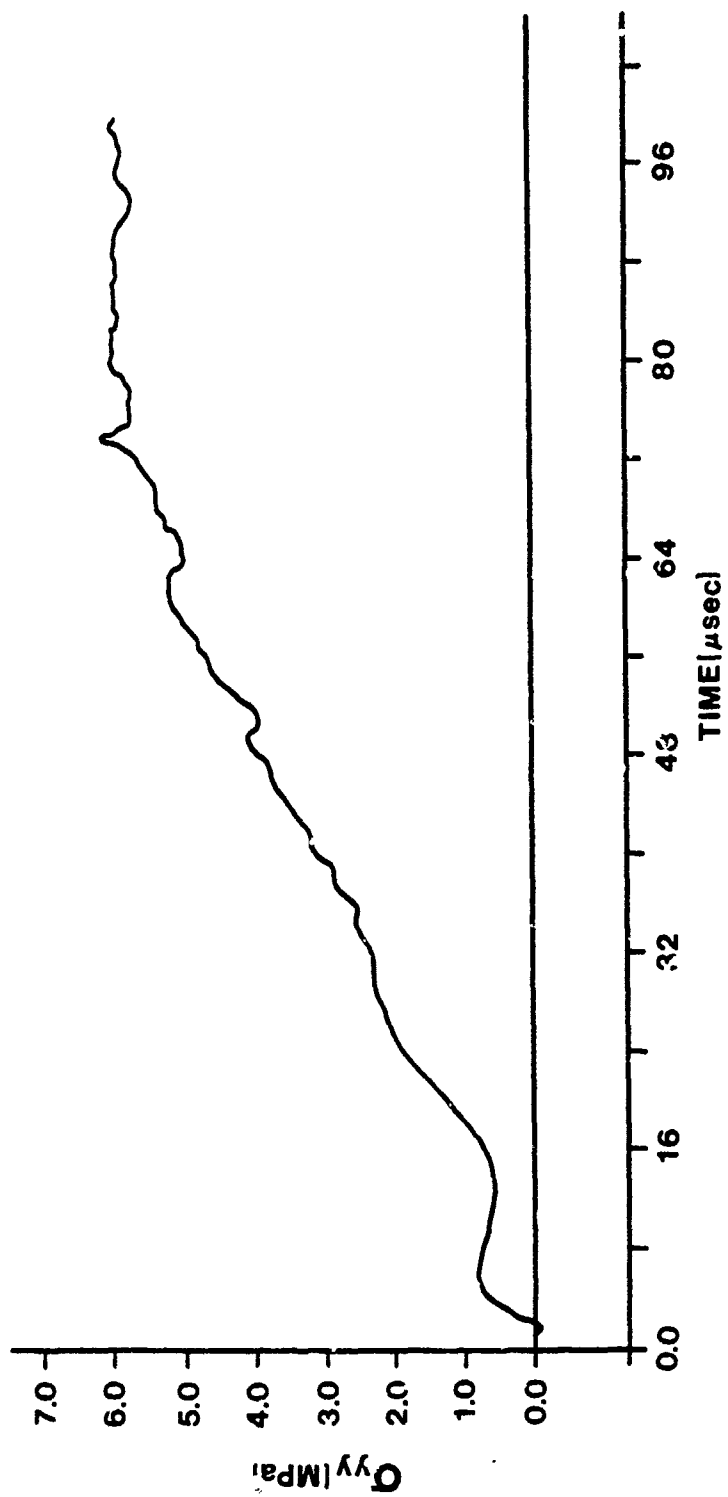


Figure 23. Time History for Vertical Stress at  $z = .125D$ , Load Case 2.

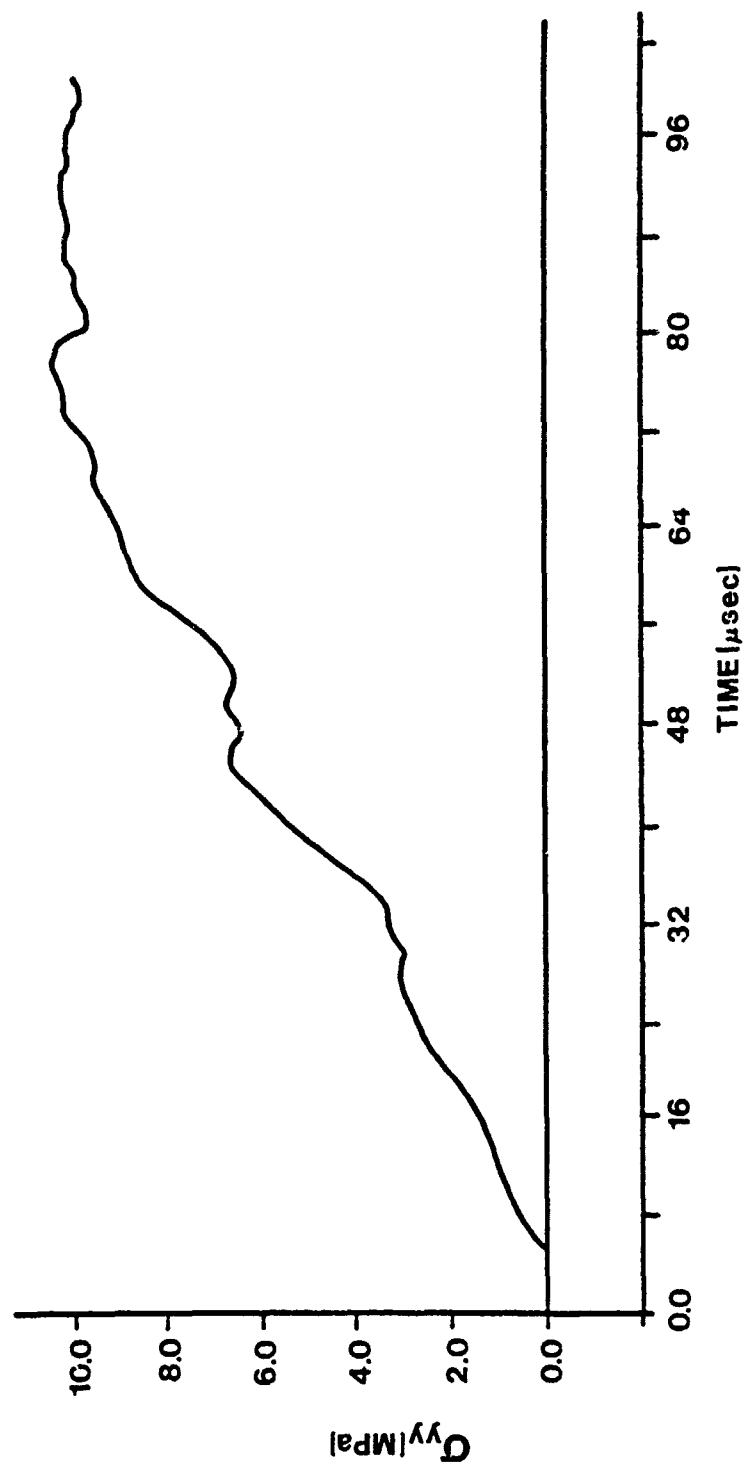


Figure 24. Time History for Vertical Stress at  $z = 0.30D$ , Load Case 2.



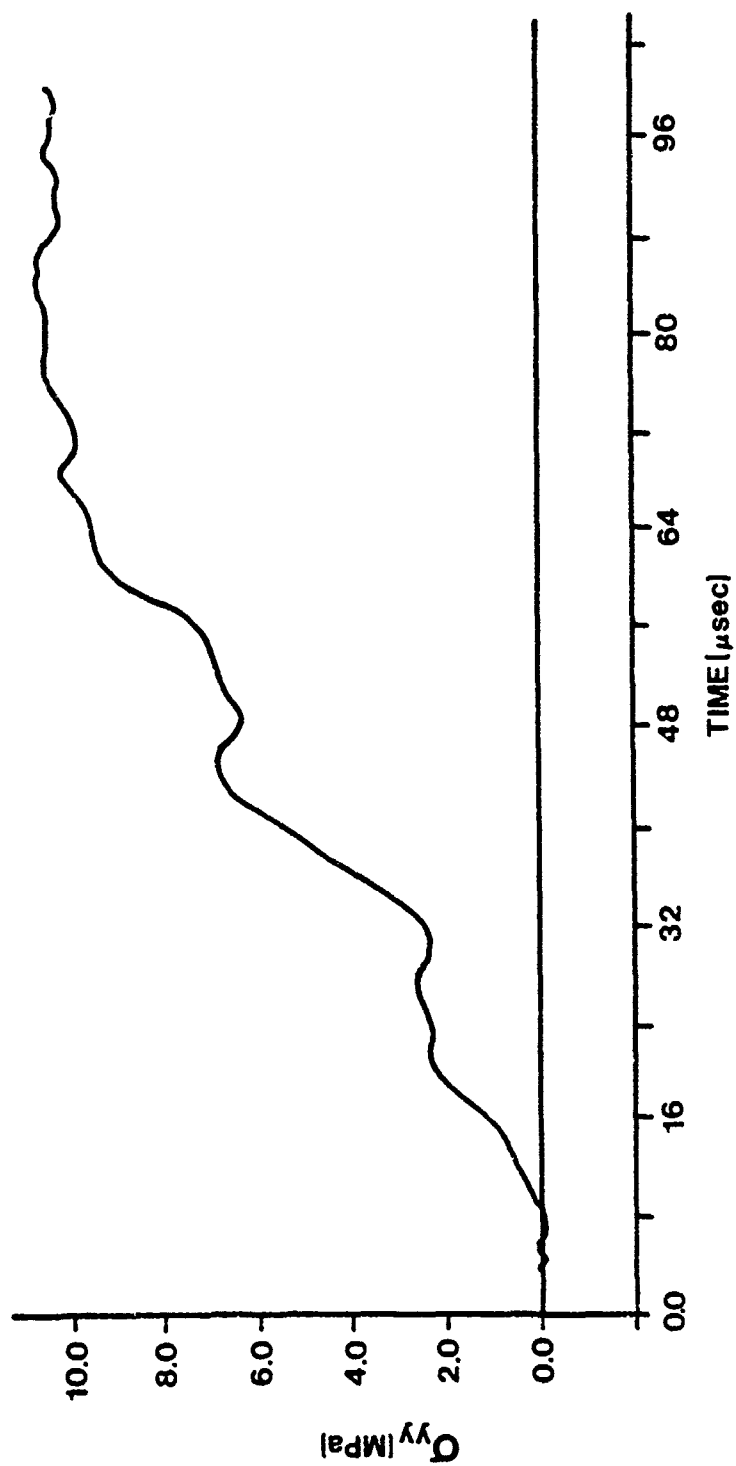


Figure 25. Time History for Vertical Stress at  $z = 0.50D$ , Load Case 2.

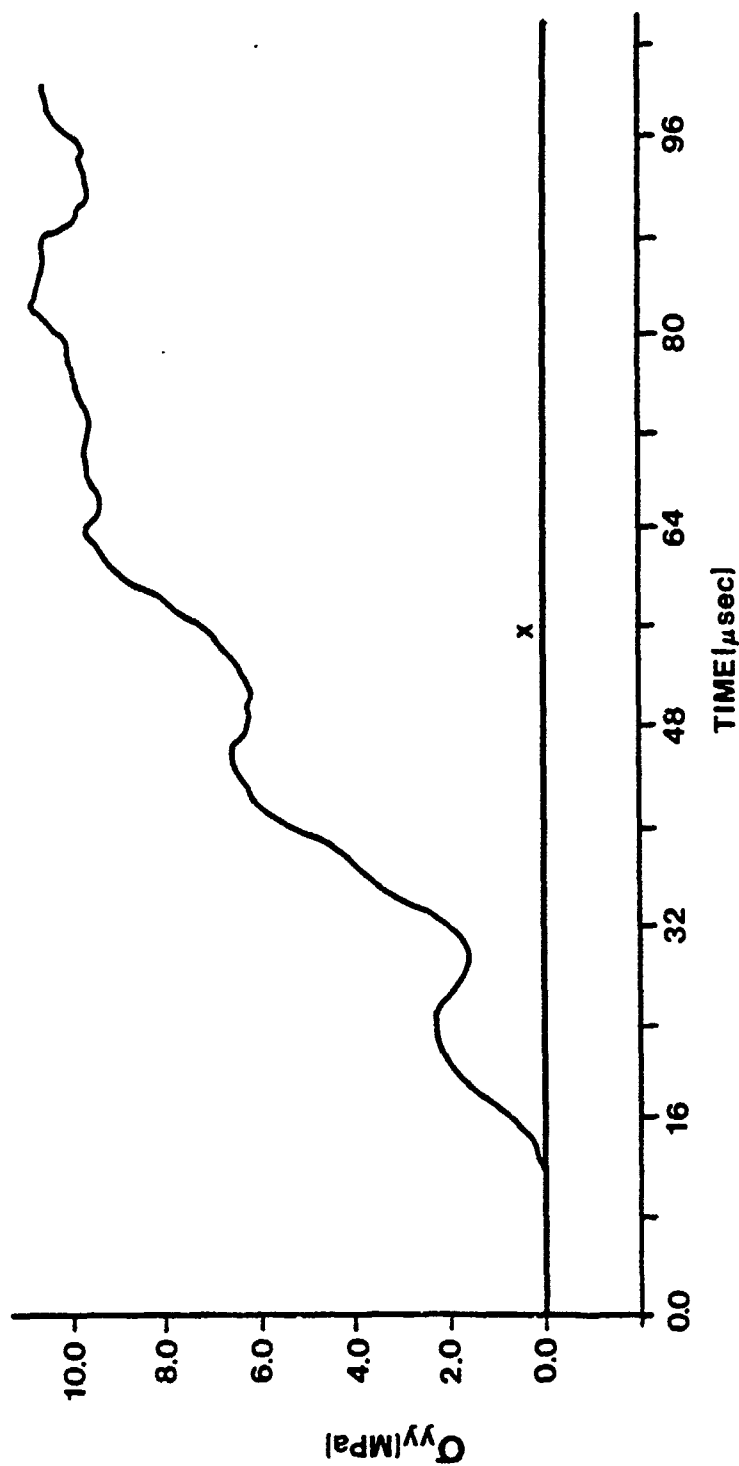


Figure 26. Time History for Vertical Stress at  $z = 0.715D$ , Load Case 2.

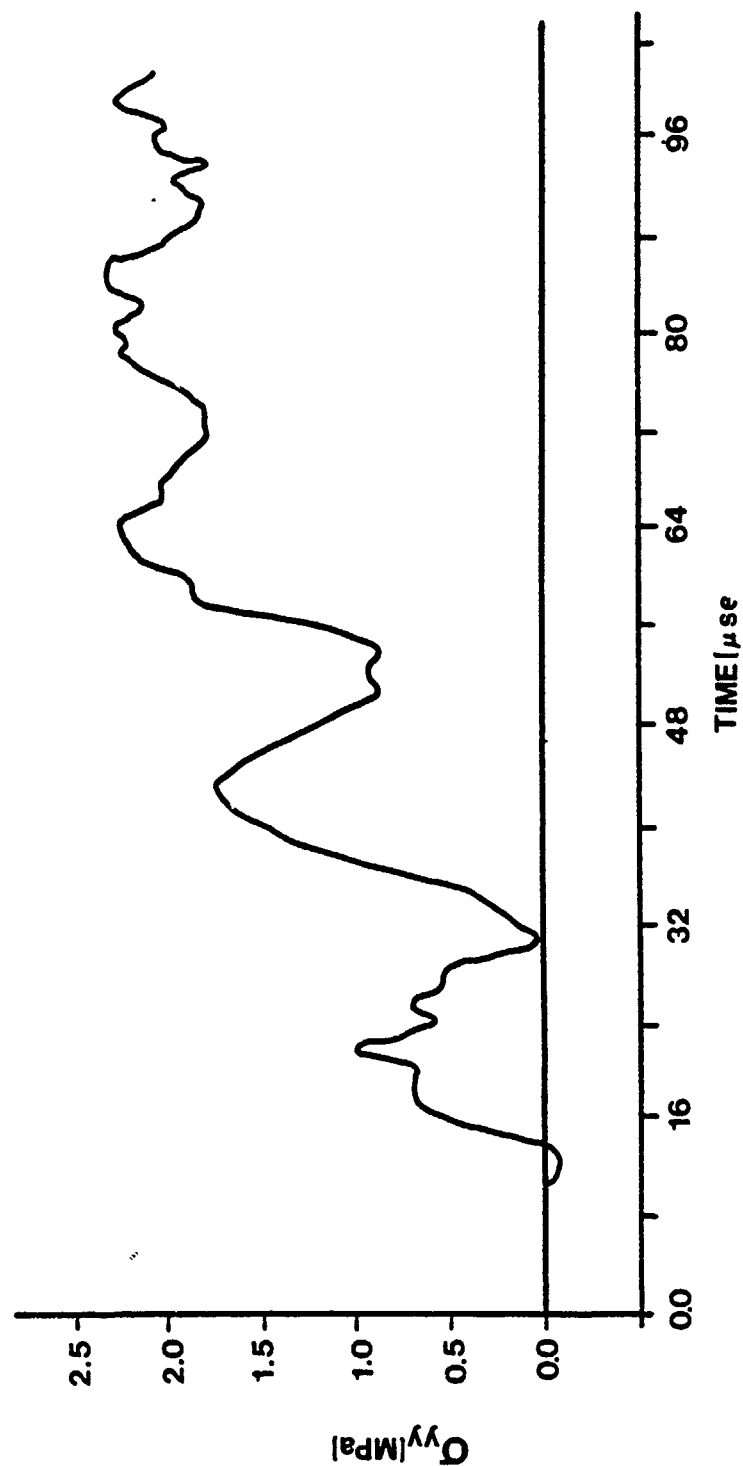


Figure 27. Time History for Vertical Stress at  $z = 0.915D$ , Load Case 2.

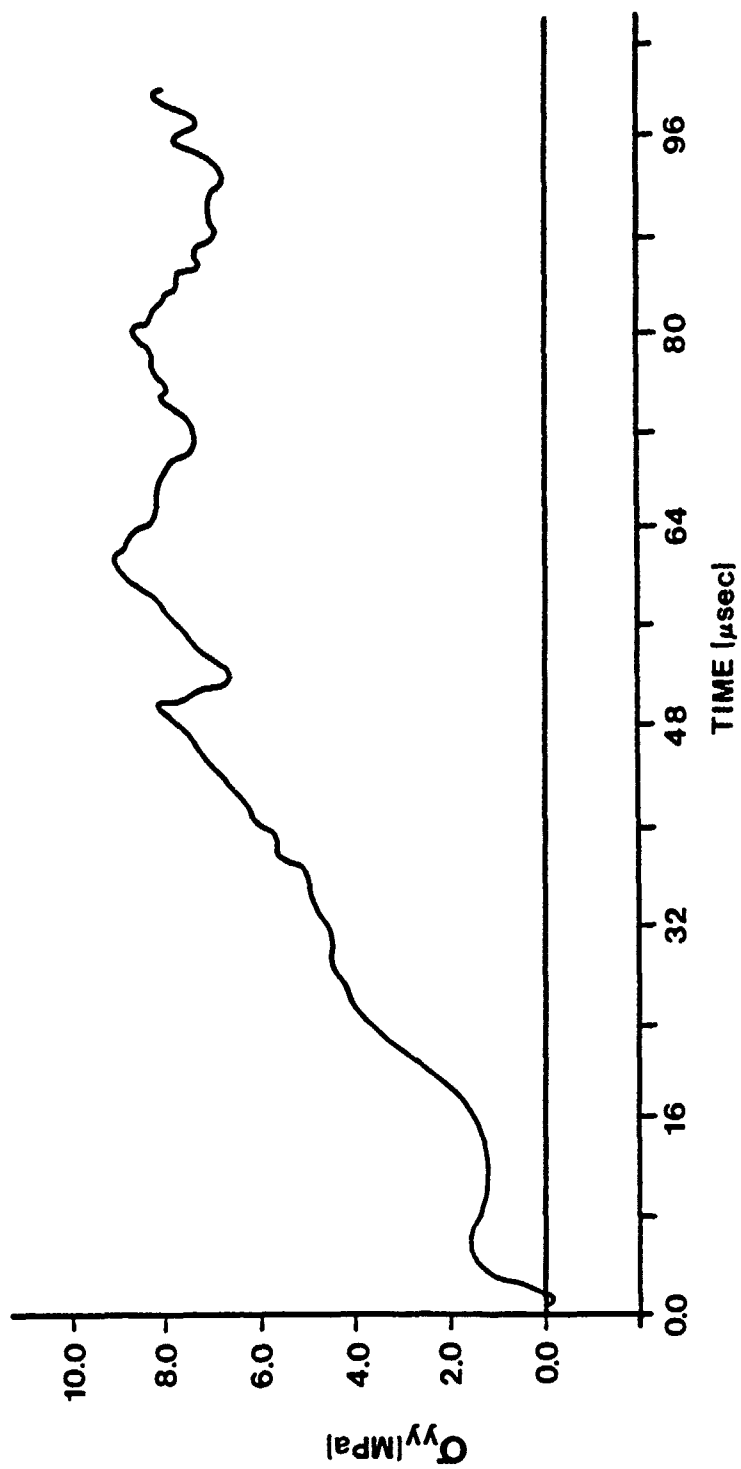


Figure 28. Time History for Vertical Stress at  $z = 0.125D$ , Load Case 3.

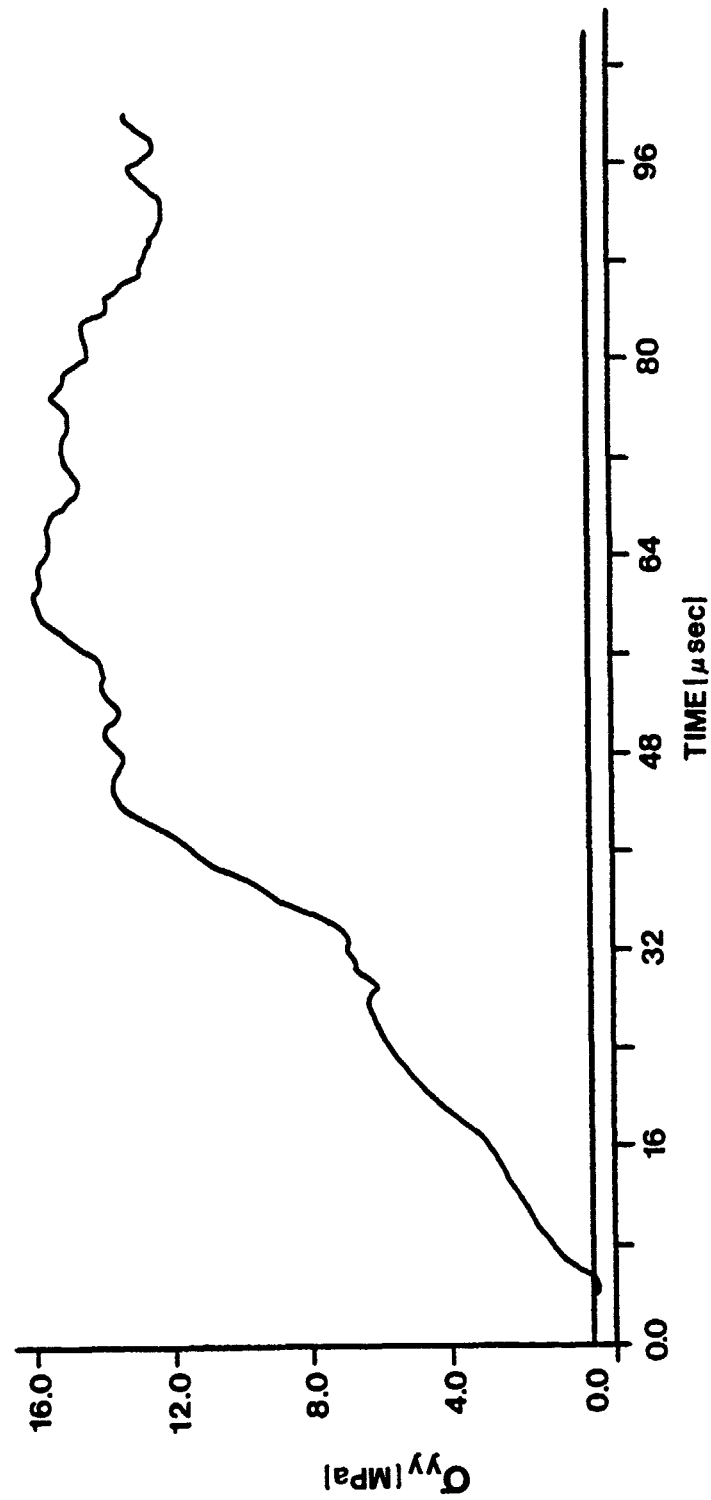


Figure 29. Time History for Vertical Stress at  $z = 0.30D$ , Load Case 3.

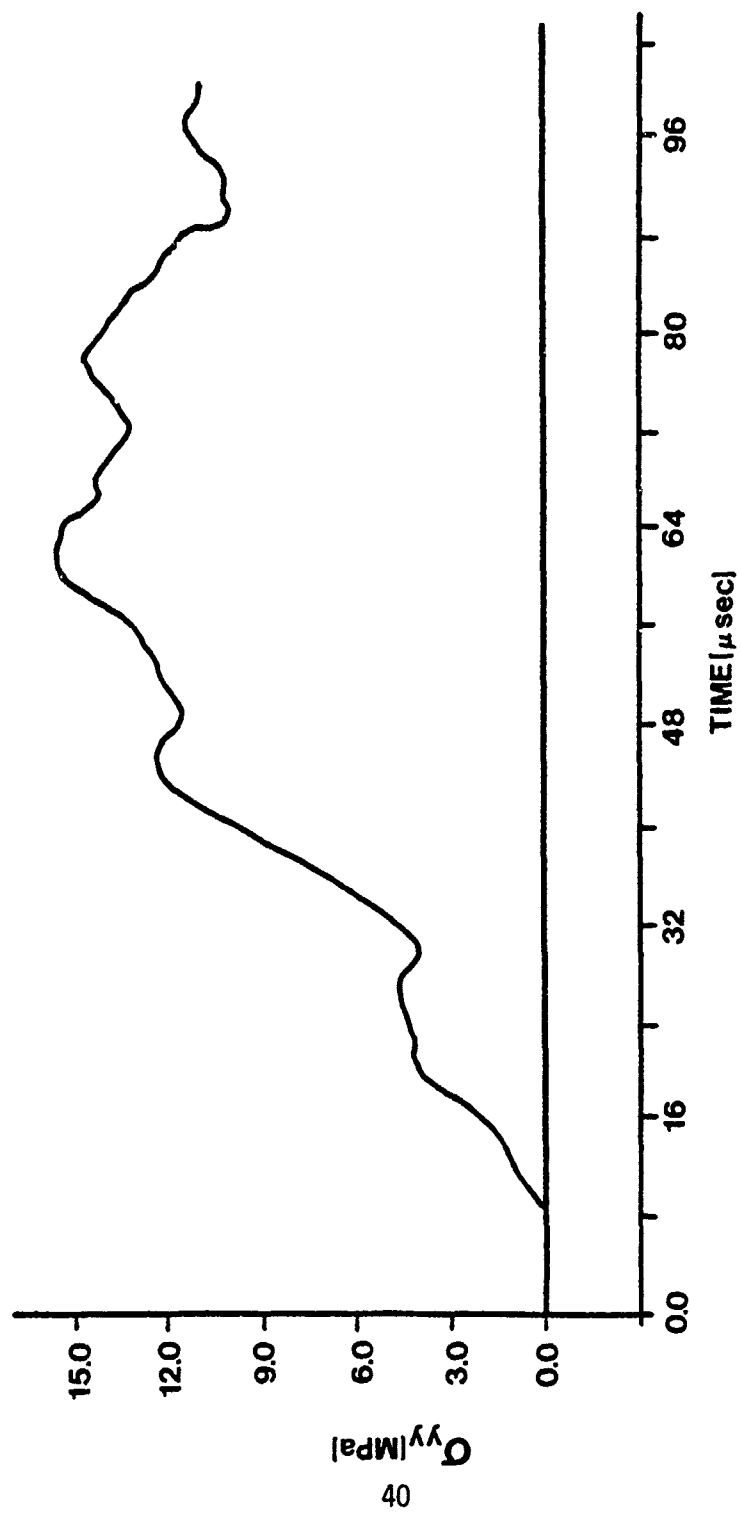


Figure 30. Time History for Vertical Stress at  $z = 0.50D$ , Load Case 3.

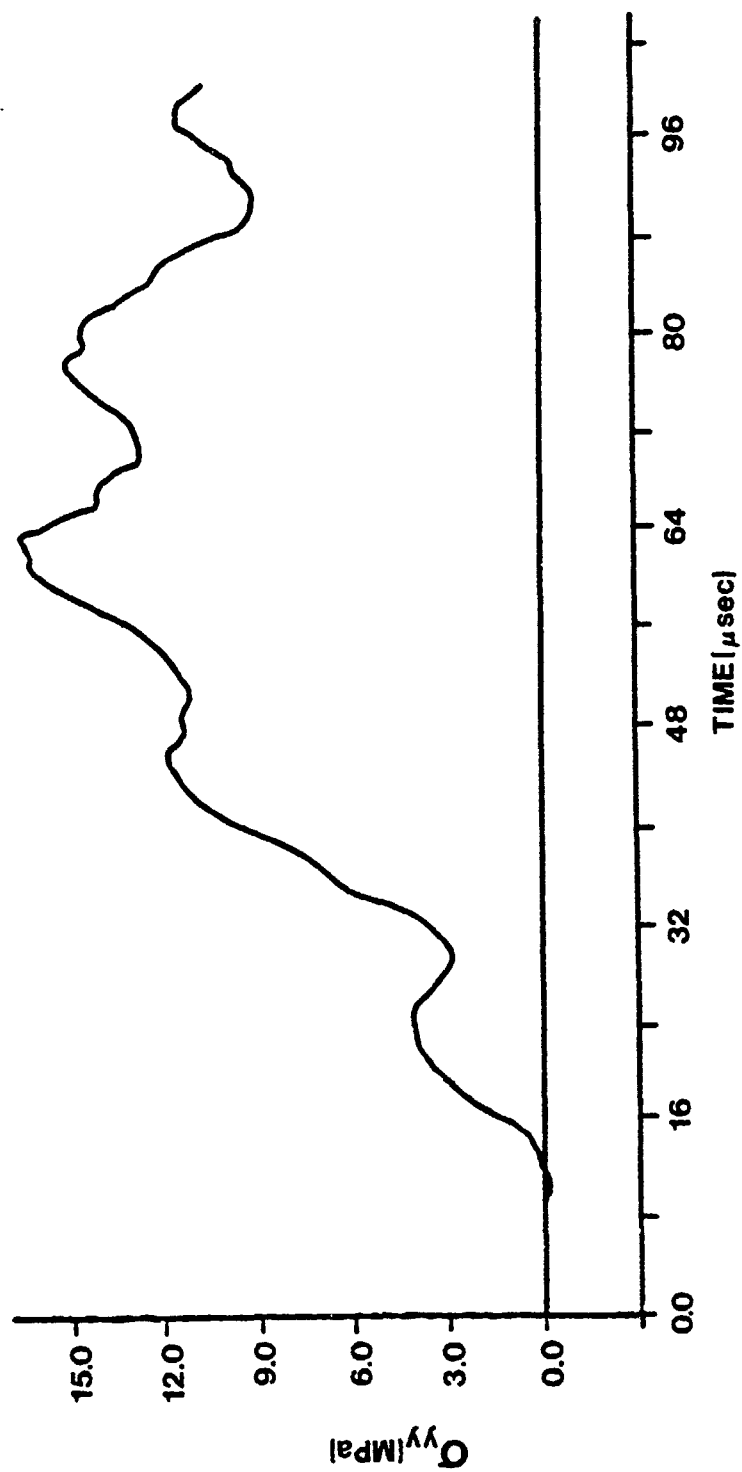


Figure 31. Time History for Vertical Stress at  $z = 0.715D$ , Load Case 3.

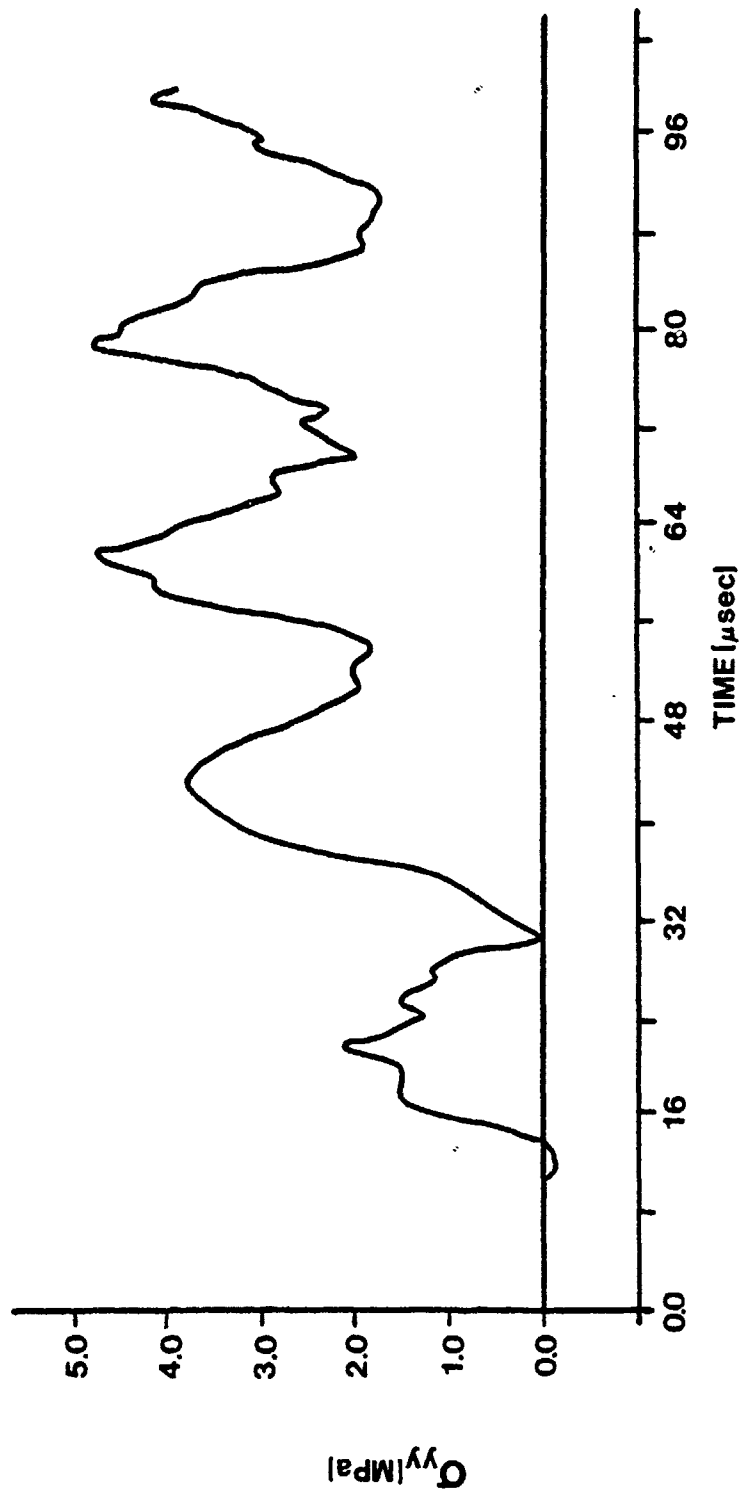


Figure 32. Time History for Vertical Stress at  $z = 0.915D$ , Load Case 3.



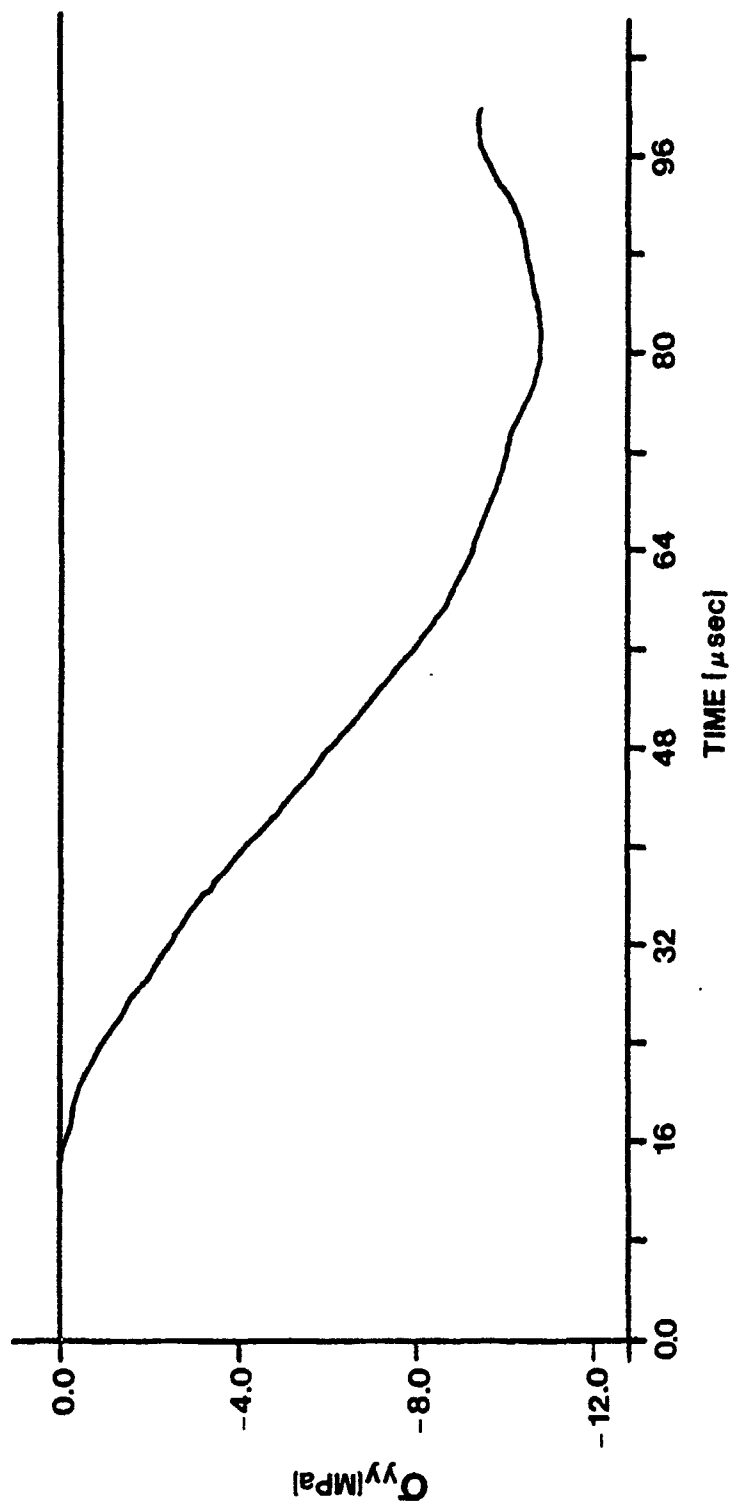


Figure 33. Time History for the Vertical Stress in the Transmitter Bar, Load Case 1.

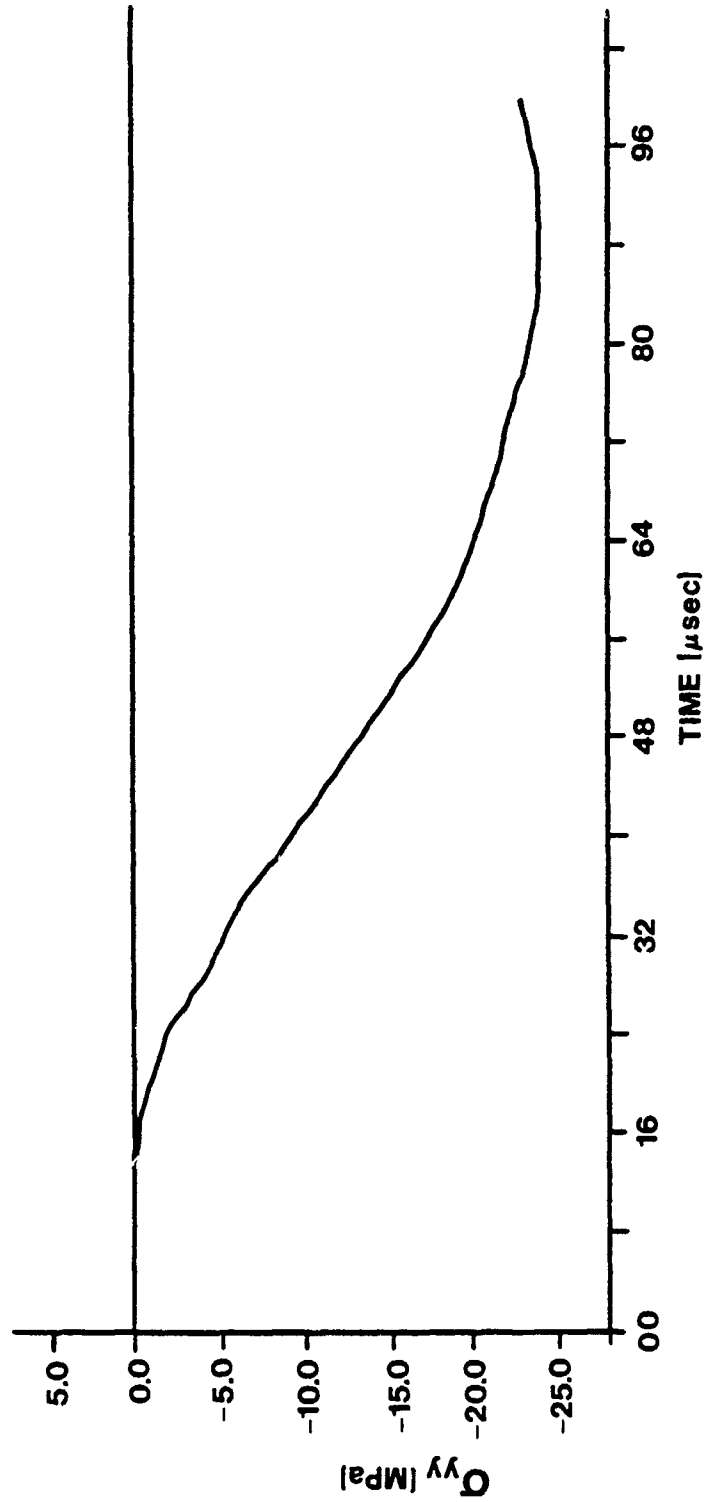


Figure 34. Time History for the Vertical Stress in the Transmitter Bar, Load Case 2.

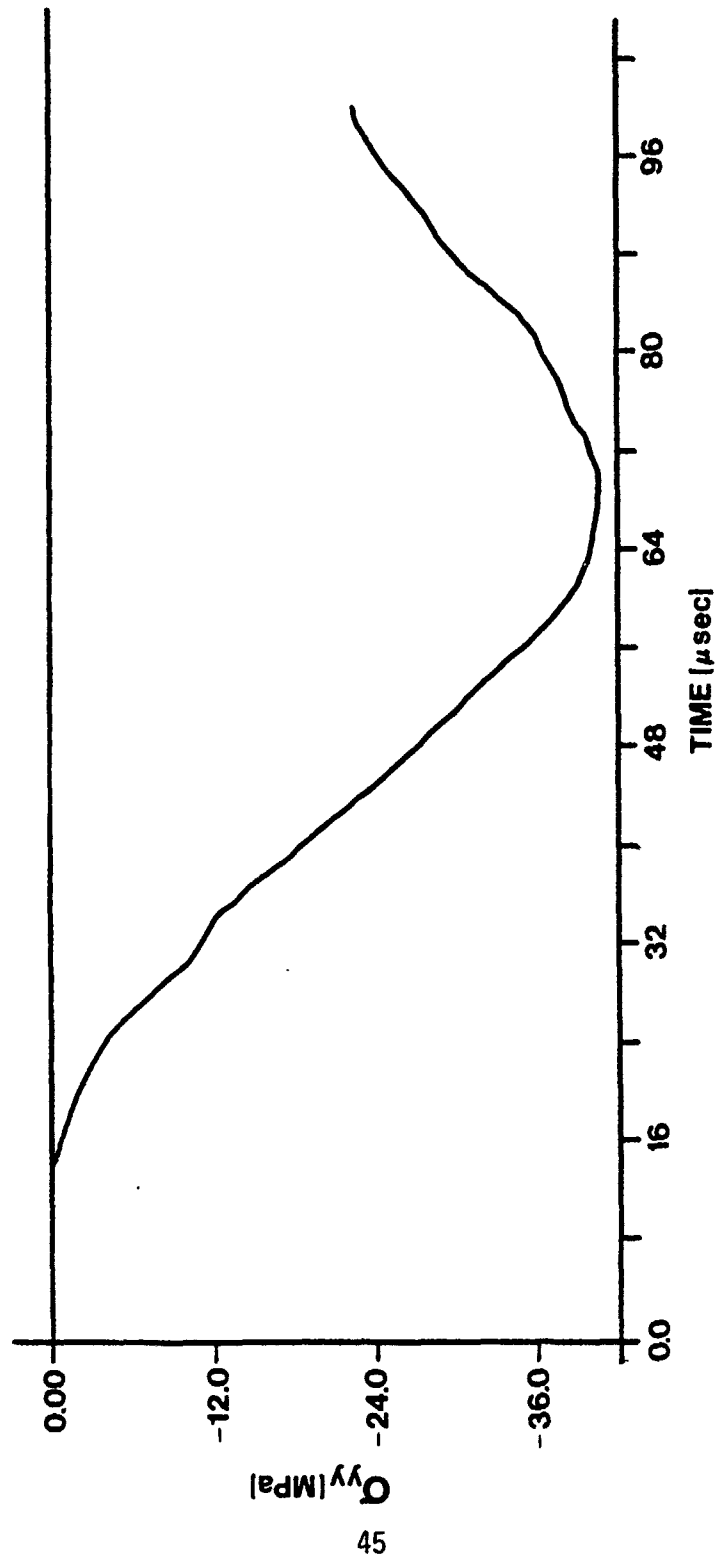


Figure 35. Time History for the Vertical Stress in the Transmitter Bar, Load Case 3.

stresses. Moreover, the transmitted stresses depend on the assumed loading stress applied to the top of the cylinder.

Profiles for the horizontal stress,  $\sigma_y$ , at selected times (see Table 4) along the vertical diameter for Load Case 1 are illustrated in Figures 36 and 37. Profiles for the horizontal stress along the horizontal diameter are illustrated in Figures 38 and 39. Similar profiles for the horizontal stress along the vertical diameter for Load Case 2 are illustrated in Figures 40 and 41, and in Figures 42 and 43 for Load Case 3. Profiles for the horizontal stress along the horizontal diameter are illustrated in Figures 44 and 45 for Load Case 2 and in Figures 46 and 47 for Load Case 3. Examination of these profiles reveals the close resemblance between the dynamic stress profiles and the corresponding static stress profiles presented in Figures 10 and 12.

The representative times for the stress profiles are presented in Table 4. The numerical results for the maximum dynamic vertical,  $(\sigma_z)_{\max}$ , and horizontal,  $(\sigma_y)_{\max}$ , stresses occurring at the center of the cylinder ( $z = 0.50D$ ) are summarized in Table 5. Also presented in Table 5 are the dynamic increase factors (DIF) for each load case

TABLE 4. SELECTED TIMES FOR STRESS PROFILES (LINEAR ANALYSIS)

Designation	Time ( $\mu\text{sec}$ )	Designation	Time ( $\mu\text{sec}$ )
$t_1$	3.14	$t_6$	18.85
$t_2$	6.28	$t_7$	25.14
$t_3$	9.43	$t_8$	50.17
$t_4$	12.57	$t_9$	78.86
$t_5$	15.71	$t_{10}$	100.00

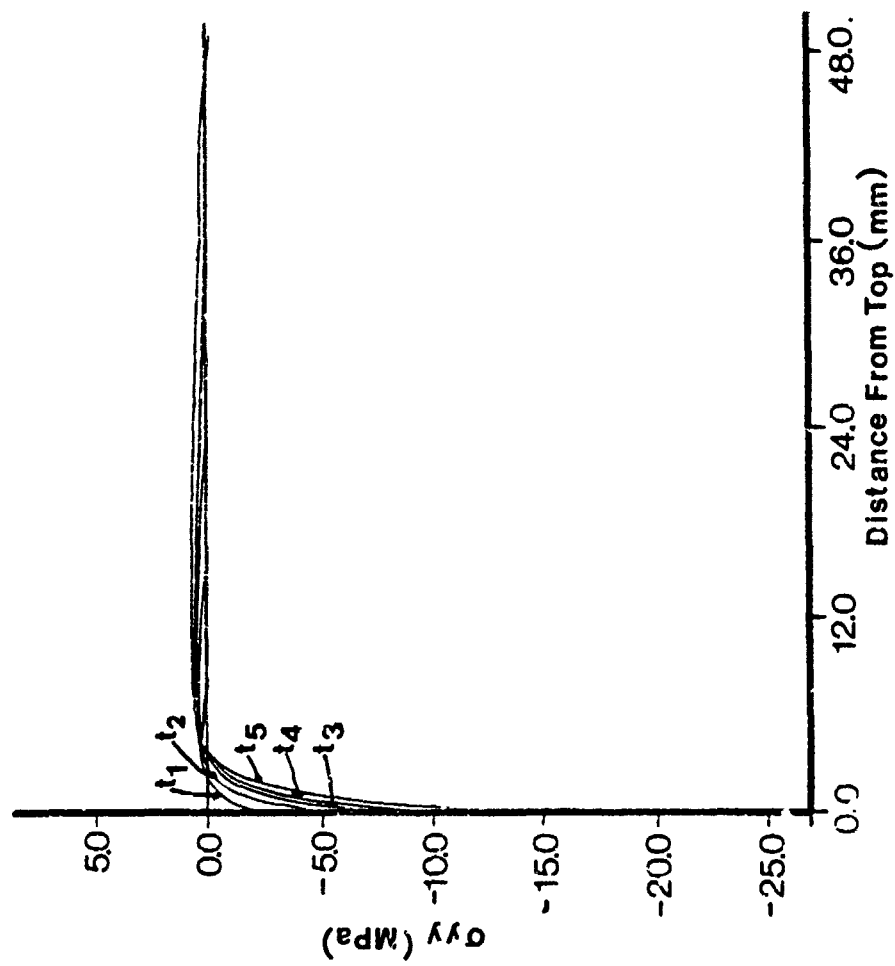


Figure 36. Profiles for the Horizontal Stress along the Vertical Diameter  
Load Case 1 ( $t_1, t_2, t_3, t_4, t_5$ ).

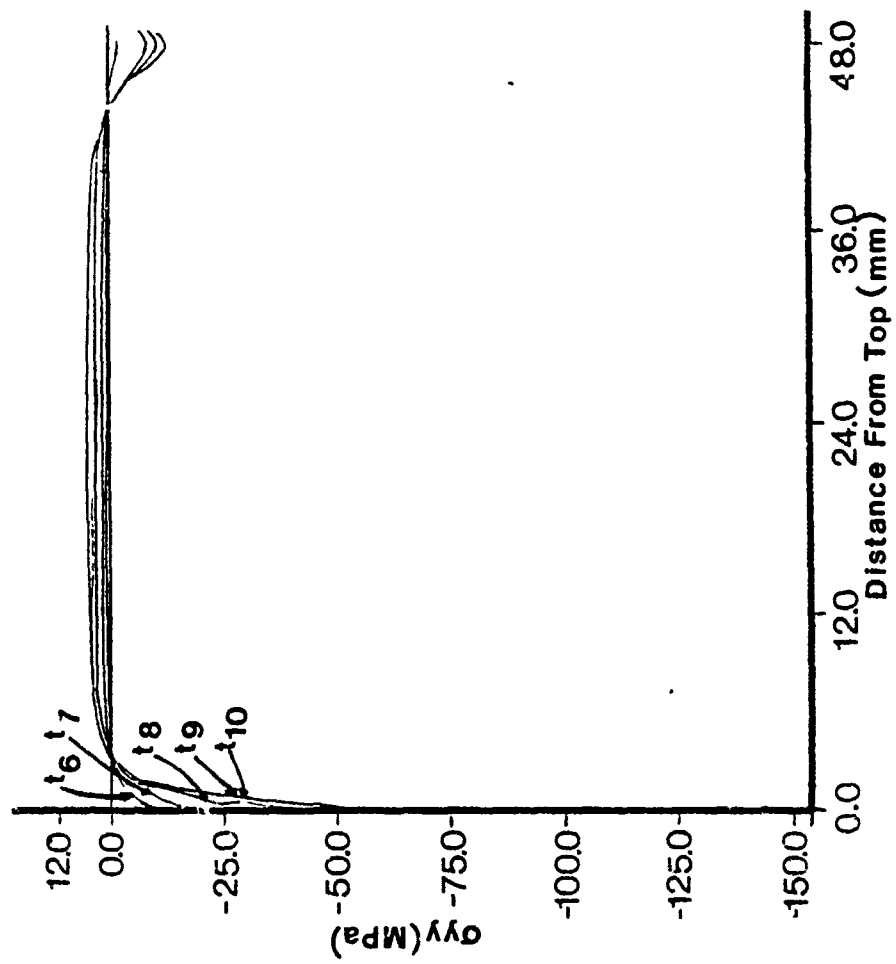


Figure 37. Profiles for the Horizontal Stress along the Vertical Diameter  
Load Case 1 ( $t_6, t_7, t_8, t_9, t_{10}$ ).

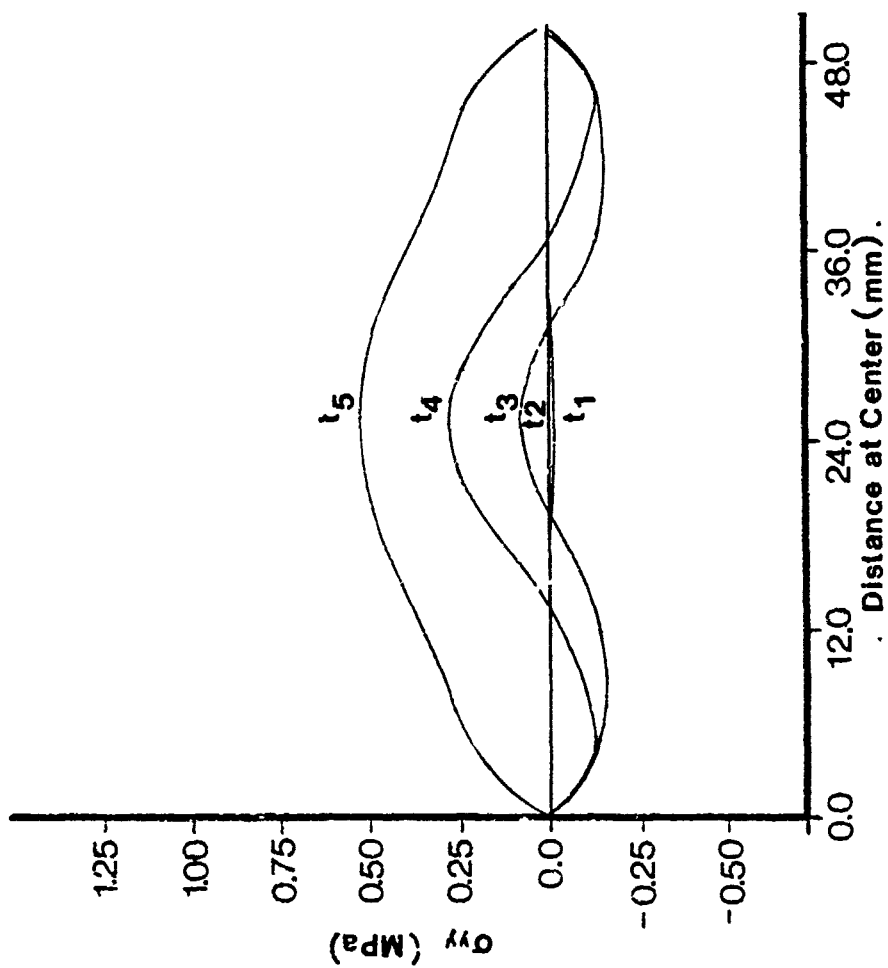


Figure 38. Profiles for the Horizontal Stress along the Horizontal Diameter  
Load Case 1 ( $t_1, t_2, t_3, t_4, t_5$ ).

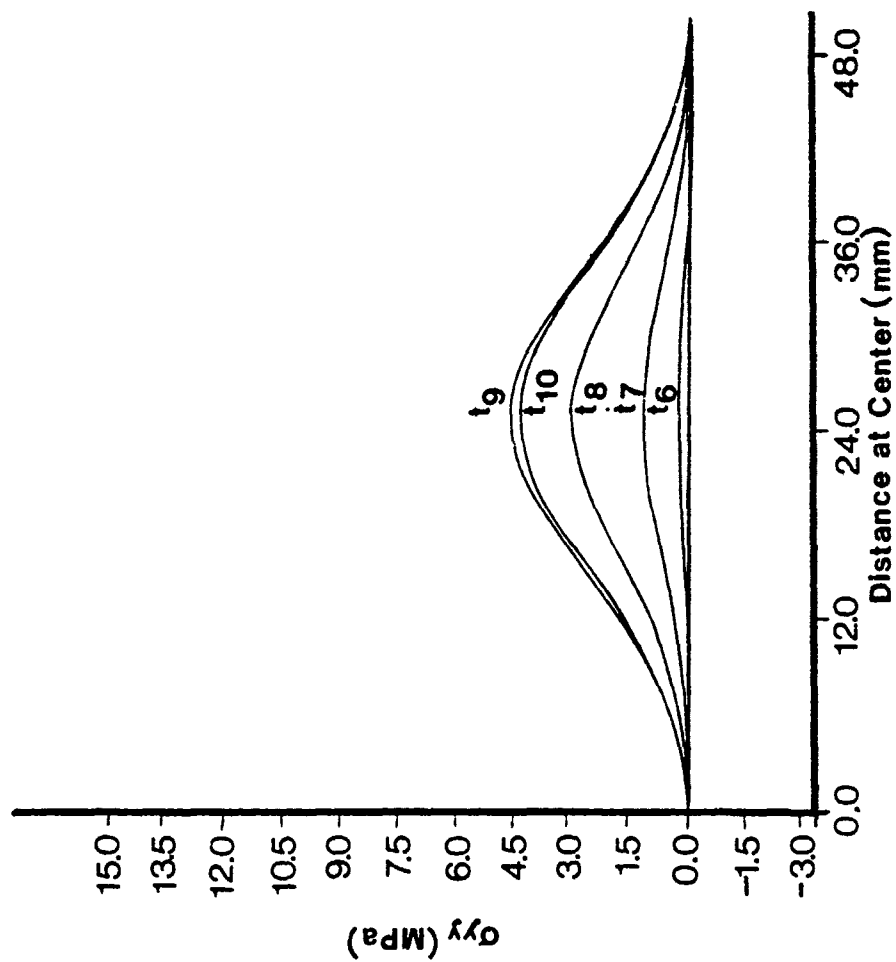


Figure 39. Profiles for the Horizontal Stress along the Horizontal Diameter  
Load Case 1 ( $t_6, t_7, t_8, t_9, t_{10}$ ).



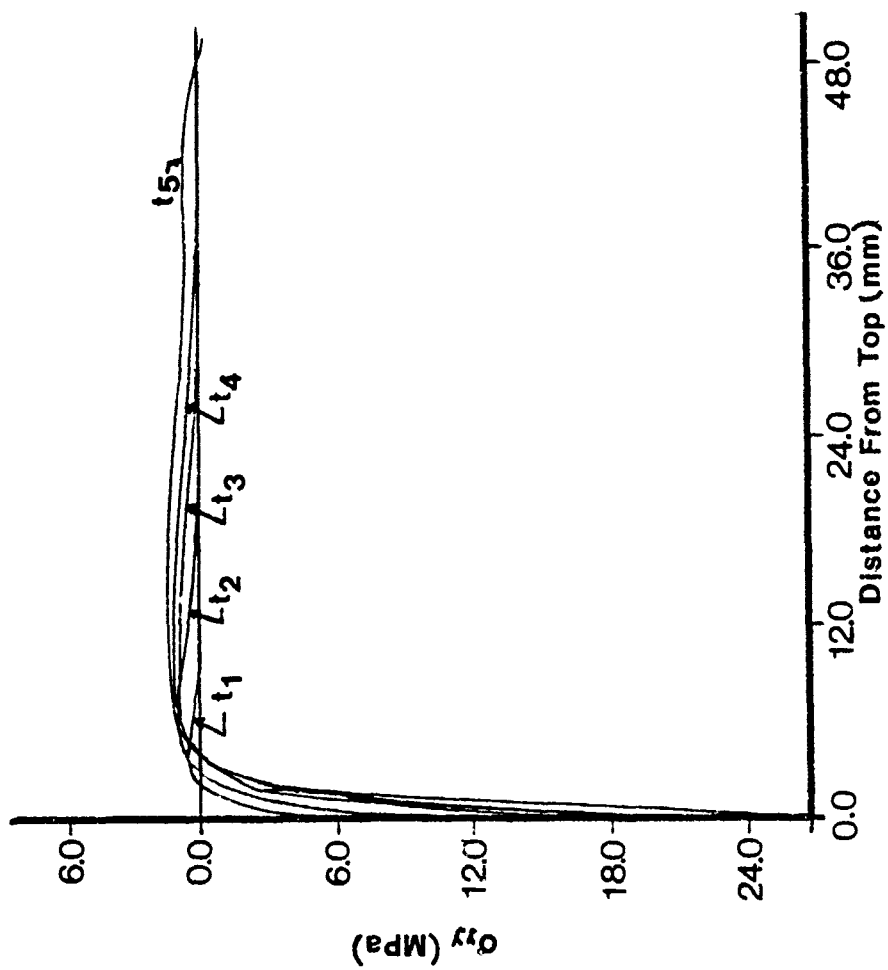


Figure 40. Profiles for the Horizontal Stress along the Vertical Diameter Load Case 2, ( $t_1, t_2, t_3, t_4, t_5$ ).

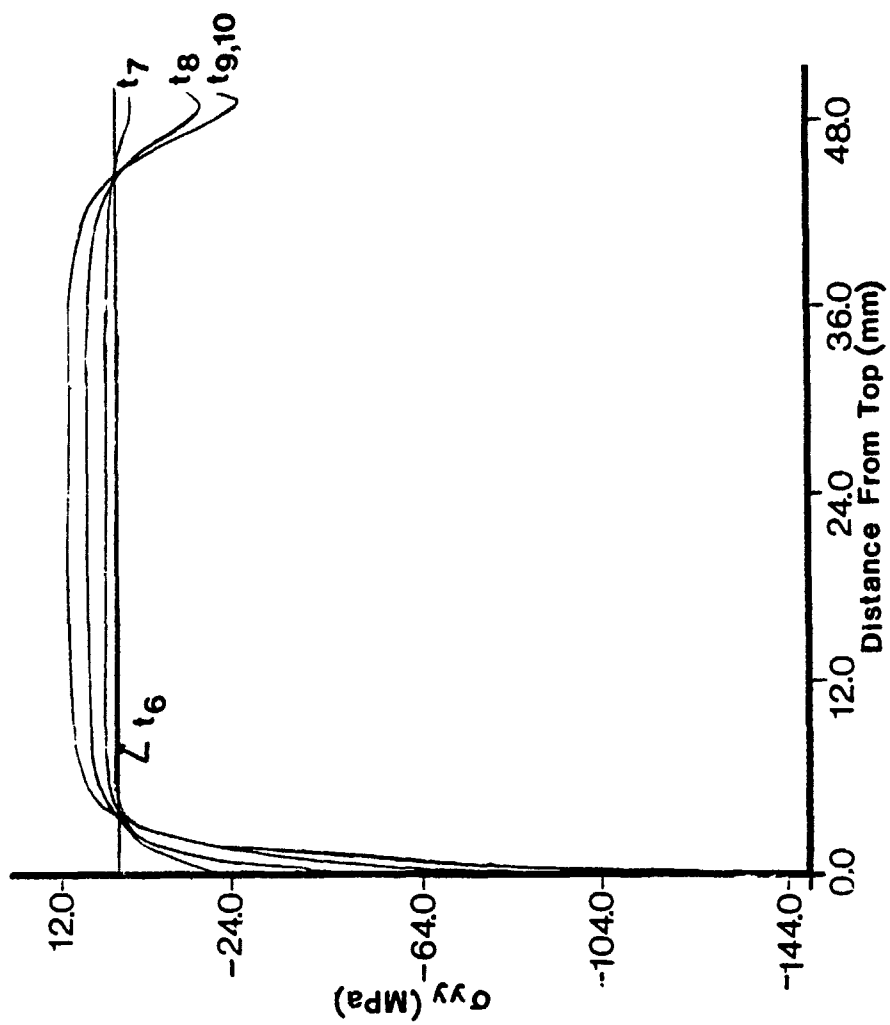


Figure 41. Profiles for the Horizontal Stress along the Vertical Diameter Load Case 2, ( $t_6, t_7, t_8, t_9, t_{10}$ ).

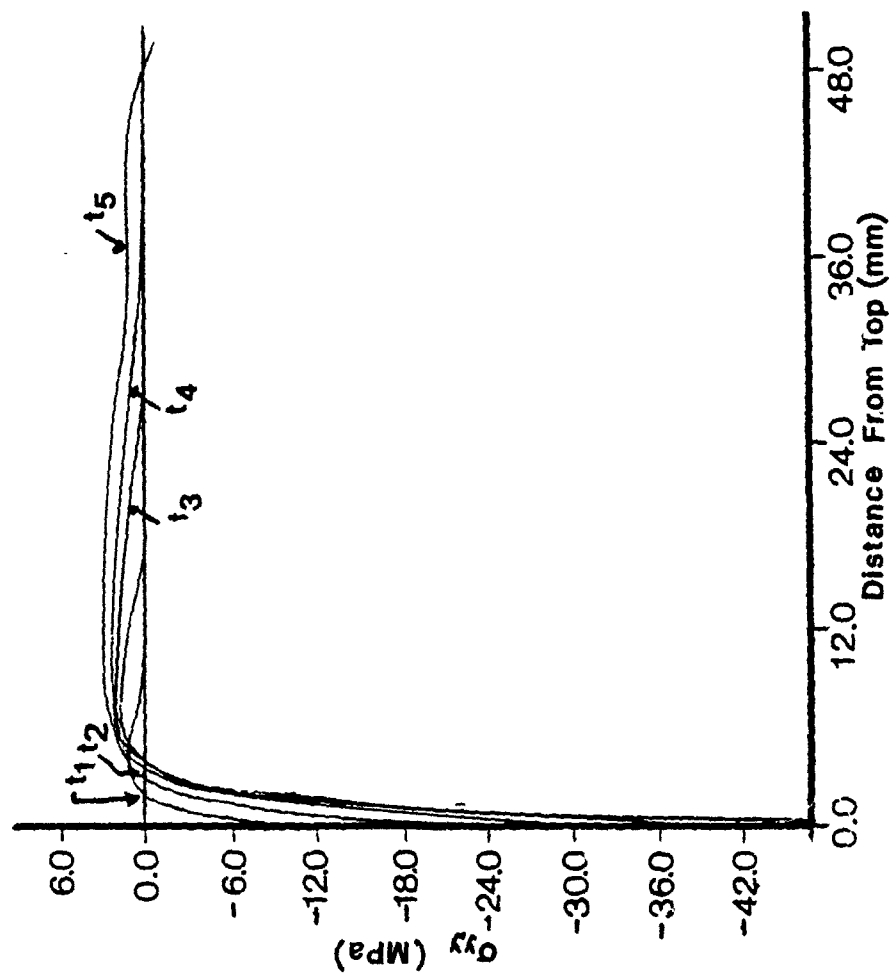


Figure 42. Profiles for the Horizontal Stress along the Vertical Diameter  
Load Case 3, ( $t_1, t_2, t_3, t_4, t_5$ ).

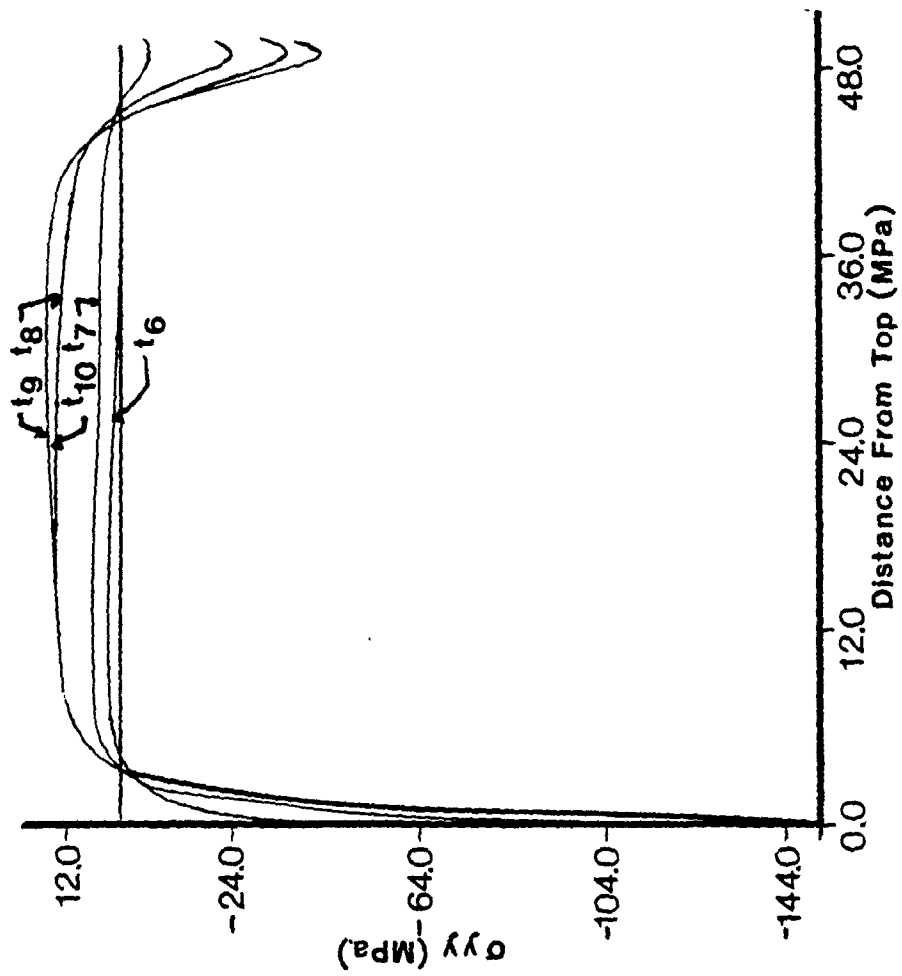


Figure 43. Profiles for the Horizontal Stress along the Vertical Diameter  
Load Case 3, ( $t_6, t_7, t_8, t_9, t_{10}$ ).

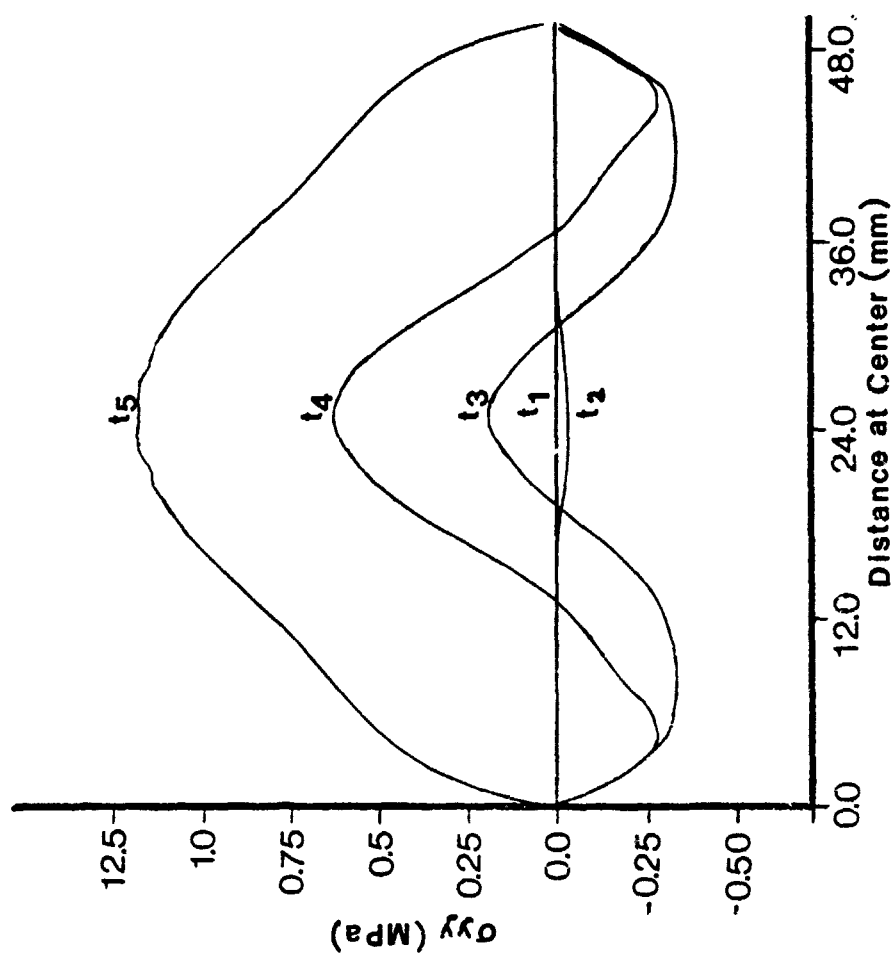


Figure 44. Profiles for the Horizontal Stress along the Horizontal Diameter  
Load Case 2 ( $t_1, t_2, t_3, t_4, t_5$ ).

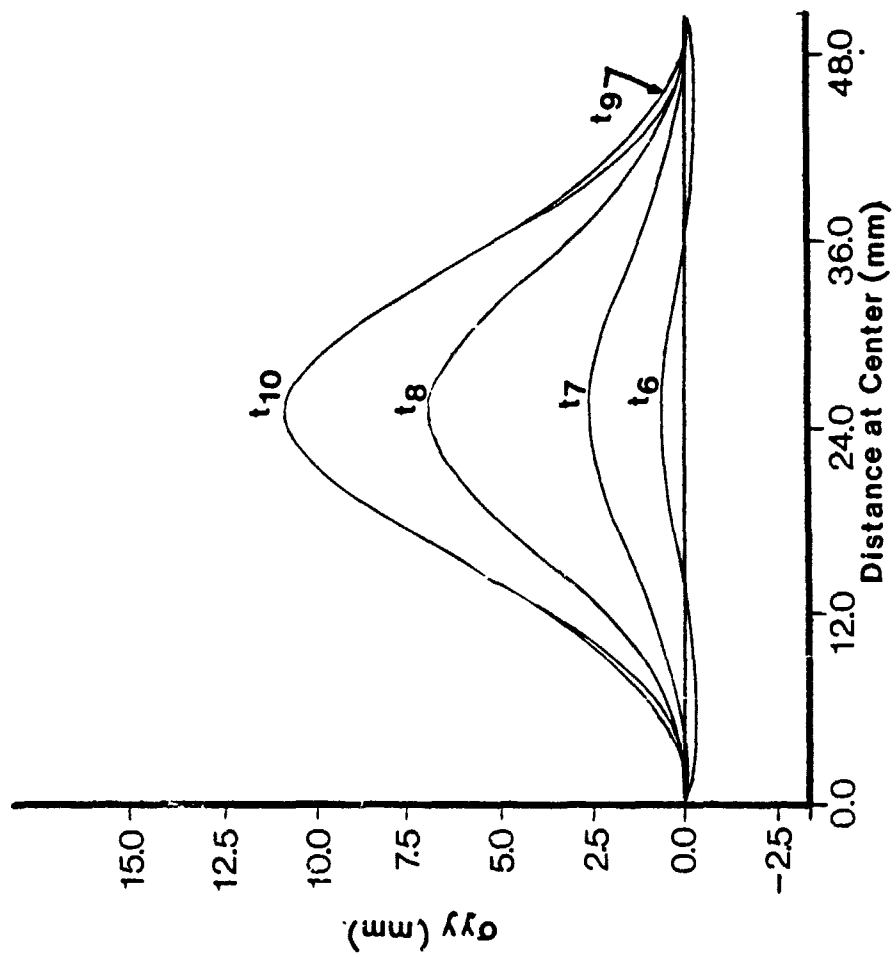


Figure 45. Profiles for the Horizontal Stress along the Horizontal Diameter  
Load Case 2 ( $t_6, t_7, t_8, t_9, t_{10}$ ).

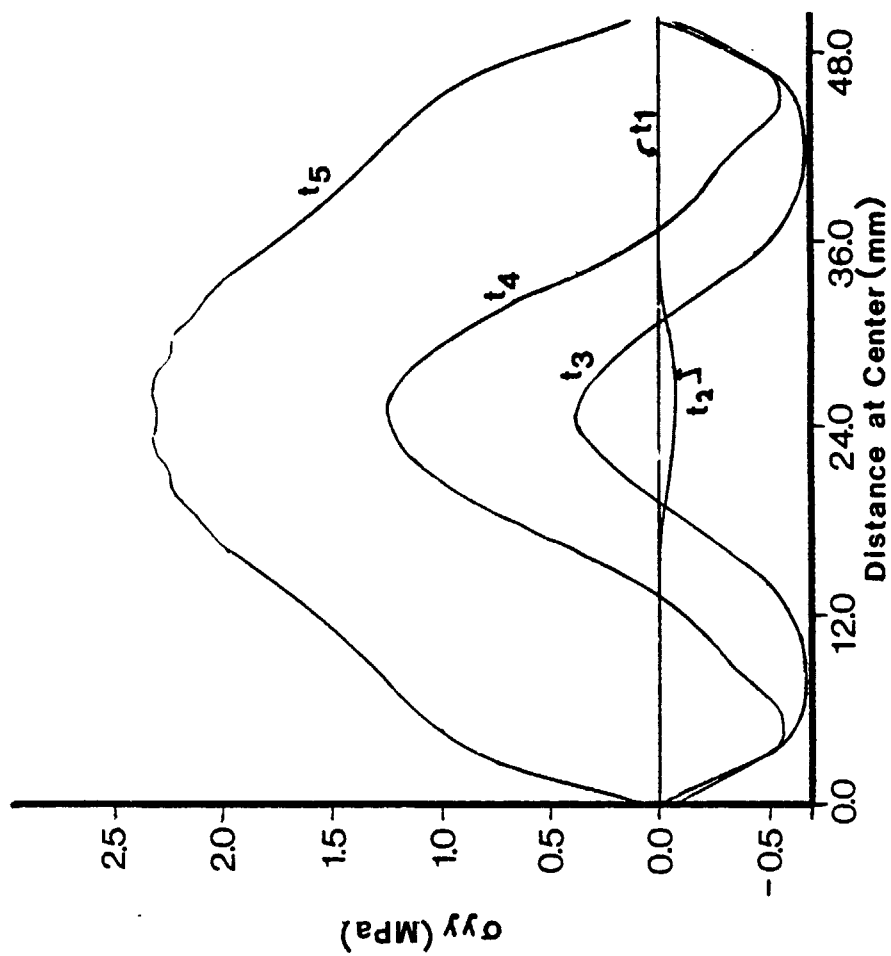


Figure 46. Profiles for the Horizontal Stress along the Horizontal Diameter Load Case 3 ( $t_1, t_2, t_3, t_4, t_5$ ).

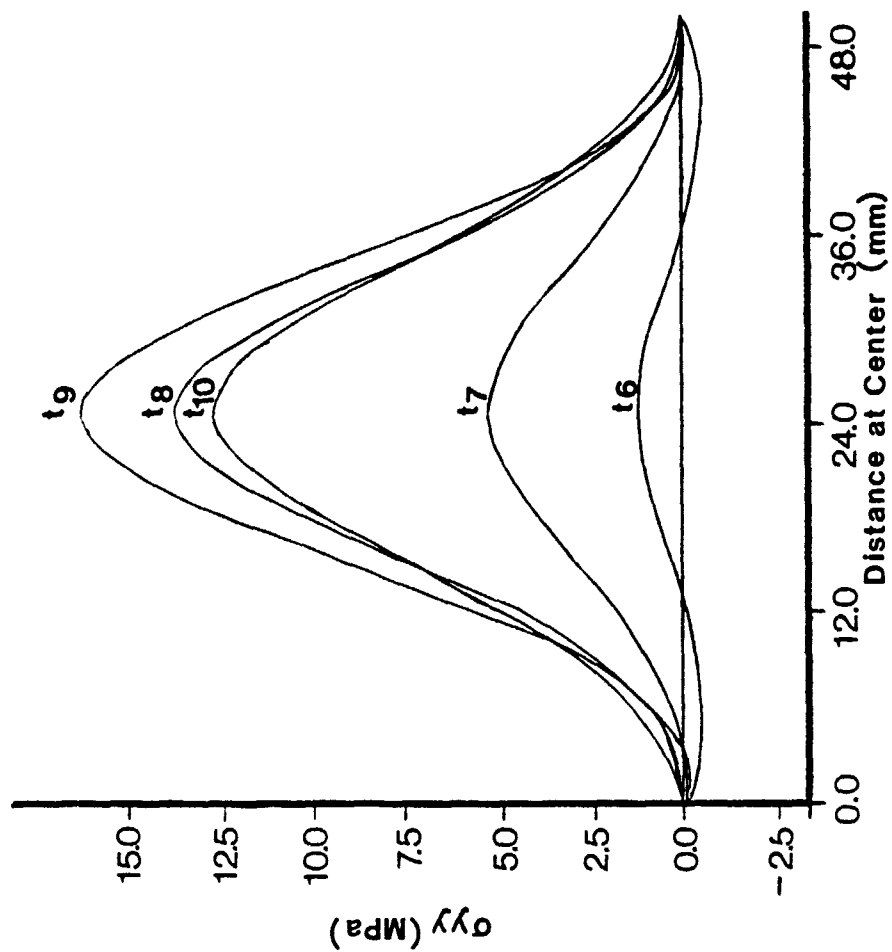


Figure 47. Profiles for the Horizontal Stress along the Horizontal Diameter, Load Case 3 ( $t_6, t_7, t_8, t_9, t_{10}$ ).



TABLE 5. DYNAMIC STRESSES AT CENTER OF CYLINDER

Load Case No.	Dynamic Impact Factors (DIF)				
	Vertical	Horizontal	$(\sigma_z)_{\text{dynamic}}$	$(\sigma_y)_{\text{dynamic}}$	$(\sigma_y)_{\text{dynamic}}$
	$\sigma_z(\text{psi})$ (MPa)	$\sigma_y(\text{psi})$ (MPa)	$(\sigma_z)_{\text{static}}$	$(\sigma_y)_{\text{static}}$	$f_{ts}$
1	-2050 -(14.14)	690 (4.76)	1.10	1.09	1.23
2	-4750 -(32.76)	1650 (11.38)	1.07	1.09	2.95
3	-7500 -(51.72)	2450 (16.90)	1.25	1.20	4.38

## C. NONLINEAR ANALYSIS

## 1. Background

A nonlinear material analysis was conducted to ascertain the failure pattern for the dynamic splitting-tensile tests. The concrete material model employed in the nonlinear analysis was a hypoelastic model based on a uniaxial stress-strain relation (Figure 48) that was generalized to take biaxial and triaxial conditions into account. The model employed three basic features to describe the material behavior: (1) a nonlinear stress-strain relation including strain softening to allow for weakening of the material under increasing compressive stresses; (2) a failure envelope that defines cracking in tension and crushing in compression; and (3) a strategy to model postcracking and crushing behavior of the material.

An appropriate failure envelope must be employed to establish the uniaxial stress-strain law accounting for multi-axial stress conditions. Since failure of the split cylinder is tension-dominated, the tension failure envelope depicted in Figure 49 was used in the concrete model. To identify

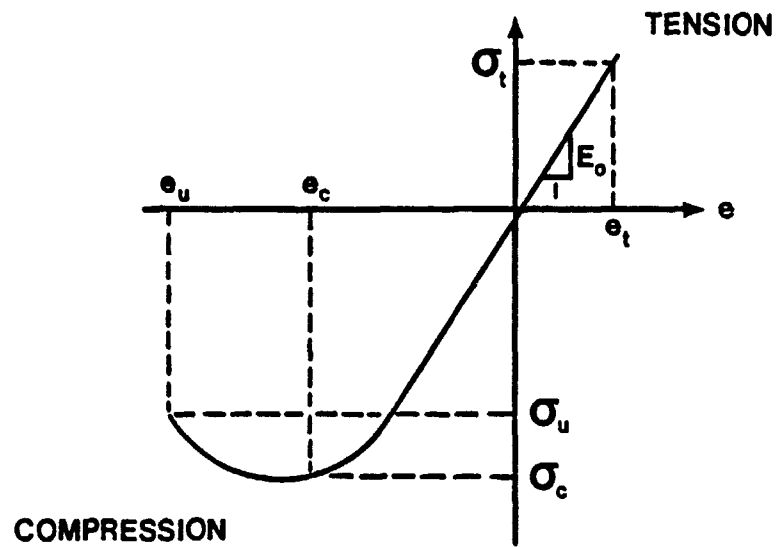


Figure 48. Uniaxial Stress-Strain Relation used in Concrete Mode

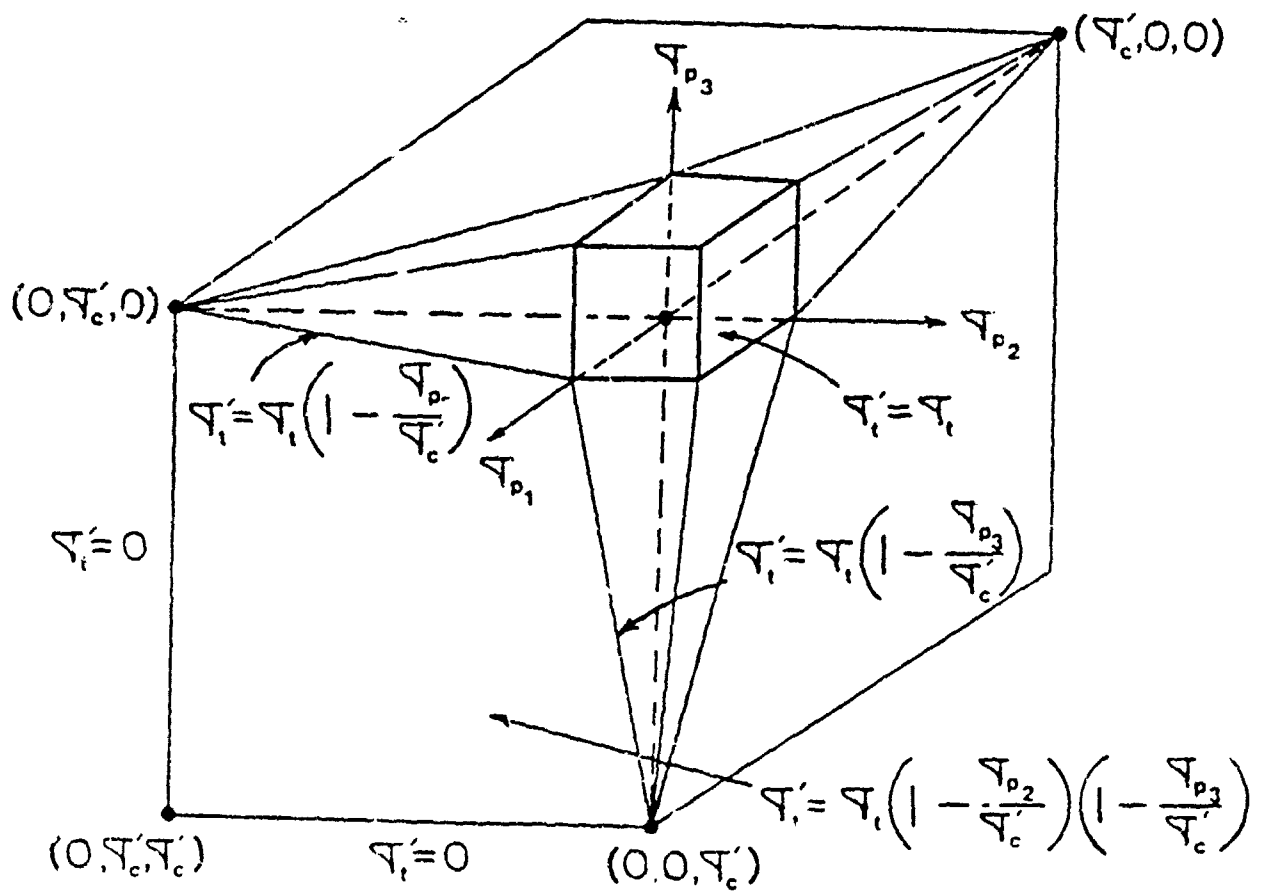


Figure 49. Three Dimensional Tensile Failure Envelope of Concrete Model

whether the material has failed, the principal stresses are used to locate the current stress state in the failure envelope. The tensile strength of the material in a principal direction does not change with the introduction of tensile stresses in other principal directions. However, the compressive stresses in the other principal directions alter the tensile strength. The pertinent material parameters for the failure envelope and the uniaxial stress strain relation are summarized in Table 6.

TABLE 6. CONCRETE MODEL PARAMETERS.

Parameter	Specified Value
$E_0$ , initial tangent modulus, psi (GPa)	5,500,000.0 (37.93)
$\sigma_t$ , uniaxial cut-off tensile strength, psi (MPa)	550.0 (3.86)
$\sigma_c$ , uniaxial maximum compressive stress, psi (MPa)	7,000.0 (48.28)
$\sigma_u$ , uniaxial ultimate compressive stress, psi (MPa)	7,000.0 (48.28)
$\sigma'_c$ , uniaxial compressive failure stress under multiaxial conditions, psi (MPa)	9,100.0 (62.76)
$e_c$ , compressive strain at $\sigma_c$	0.0022
$e_u$ , uniaxial ultimate compressive strain	0.005
$\sigma_{p1}$ , $\sigma_{p2}$ , $\sigma_{p3}$ , principal stresses in directions 1, 2, 3, respectively	(Figure 49)
$\sigma'_t$ , uniaxial cut-off tensile stress under multiaxial conditions	(Figure 49)

Because of the complexity of the material description used for the FEM model, an appropriate strategy for solving the nonlinear finite element equations was selected, specifically, the Newton-Raphson iteration scheme. In the Newton-Raphson formulation, the equilibrium conditions at time  $t + \Delta t$  are satisfied by successive approximations of the form (Reference 23)

$$[K]^{i-1} \{\Delta U\}^i = \{R\} - \{F\}^{i-1}, \quad (19)$$

in which  $[K]^{i-1}$  is the tangent stiffness matrix at the iteration  $i - 1$  and time  $t + \Delta t$ ;  $\{\Delta U\}^i$  is the  $i^{\text{th}}$  correction to the current displacement vector;

$\{R\}$  is the externally applied load vector;  $\{F\}^{i-1}$  is the force vector that corresponds to the current element stresses. The displacement increment correction is used to obtain the next displacement approximation (Reference 21)

$$\{U\}^i = \{U\}^{i-1} + \{\Delta U\}^i. \quad (20)$$

Equations (19) and (20) constitute the Newton-Raphson solution of the equilibrium equations subjected to the initial conditions  $[K(t + \Delta T)]^0 = [K(t)]$ ,  $\{F(t + \Delta t)\}^0 = \{F(t)\}$ , and  $\{U(t + \Delta t)\}^0 = \{U(t)\}$ . The iteration continues until appropriate convergence criteria are satisfied.

Using the Newton-Raphson iteration, the governing equilibrium equations (neglecting the effects of a damping matrix for the sake of clarity) presented in Equation (12) become

$$[M]^{t+\Delta t} \ddot{\{U\}}^i + {}^t[K] \{\Delta U\}^i = {}^{t+\Delta t}\{R\} - {}^{t+\Delta t}\{F\}^{i-1} \quad (21)$$

$${}^{t+\Delta t}\{U\}^i = {}^{t+\Delta t}\{U\}^{i-1} + \{\Delta U\}^i. \quad (22)$$

Using the relations in Equations (21) and (22), along with the assumptions employed in Equations (13) and (14) for the Newmark method, results in

$${}^{t+\Delta t}\ddot{\{U\}}^i = \frac{4}{\Delta t^2} ({}^{t+\Delta t}\{U\}^{i-1} - {}^t\{U\} + \{\Delta U\}^i) - \frac{4}{\Delta t} {}^t\ddot{\{U\}} \quad (23)$$

and substituting into Equation (21) yields

$$\begin{aligned} {}^t[\hat{K}] \{\Delta U\}^i &= {}^{t+\Delta t}\{R\} - {}^{t+\Delta t}\{F\}^{i-1} - [M] \left( \frac{4}{\Delta t^2} ({}^{t+\Delta t}\{U\}^{i-1} - {}^t\{U\}) \right. \\ &\quad \left. - \frac{4}{\Delta t} {}^t\dot{\{U\}} - {}^t\ddot{\{U\}} \right) \end{aligned} \quad (24)$$

where

$${}^t[\hat{K}] = {}^t[K] + \frac{4}{\Delta t^2} [M]. \quad (25)$$

## 2. Results of Nonlinear Analysis (Load Case 1)

Time histories for the horizontal stress,  $\sigma_y$ , and the horizontal strain,  $\epsilon_y$ , at three locations along the vertical diameter are illustrated in Figures 50, 51, and 52 for  $z$  equal to 0.1D, 0.3D, and 0.5D, respectively. Similar time histories for the vertical stress,  $\sigma_z$ , and vertical strain,  $\epsilon_z$ , at the same locations are presented in Figures 53, 54, and 55. Time histories for the horizontal stress and strain at three locations along the horizontal diameter are presented in Figures 56, 57, and 58 for  $y$  equal to 0.25D, 0.38D, and 0.5D, respectively. Similar time histories for the vertical stress and strain at the same locations are presented in Figures 59, 60, and 61. Time histories for the vertical stress and strain in the transmitter bar are presented in Figure 62. The maximum stresses and strain rates predicted at each of these locations are summarized in Table 7.

TABLE 7. MAXIMUM STRESSES AND STRAIN RATES  
AT SELECTED LOCATIONS (LOAD CASE 1)

Location	$(\sigma_y)_{\max}$ psi (MPa)	$(\sigma_z)_{\max}$ psi (MPa)	$\dot{\epsilon}_y$ (sec) <sup>-1</sup>	$\dot{\epsilon}_z$ (sec) <sup>-1</sup>
$z = 0.1D$	458.5 (3.16)	-8418 (-58.1)	4.466	-14.9
$z = 0.3D$	519 (3.58)	-3641 (-25.12)	3.555	- 7.29
$z = 0.5D$	520.4 (3.59)	-1995 (-13.77)	5.67	- 6.625
$y = 0.25D$	229 (1.58)	-1142 (-7.88)	NA	- 3.35
$y = 0.38D$	NA	- 568 (-3.92)	NA	- 1.80
$y = 0.50D$	NA	NA	NA	NA
Bar	NA	-1309 (-9.03)	NA	- 1.0

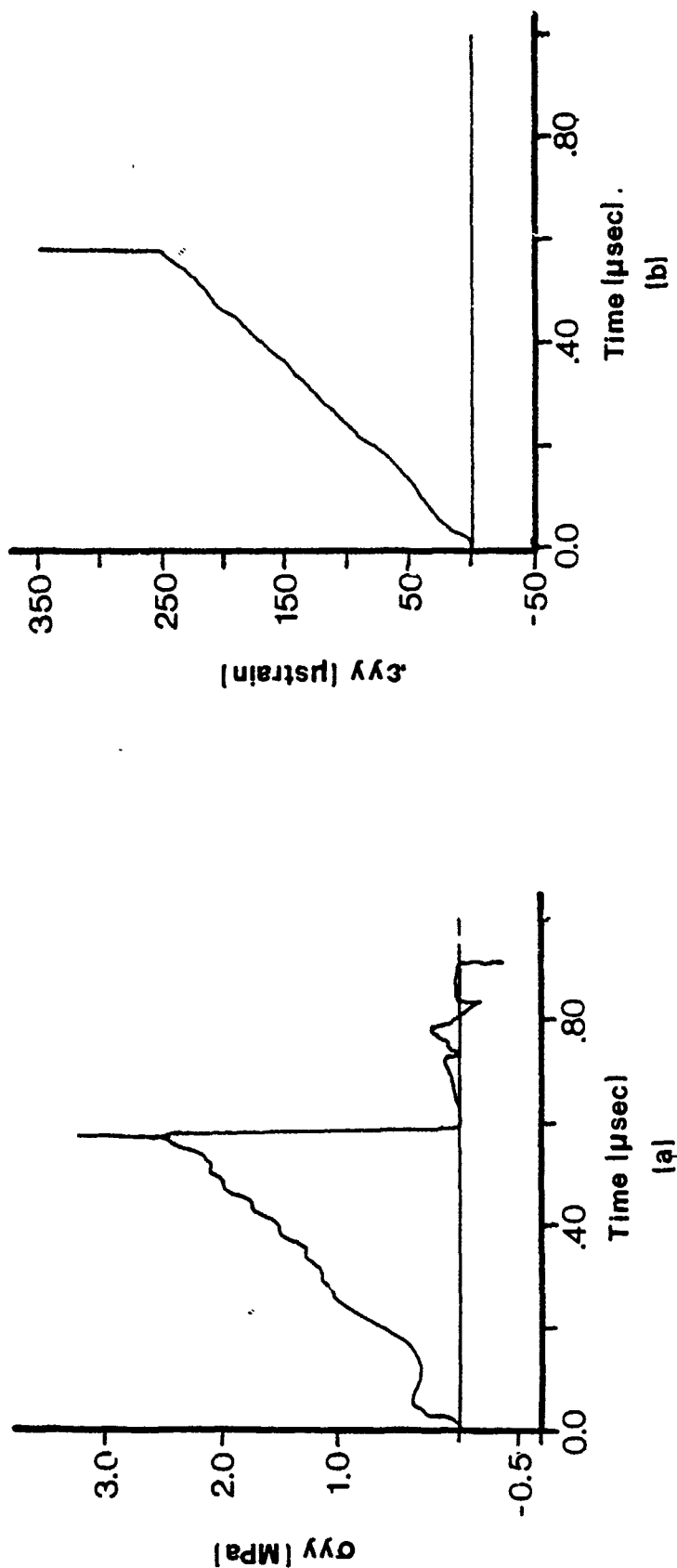
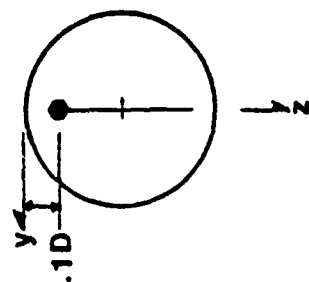


Figure 50. Time Histories for (a) Horizontal Stress and (b) Horizontal Strain at  $z = 0.1D$ , Load Case 1, Nonlinear Analysis

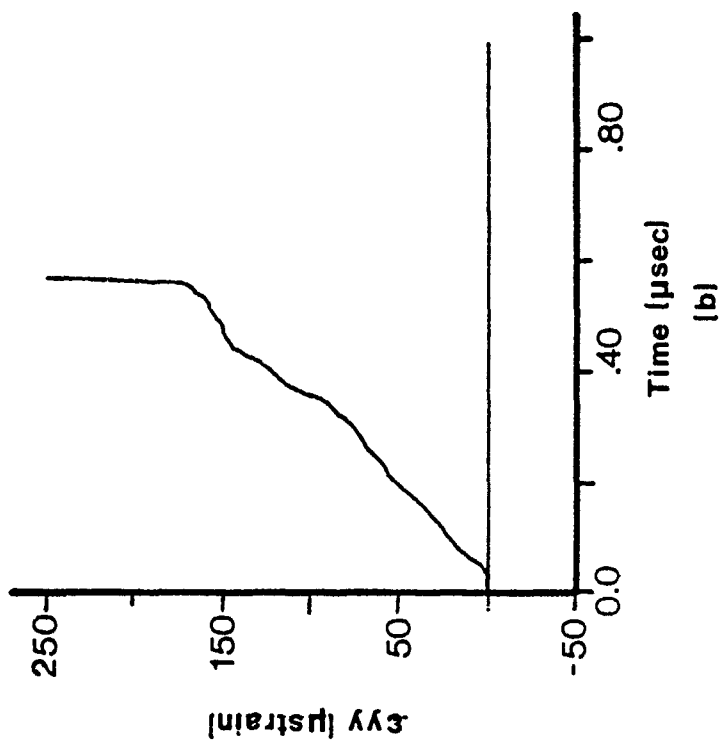
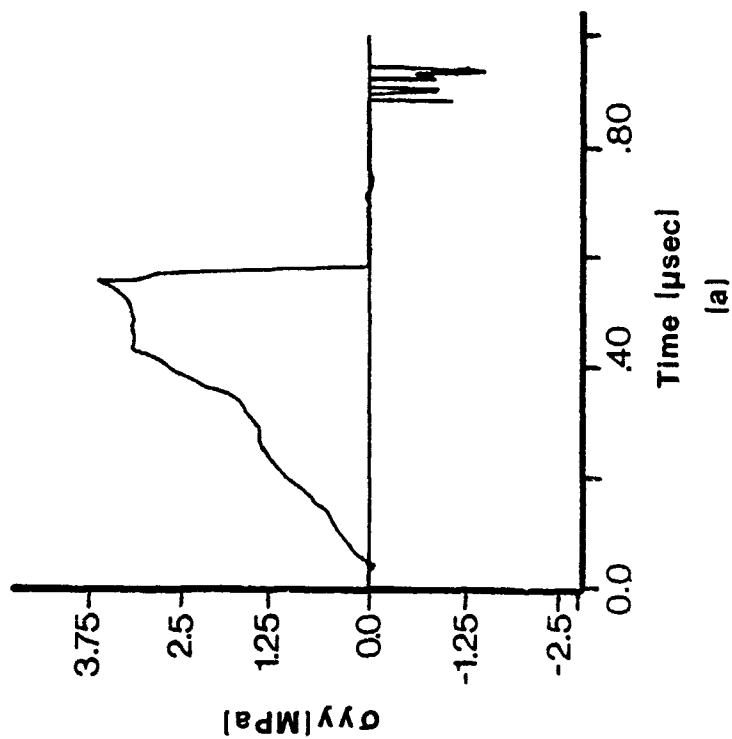
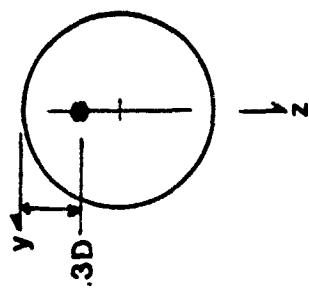


Figure 51. Time Histories for (a) Horizontal Stress and (b) Horizontal Strain at  $z = 0.3D$ , Load Case 1, Nonlinear Analysis



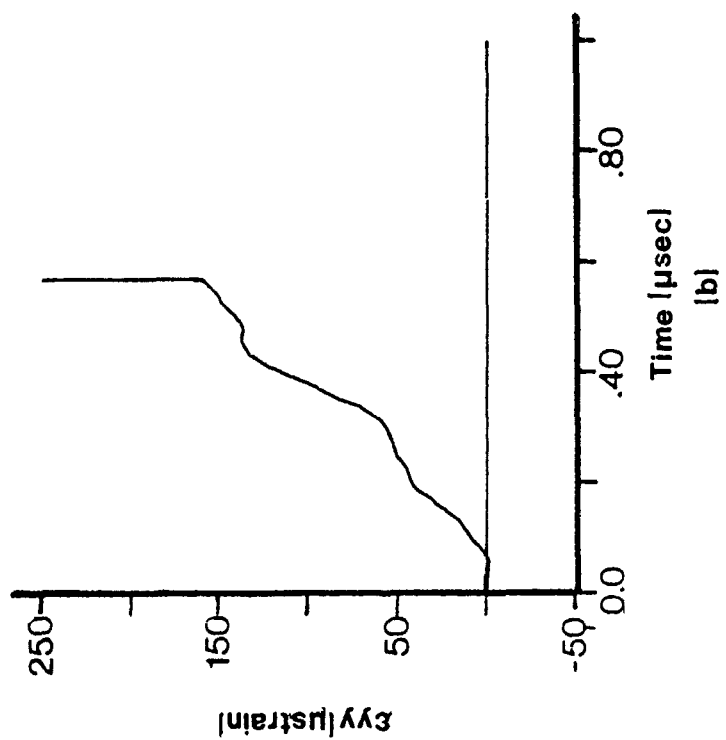
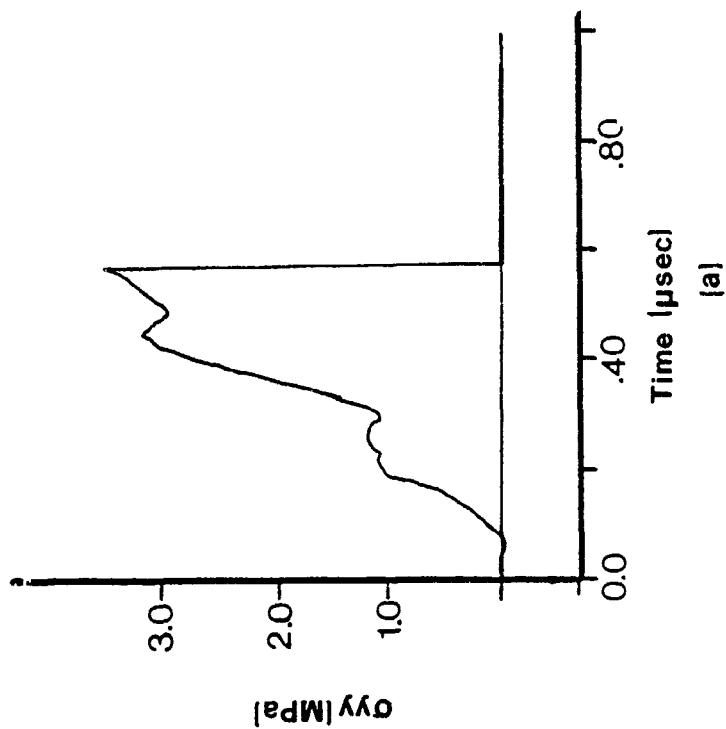
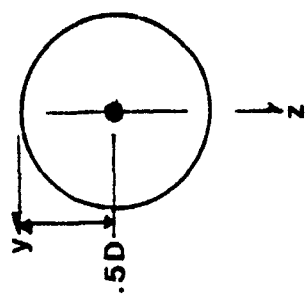


Figure 52. Time Histories for (a) Horizontal Stress and (b) Horizontal Strain at  $z = 0.5D$ , Load Case 1, Nonlinear Analysis

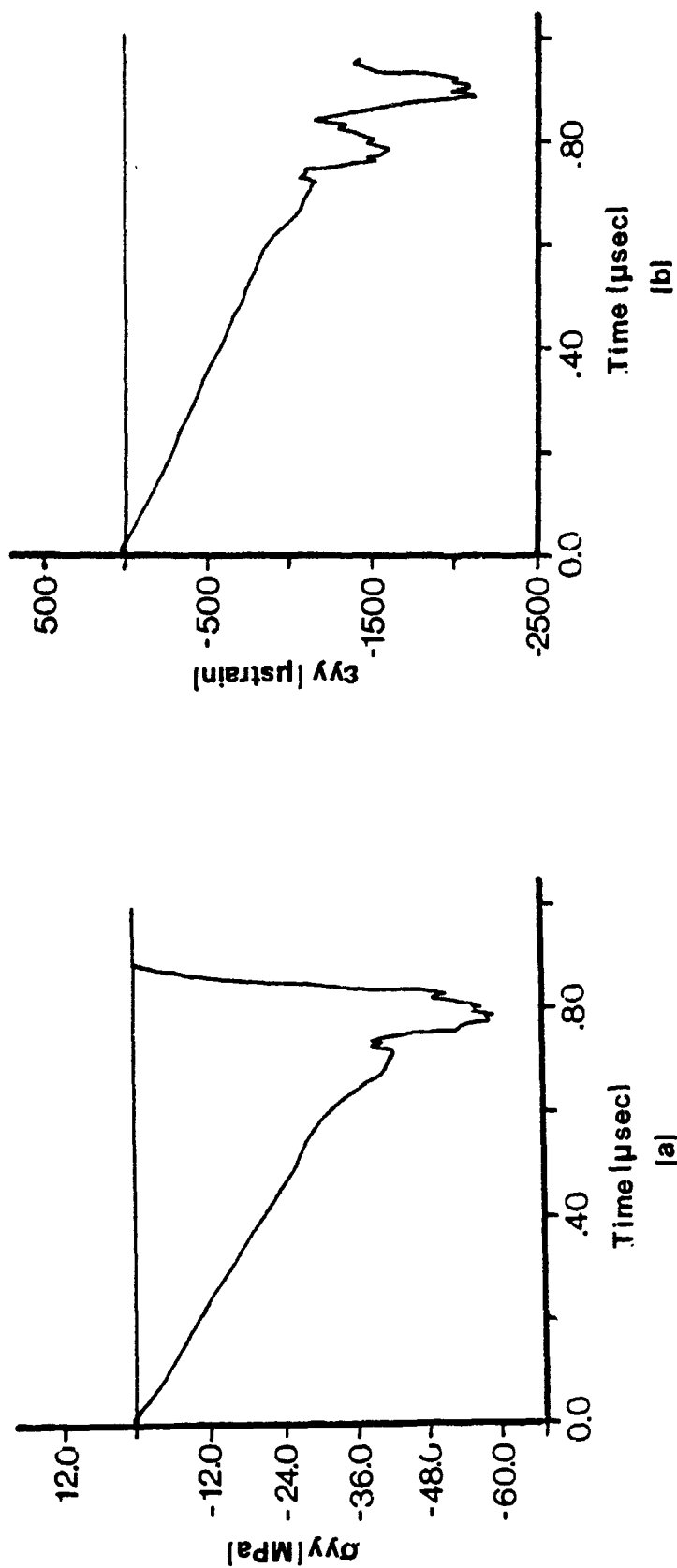
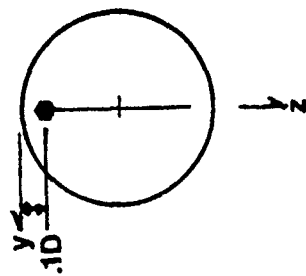


Figure 53. Time Histories for (a) Vertical Stress and (b) Vertical Strain at  $z = 0.1D$ , Load Case 1, Nonlinear Analysis

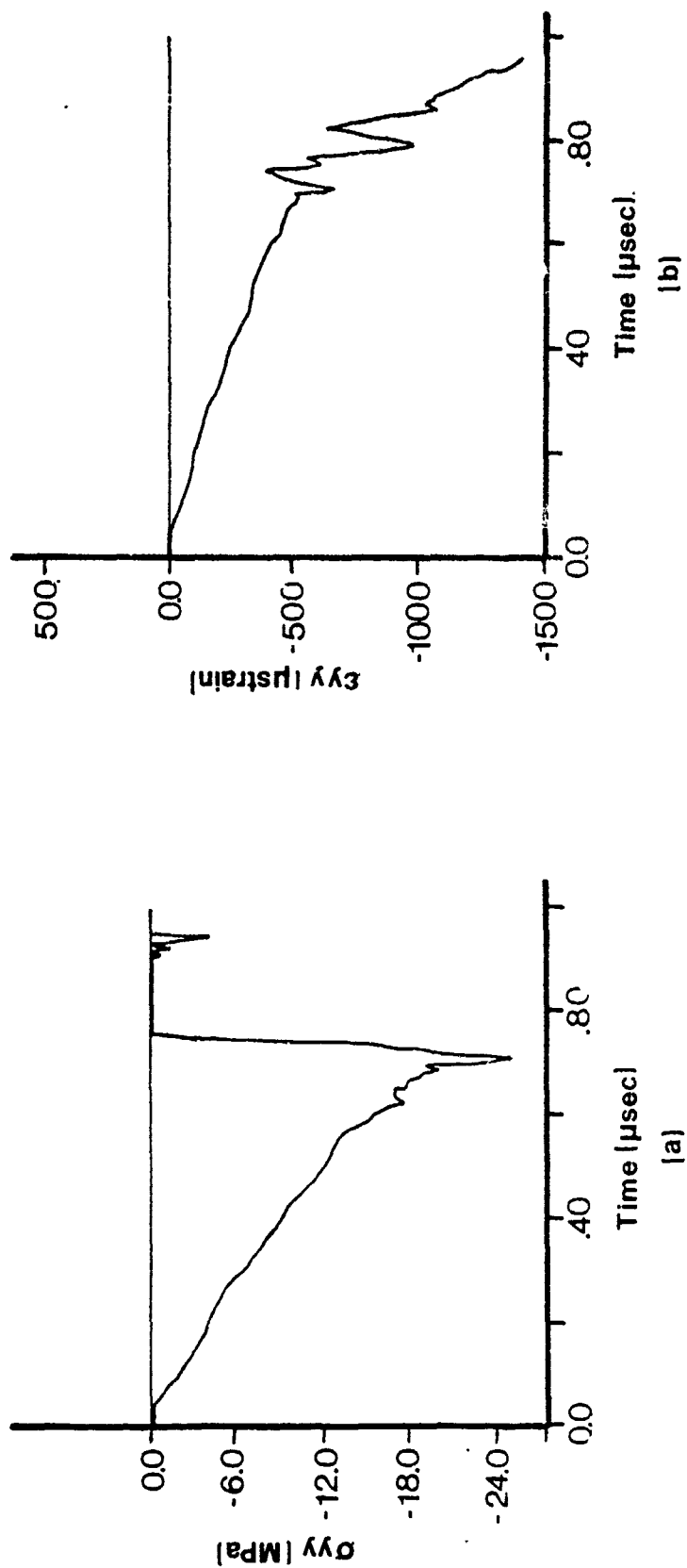
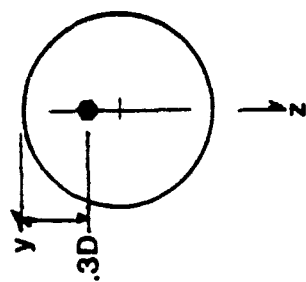


Figure 54. Time Histories for (a) Vertical Stress and (b) Vertical Strain at  $z = 0.3D$ , Load Case I, Nonlinear Analysis

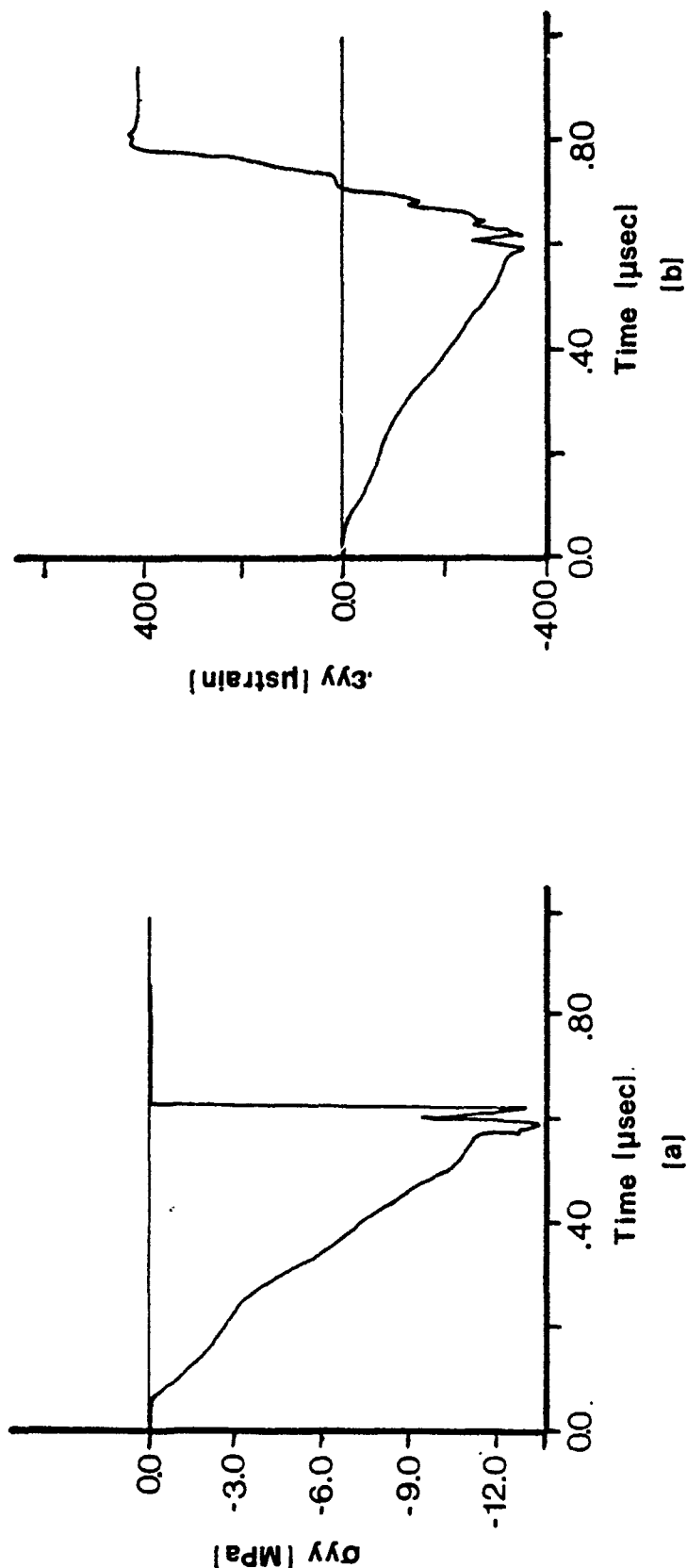
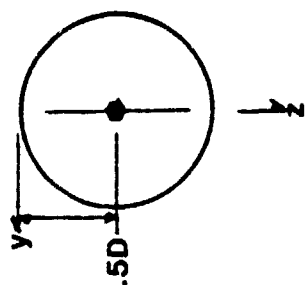
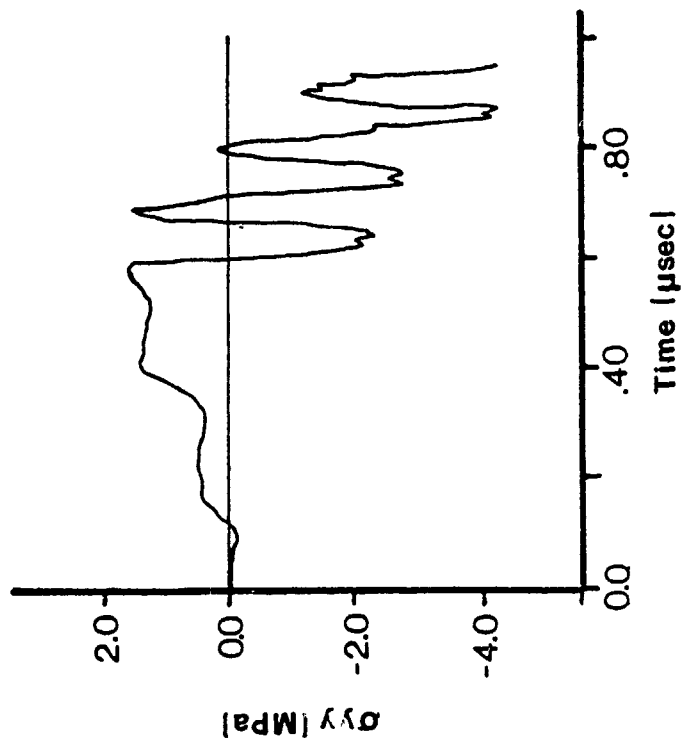
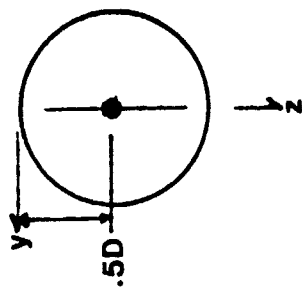
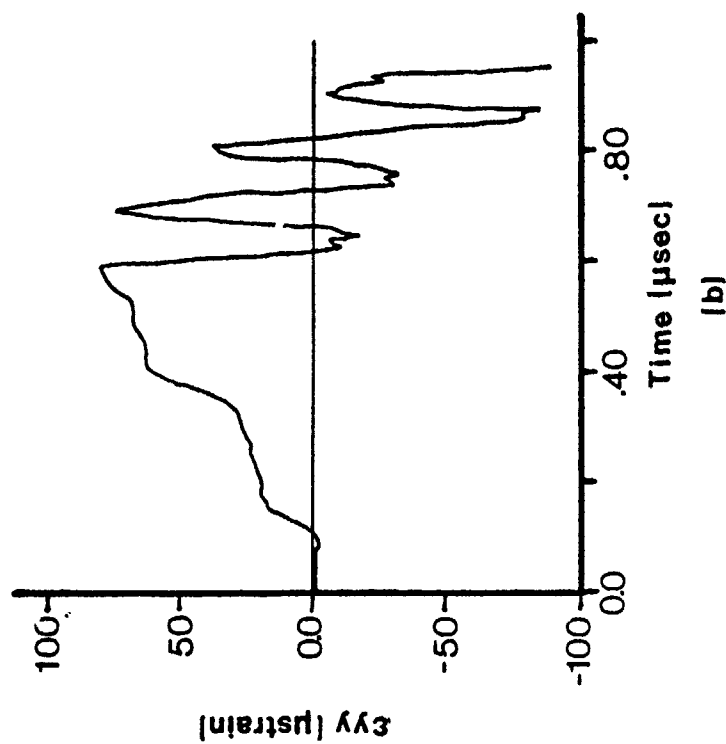


Figure 55. Time Histories for (a) Vertical Stress and (b) Vertical Strain at  $z = 0.5D$ , Load Case 1, Nonlinear analysis



(a)



(b)

Figure 56. Time Histories for (a) Horizontal Stress and (b) Horizontal Strain at  $y = 0.25D$ , Load Case 1, Nonlinear Analysis

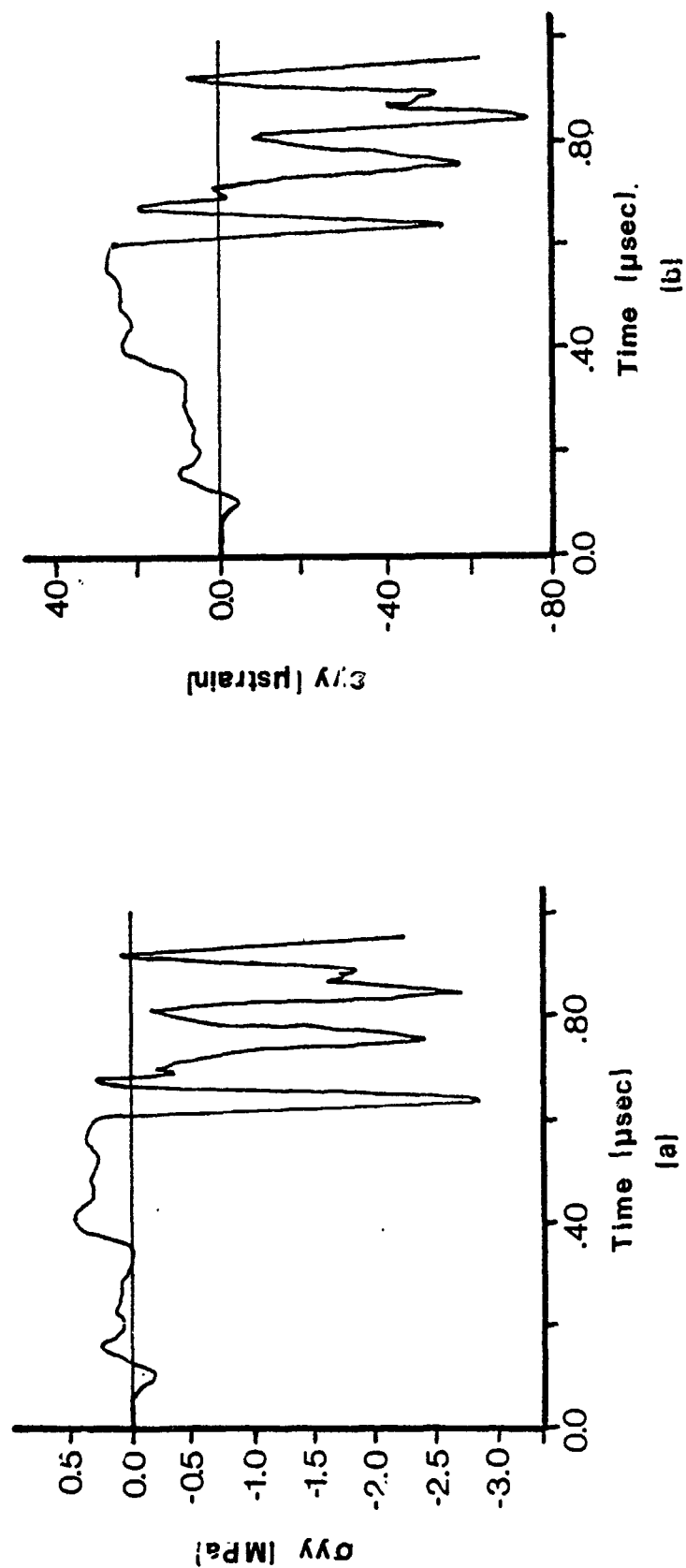
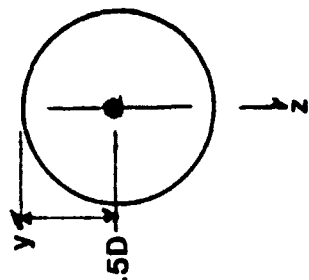


Figure 57. Time Histories for (a) Horizontal Stress and (b) Horizontal Strain at  $y = 0.38D$ , Load Case 1, Nonlinear Analysis

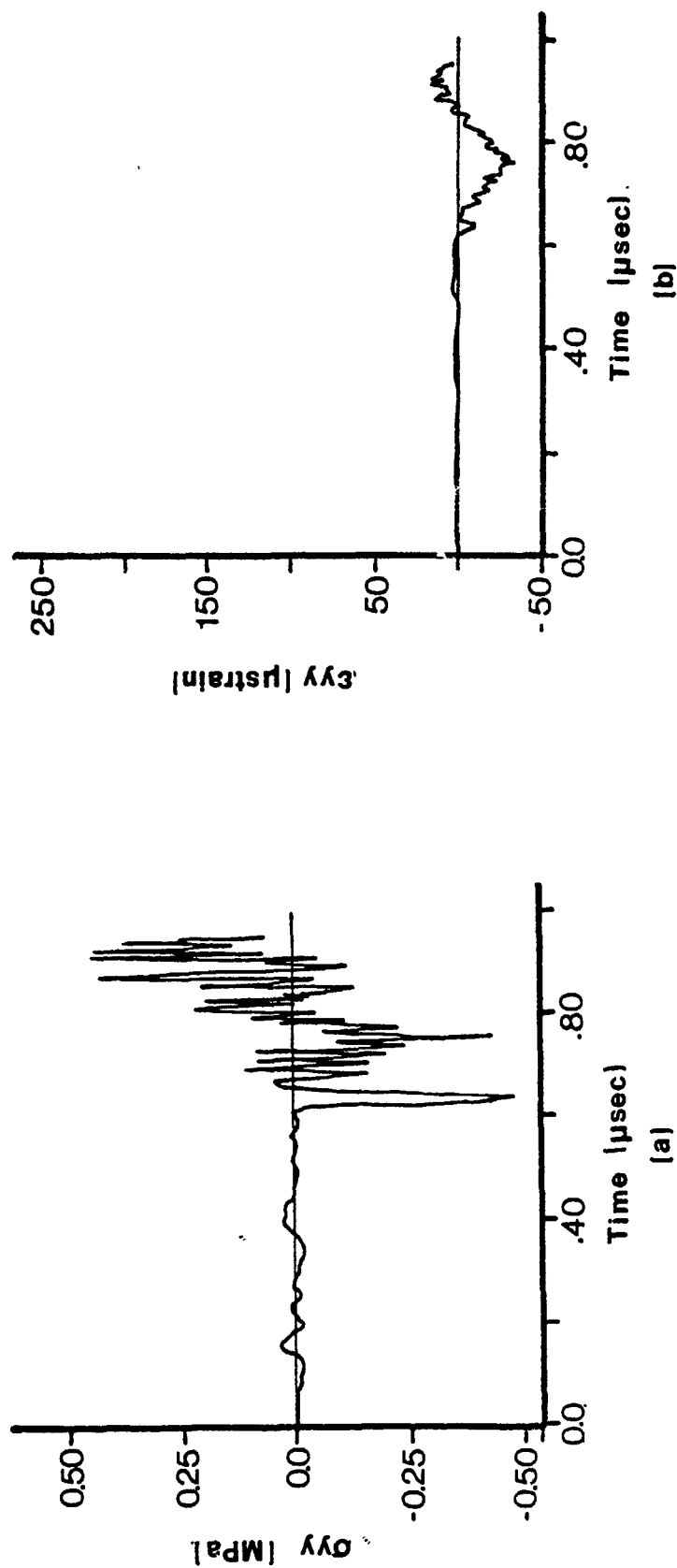
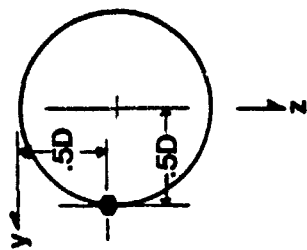


Figure 58. Time Histories for (a) Horizontal Stress and (b) Horizontal Strain at  $y = 0.50D$ , Load Case 1, Nonlinear Analysis

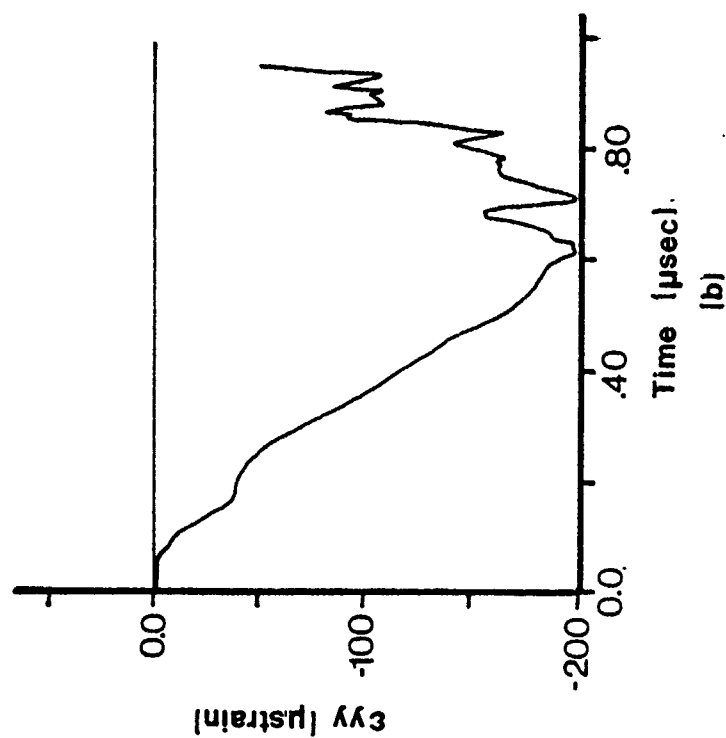
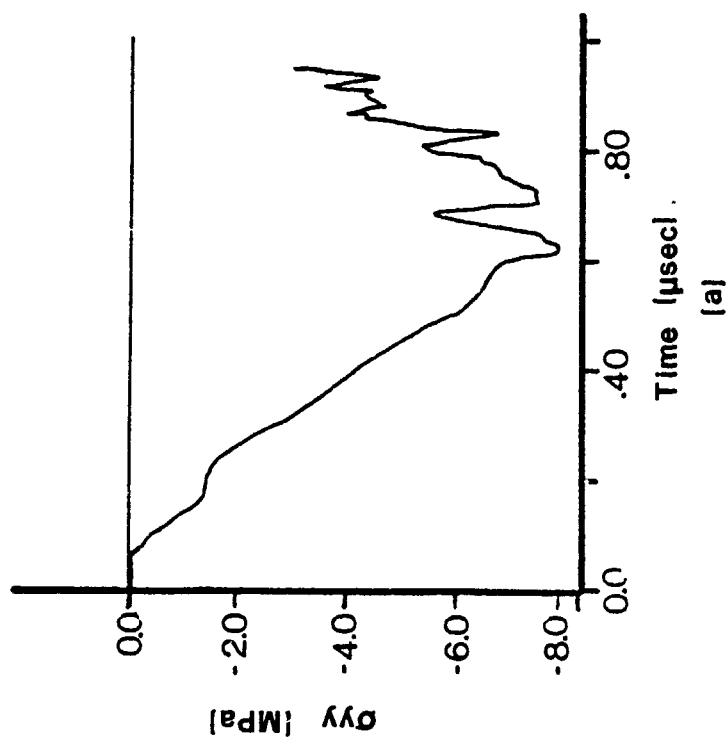
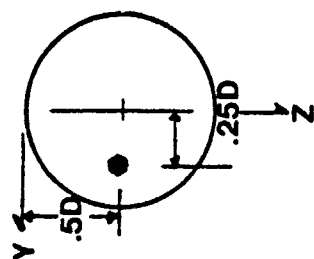


Figure 59. Time Histories for (a) Vertical Stress and (b) Vertical Strain at  $y = 0.25D$ , Load Case 1, Nonlinear Analysis



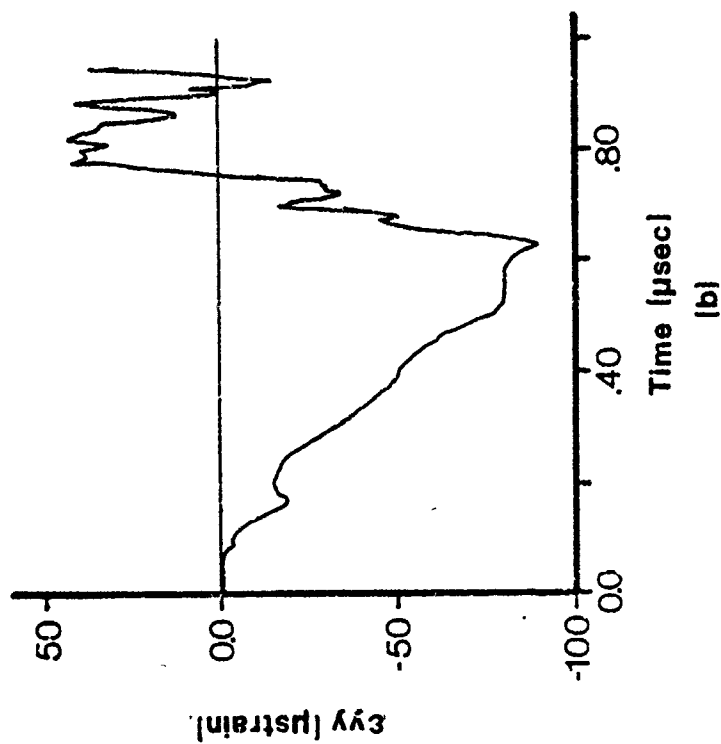
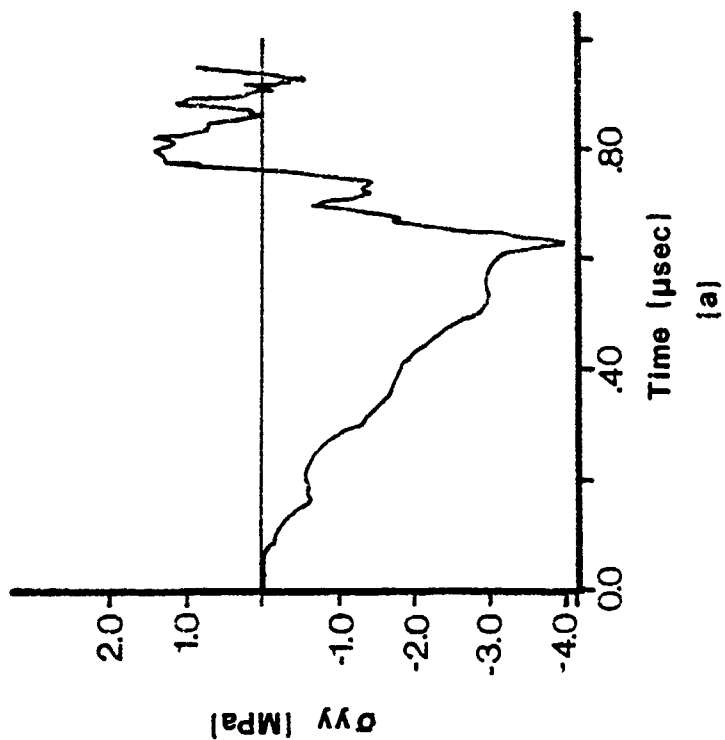
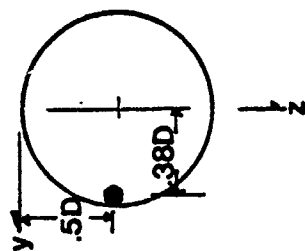


Figure 60. Time Histories for (a) Vertical Stress and (b) Vertical Strain at  $y = 0.38D$ , Load Case 1, Nonlinear Analysis

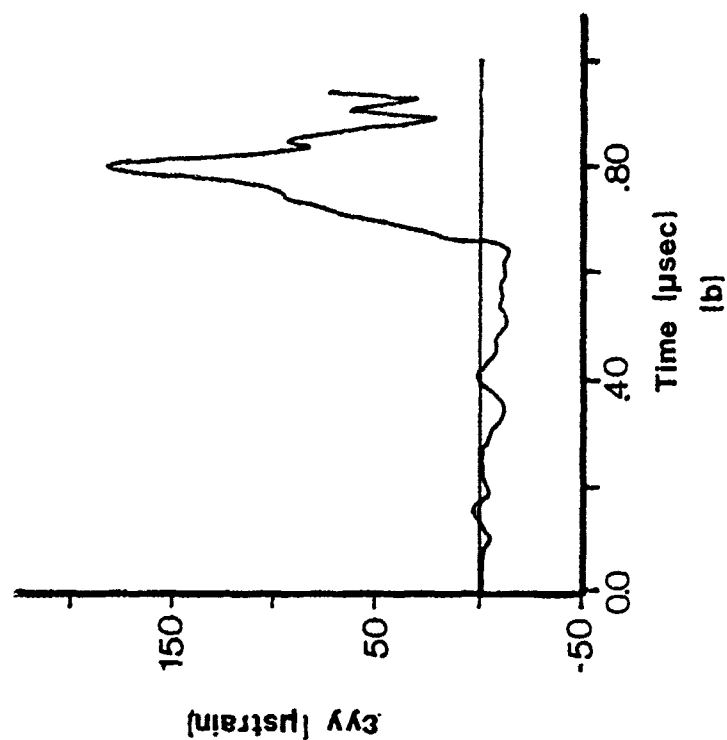
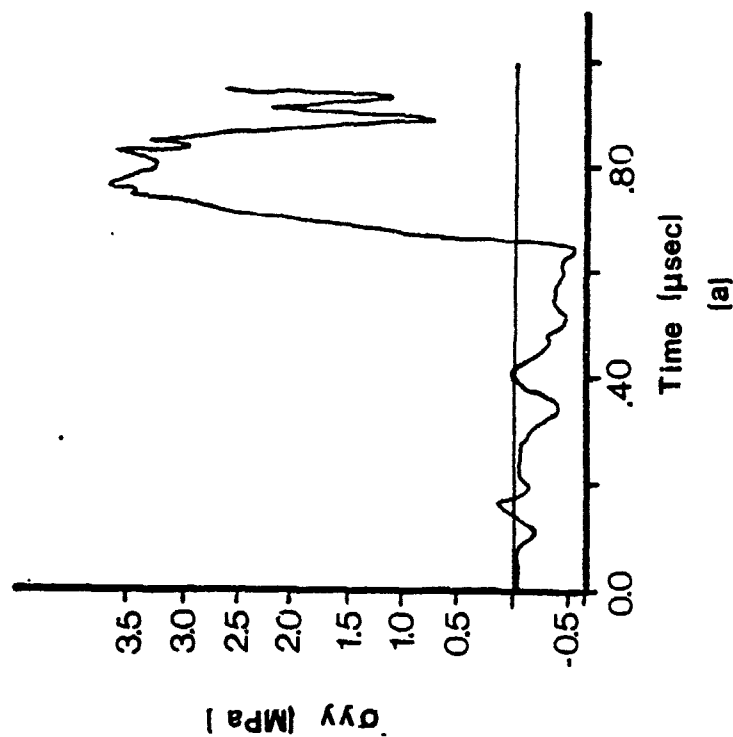
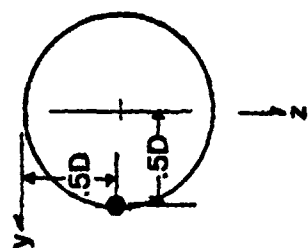


Figure 61. Time Histories for (a) Vertical Stress and (b) Vertical Strain at  $y = 0.50D$ , Load Case 1, Nonlinear Analysis

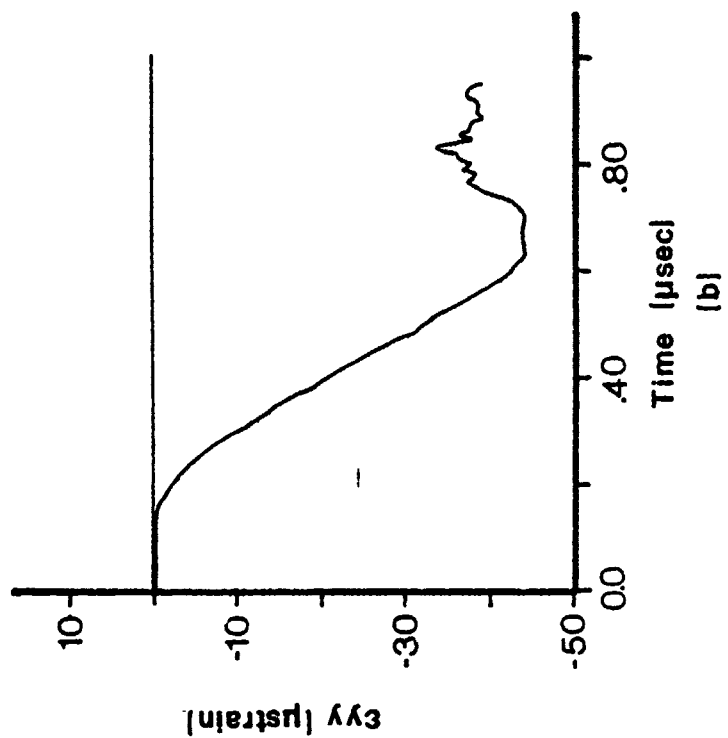
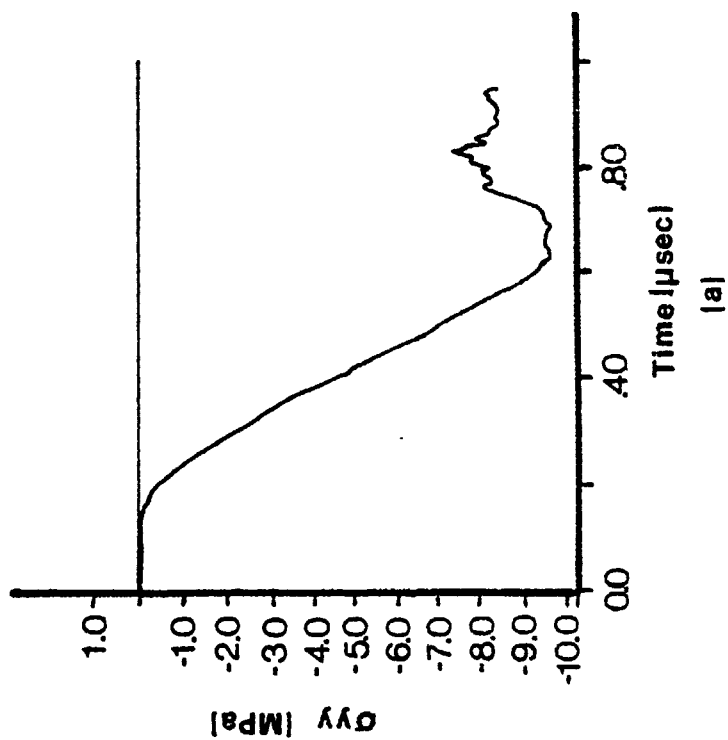
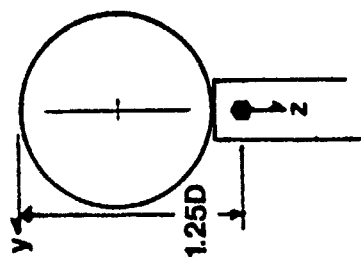


Figure 62. Time Histories for (a) Vertical Stress and (b) Vertical Strain in the transmitter bar, Load Case 1, Nonlinear Analysis

Profiles for the horizontal stress,  $\sigma_y$ , and the horizontal strain,  $\epsilon_y$ , along the vertical diameter at five selected time increments (56.1  $\mu\text{sec}$ , 56.3  $\mu\text{sec}$ , 58.0  $\mu\text{sec}$ , 66.0  $\mu\text{sec}$ , and 85.0  $\mu\text{sec}$ ) are presented in Figures 63 through 67, respectively. The initiation of the first crack is indicated in Figure 63, and failure of the cylinder is indicated in Figure 67. Profiles for the horizontal stress and strain along the horizontal diameter, for the same selected times, are presented in Figures 68 through 72. The propagation of the crack to the center of the cylinder is illustrated in Figure 70 at time  $t = 58 \mu\text{sec}$ . Profiles for the vertical stress and strain along the horizontal diameter at the same selected times are presented in Figures 73 through 77.

The cracking sequence simulated in the numerical analysis, from initiation of the first crack until failure, is illustrated in Figure 78. The first crack occurs along the vertical diameter at a location approximately 0.5 inches (12.7 mm) from the top of the cylinder, at a time  $t = 56.1 \mu\text{sec}$  (Figure 78a). At a time  $t = 58.0 \mu\text{sec}$ , the crack is observed to propagate in both directions along the vertical diameter (Figure 78b), past midcylinder in one direction and 0.2 inches (5.1 mm) from the top in the other direction. At time  $t = 66 \mu\text{sec}$ , the crack has propagated 0.15 inches (3.8 mm) from the bottom of the cylinder and 0.075 inches (1.9 mm) from the top of the cylinder (Figure 78c). Finally, at time  $t = 85 \mu\text{sec}$ , failure occurs (Figure 78d). The crack has nearly propagated through the entire depth of the cylinder, and flexural tensile cracks have developed at either end of the cylinder along the horizontal diameter. No bifurcation of the primary vertical crack was predicted in this simulation.

### 3. Results of Nonlinear Analysis (Load Case 2)

Time histories for the horizontal stress,  $\sigma_y$ , and the horizontal strain,  $\epsilon_y$ , at three locations along the vertical diameter are illustrated in Figures 79, 80, and 81 for  $z$  equal to 0.1D, 0.3D, and 0.5D, respectively. Similar time histories for the vertical stress,  $\sigma_z$ , and the vertical strain,  $\epsilon_z$ , at the same locations are presented in Figures 82, 83, and 84. Time histories for the horizontal stress and strain at three locations along the horizontal diameter are presented in Figures 85, 86, and 87 for  $y$  equal to 0.25D, 0.38D, and 0.5D, respectively. Similar time histories for the vertical stress and strain at the same locations are presented in Figures 88, 89, and 90.

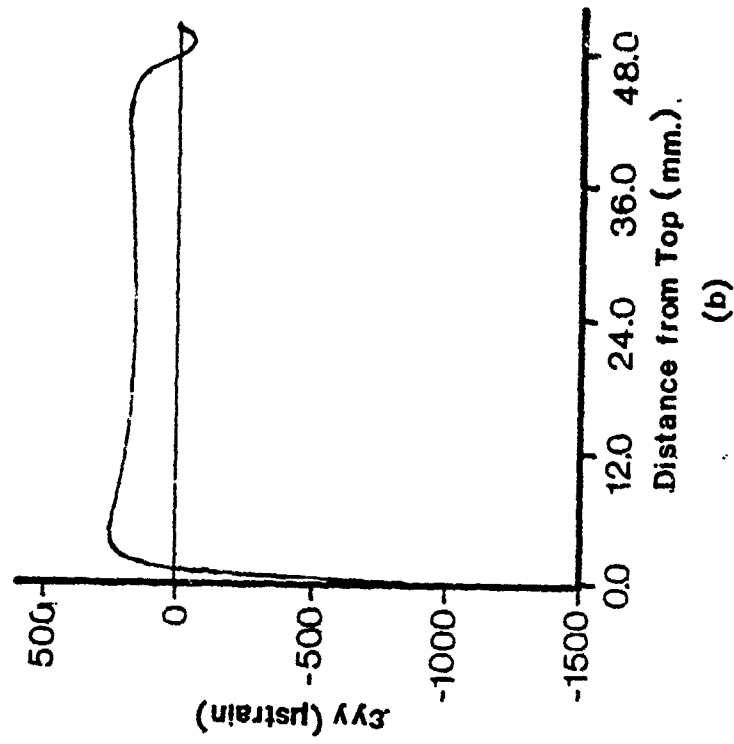
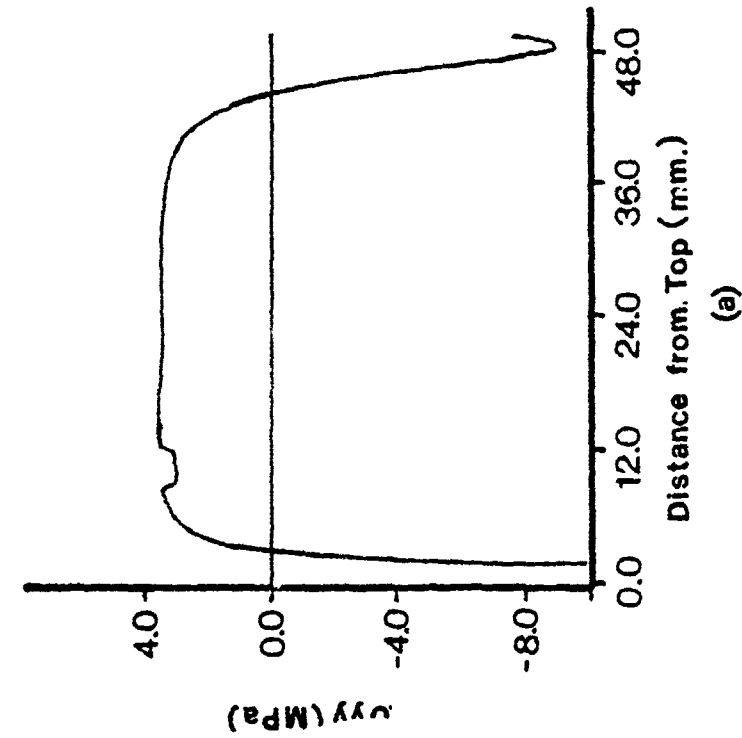


Figure 63. Profiles for (a) horizontal stress and (b) horizontal strain along the vertical diameter, Load Case 1, nonlinear analysis,  $t = 56.1 \mu\text{sec}$ .

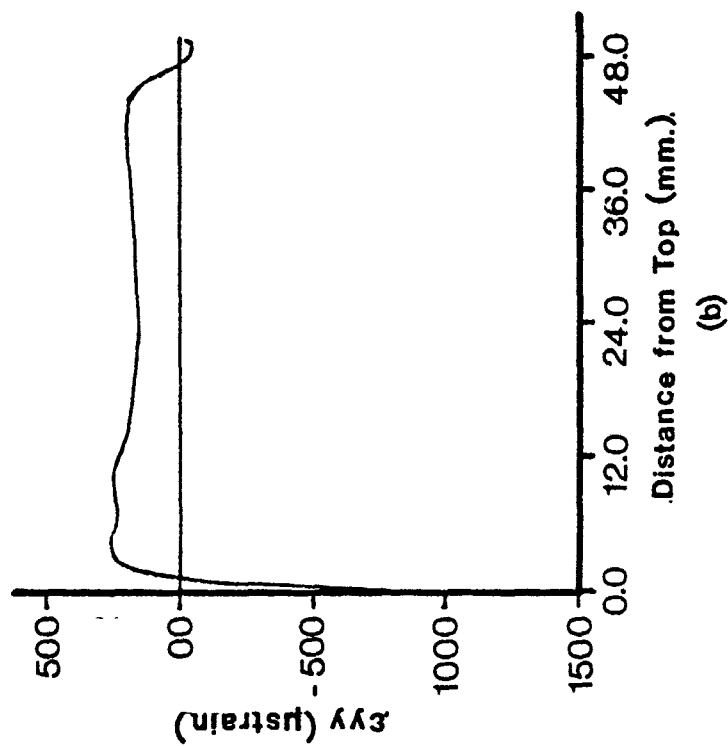
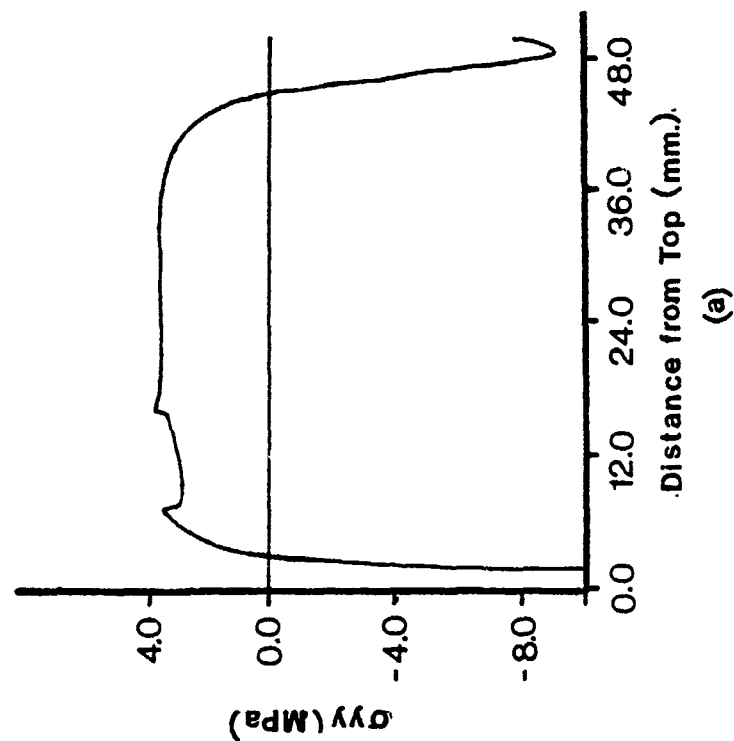


Figure 64. Profiles for (a) horizontal stress and (b) horizontal strain along the vertical diameter, Load Case 1, nonlinear analysis,  $t = 56.3 \mu\text{sec}$ .

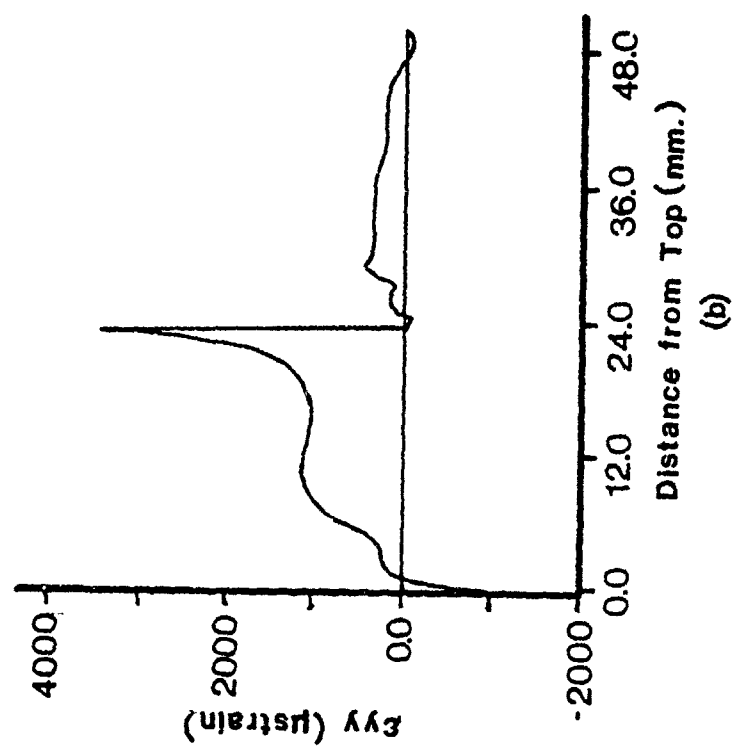
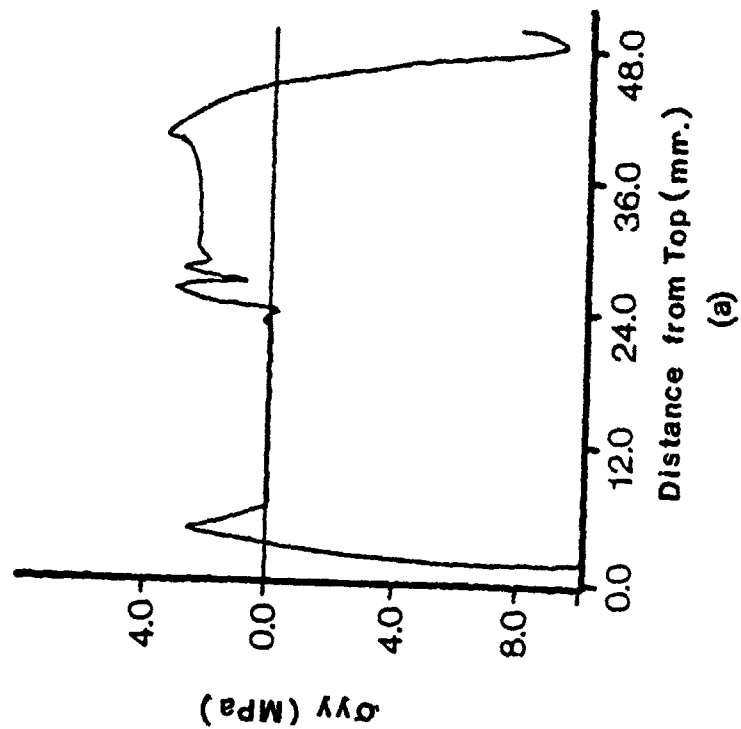


Figure 65. Profiles for (a) horizontal stress and (b) horizontal strain along the vertical diameter, Load Case 1, nonlinear analysis,  $t = 58.0 \mu$ sec.

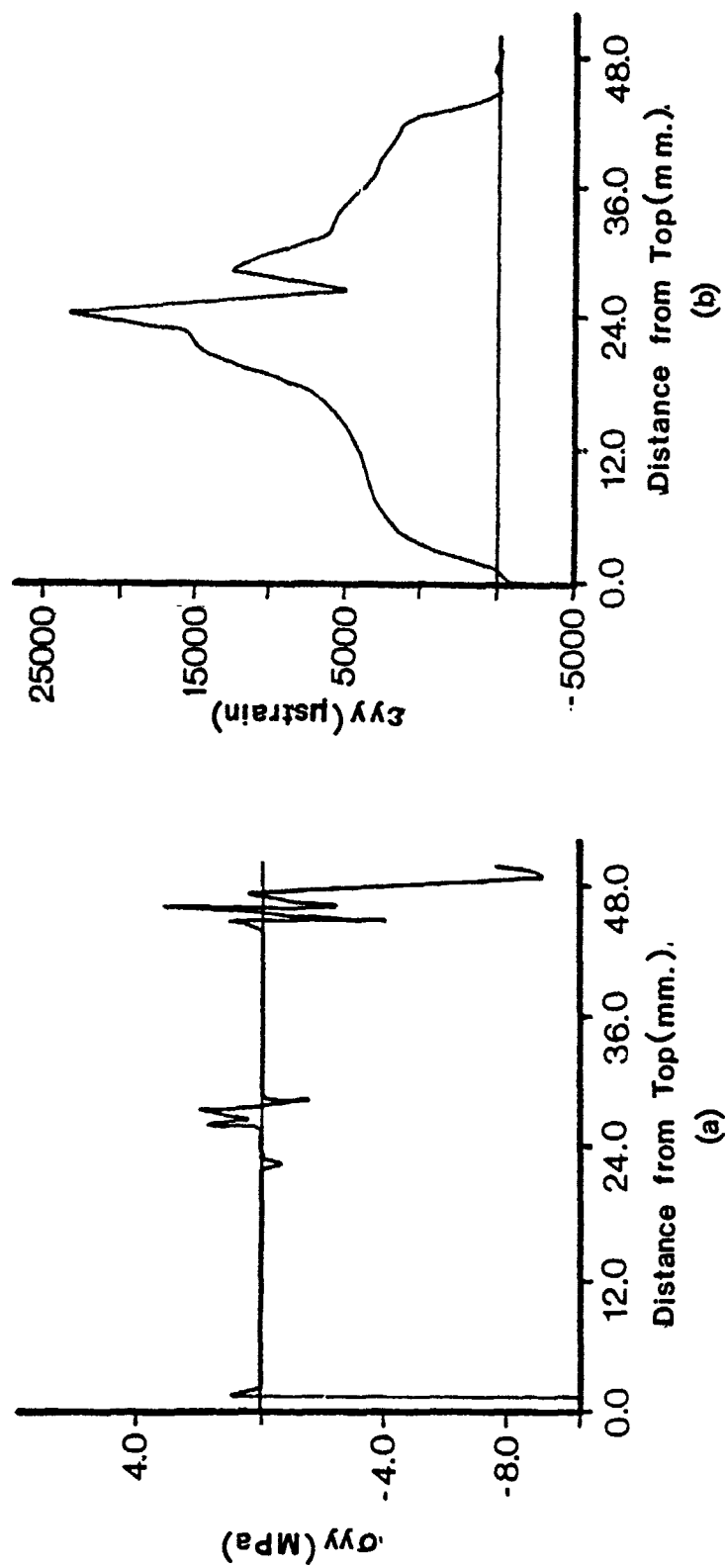


Figure 66. Profiles for (a) horizontal stress and (b) horizontal strain along the vertical diameter, Load Case 1, nonlinear analysis,  $t = 66.0 \mu\text{sec}$ .



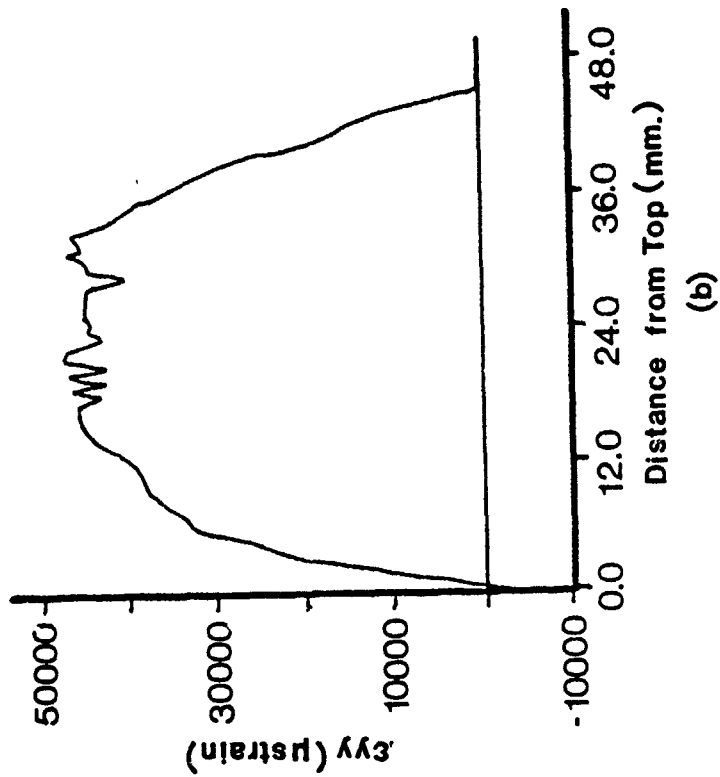
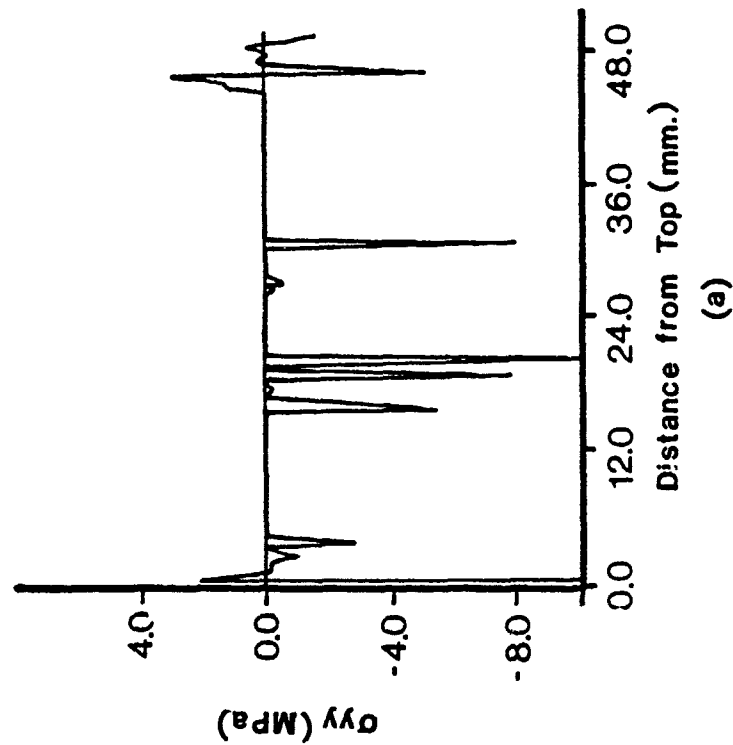


Figure 67. Profiles for (a) horizontal stress and (b) horizontal strain along the vertical diameter, Load Case 1, nonlinear analysis,  $t = 85.0 \mu\text{sec.}$

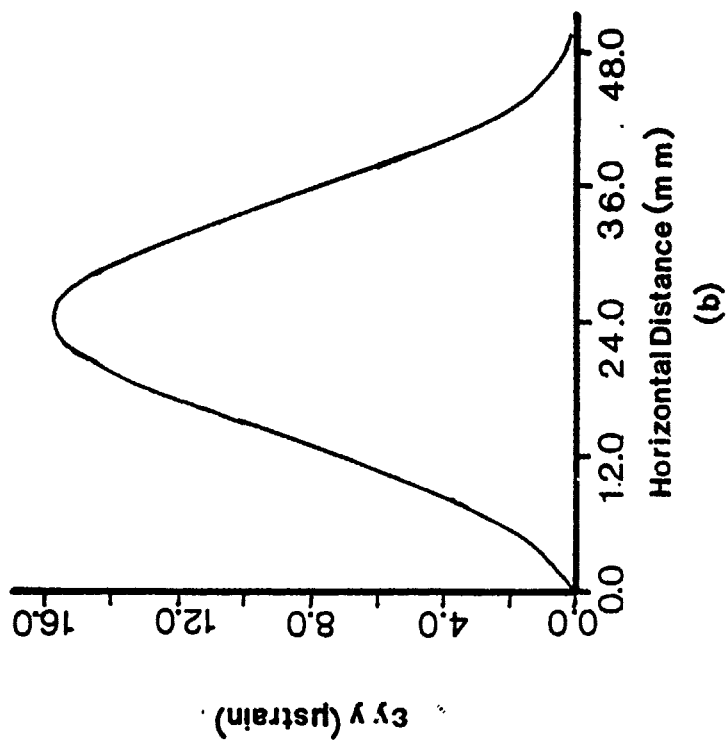
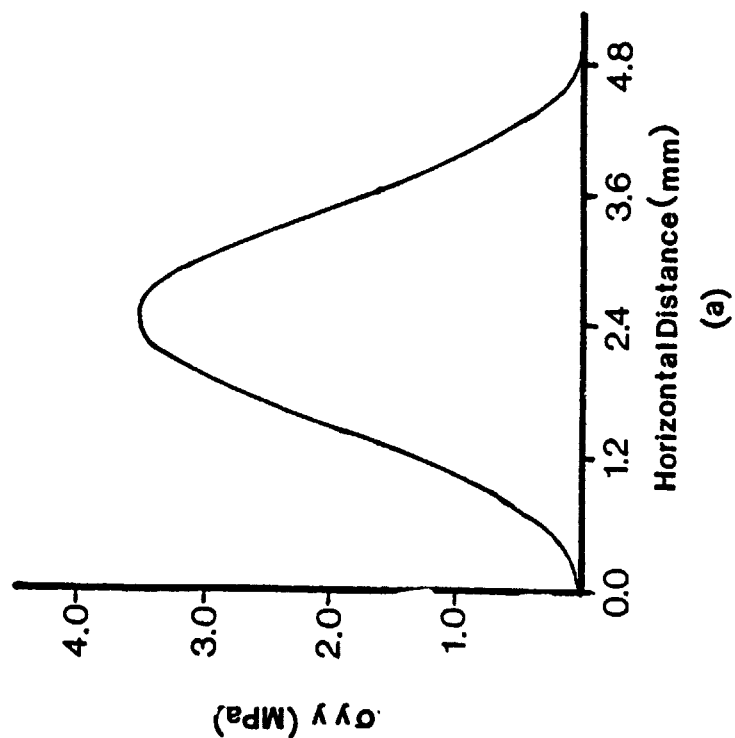


Figure 68. Profiles for (a) horizontal stress and (b) horizontal strain along the horizontal diameter, Load Case 1, nonlinear analysis,  $t = 56.1 \text{ } \mu\text{sec}$ .

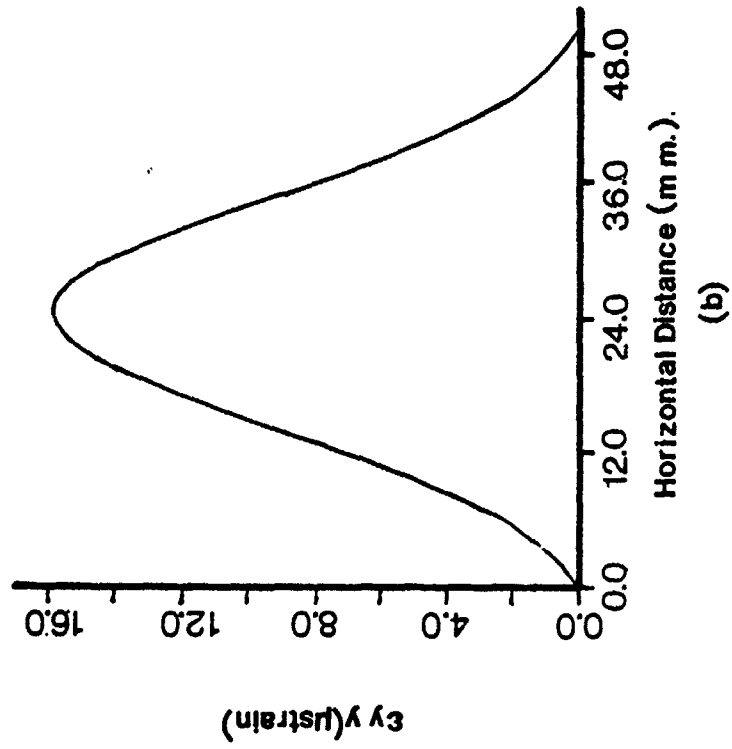
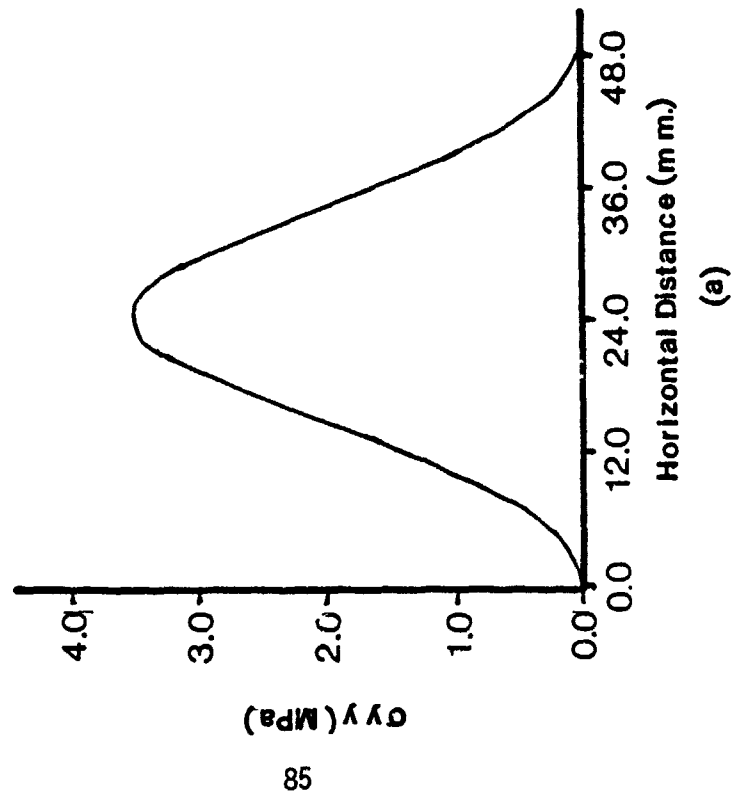


Figure 69. Profiles for (a) horizontal stress and (b) horizontal strain along the horizontal diameter, Load Case 1, nonlinear analysis,  $t = 56.3 \mu\text{sec}$ .

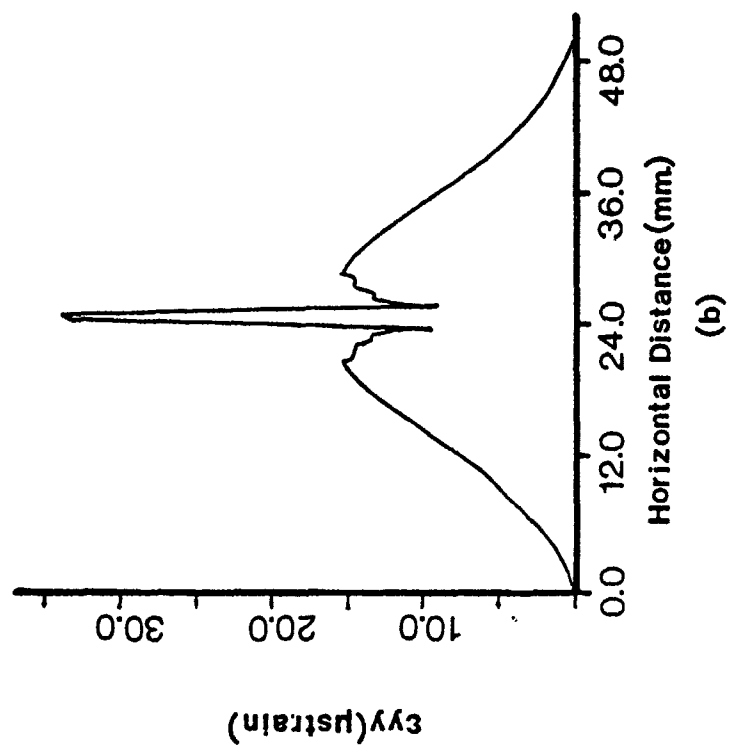
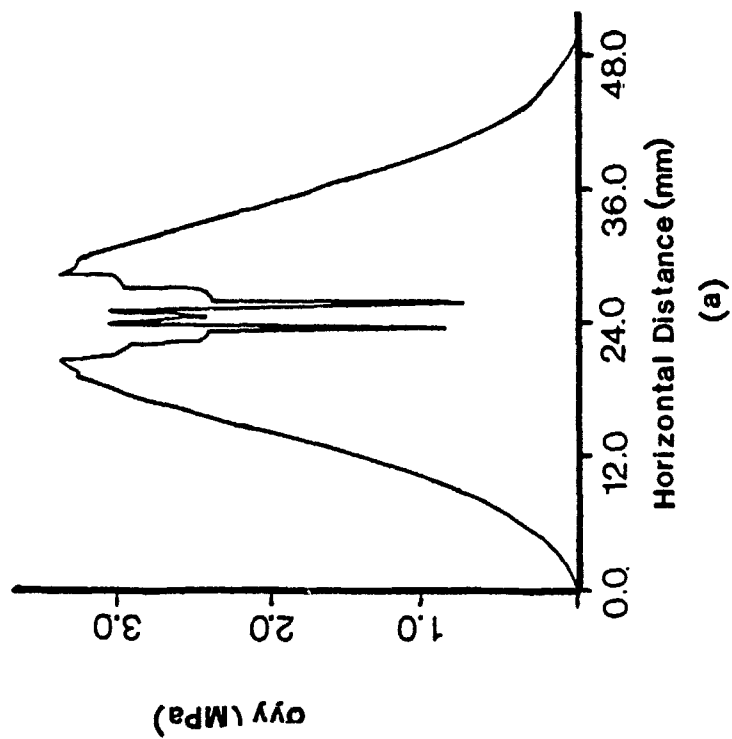


Figure 70. Profiles for (a) horizontal stress and (b) horizontal strain along the horizontal diameter, Load Case 1, nonlinear analysis,  $t = 58.0 \mu\text{sec}$ .

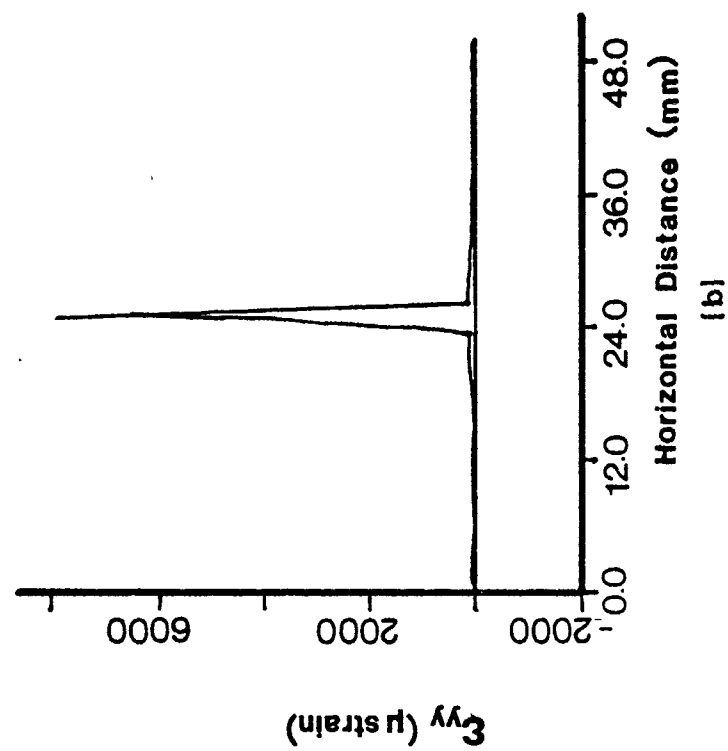
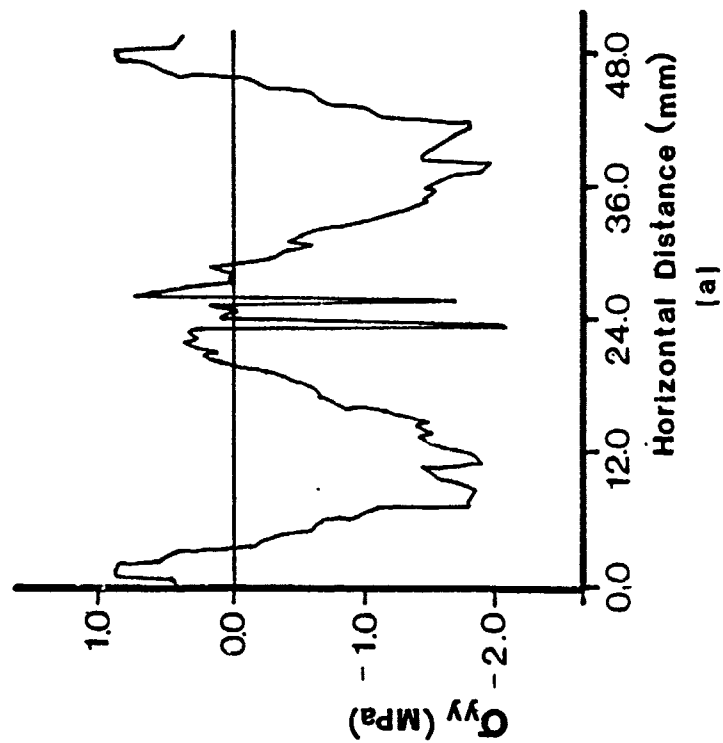


Figure 71. Profiles for (a) horizontal stress and (b) horizontal strain along the horizontal diameter, Load Case 1, nonlinear analysis,  $t = 66.0 \mu\text{sec}$ .

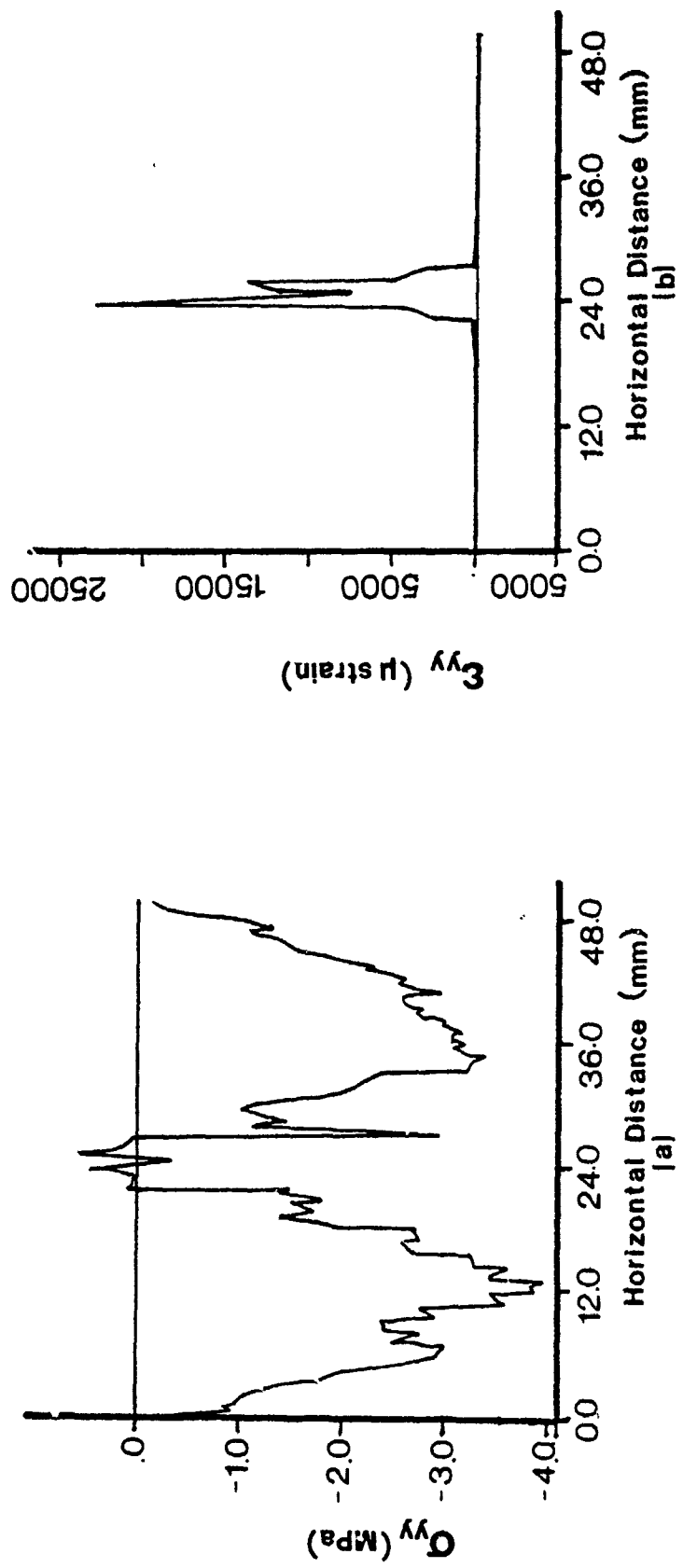


Figure 72. Profiles for (a) horizontal stress and (b) horizontal strain along the horizontal diameter, Load Case 1, nonlinear analysis,  $t = 85.0 \mu\text{sec}$ .

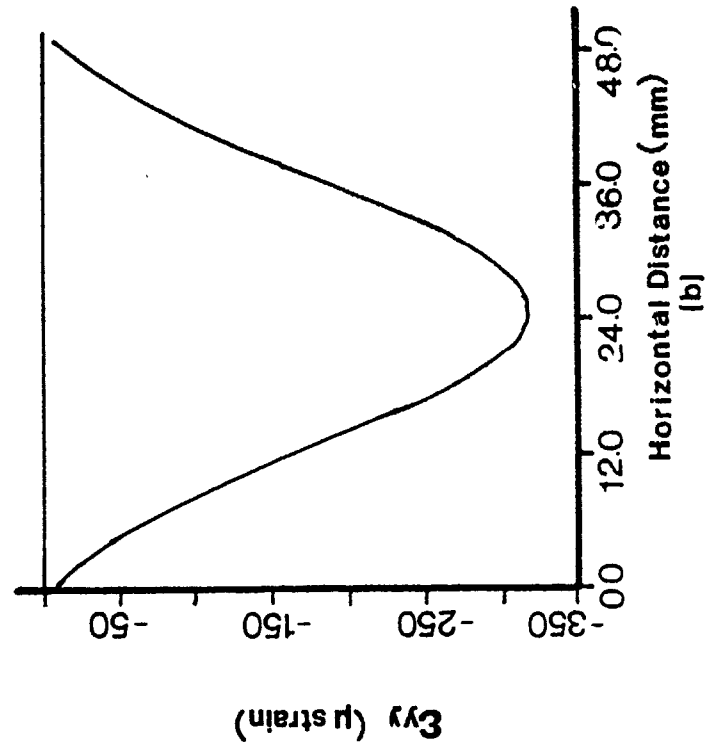
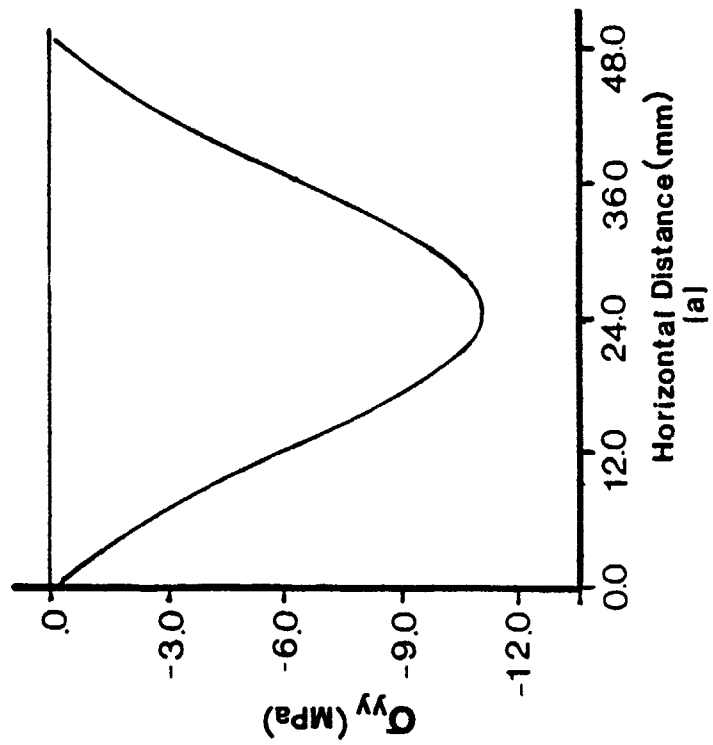


Figure 73. Profiles for (a) vertical stress and (b) vertical strain along the horizontal diameter, Load Case 1, nonlinear analysis,  $t = 56.1 \mu\text{sec}$ .

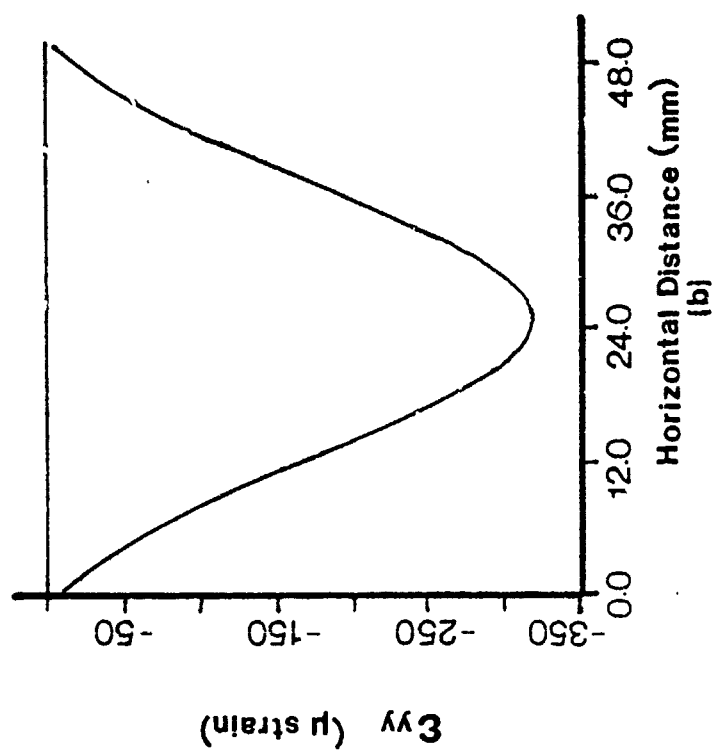
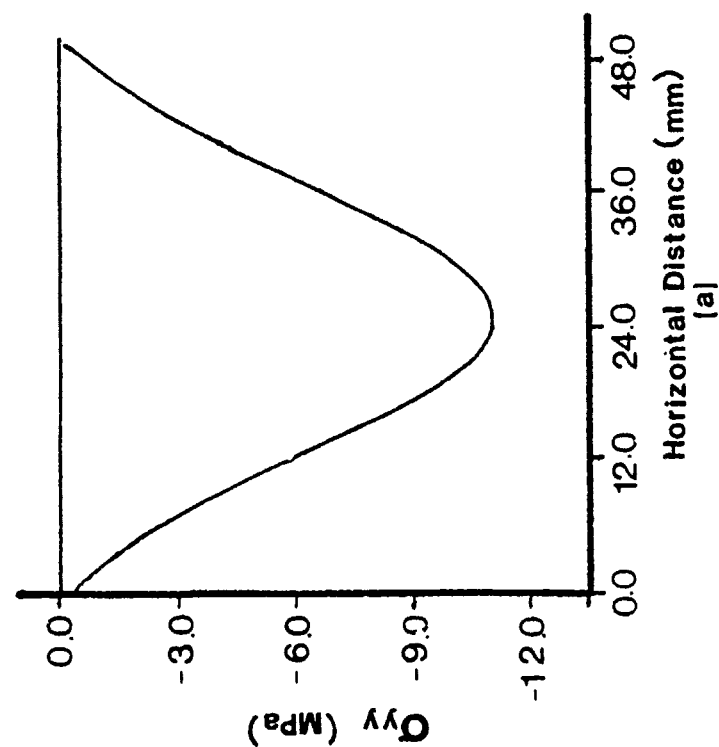


Figure 74. Profiles for (a) vertical stress and (b) vertical strain along the horizontal diameter, Load Case 1, nonlinear analysis,  $t = 56.3 \mu\text{sec}$ .



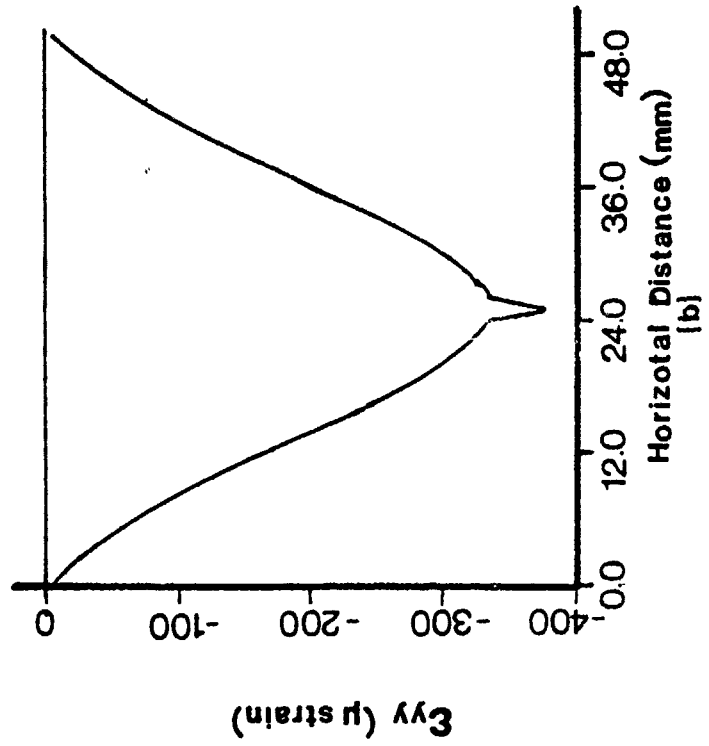
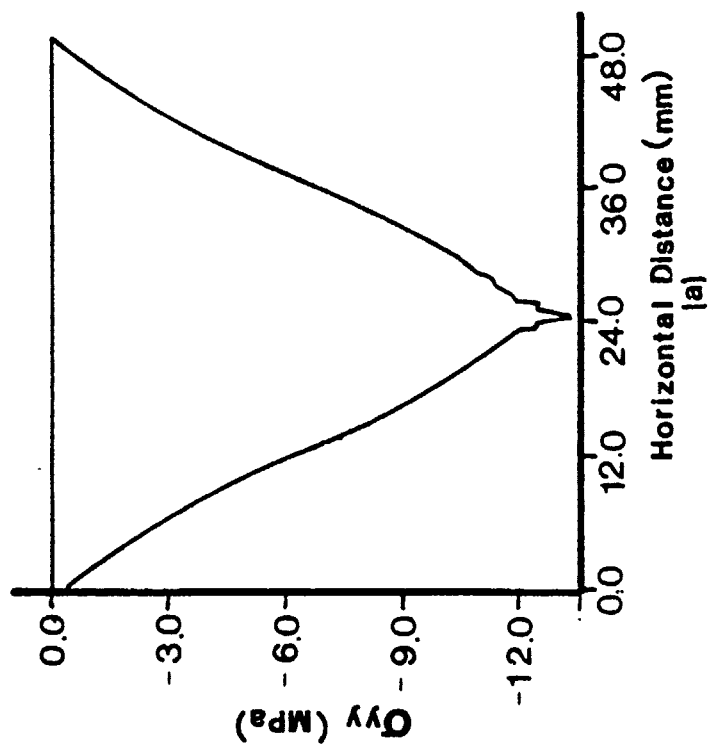


Figure 75. Profiles for (a) vertical stress and (b) vertical strain along the horizontal diameter, Load Case 1, nonlinear analysis,  $t = 58.0 \mu\text{sec}$ .

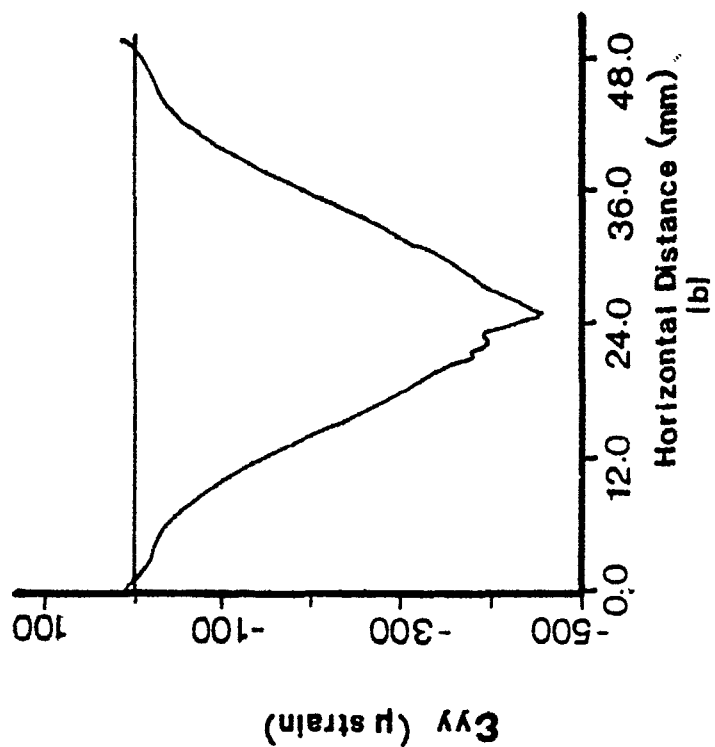
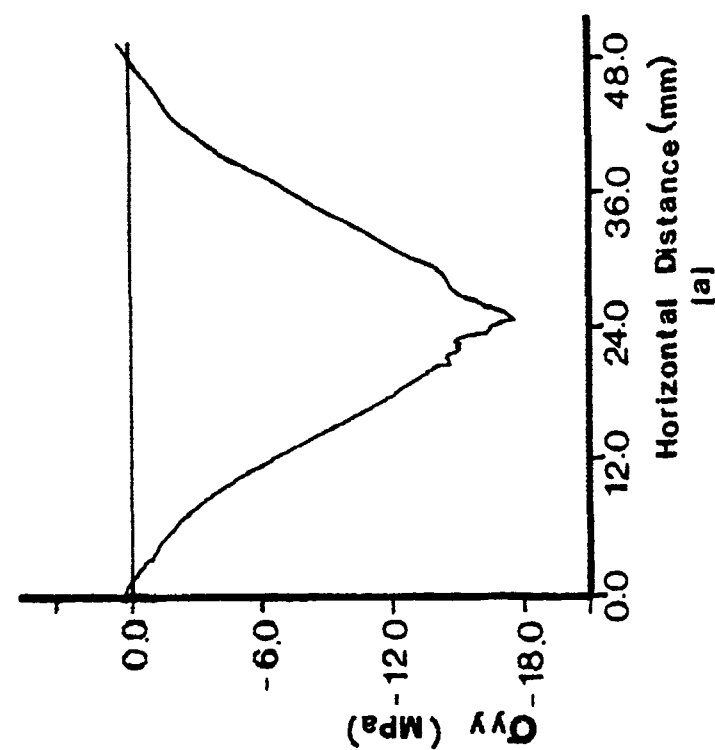


Figure 76. Profiles for (a) vertical stress and (b) vertical strain along the horizontal diameter, Load Case 1, nonlinear analysis,  $t = 66.0 \mu\text{sec}$ .

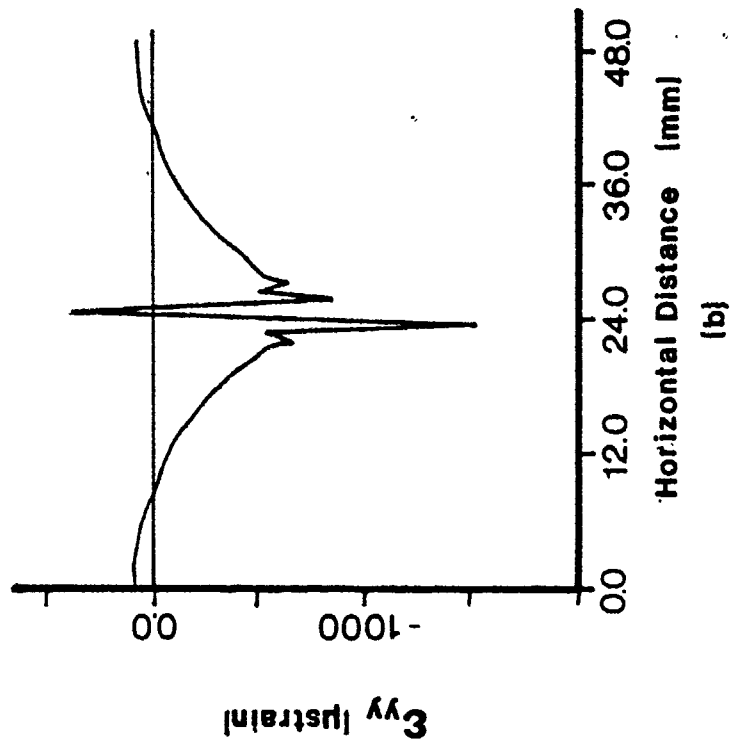
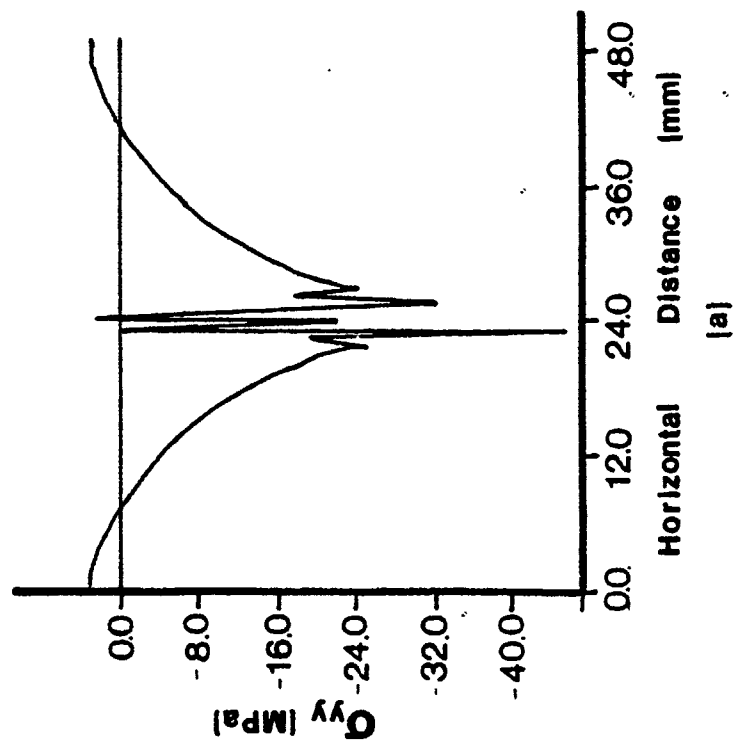
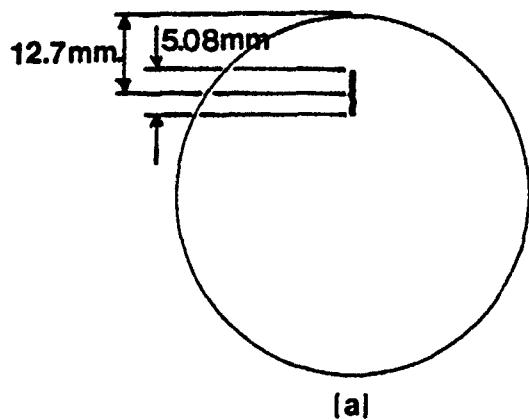
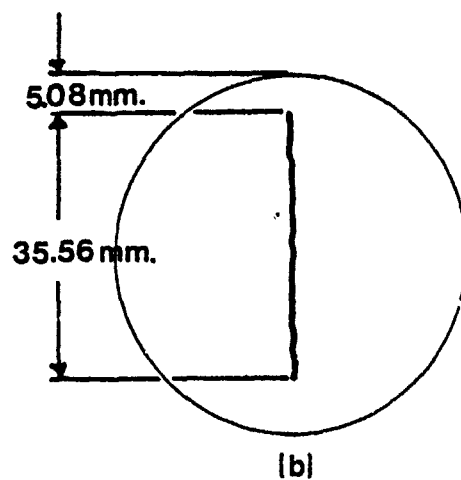


Figure 77. Profiles for (a) vertical stress and (b) vertical strain along the horizontal diameter, Load Case 1, nonlinear analysis,  $t = 85.0 \mu\text{sec}$ .

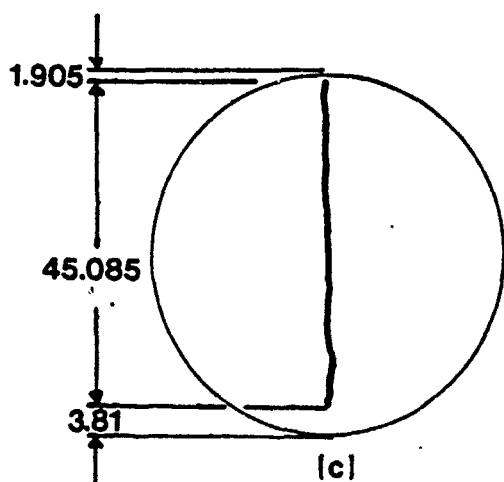
$t = 56.10 \mu\text{sec}$



$t = 58.0 \mu\text{sec}$



$t = 66.0 \mu\text{sec}$



$t = 85.0 \mu\text{sec}$

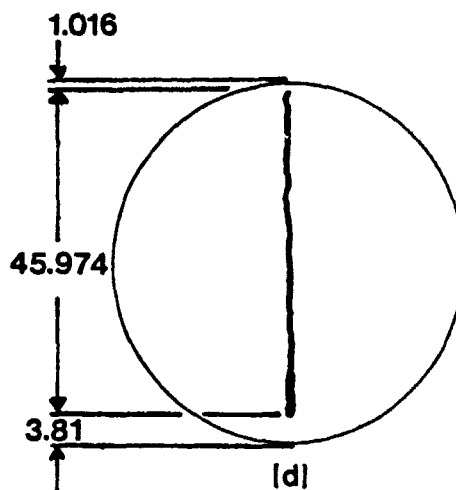


Figure 78. Failure pattern for splitting-tensile specimen, Load Case 1, nonlinear analysis.

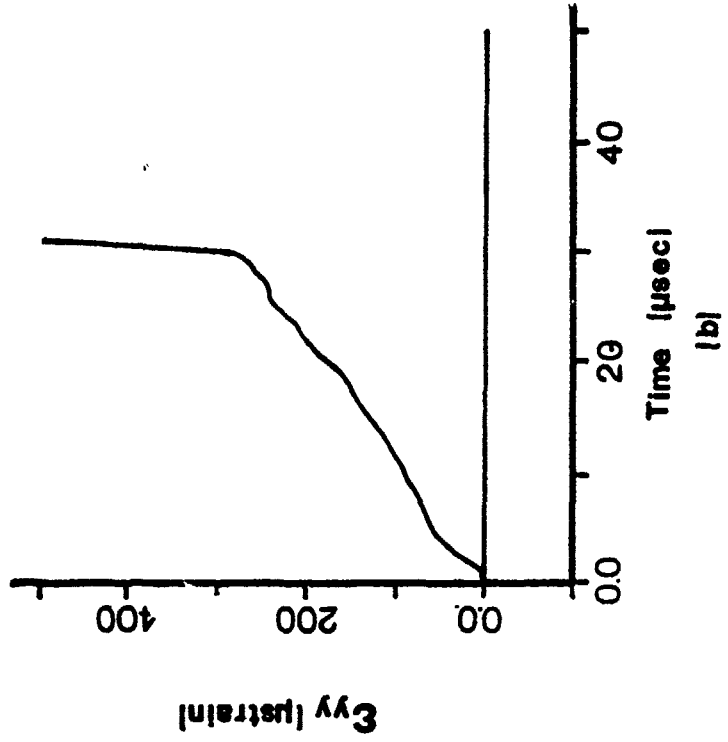
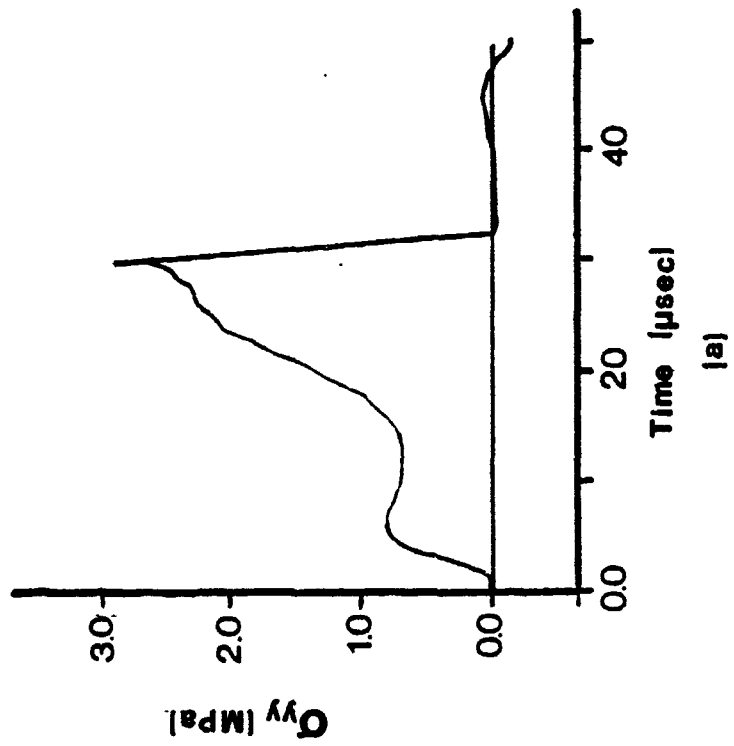
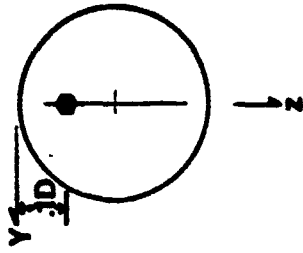


Figure 79. Time histories for (a) horizontal stress and (b) horizontal strain  
@  $z = 0.1D$ , Load Case 2, nonlinear analysis.

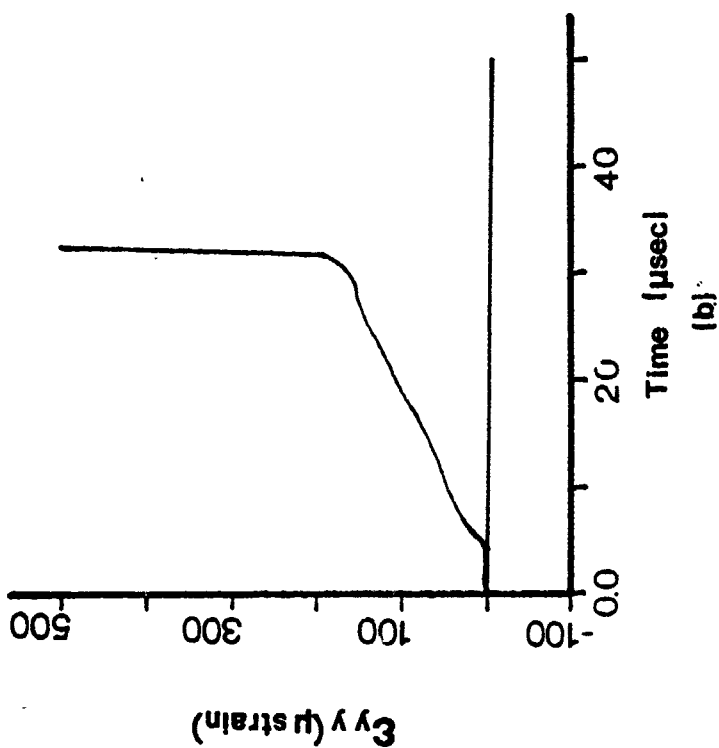
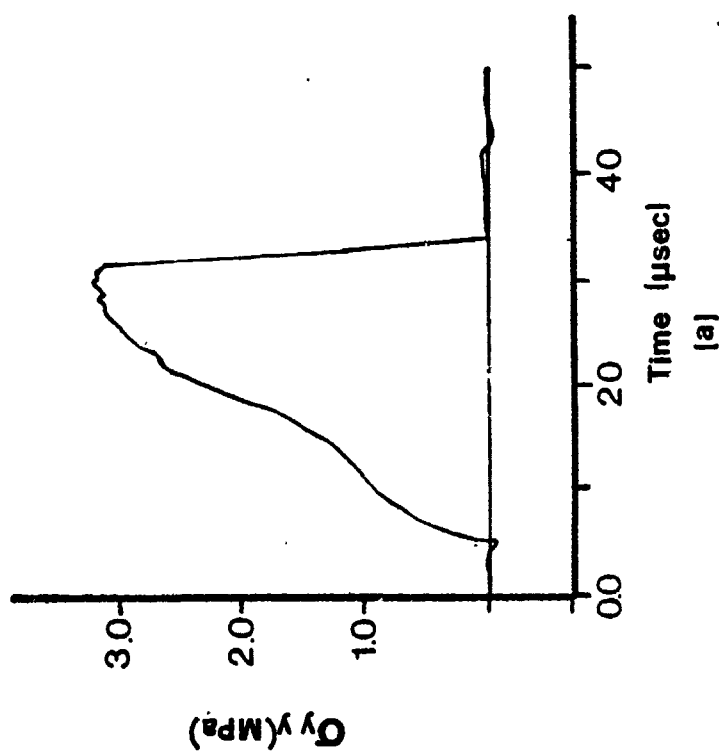
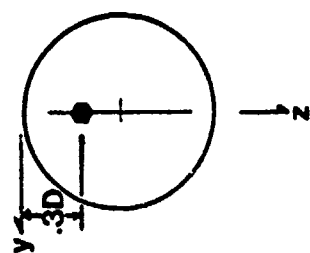


Figure 80. Time histories for (a) horizontal stress and (b) horizontal strain  
@  $z = 0.3D$ , Load Case 2, nonlinear analysis.

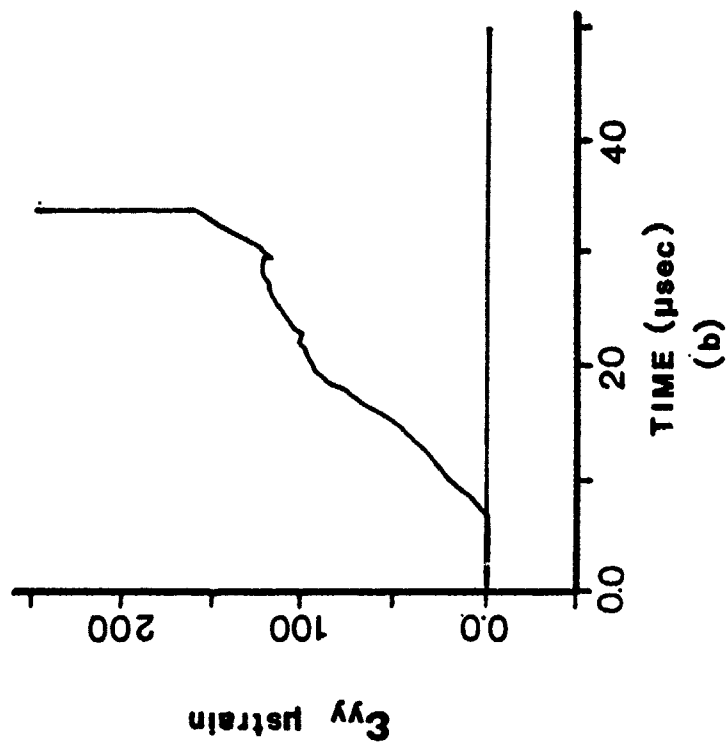
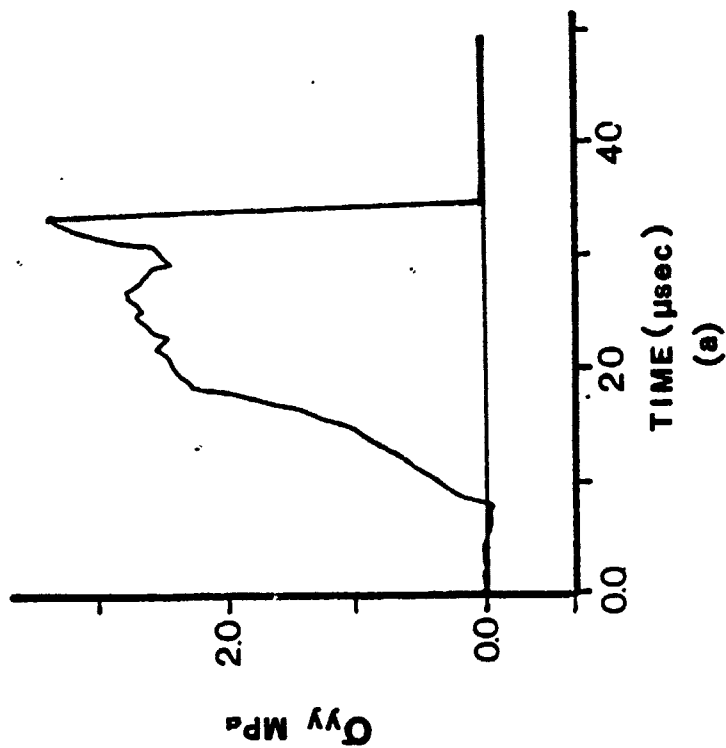
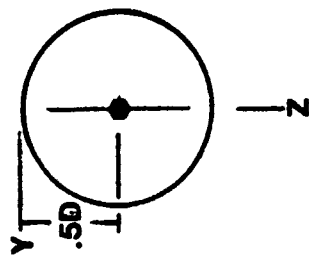


Figure 81. Time histories for (a) horizontal stress and (b) horizontal strain  
 @  $z = 0.5D$ , Load Case 2, nonlinear analysis.

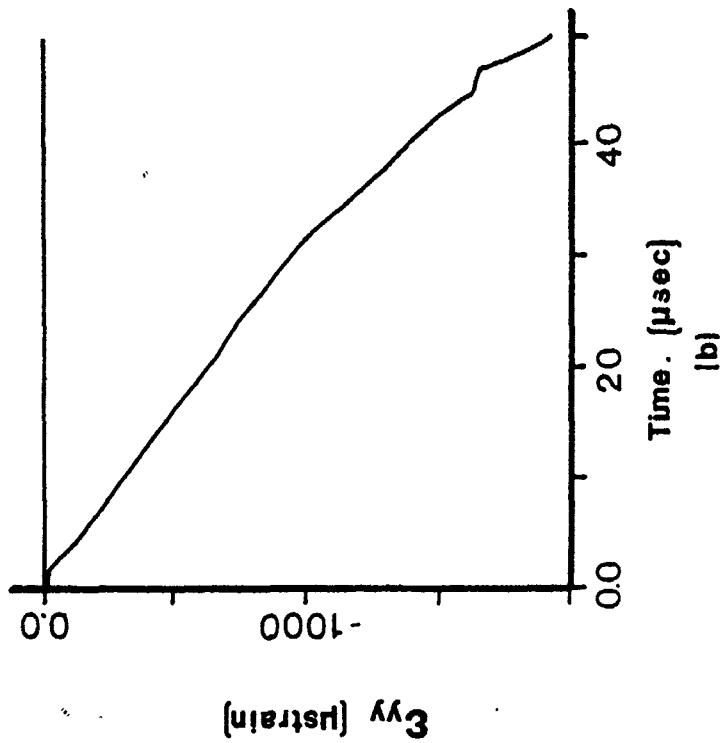
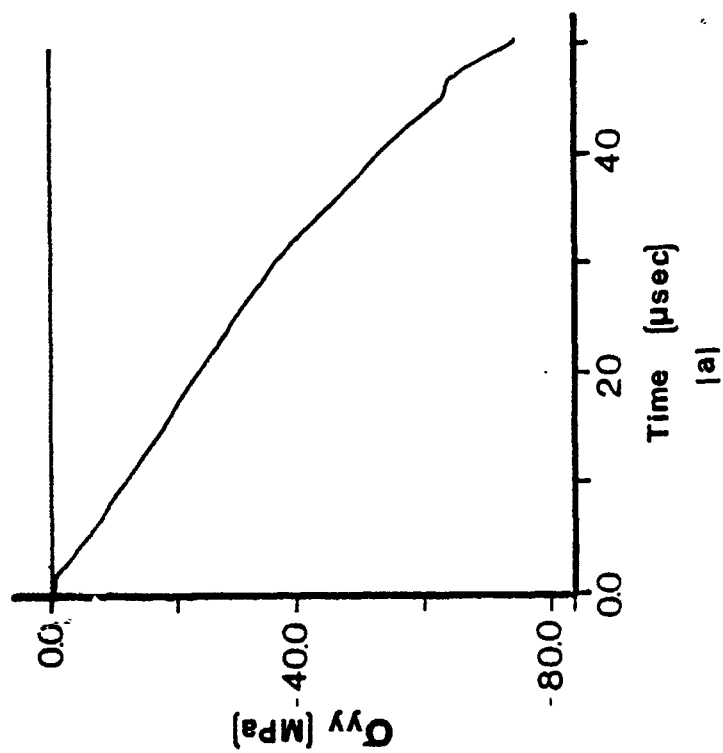
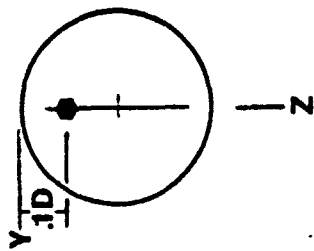


Figure 82. Time histories for (a) vertical stress and (b) vertical strain @  $z = 0.1D$ , Load Case 2, nonlinear analysis.



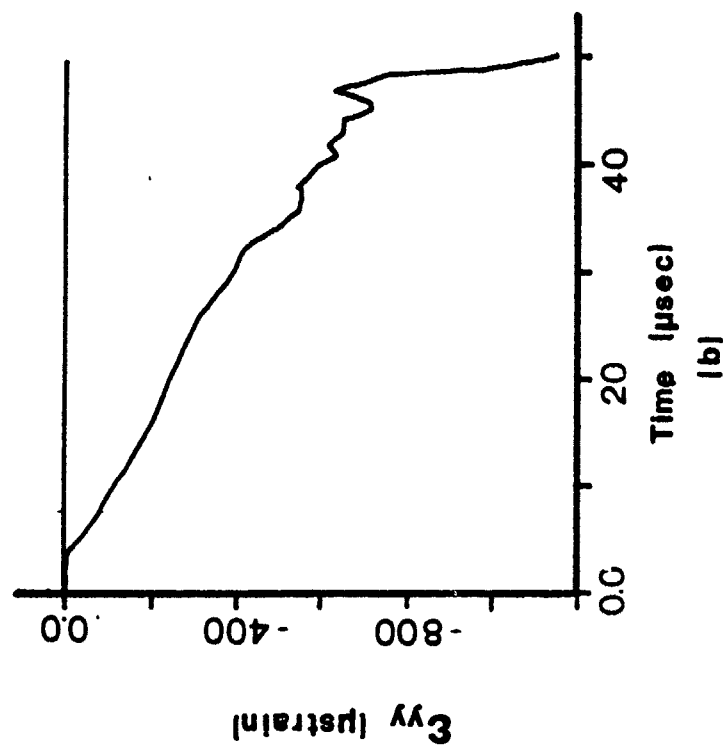
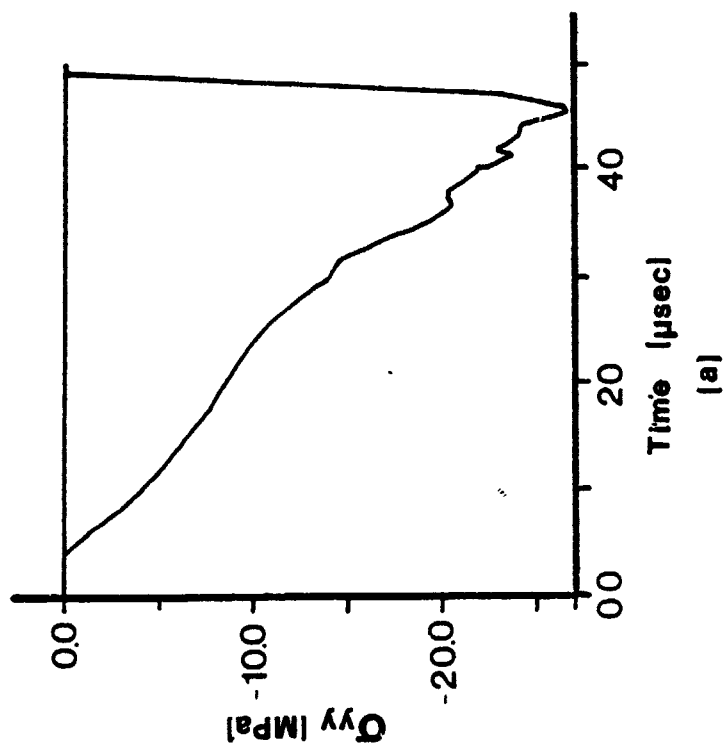
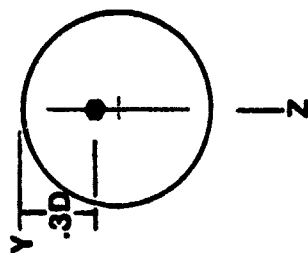


Figure 83. Time histories for (a) vertical stress and (b) vertical strain @  $z = 0.3D$ , Load Case 2, nonlinear analysis.

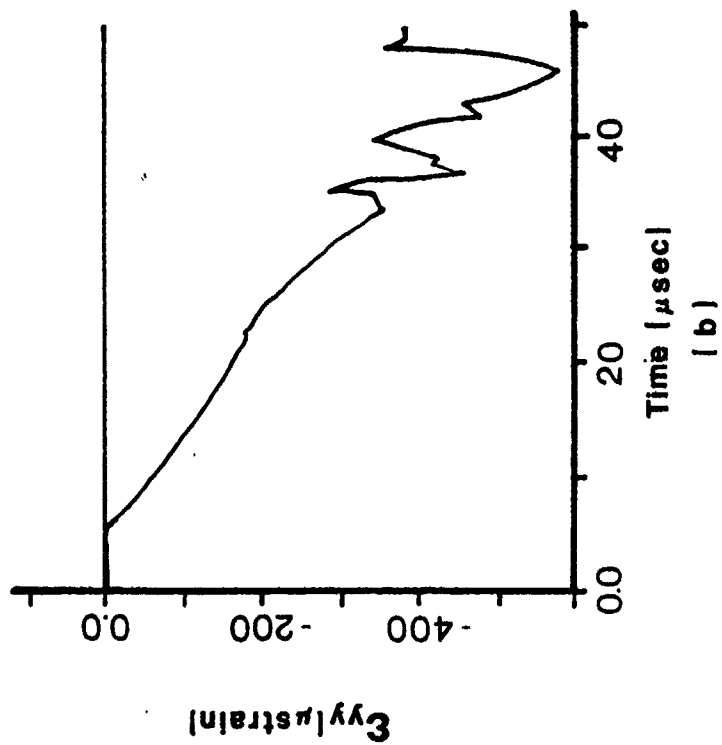
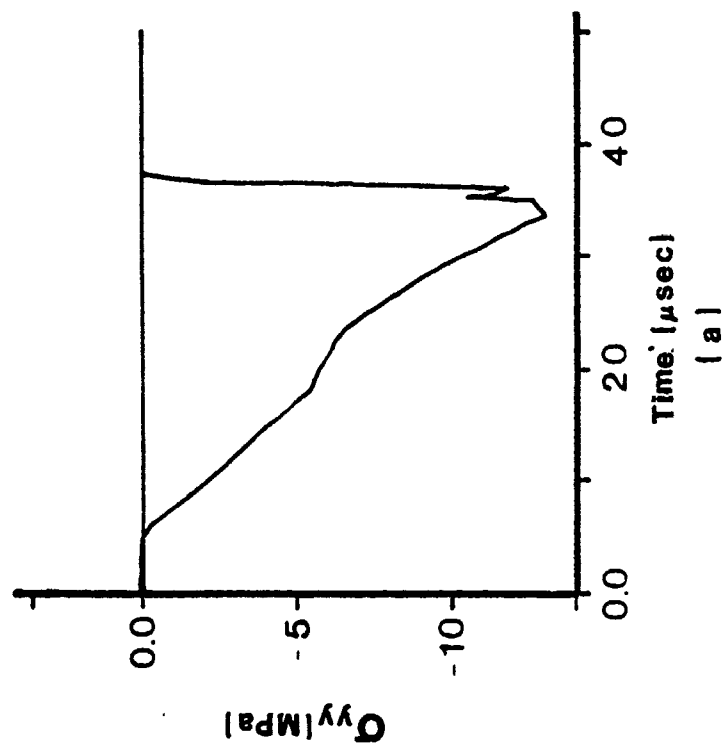
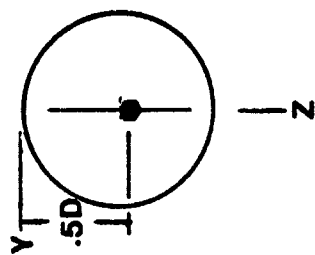


Figure 84. Time histories for (a) vertical stress and (b) vertical strain @  $z = 0.5D$ , Load Case 2, nonlinear analysis.

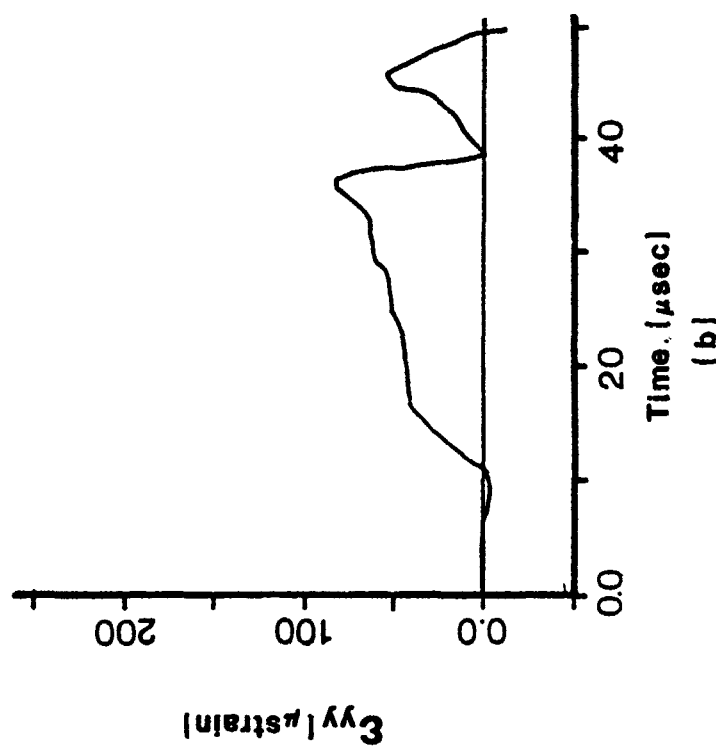
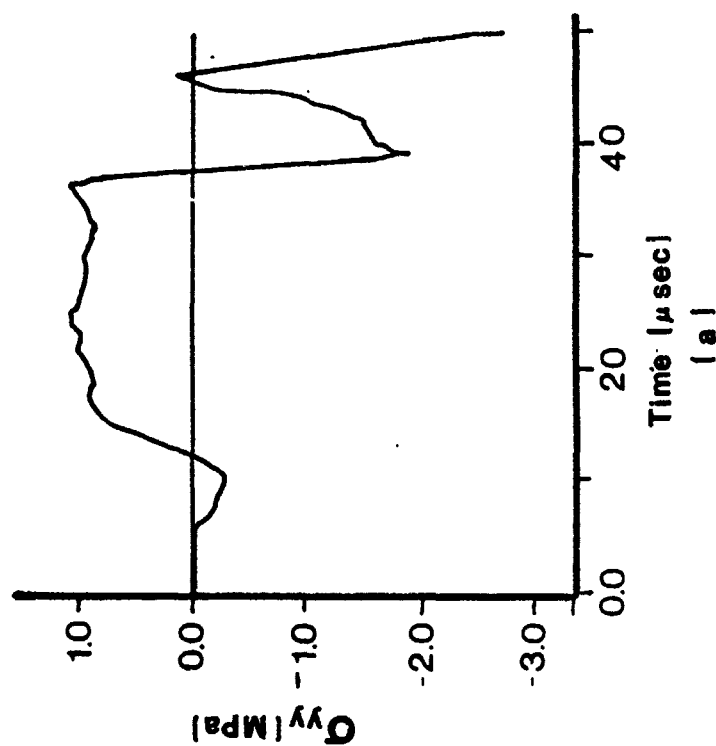
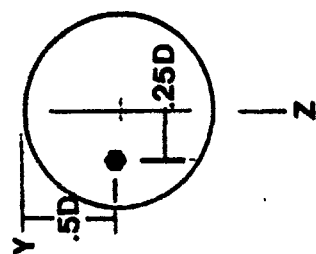


Figure 85. Time histories for (a) horizontal stress and (b) horizontal strain @  $y = 0.25D$ , Load Case 2, nonlinear analysis.

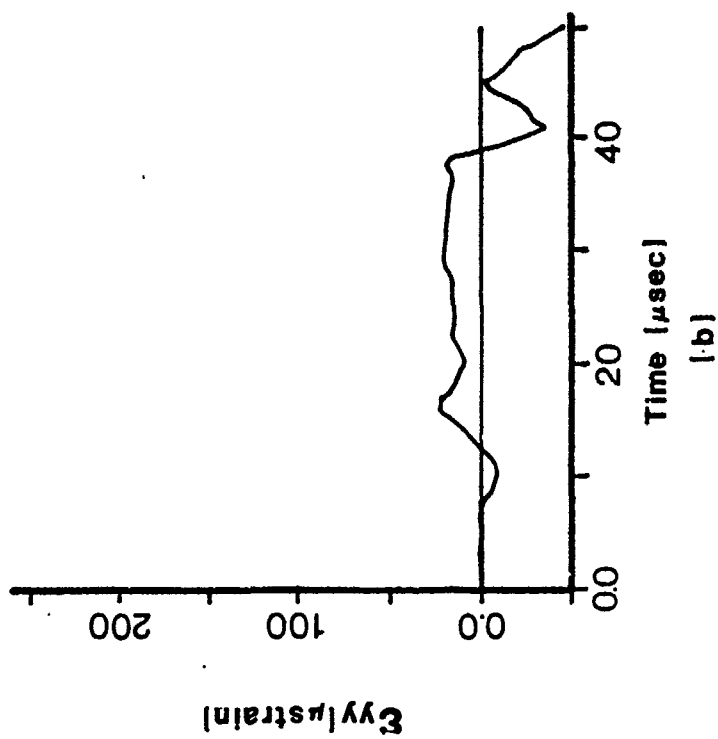
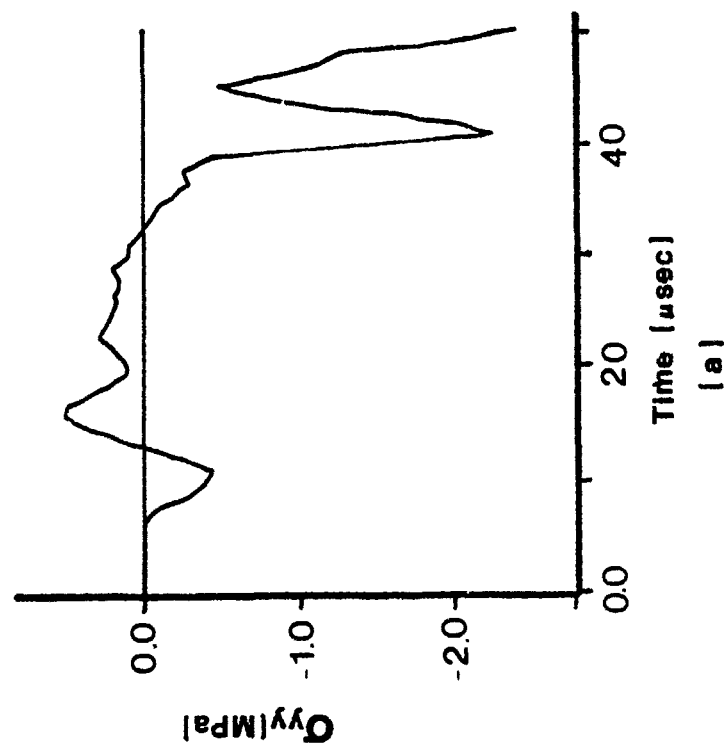
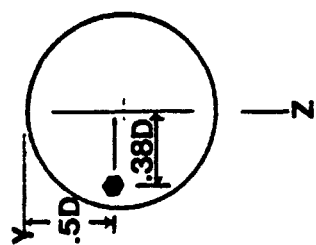


Figure 86. Time histories for (a) horizontal stress and (b) horizontal strain @  $y = 0.38D$ , Load Case 2, nonlinear analysis.

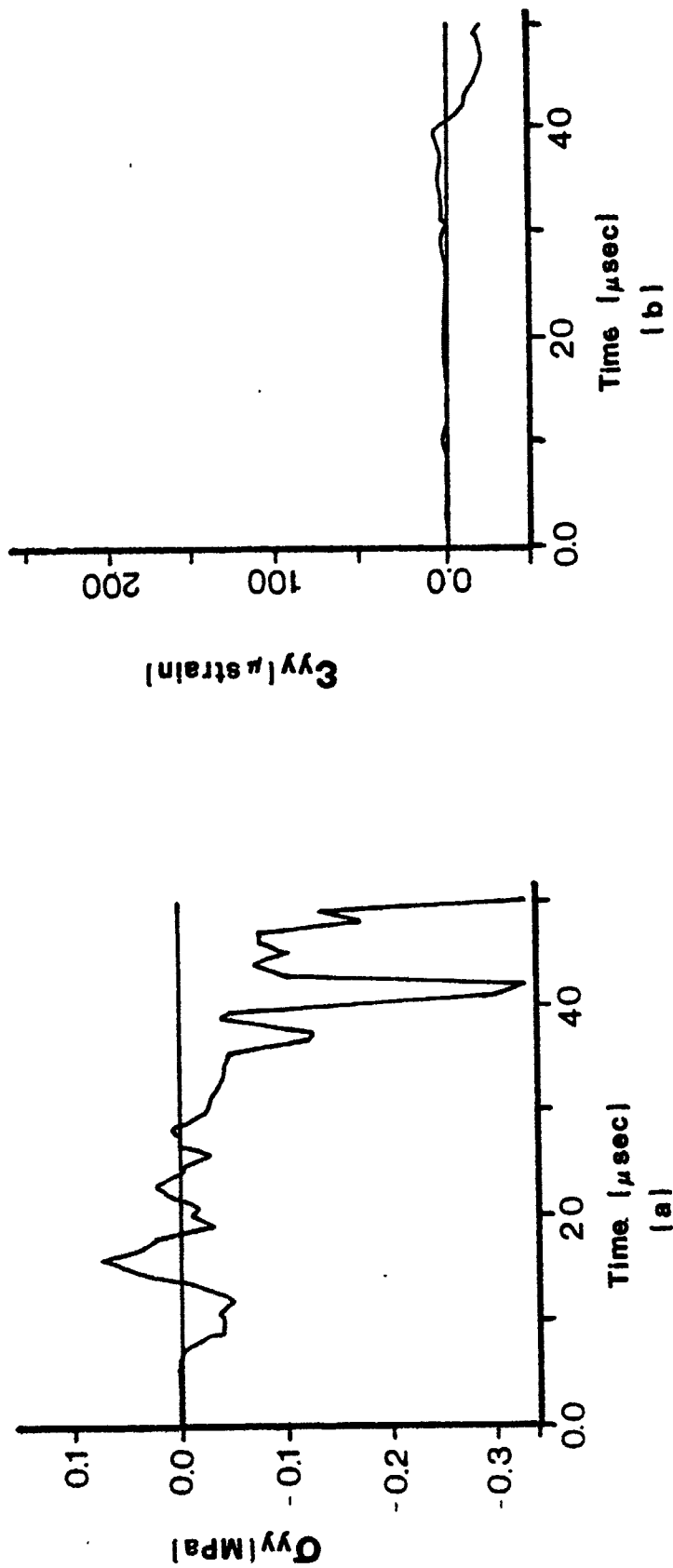
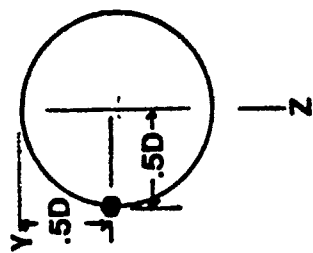


Figure 87. Time histories for (a) horizontal stress and (b) horizontal strain  
@  $y = 0.5D$ , Load Case 2, nonlinear analysis.

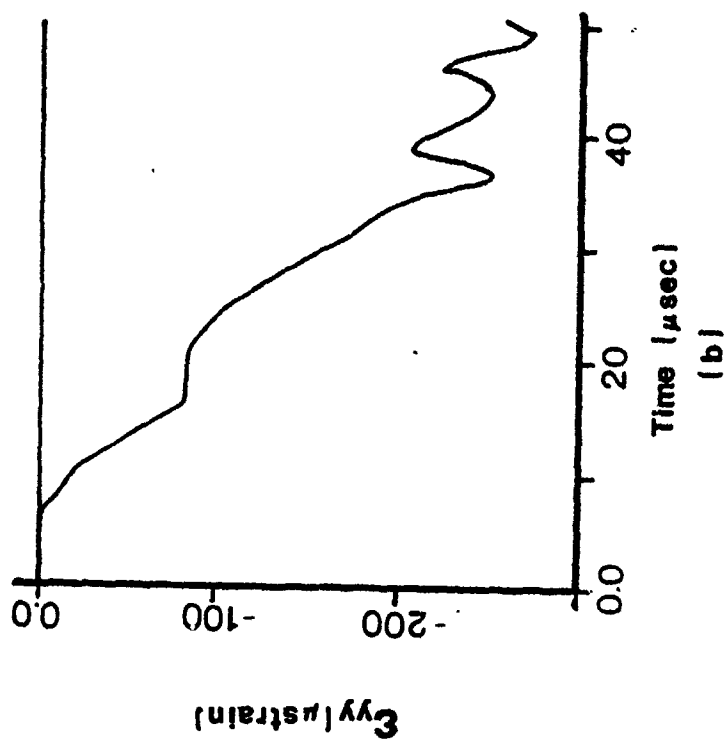
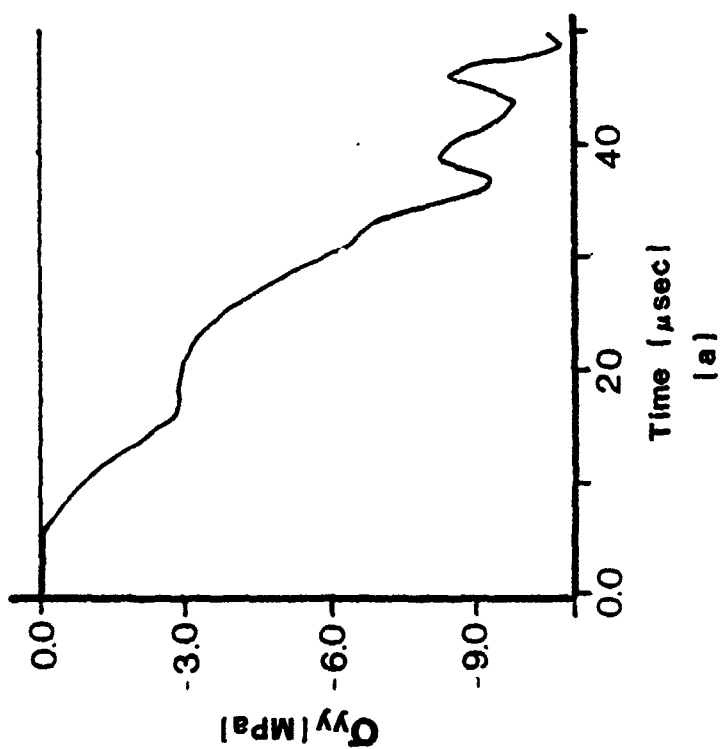
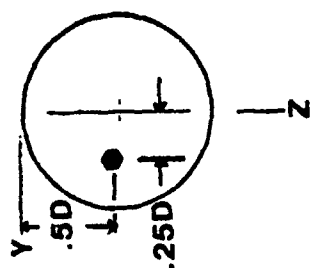


Figure 88. Time histories for (a) vertical stress and (b) vertical strain  
@  $y = 0.25D$ , Load Case 2, nonlinear analysis.

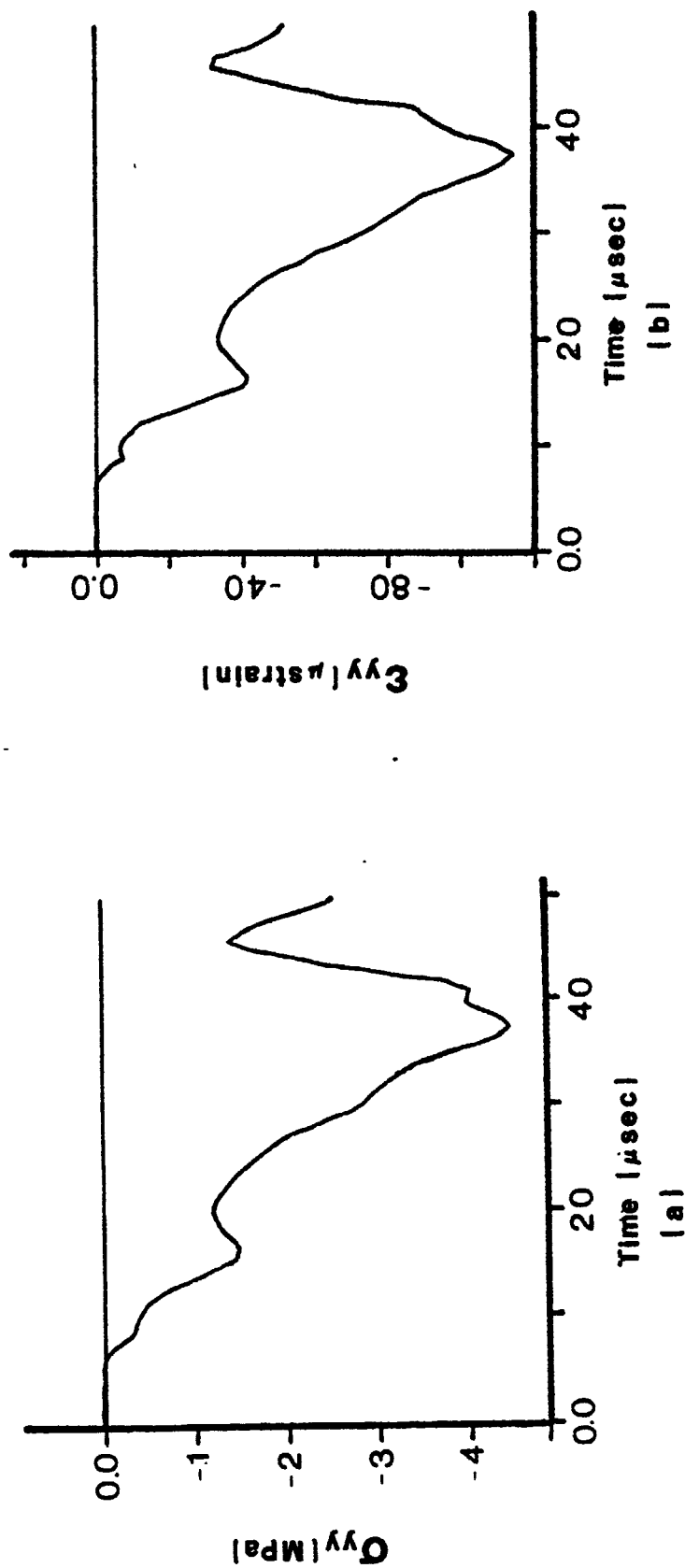
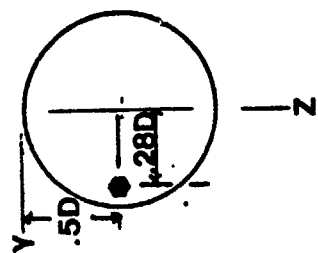


Figure 89. Time histories for (a) vertical stress and (b) vertical strain @  $y = 0.38D$ , Load Case 2, nonlinear analysis.

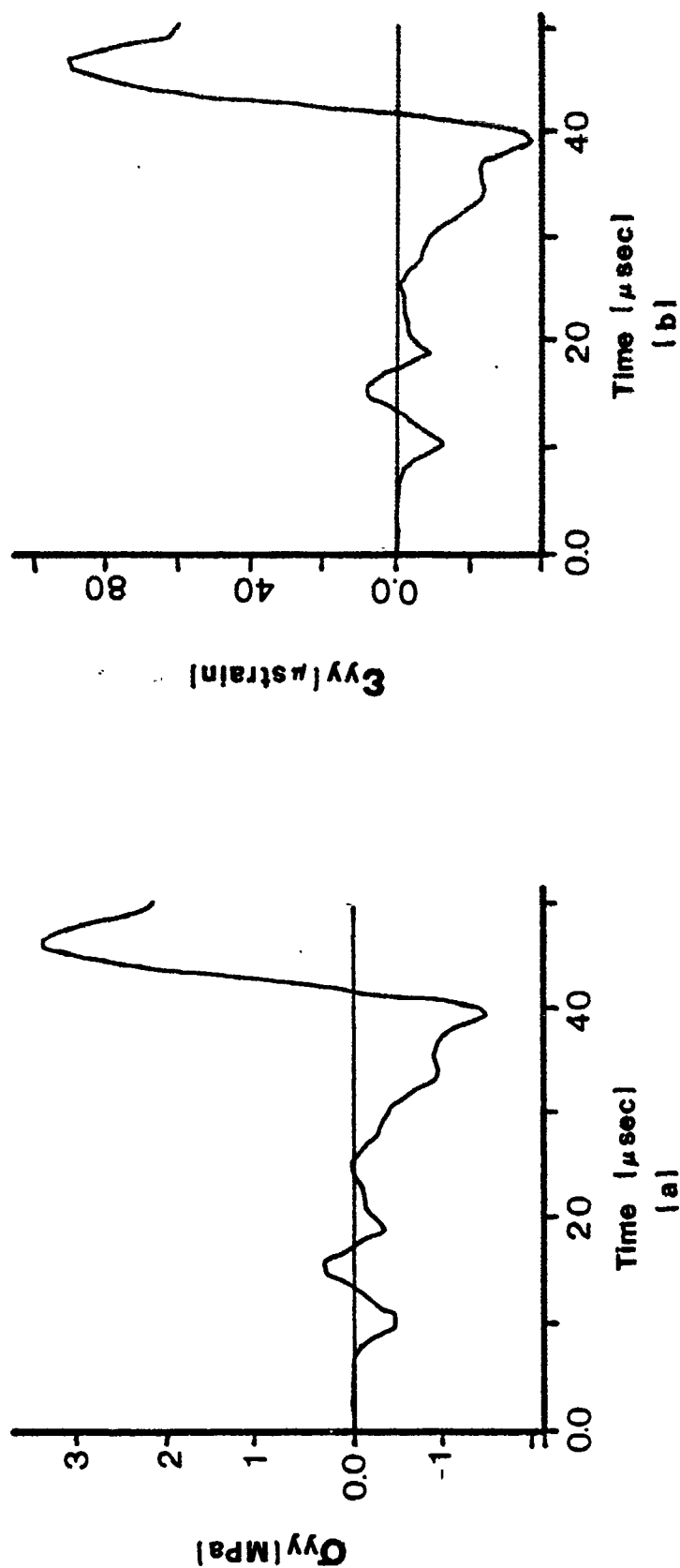
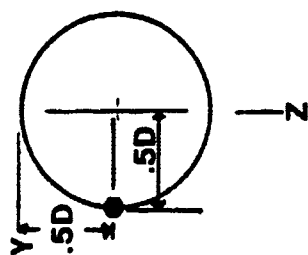


Figure 90. Time histories for (a) vertical stress and (b) vertical strain @  $y = 0.5D$ , Load Case 2, nonlinear analysis.



Time histories for the vertical stress and strain in the transmitter bar are presented in Figure 91. The maximum stresses and strain rates predicted at each of these locations are summarized in Table 8.

TABLE 8. MAXIMUM STRESSES AND STRAIN RATES  
AT SELECTED LOCATIONS (LOAD CASE 2)

Location	$(\sigma_y)_{\max}$ psi (MPa)	$(\sigma_z)_{\max}$ psi (MPa)	$\dot{\epsilon}_y$ (sec) <sup>-1</sup>	$\dot{\epsilon}_z$ (sec) <sup>-1</sup>
z = 0.1D	424.9 (2.93)	NA ( )	10.4	-31.6
z = 0.3D	461.0 (3.18)	-3948 (-27.24)	9.75	-15.83
z = 0.5D	479.8 (3.31)	-1840 (-12.69)	7.367	-10.4
y = .25D	NA	NA	NA	- 7.5
y = .38D	NA	- 635.7 (-4.39)	NA	- 4.1
y = .50D	NA	NA	NA	NA
Bar	NA	-2141 (-14.77)	NA	- 2.08

Profiles for the horizontal stress,  $\sigma_y$ , and the horizontal strain,  $\epsilon_y$ , along the vertical diameter at four selected time increments (29.2  $\mu$ sec, 31.2  $\mu$ sec, 35  $\mu$ sec, and 45  $\mu$ sec) are presented in Figures 92 through 95, respectively. The initiation of the first crack is indicated in Figure 92, and failure of the cylinder is indicated in Figure 95. Profiles for the horizontal stress and strain along the horizontal diameter, for the same selected times, are presented in Figures 96 through 99. The propagation of the crack to the center of the cylinder is illustrated in Figure 98 at time  $t = 35 \mu$ sec.

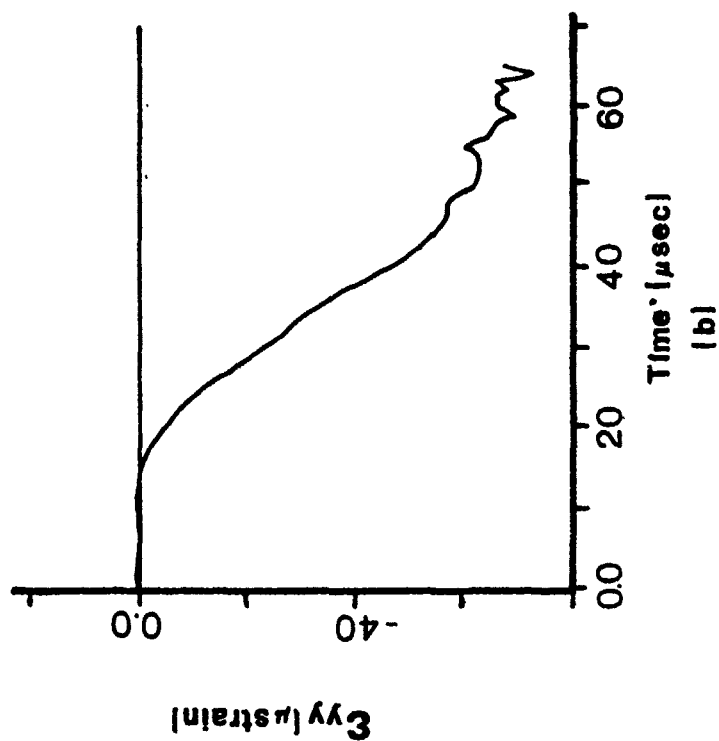
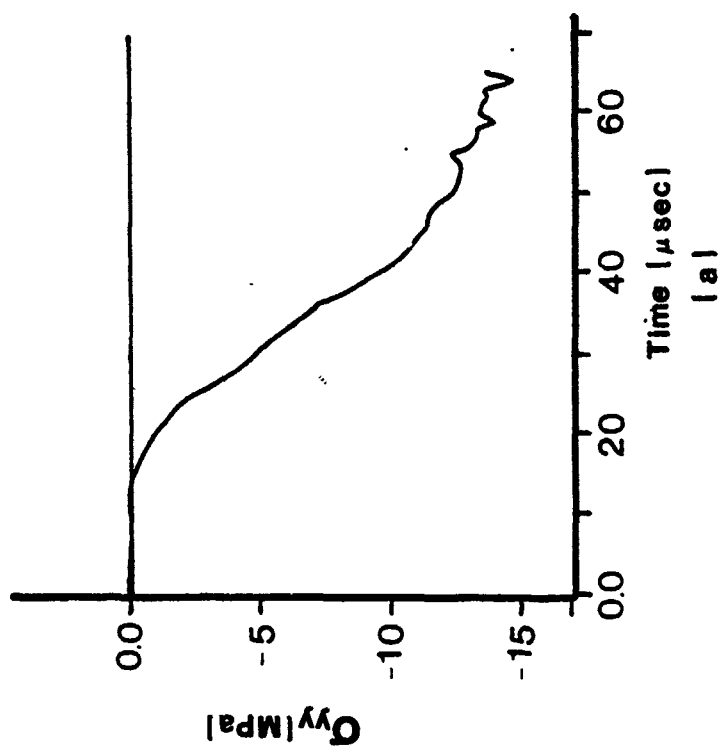
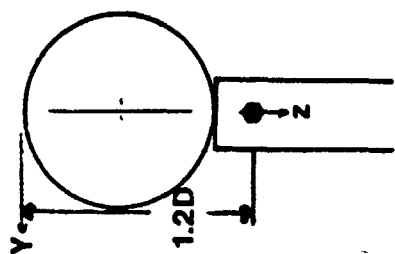


Figure 91. Time histories for (a) vertical stress and (b) vertical strain in the transmitter bar, Load Case 2, nonlinear analysis.

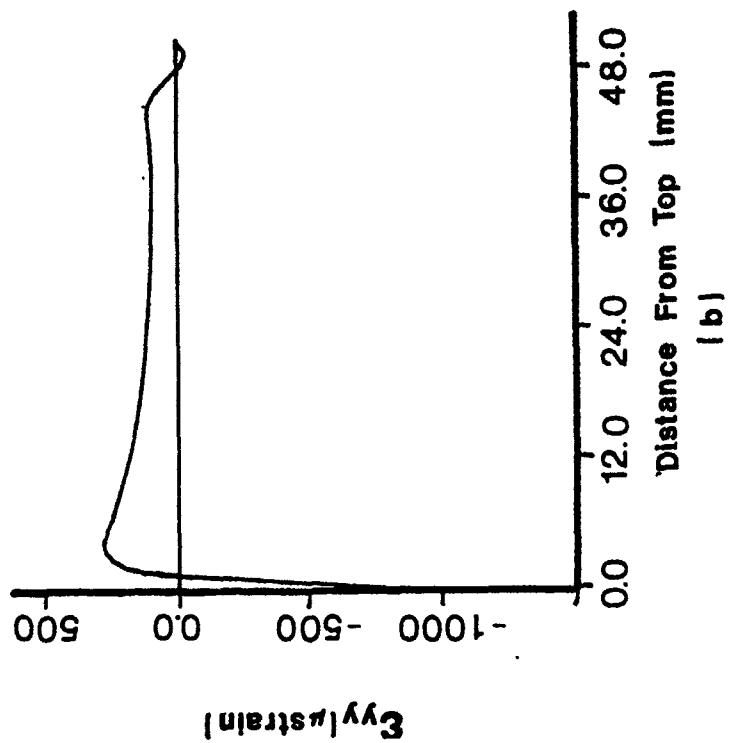
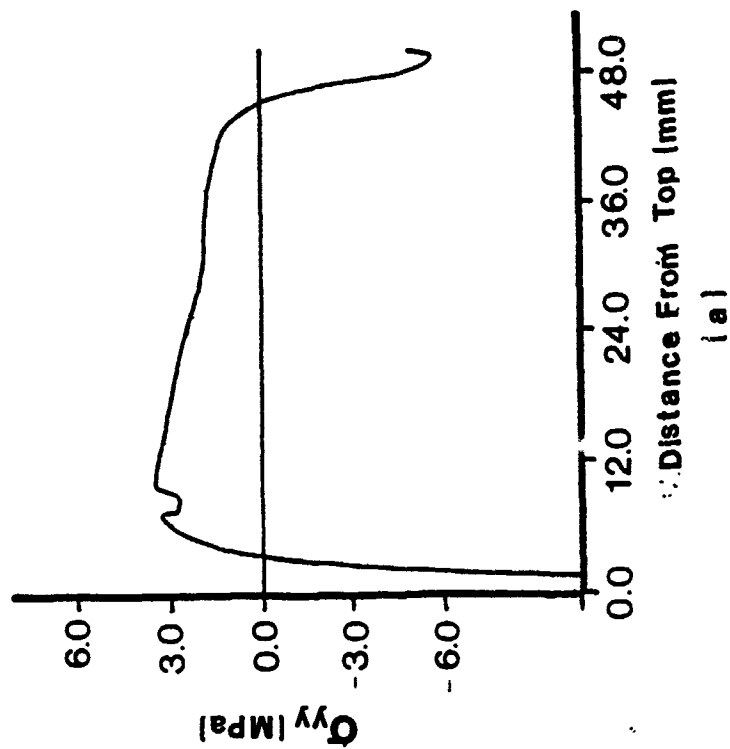


Figure 92. Profiles for (a) horizontal stress and (b) horizontal strain along the vertical diameter, load Case 2, nonlinear analysis,  $t = 29.2 \mu\text{sec}$ .

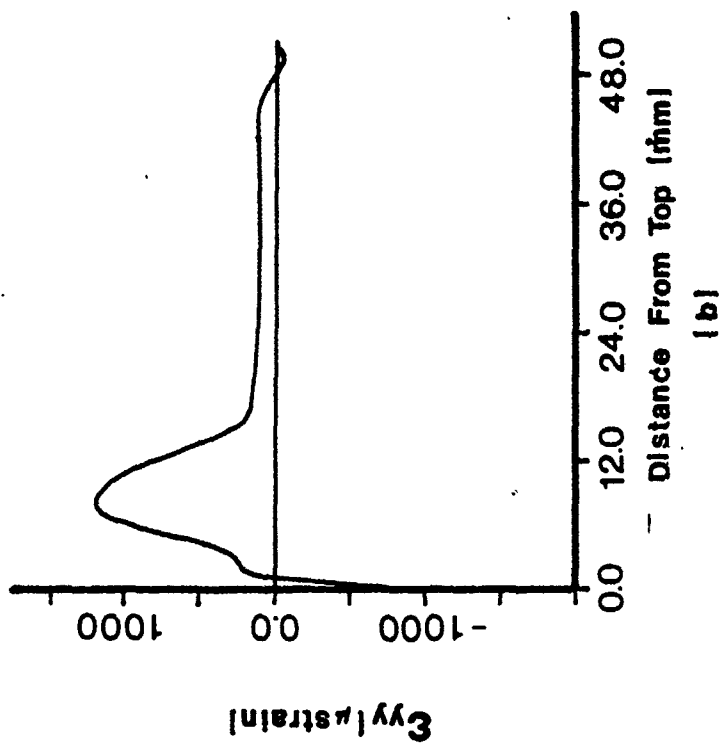
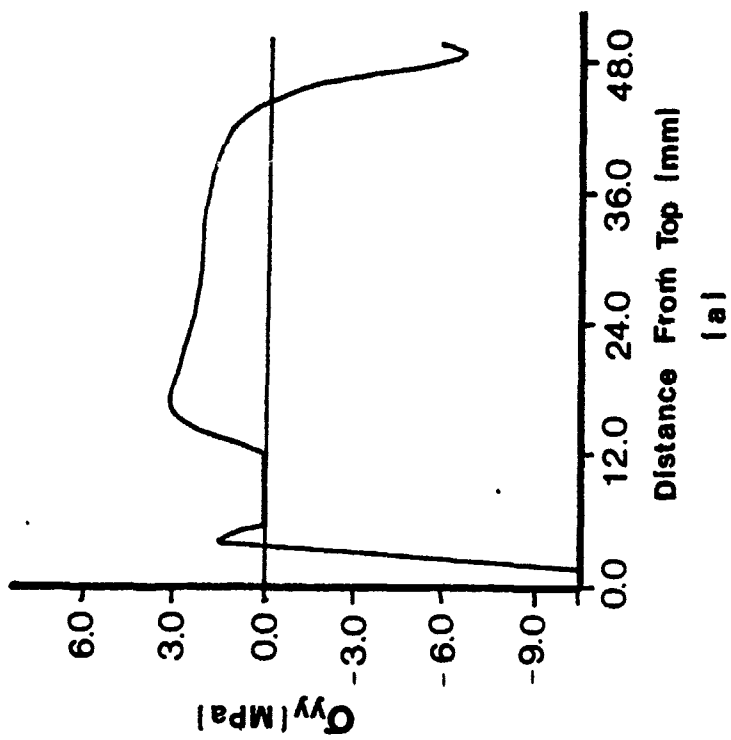


Figure 93. Profiles for (a) horizontal stress and (b) horizontal strain along the vertical diameter, Load Case 2, nonlinear analysis,  $t = 31.2 \mu\text{sec}$ .

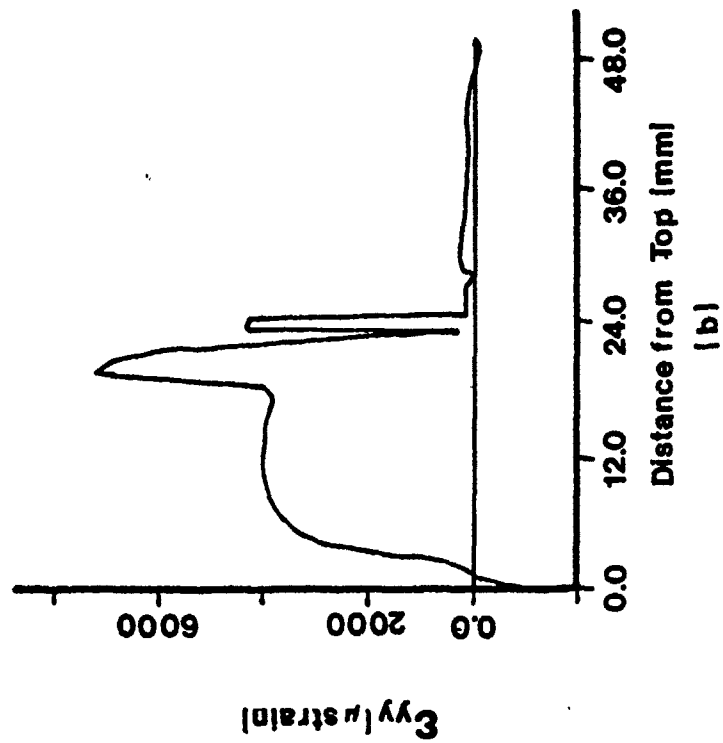
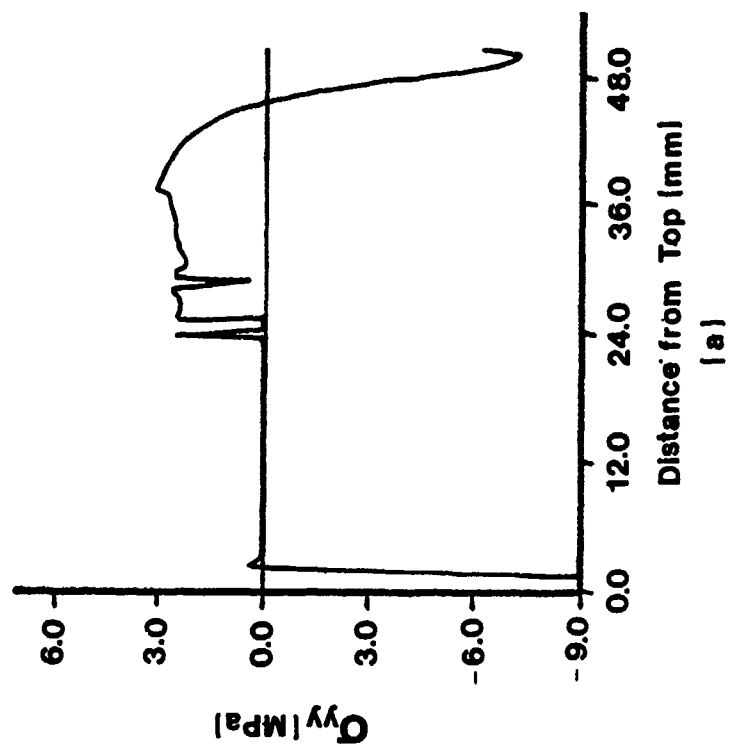


Figure 94. Profiles for (a) horizontal stress and (b) horizontal strain along the vertical diameter, Load Case 2, nonlinear analysis,  $t = 35 \mu\text{sec}$ .

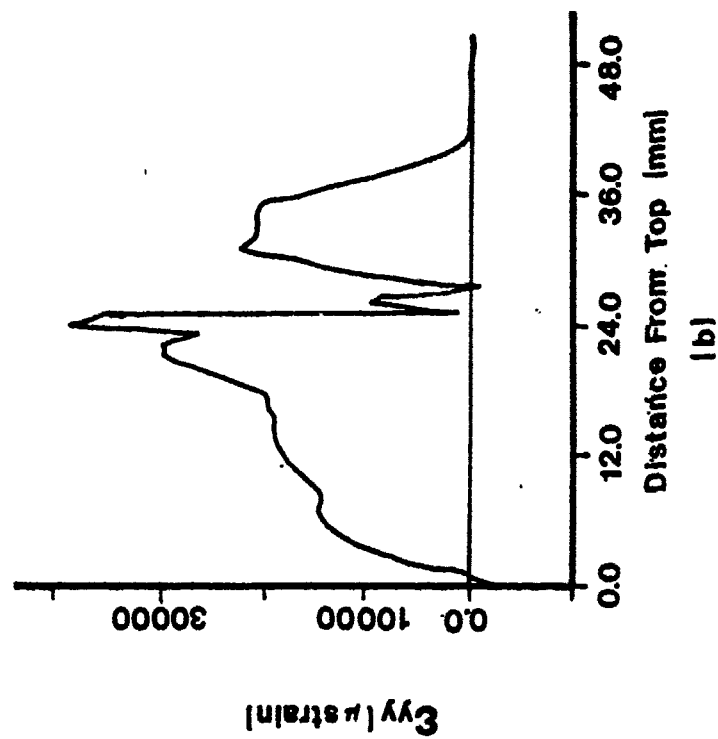
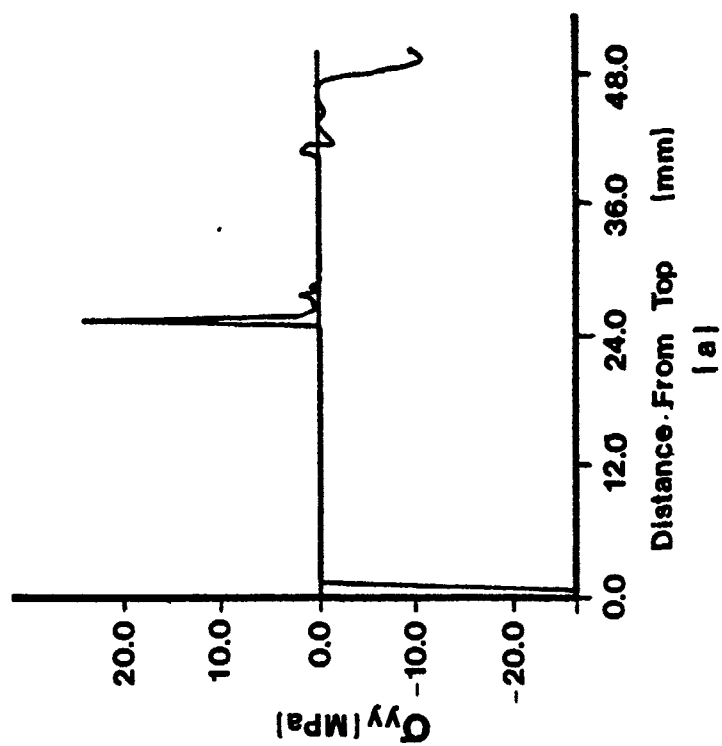


Figure 95. Profiles for (a) horizontal stress and (b) horizontal strain along the vertical diameter, Load Case 2, nonlinear analysis,  $t = 45 \mu\text{sec}$ .

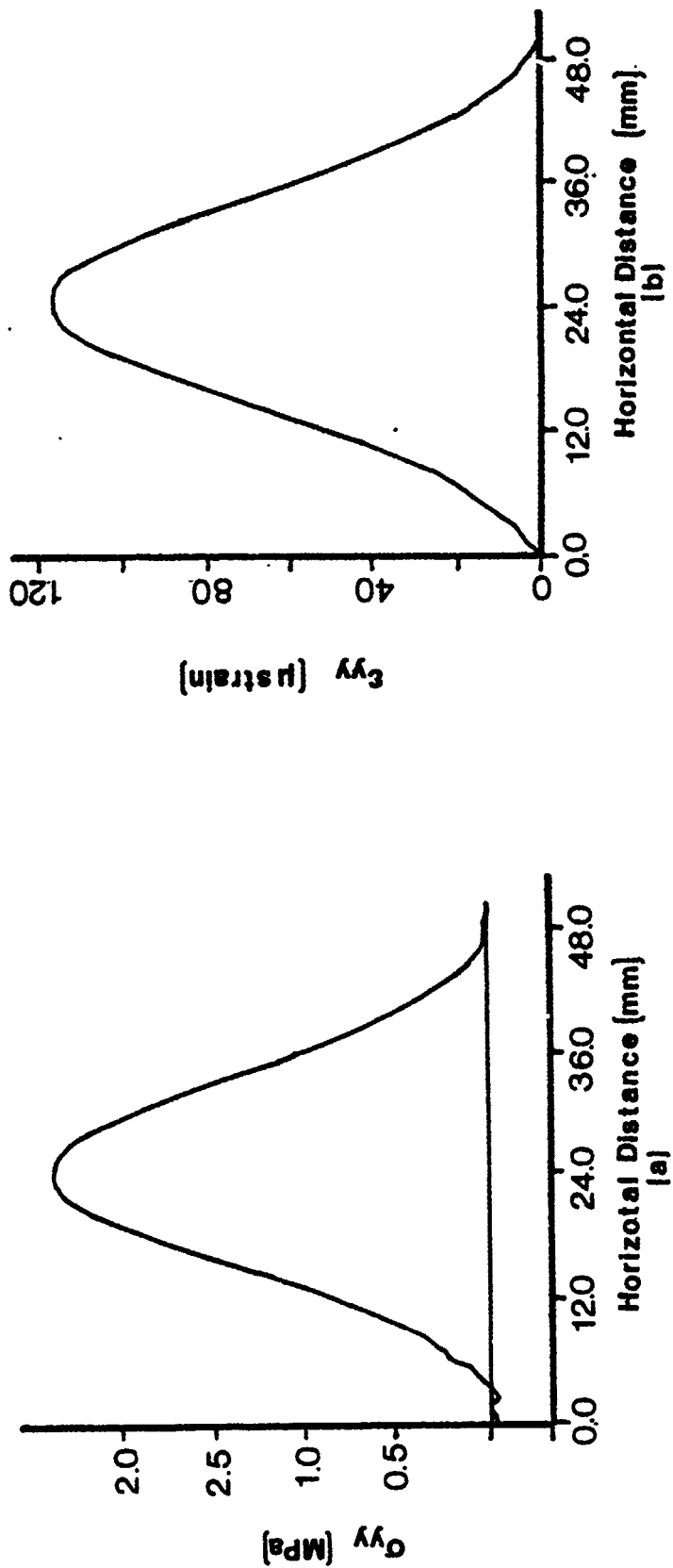


Figure 96. Profiles for (a) horizontal stress and (b) horizontal strain along the horizontal diameter, Load Case 2, nonlinear analysis,  $t = 29.2 \mu\text{sec}$ .

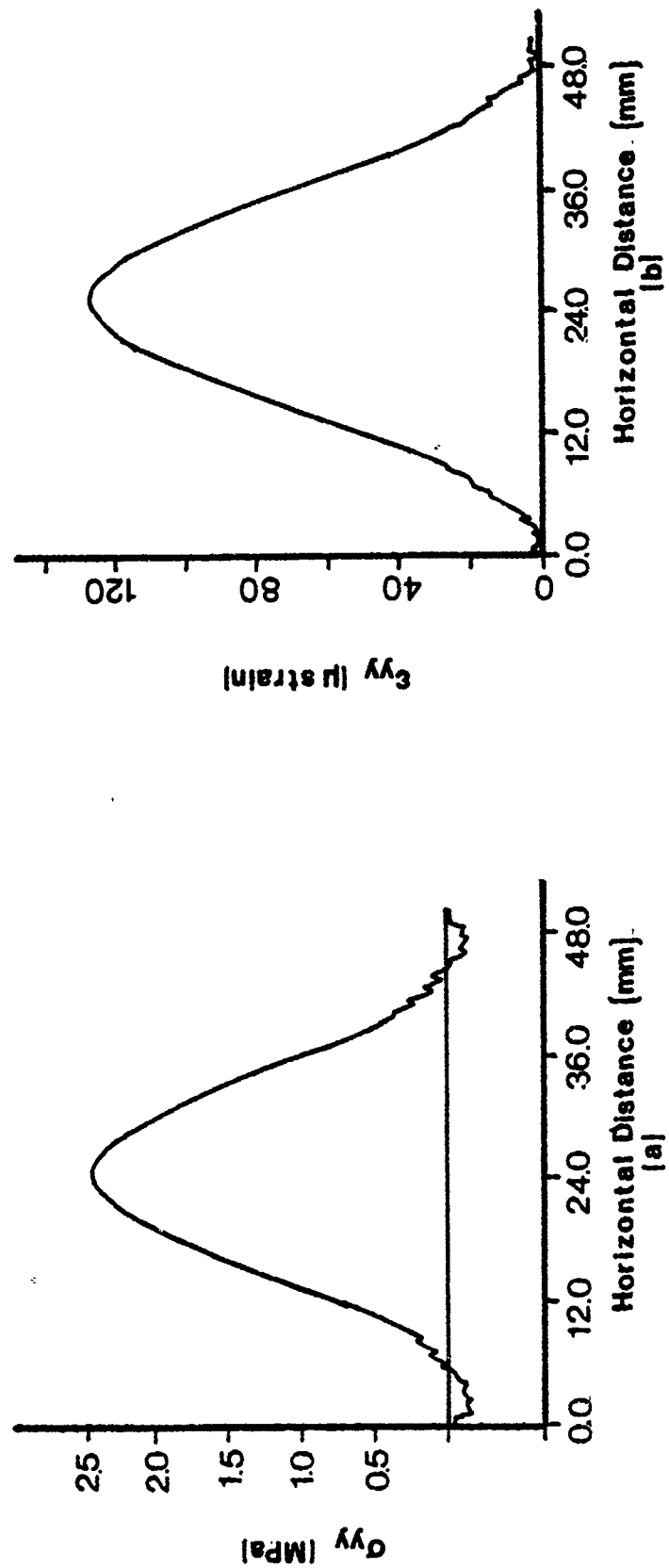


Figure 97. Profiles for (a) horizontal stress and (b) horizontal strain along the horizontal diameter, Load Case 2, nonlinear analysis,  $t = 31.2 \mu\text{sec}$ .



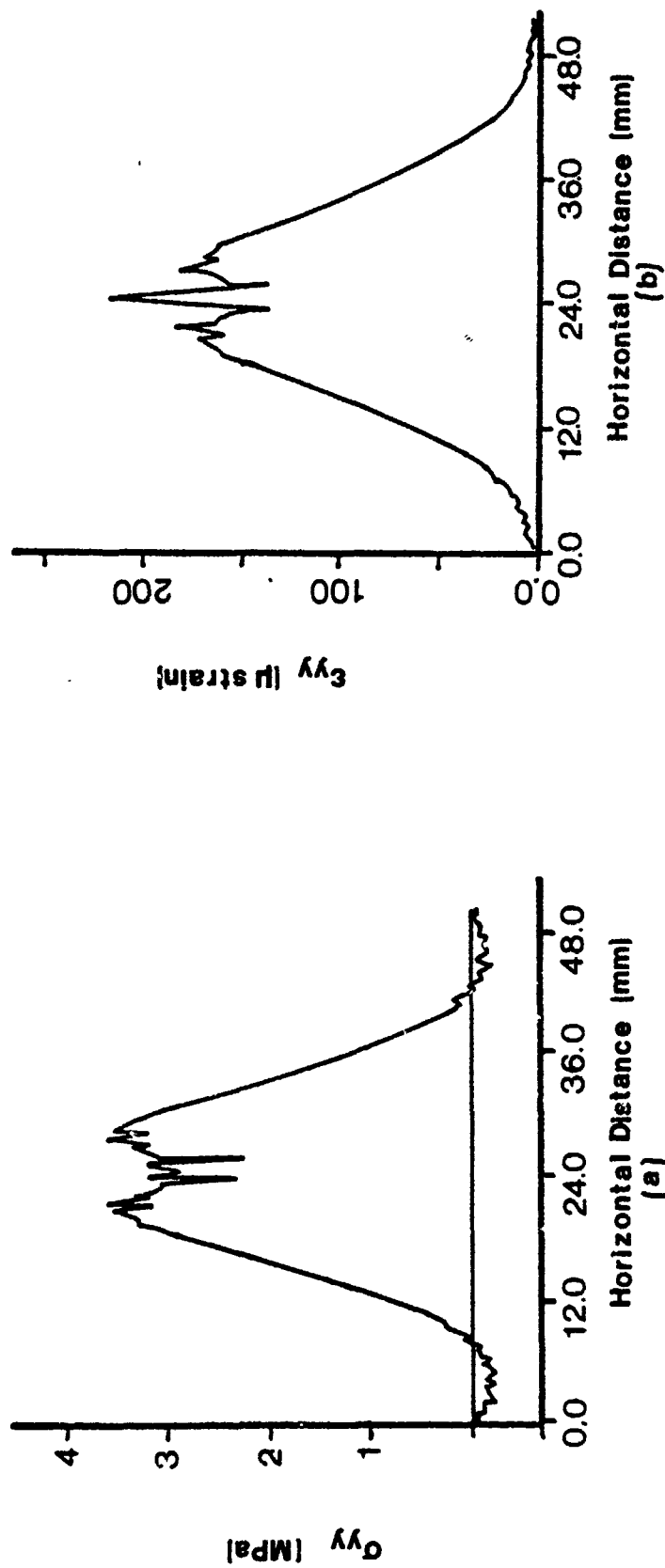


Figure 98. Profiles for (a) horizontal stress and (b) horizontal strain along the horizontal diameter, Load Case 2, nonlinear analysis,  $t = 35 \mu\text{sec}$ .

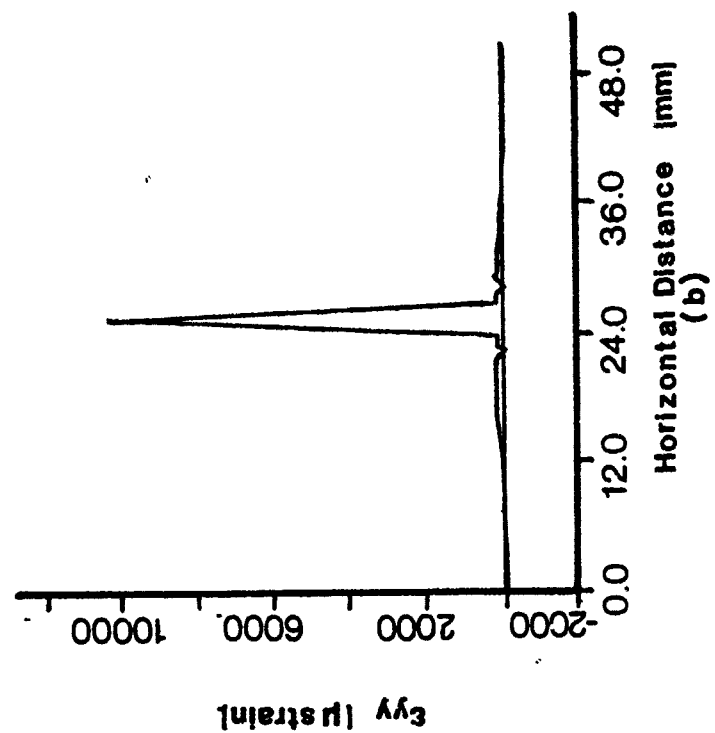
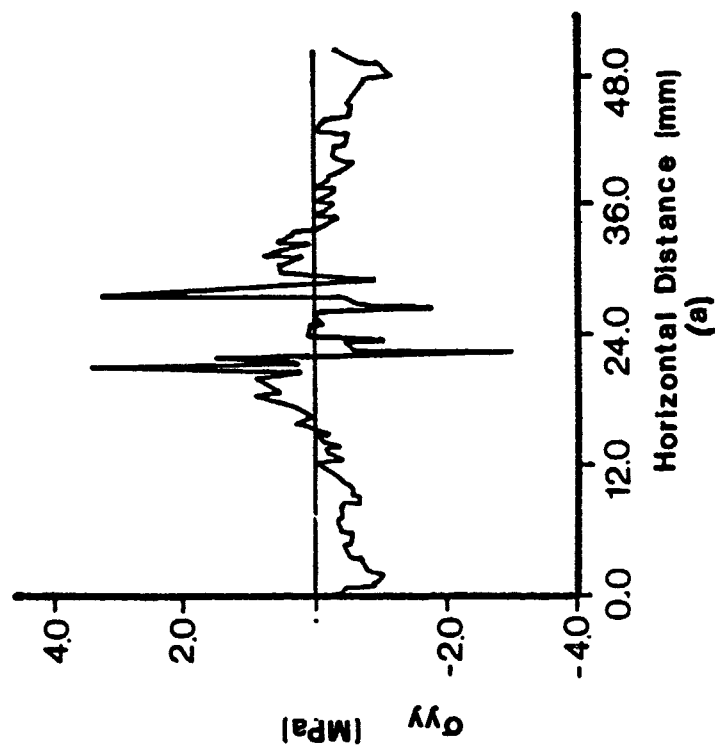


Figure 99. Profiles for (a) horizontal stress and (b) horizontal strain along the horizontal diameter, Load Case 2, nonlinear analysis,  $t = 45 \mu\text{sec}$ .

Profiles for the vertical stress and strain along the horizontal diameter at the same selected times are presented in Figures 100 through 103.

The cracking sequence simulated in the numerical analysis, from initiation of the first crack until failure, is illustrated in Figure 104. The first crack occurs along the vertical diameter at a location approximately 0.35 inches from the top of the cylinder, at a time  $t = 29.2 \mu\text{sec}$ . (Figure 104a). At time  $t = 31.0 \mu\text{sec}$ , the crack is observed to propagate in both directions along the vertical diameter (Figure 104b). At time  $t = 35 \mu\text{sec}$ , the crack has propagated along the vertical diameter through the center of the cylinder in one direction, and has nearly reached the top of the cylinder in the other direction (Figure 104c). Finally, at time  $t = 45 \mu\text{sec}$ , failure occurs (Figure 104d).

During the failure sequence in the numerical simulation, four different bifurcations of the crack pattern are observed (see Figure 104d). The first bifurcation occurs at the center of the cylinder. The second and third bifurcations occur at approximately the same time; one at the crack front propagating toward the top of the cylinder at a distance 0.05 inches (1.3 mm) from the top, the other at the crack front propagating toward the bottom of the cylinder, at a distance 1.60 inches (41 mm) from the top. The cracks formed by the top bifurcation eventually propagate to the top surface of the cylinder. However, the two cracks formed by the bifurcation occurring below the center of the cylinder begin to move back toward each other before bifurcating once again at a distance of 0.4 inches (10.2 mm) from the bottom of the cylinder. The cracks of this final bifurcation eventually propagate to the bottom surface of the cylinder at which time failure occurs.

Time histories for the horizontal stress,  $\sigma_y$ , and horizontal strain,  $\epsilon_y$ , occurring at the branch of the crack bifurcation located a distance of 0.05 inches (1.3 mm) from the top of the cylinder are presented in Figure 105. Similar time histories for the vertical stress,  $\sigma_z$ , and vertical strain,  $\epsilon_z$ , occurring at the same location are illustrated in Figure 106. Time histories for the horizontal stress and strain occurring at the branch of the crack bifurcation located 0.4 inches (10.2 mm) from the bottom of the cylinder is presented in Figure 107. Similar time histories for the vertical stress and strain at the same location are presented in Figure 108.

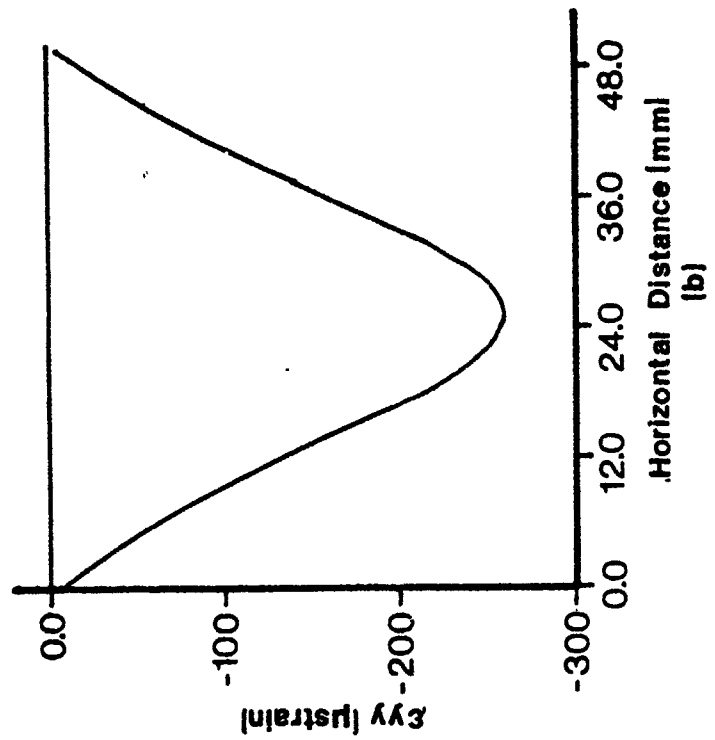
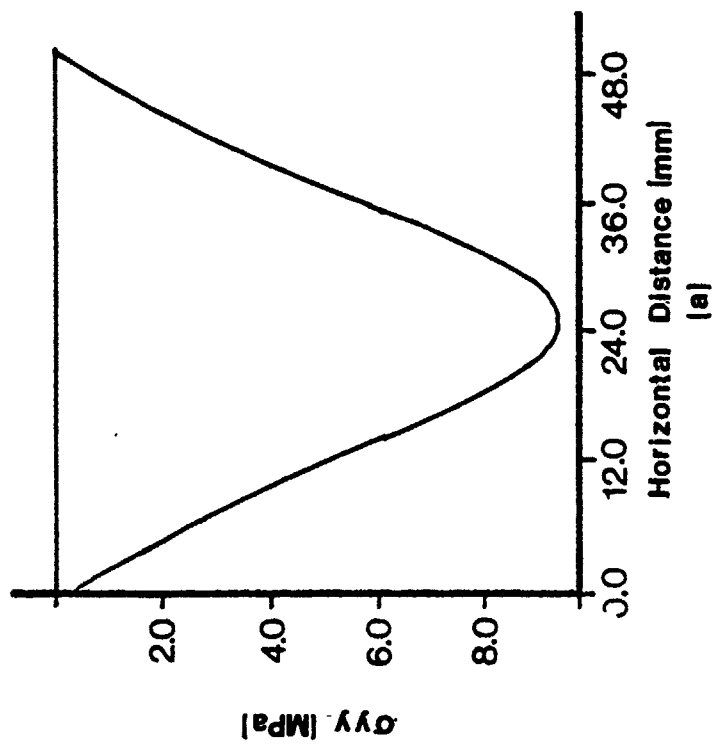


Figure 100. Profiles for (a) vertical stress and (b) vertical strain along the horizontal diameter, Load Case 2, nonlinear analysis,  $t = 29.2 \mu\text{sec}$ .

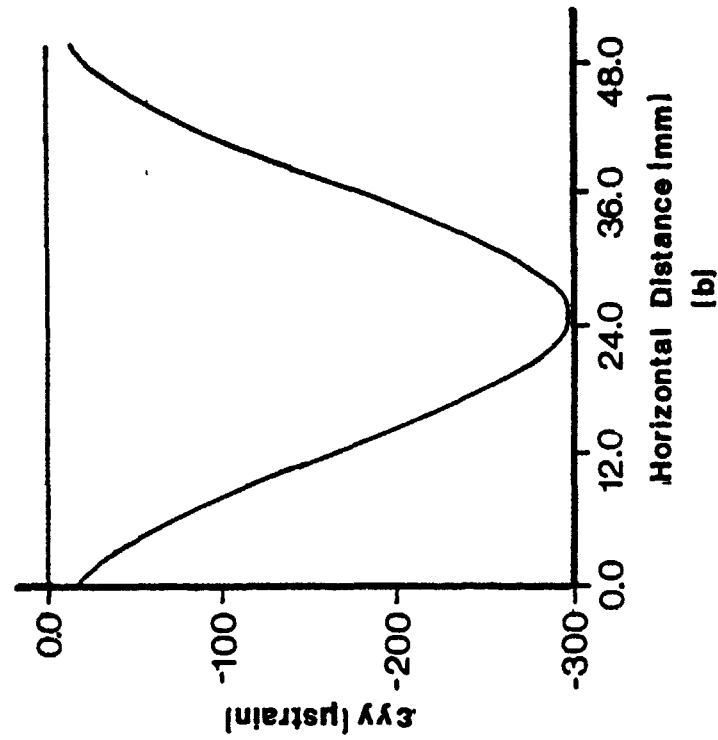
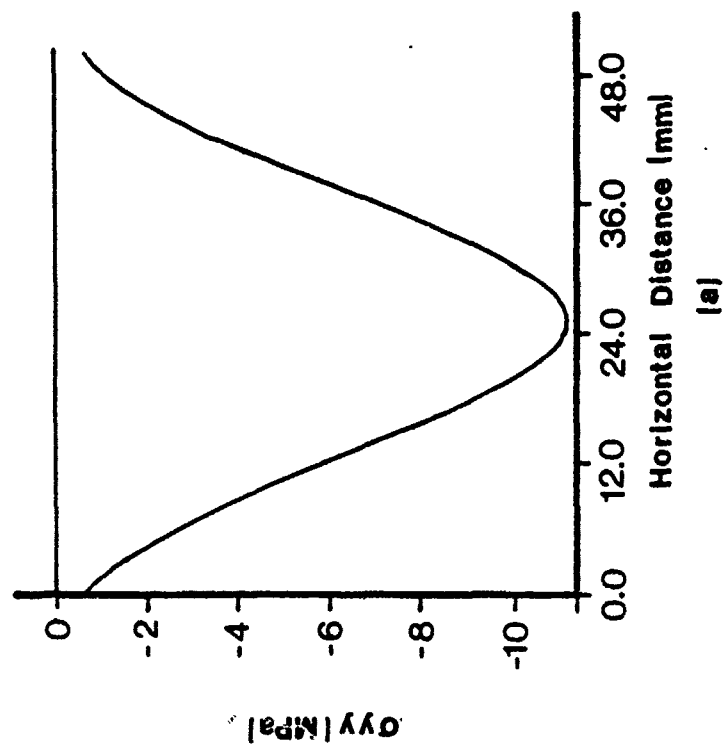


Figure 101. Profiles for (a) vertical stress and (b) vertical strain along the horizontal diameter, Load Case 2, nonlinear analysis,  $t = 31.2 \mu\text{sec}$ .

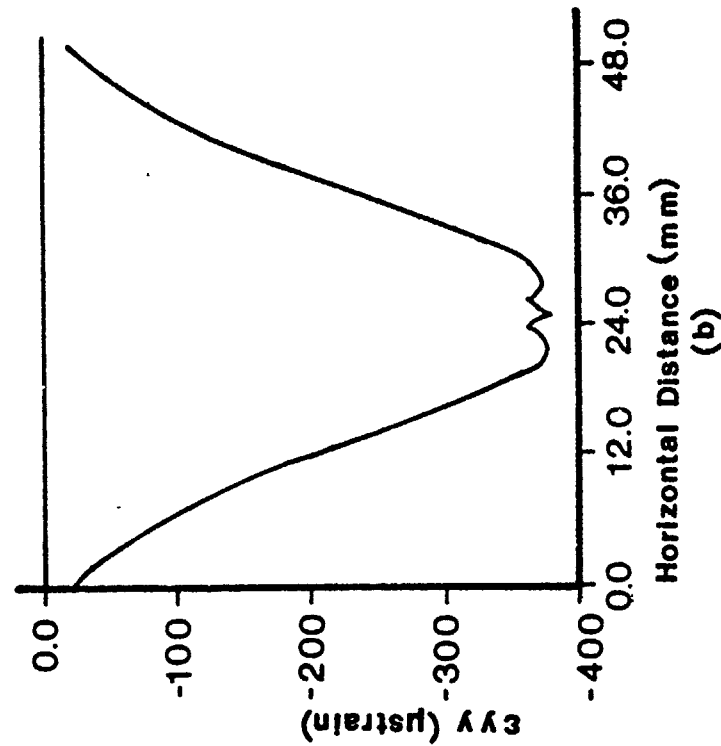
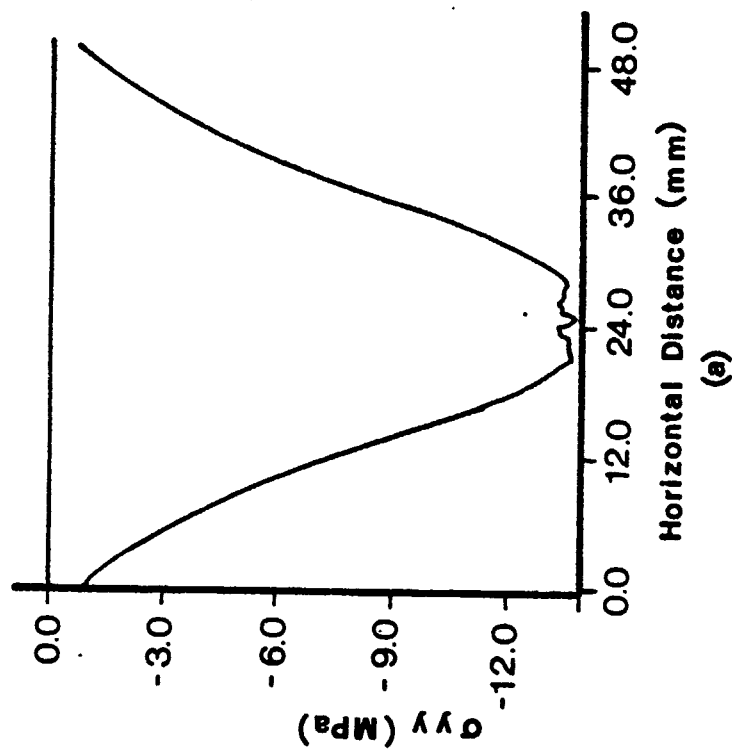


Figure 102. Profiles for (a) vertical stress and (b) vertical strain along the horizontal diameter, Load Case 2, nonlinear analysis,  $t = 35 \mu\text{sec}$ .

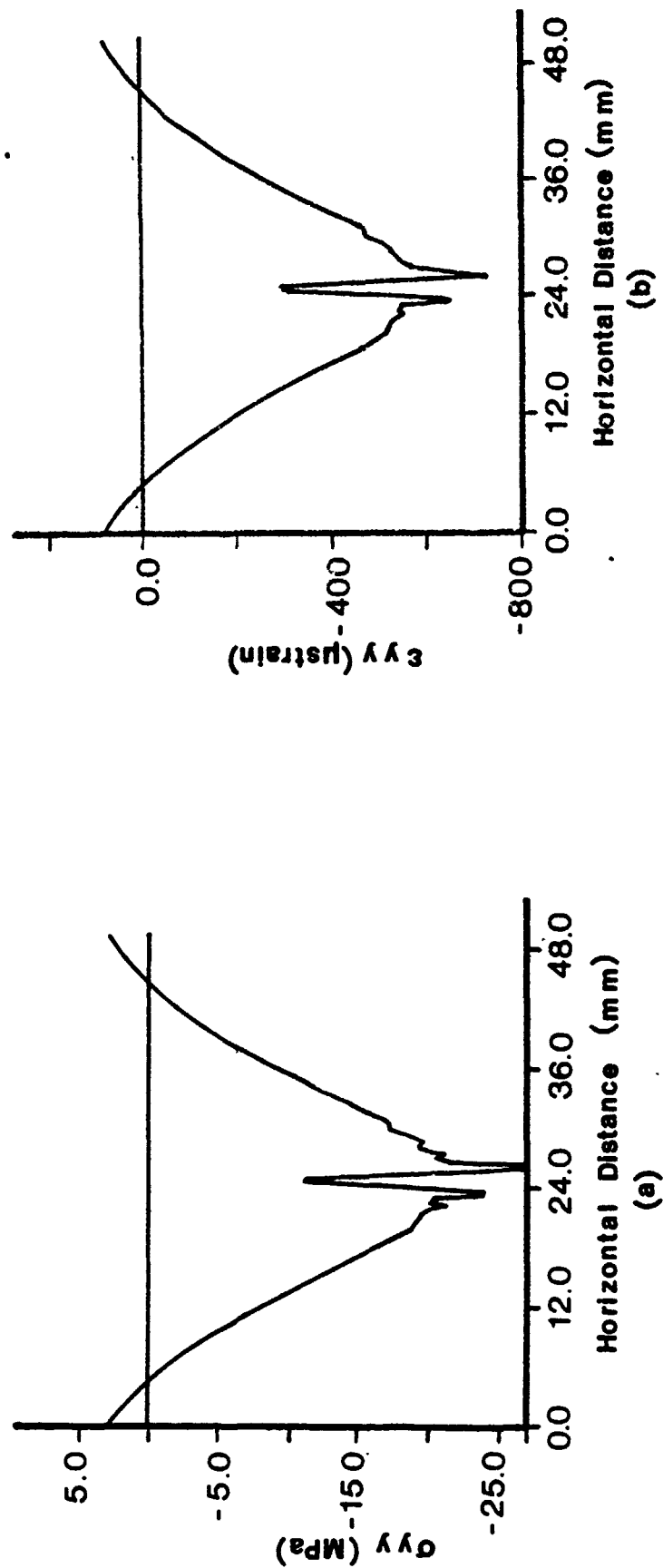


Figure 103. Profiles for (a) vertical stress and (b) vertical strain along the horizontal diameter, Load Case 2, nonlinear analysis,  $t = 45 \mu\text{sec}$ .

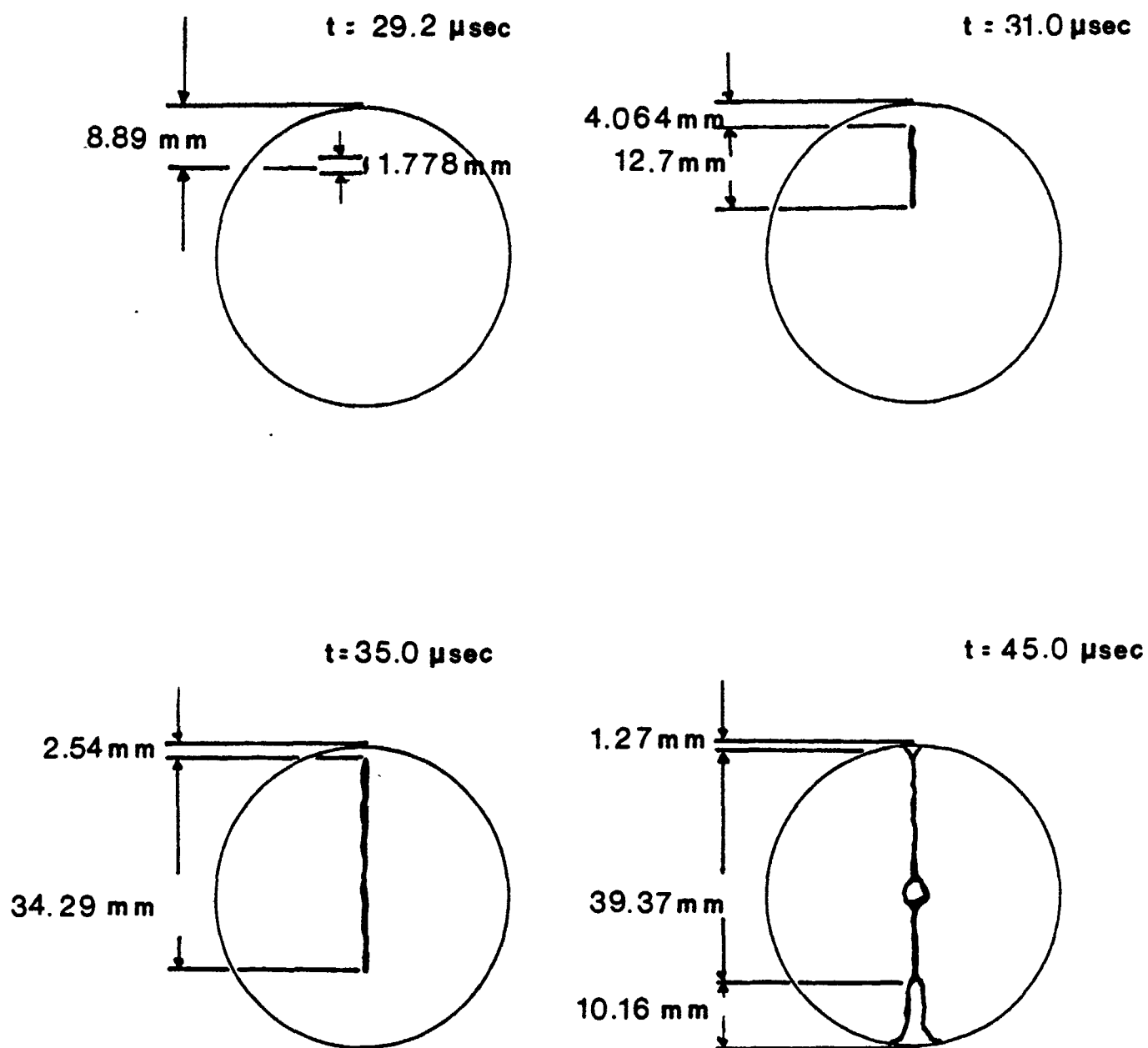


Figure 104. Failure pattern for splitting-tensile specimen, Load Case 2, nonlinear analysis.



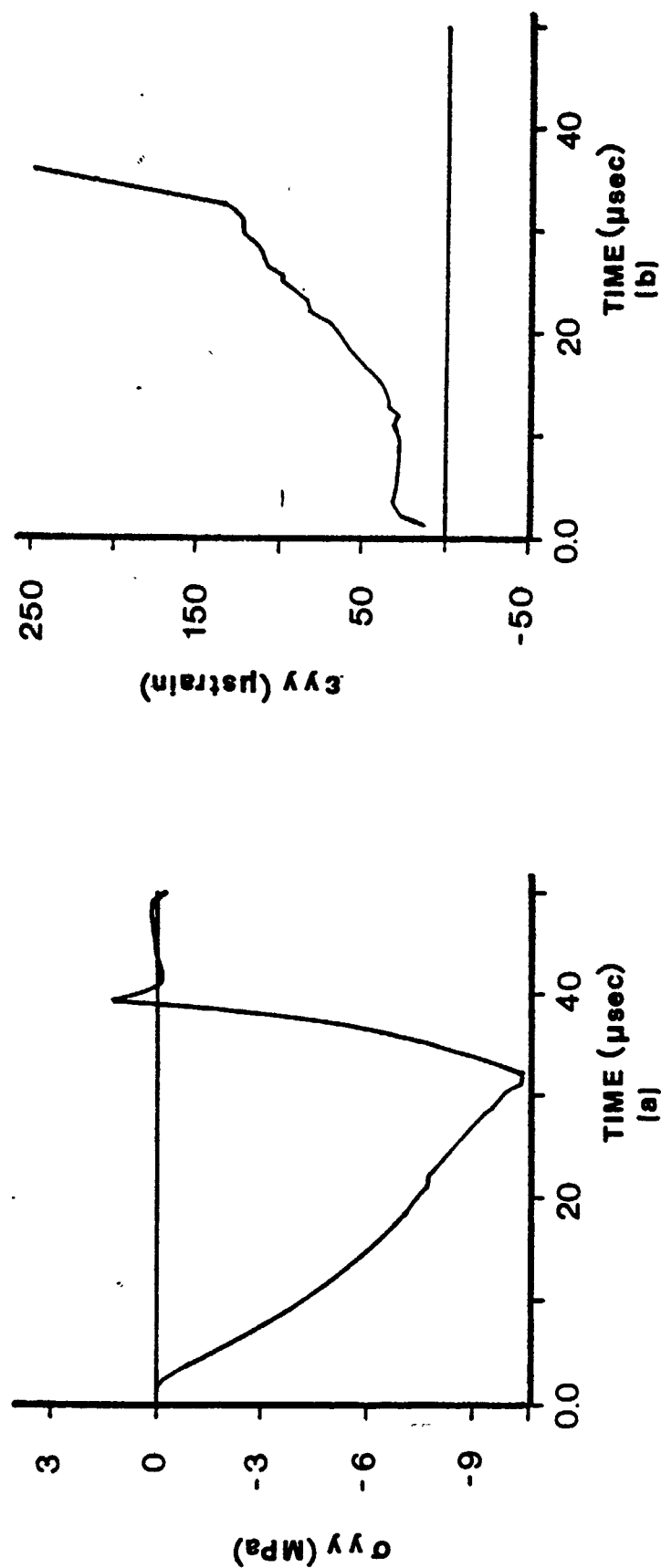
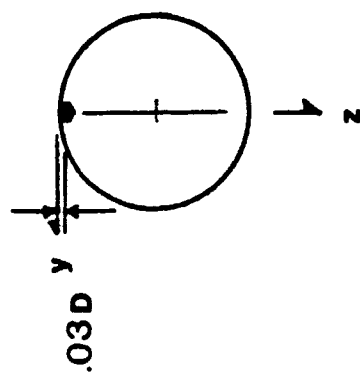


Figure 105. Time histories for (a) horizontal stress and (b) horizontal strain at root of bifurcation at top of cylinder, Load Case 2, nonlinear analysis.

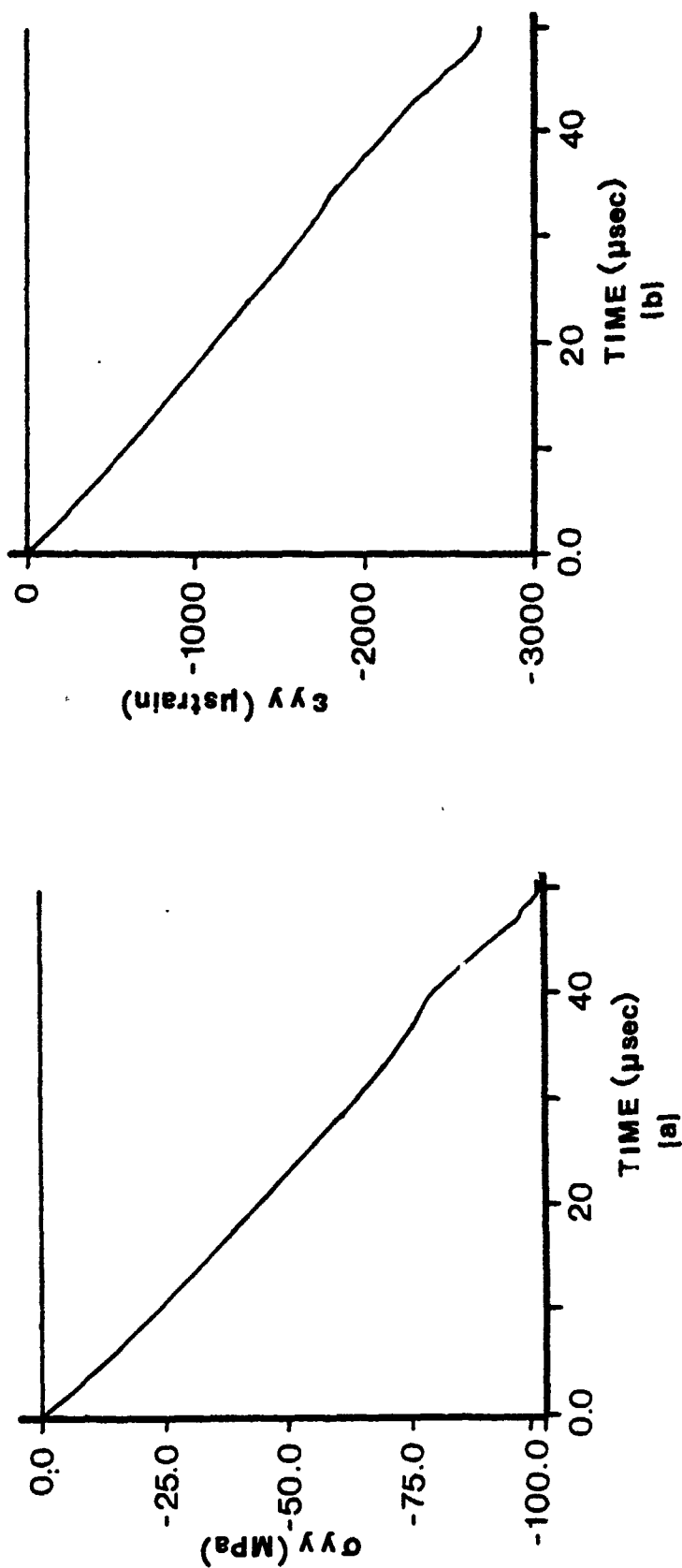
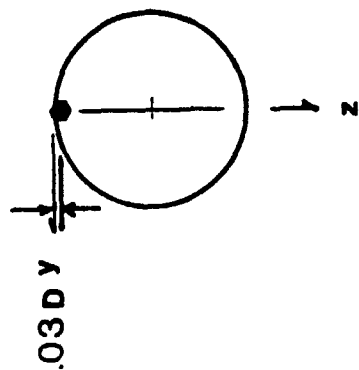


Figure 106. Time histories for (a) vertical stress and (b) vertical strain at root of bifurcation at top of cylinder, Load Case 2, nonlinear analysis.

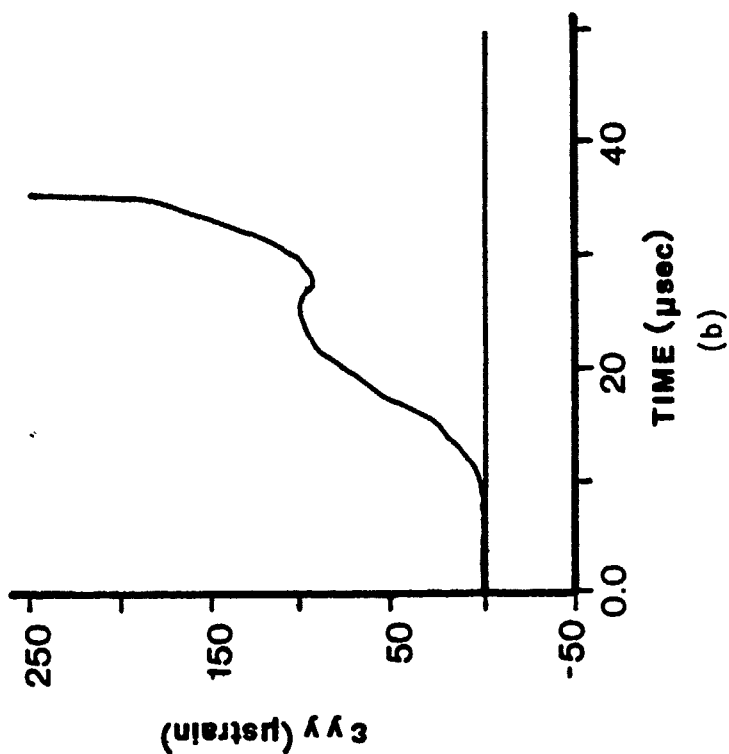
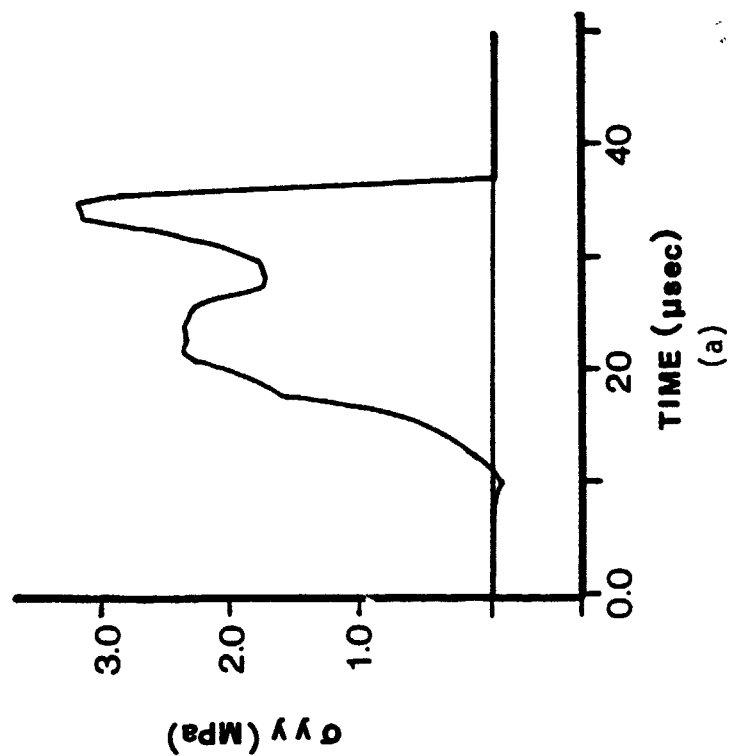
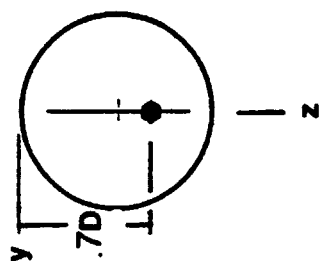


Figure 107. Time histories for (a) horizontal stress and (b) horizontal strain at root of bifurcation at bottom of cylinder, Load Case 2, nonlinear analysis.

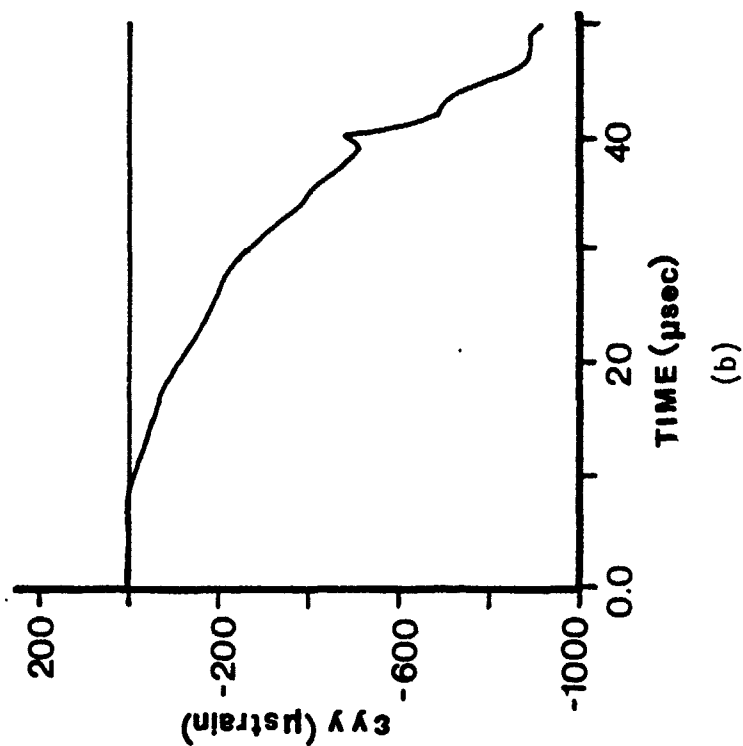
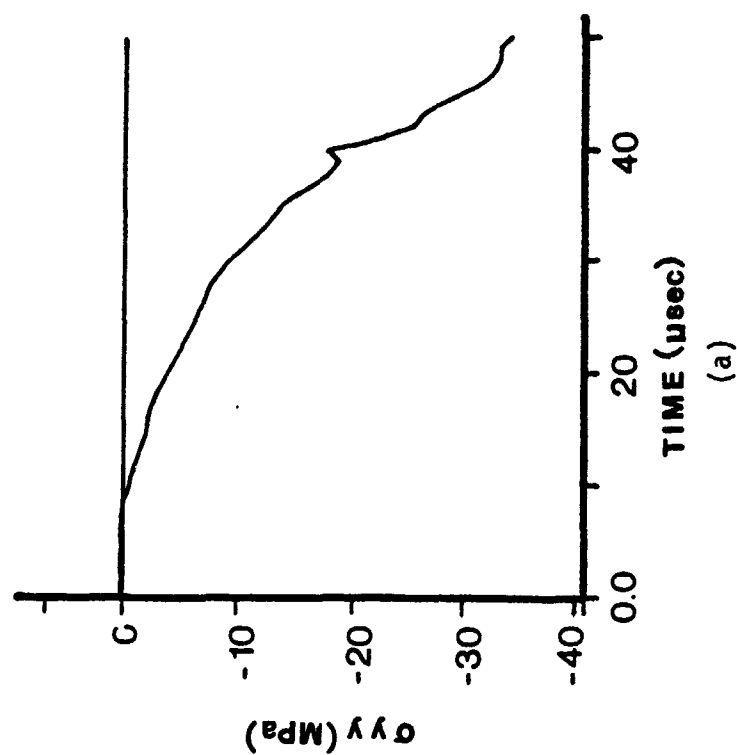
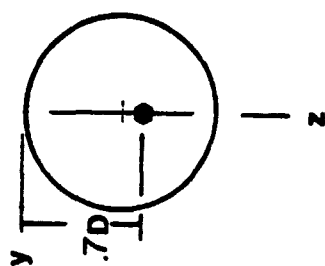


Figure 108. Time histories for (a) vertical stress and (b) vertical strain at root of bifurcation at bottom of cylinder, Load Case 2, nonlinear analysis.

#### 4. Results of Nonlinear Analysis (Load Case 3)

Time histories for the horizontal stress,  $\sigma_y$ , at three locations along the vertical diameter are illustrated in Figures 109, 110, and 111 for  $z$  equal to  $0.1D$ ,  $0.3D$ , and  $0.5D$ , respectively. Time histories for the vertical stress,  $\sigma_z$ , at two locations along the vertical diameter are illustrated in Figures 112 and 113 for  $z$  equal to  $0.2D$  and  $0.5D$ , respectively.

Profiles for the horizontal stress,  $\sigma_y$ , along the vertical diameter at five selected time increments ( $27.1 \mu\text{sec}$ ,  $28.1 \mu\text{sec}$ ,  $28.9 \mu\text{sec}$ ,  $30.5 \mu\text{sec}$ , and  $35.0 \mu\text{sec}$ ) are presented in Figures 114 through 118, respectively. The initiation of the first crack is depicted in Figure 114, and failure of the cylinder is illustrated in Figure 118. Profiles for the horizontal stress along the horizontal diameter, for the same selected times, are presented in Figures 119 through 123. The propagation of the crack to the center of the cylinder is illustrated in Figure 121 at time  $t = 29.6 \mu\text{sec}$ .

The cracking sequence, from the initiation of the first crack until failure, is illustrated in Figure 124. The first crack occurs at a location approximately 0.4 inches (10.2 mm) from the top of the cylinder, at a time  $t = 27.0 \mu\text{sec}$  (Figure 124a). At time  $t = 27.07 \mu\text{sec}$ , the crack is observed to propagate in either direction along the vertical diameter (Figure 124b). At time  $t = 28.65 \mu\text{sec}$ , the crack has propagated along the vertical diameter through the center of the cylinder in one direction, and has nearly reached the top of the cylinder in the other direction (Figure 124c). Finally, at time  $t = 35 \mu\text{sec}$ , failure occurs (Figure 124d).

During the failure sequence of the numerical analysis, three different bifurcations of the crack pattern are observed (see Figure 124d). The first bifurcation occurs just below the center of the cylinder. At approximately the same time, a second bifurcation occurs at the crack front, propagating toward the top of the cylinder at an approximate distance of 0.2 inches (5.1 mm) from the top. The cracks formed in the top bifurcation eventually propagate to the top surface of the cylinder. However, the two cracks formed by the bifurcation occurring just below the center of the cylinder begin to move back toward each other before bifurcating once again at a distance 0.3 inches (7.6 mm) from the bottom of the cylinder. The cracks of this final bifurcation eventually propagate to the bottom surface of the cylinder at which time failure occurs.

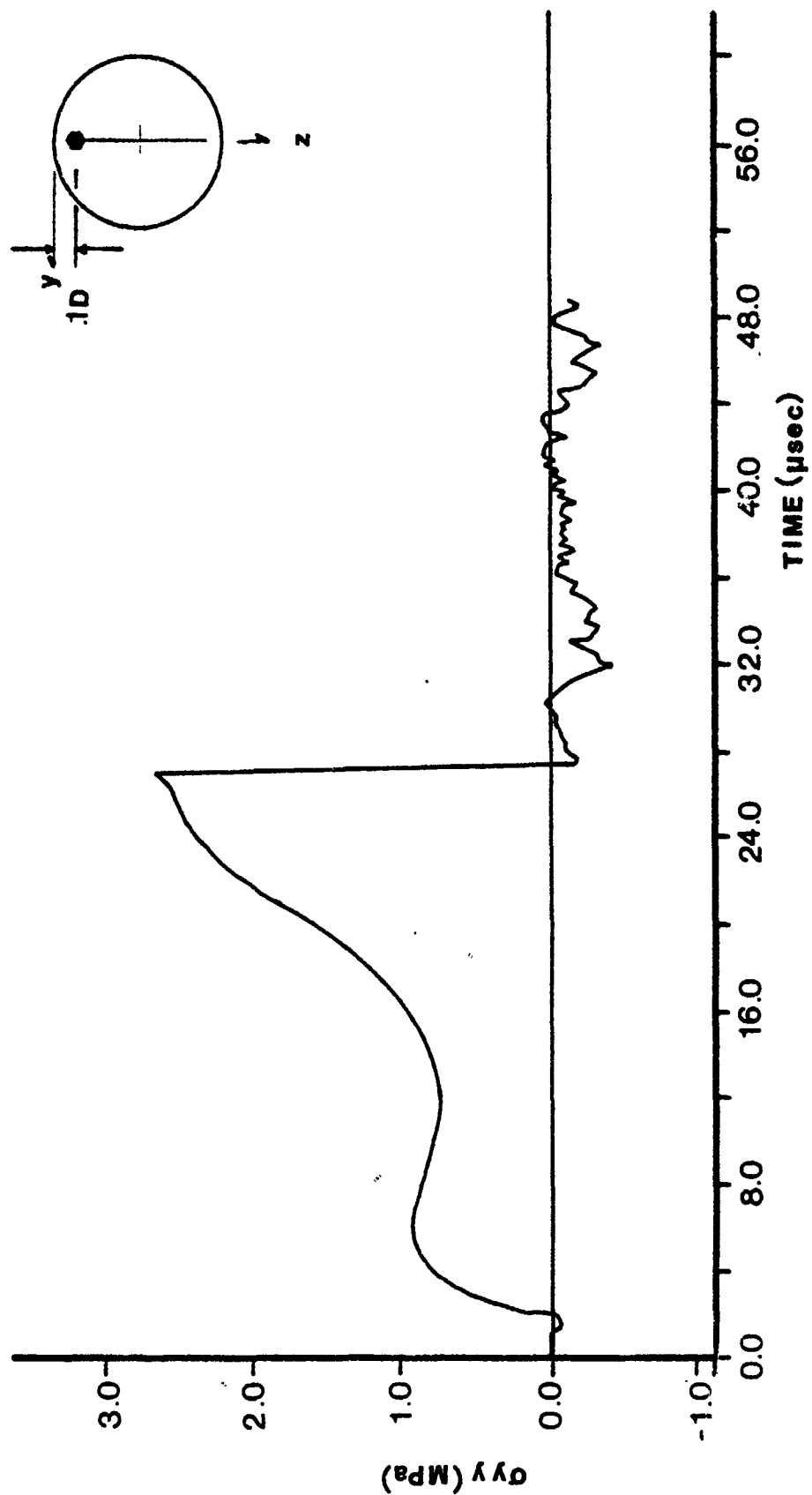


Figure 109. Time history for horizontal stress at  $z = 0.1D$ , Load Case 3, nonlinear analysis.

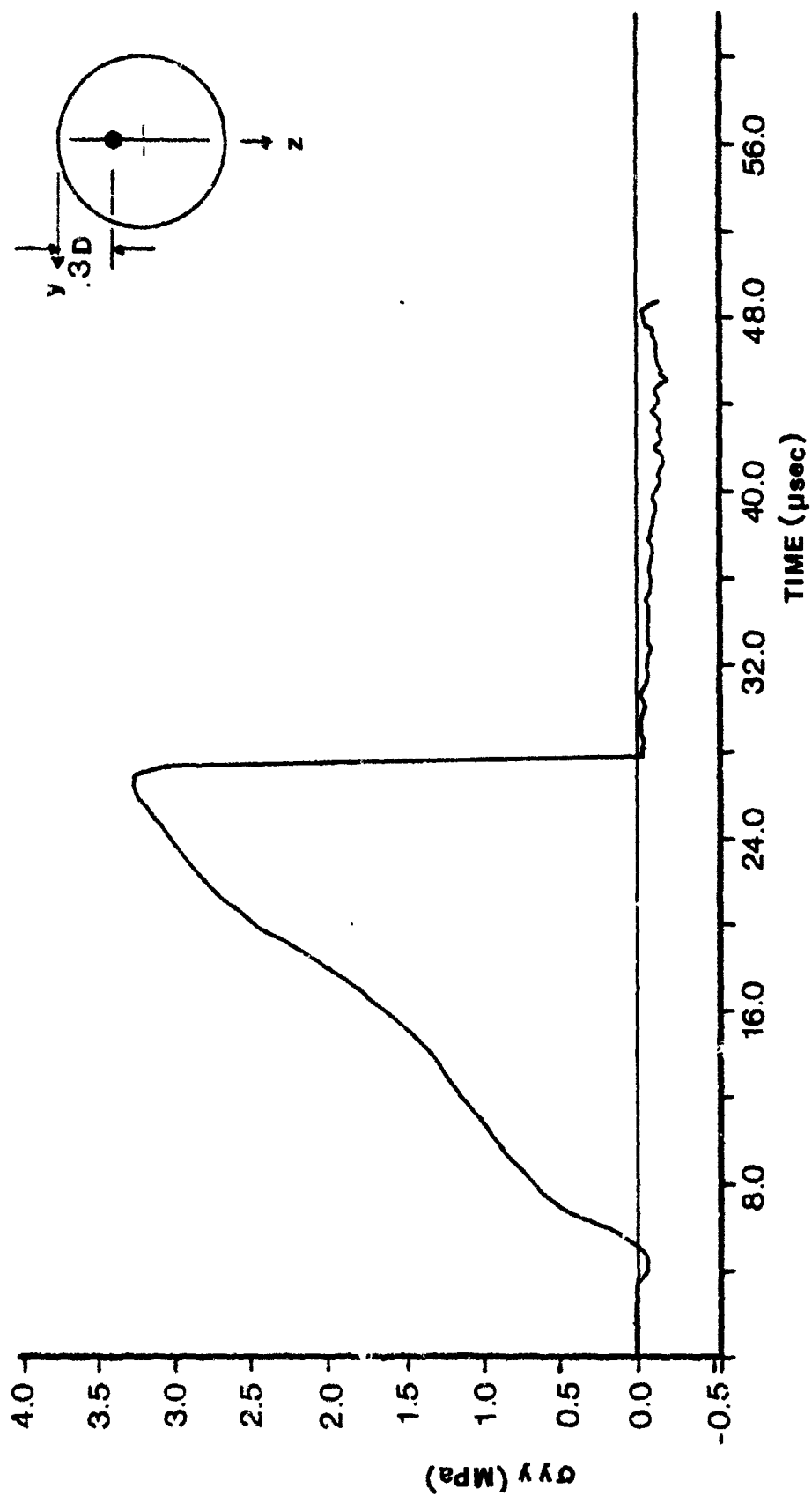


Figure 110. Time history for horizontal stress at  $z = 0.3D$ , Load Case 3, nonlinear analysis.

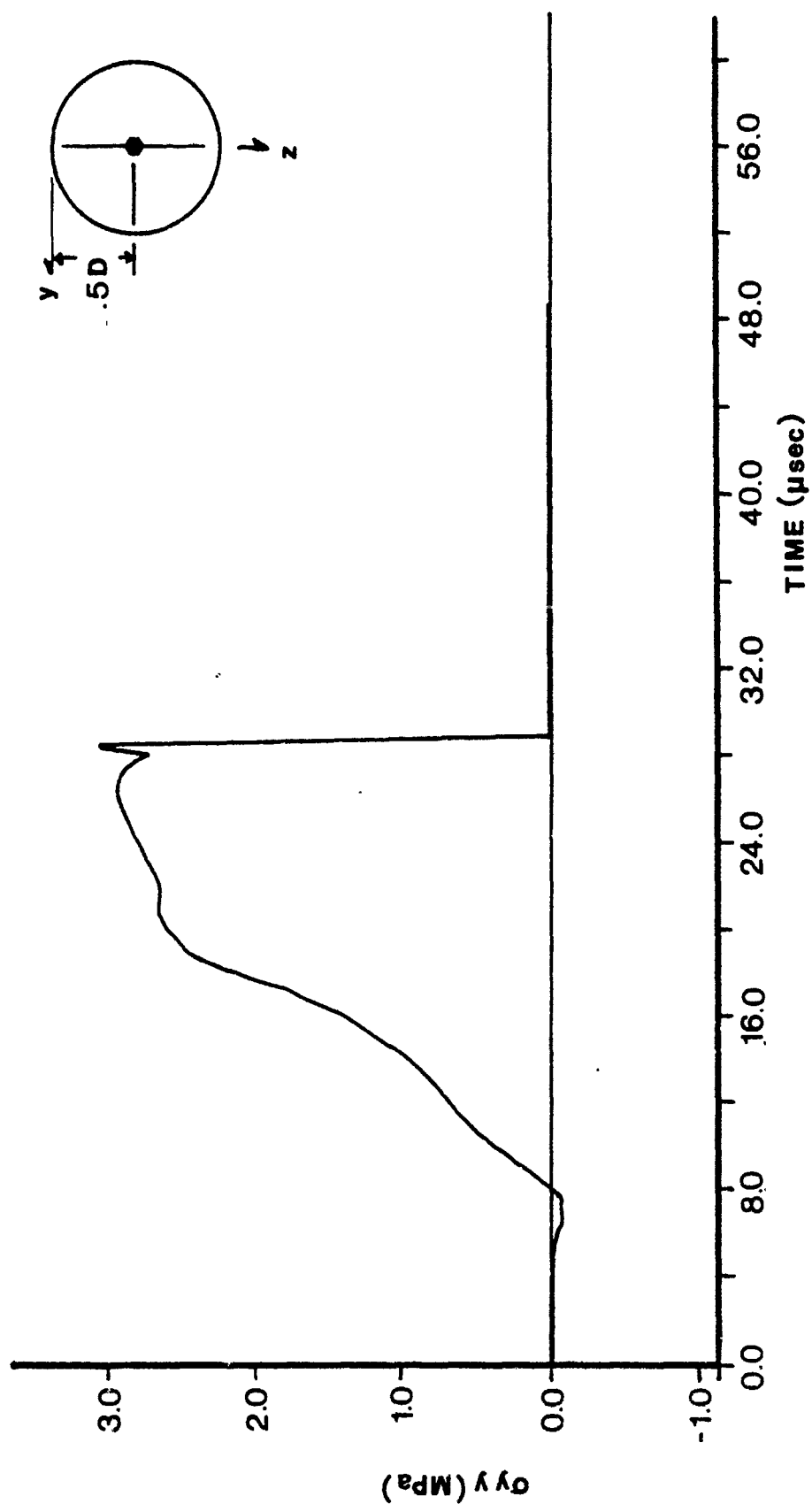


Figure 111. Time history for horizontal stress at  $z = 0.5D$ , Load Case 3, nonlinear analysis.



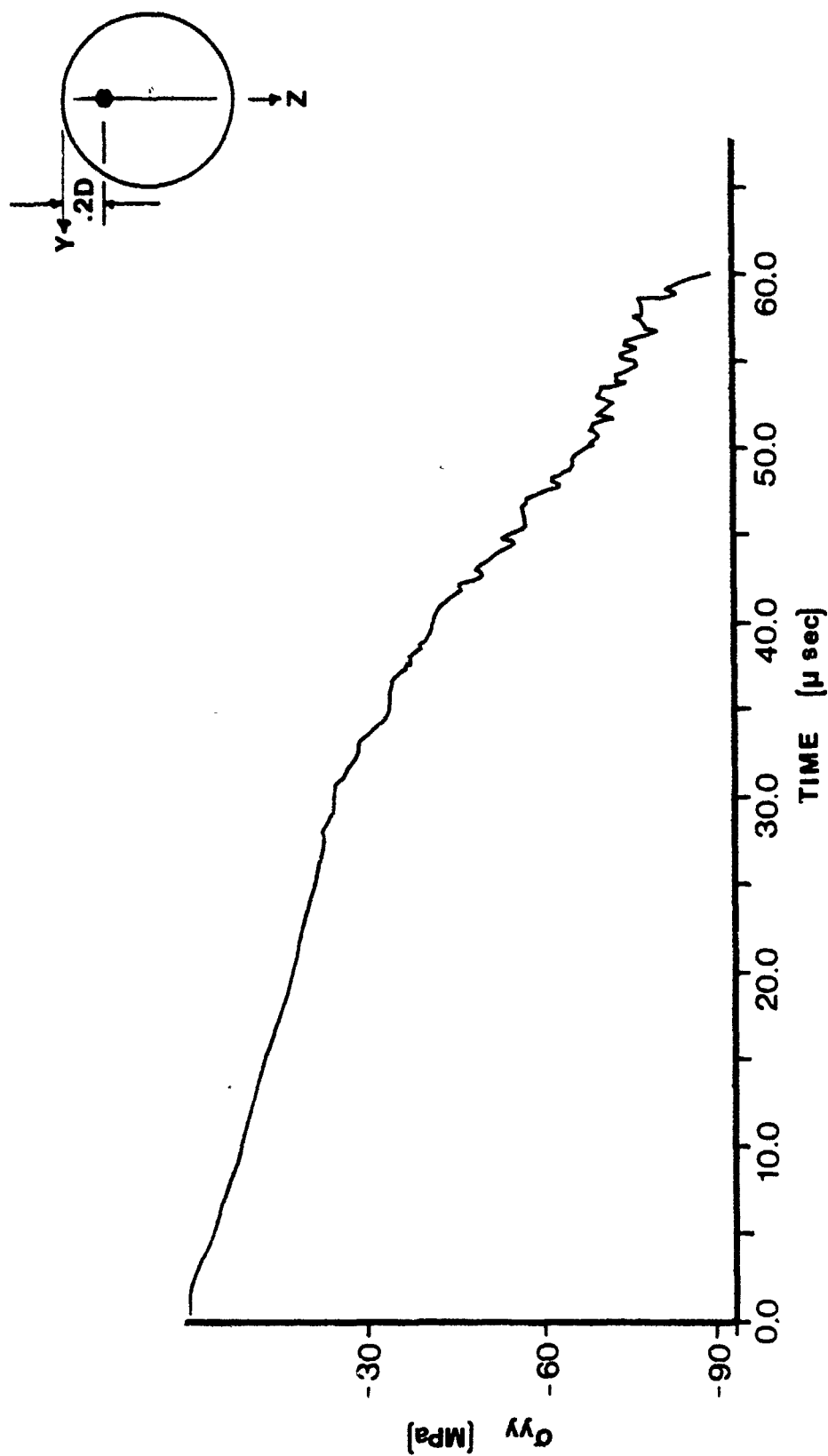


Figure 112. Time history for vertical stress at  $z = 0.2D$ , Load Case 3, nonlinear analysis.

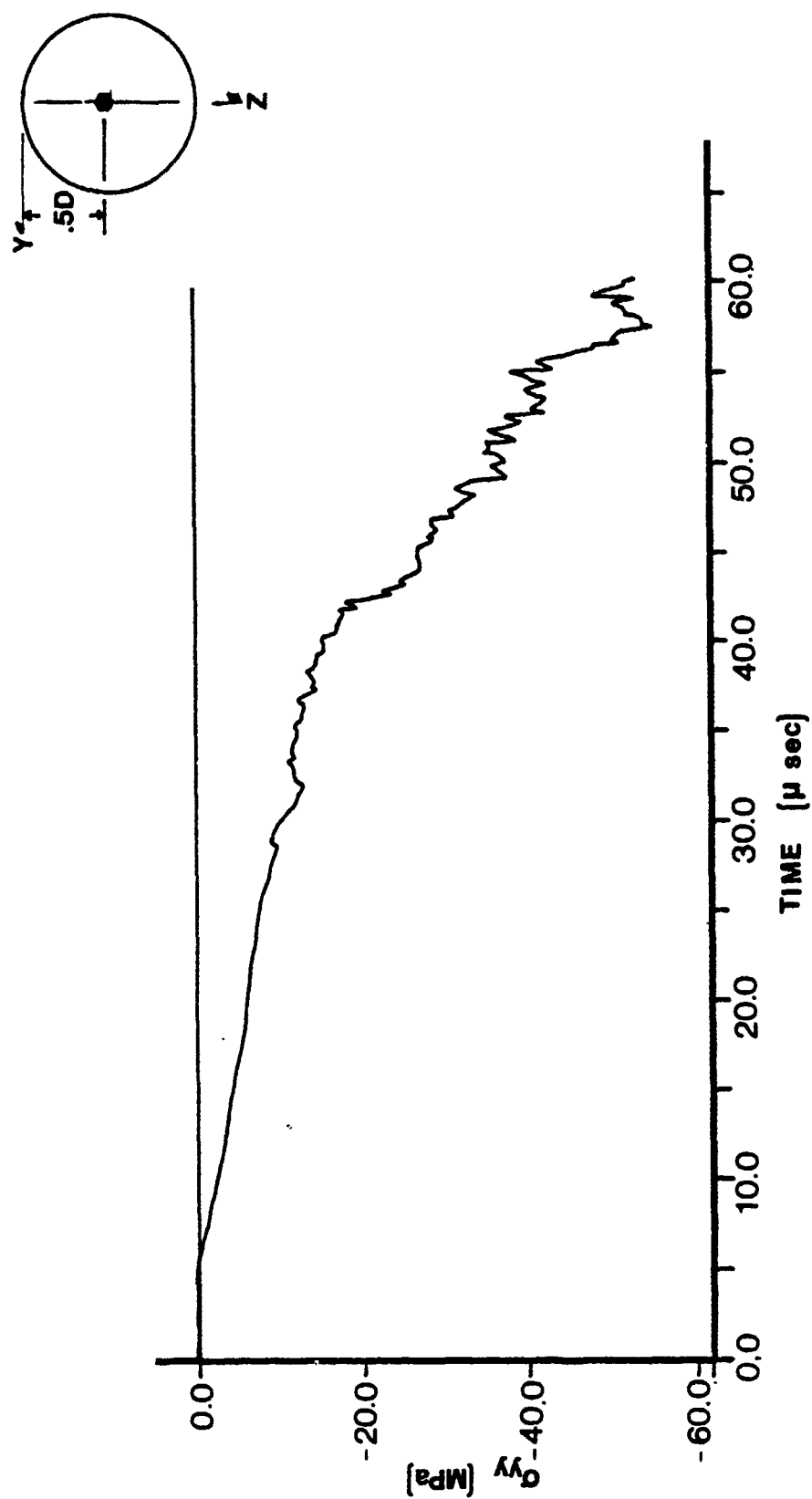


Figure 113. Time history for vertical stress at  $z = 0.5D$ , Load Case 3, nonlinear analysis.

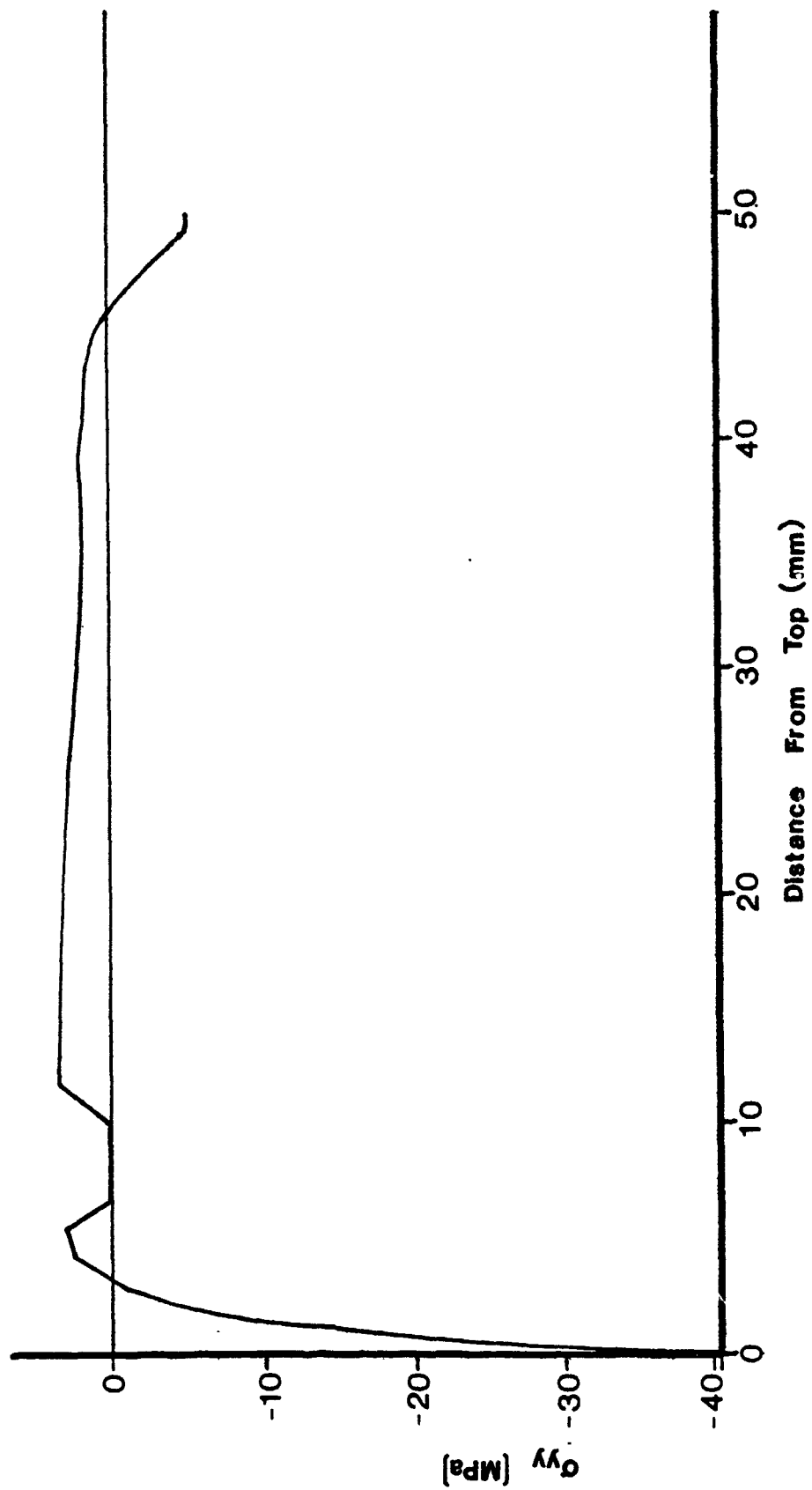


Figure 114. Profile for horizontal stress along the vertical diameter,  
Load Case 3, nonlinear analysis,  $t = 27.1 \mu\text{sec}$ .

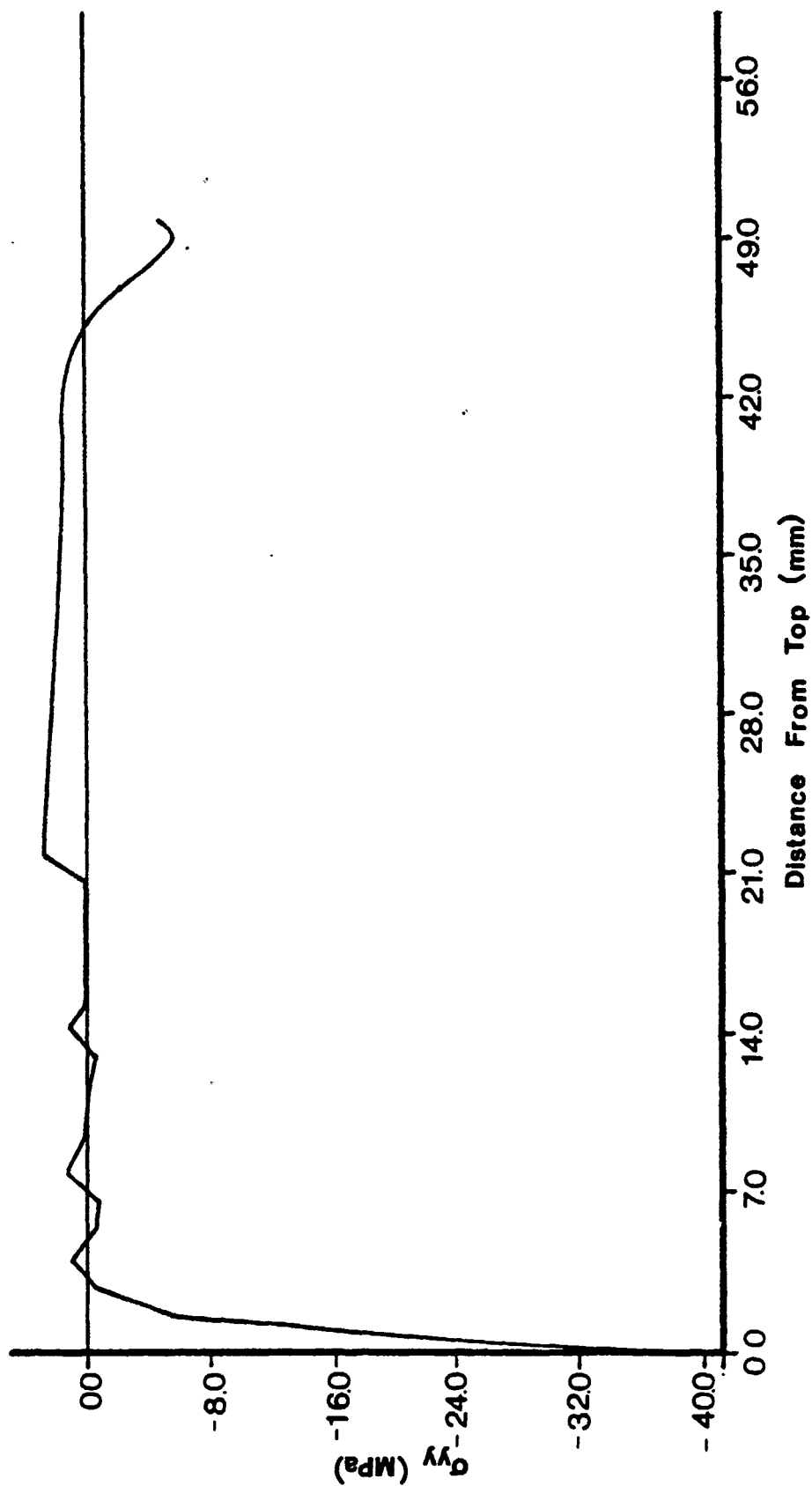


Figure 115. Profile for horizontal stress along the vertical diameter, Load Case 3, nonlinear analysis,  $t = 28.1 \mu\text{sec}$ .

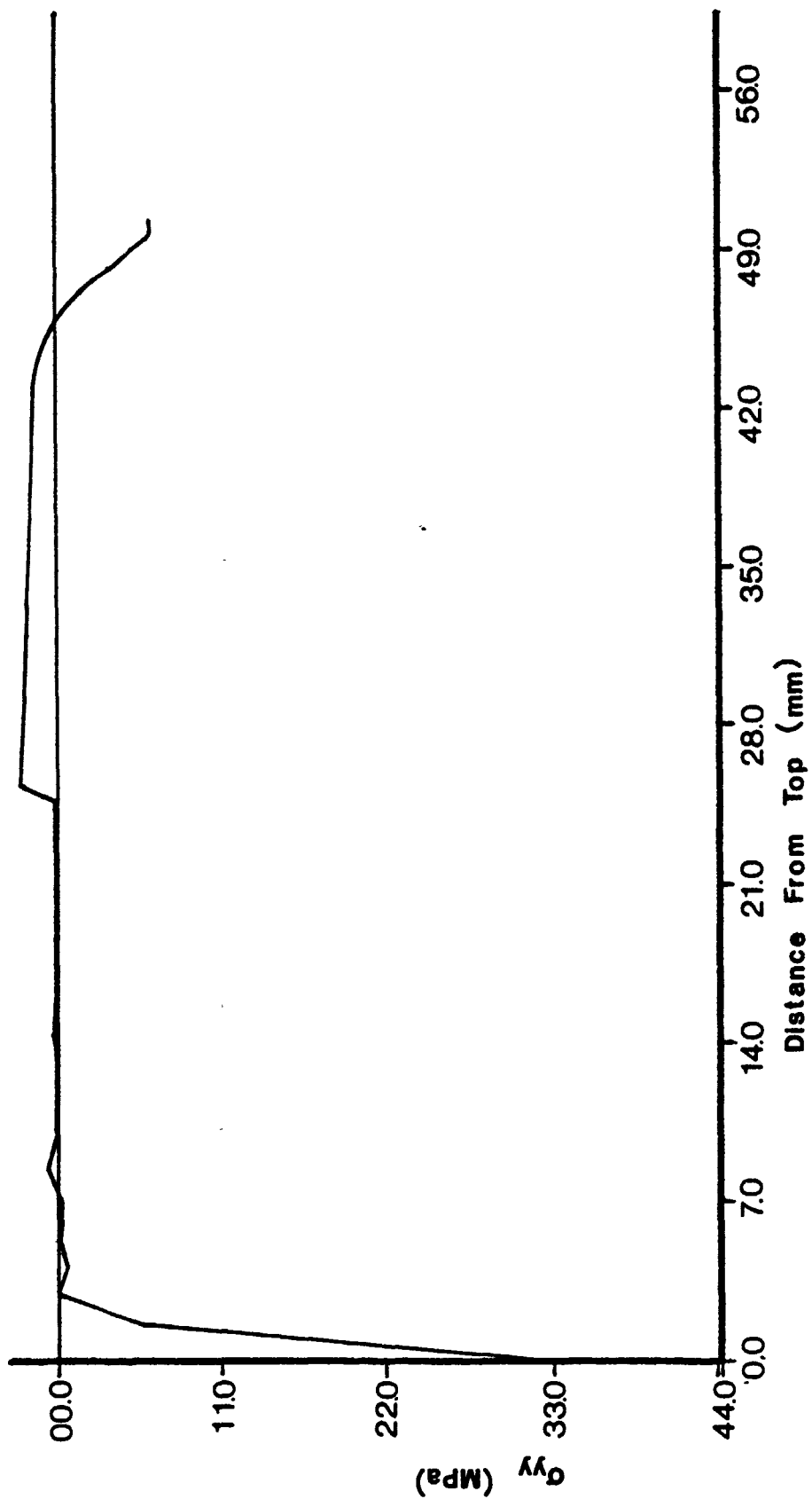


Figure 116. Profile for horizontal stress along the vertical diameter,  
Load Case 3, nonlinear analysis,  $t = 28.9 \mu\text{sec}$ .

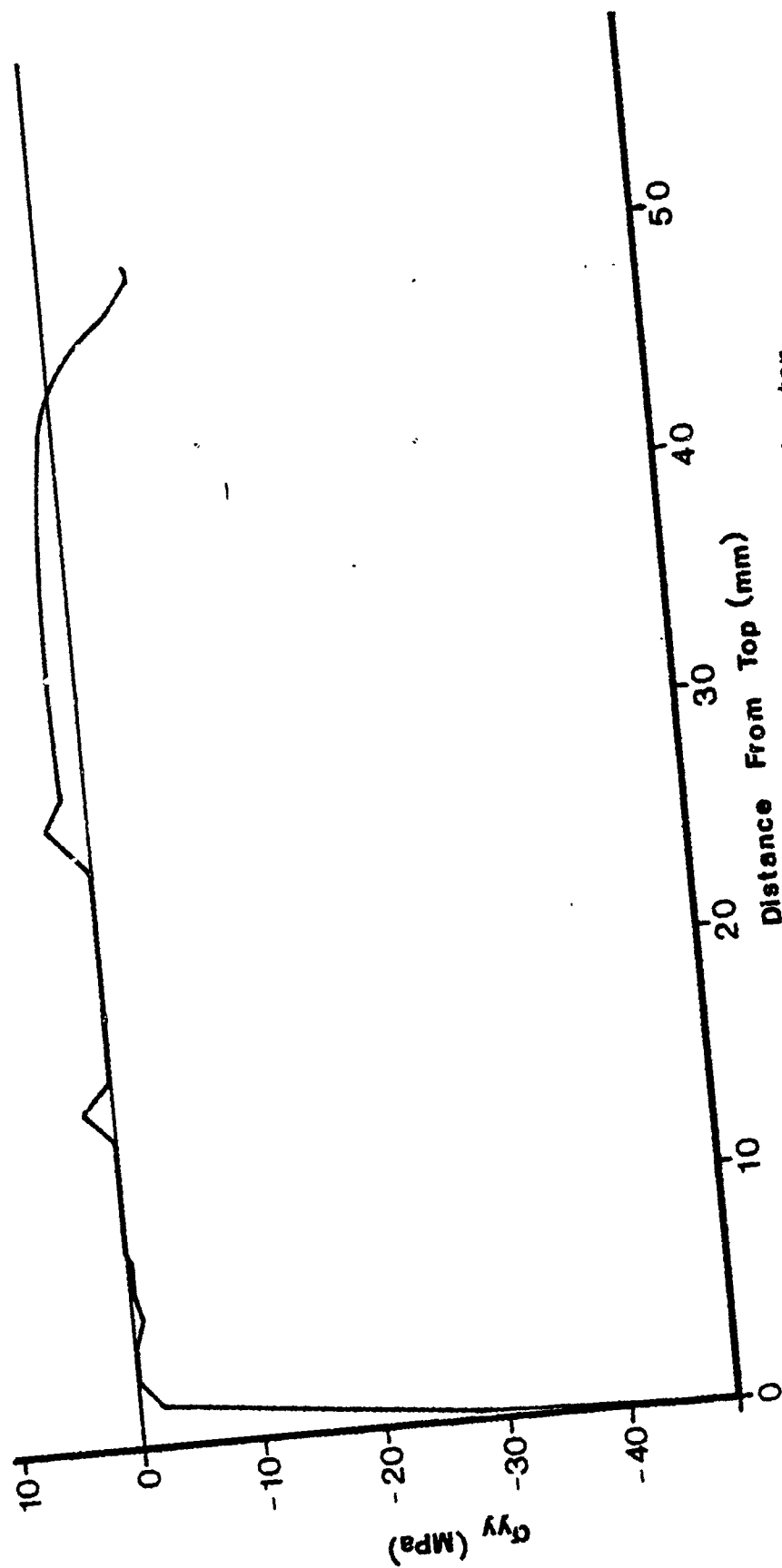


Figure 117. Profile for horizontal stress along the vertical diameter, Load Case 3, nonlinear analysis,  $t = 30.5 \mu\text{sec}$ .

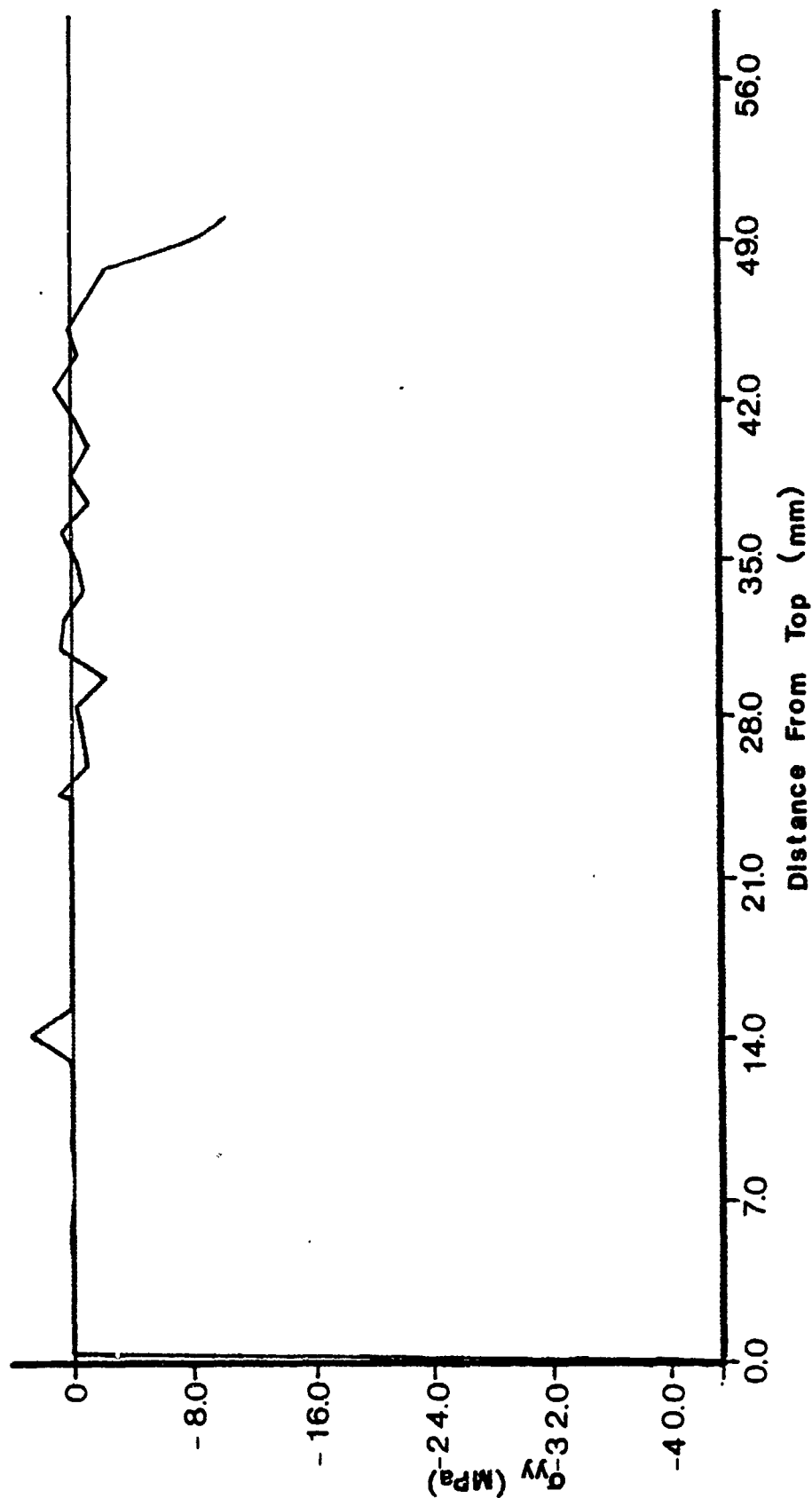


Figure 118. Profile for horizontal stress along the vertical diameter, Load Case 3, nonlinear analysis,  $t = 35.0 \mu\text{sec}$ .

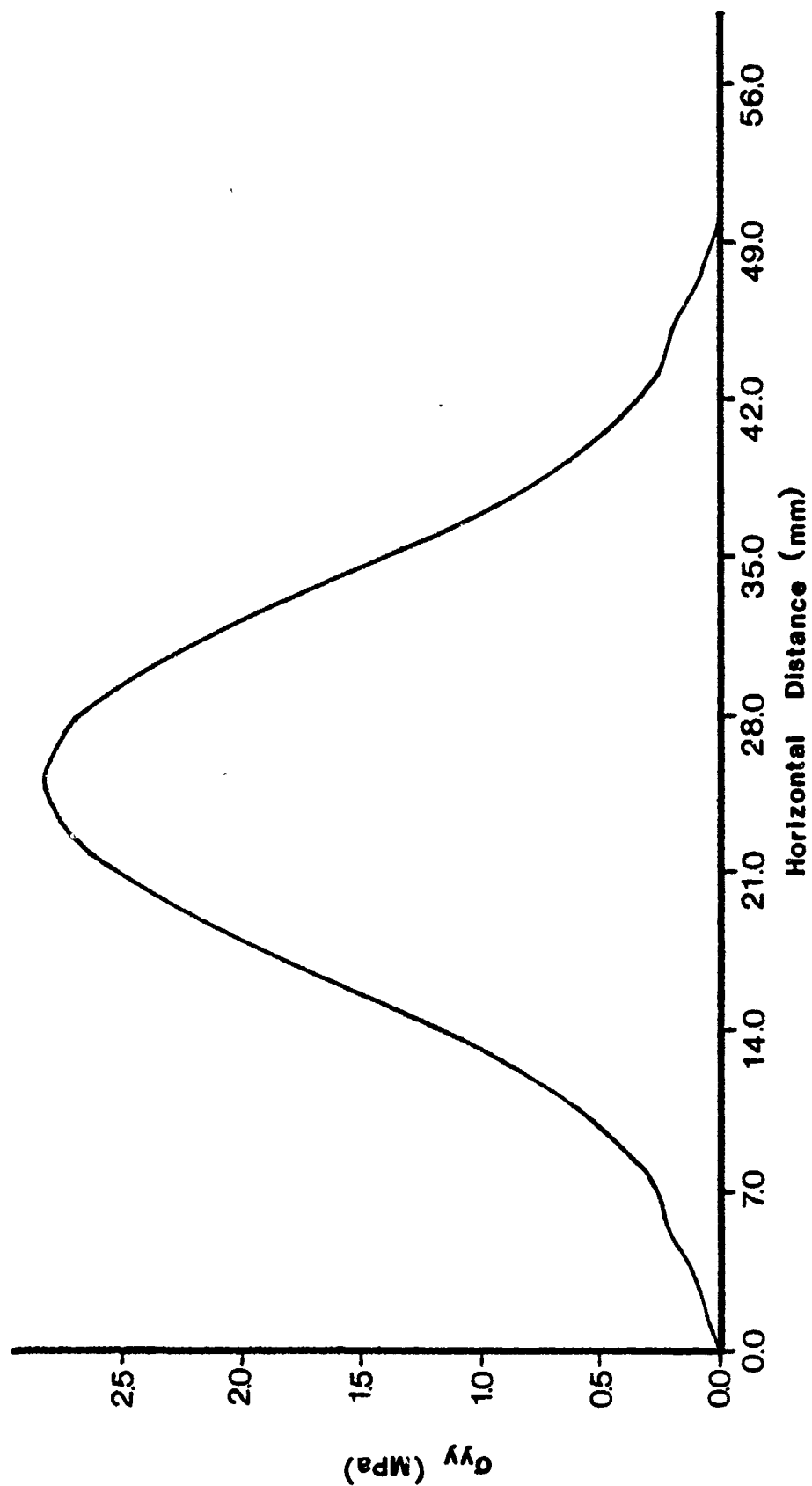


Figure 119. Profile for horizontal stress along the horizontal diameter, Load Case 3, nonlinear analysis,  $t = 27.1 \mu\text{sec}$ .



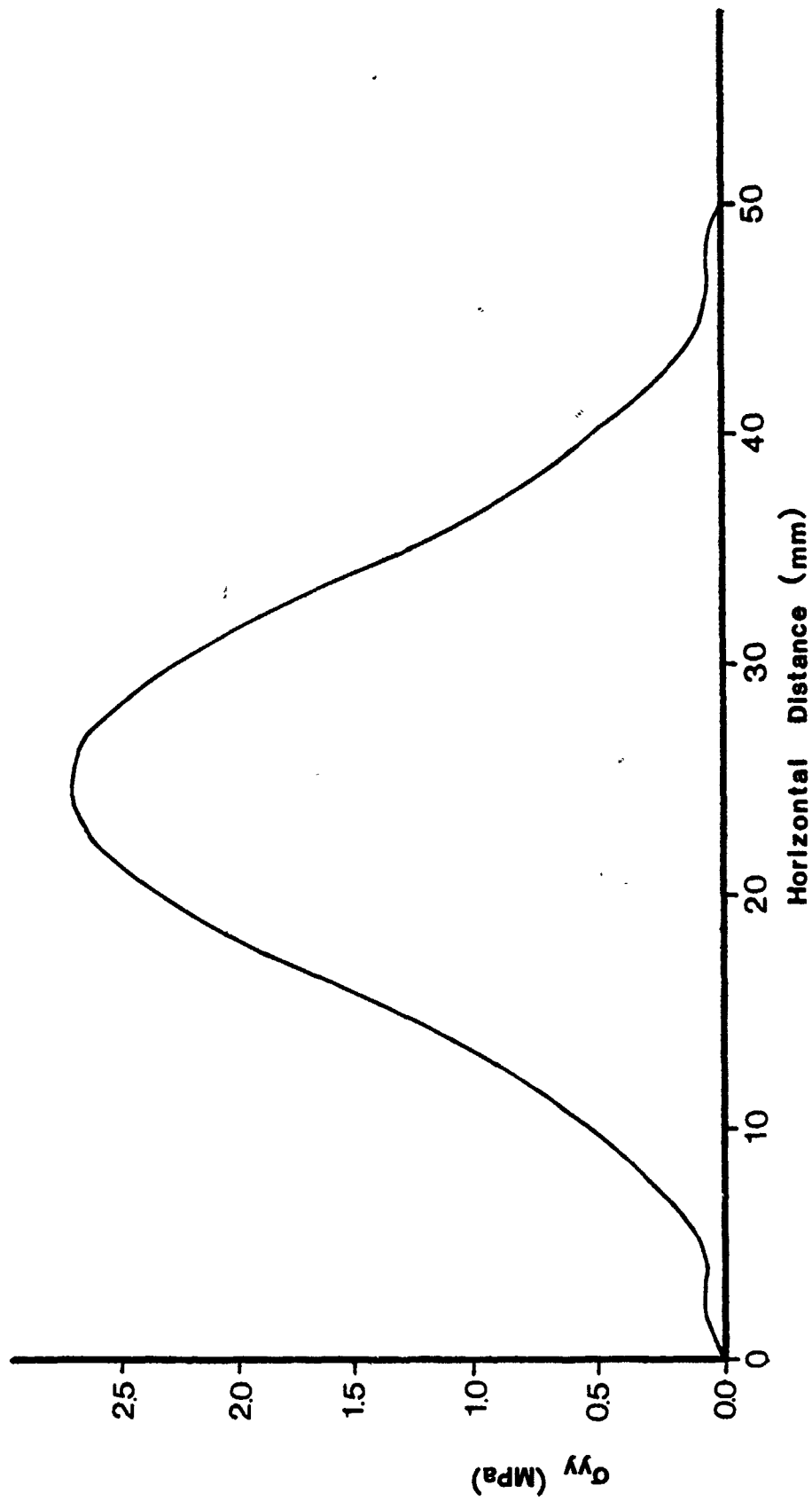


Figure 120. Profile for horizontal stress along the horizontal diameter, Load Case 3, nonlinear analysis,  $t = 28.1 \mu\text{sec}$ .

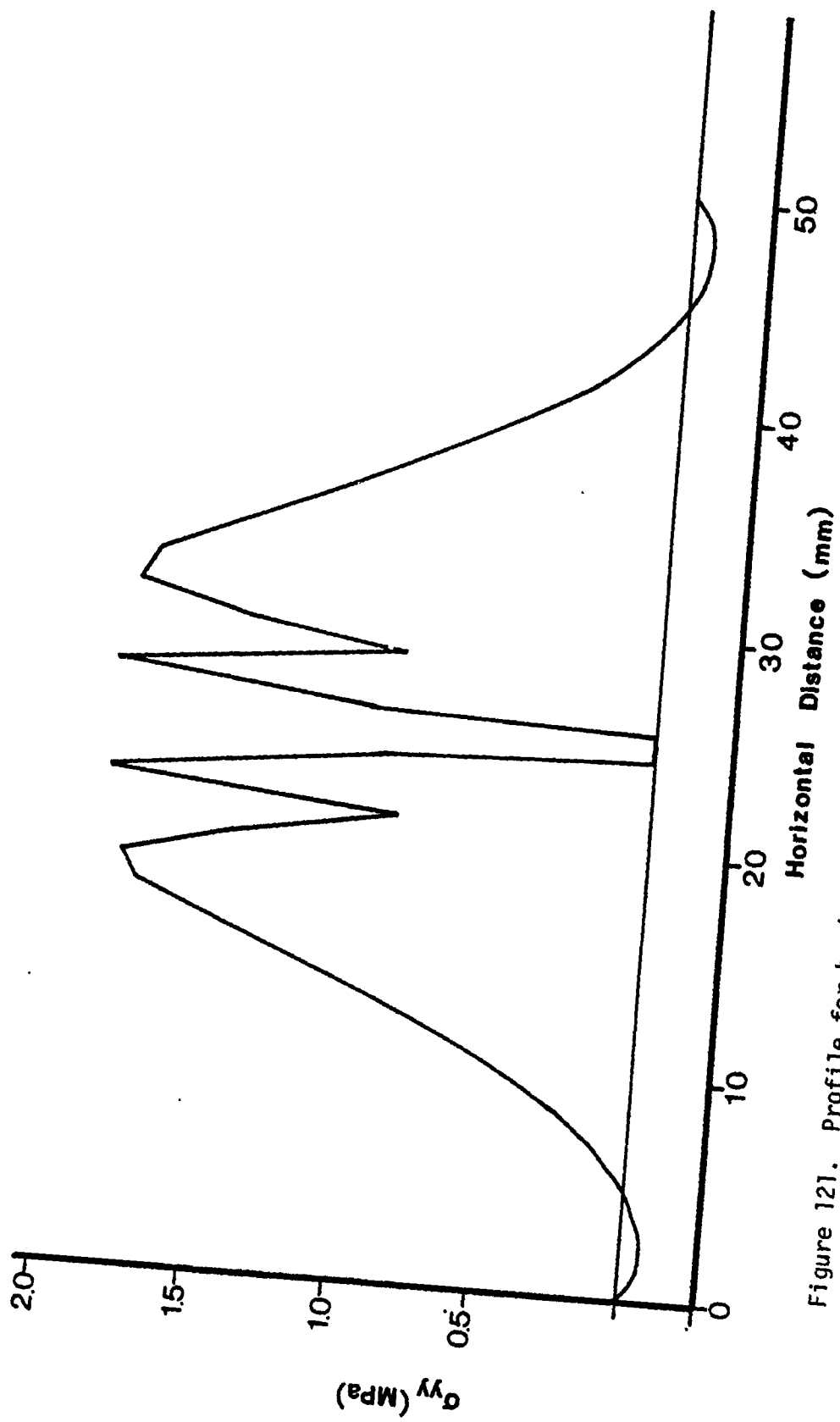


Figure 121. Profile for horizontal stress along the horizontal diameter, Load Case 3, nonlinear analysis,  $t = 28.9 \mu\text{sec}$ .

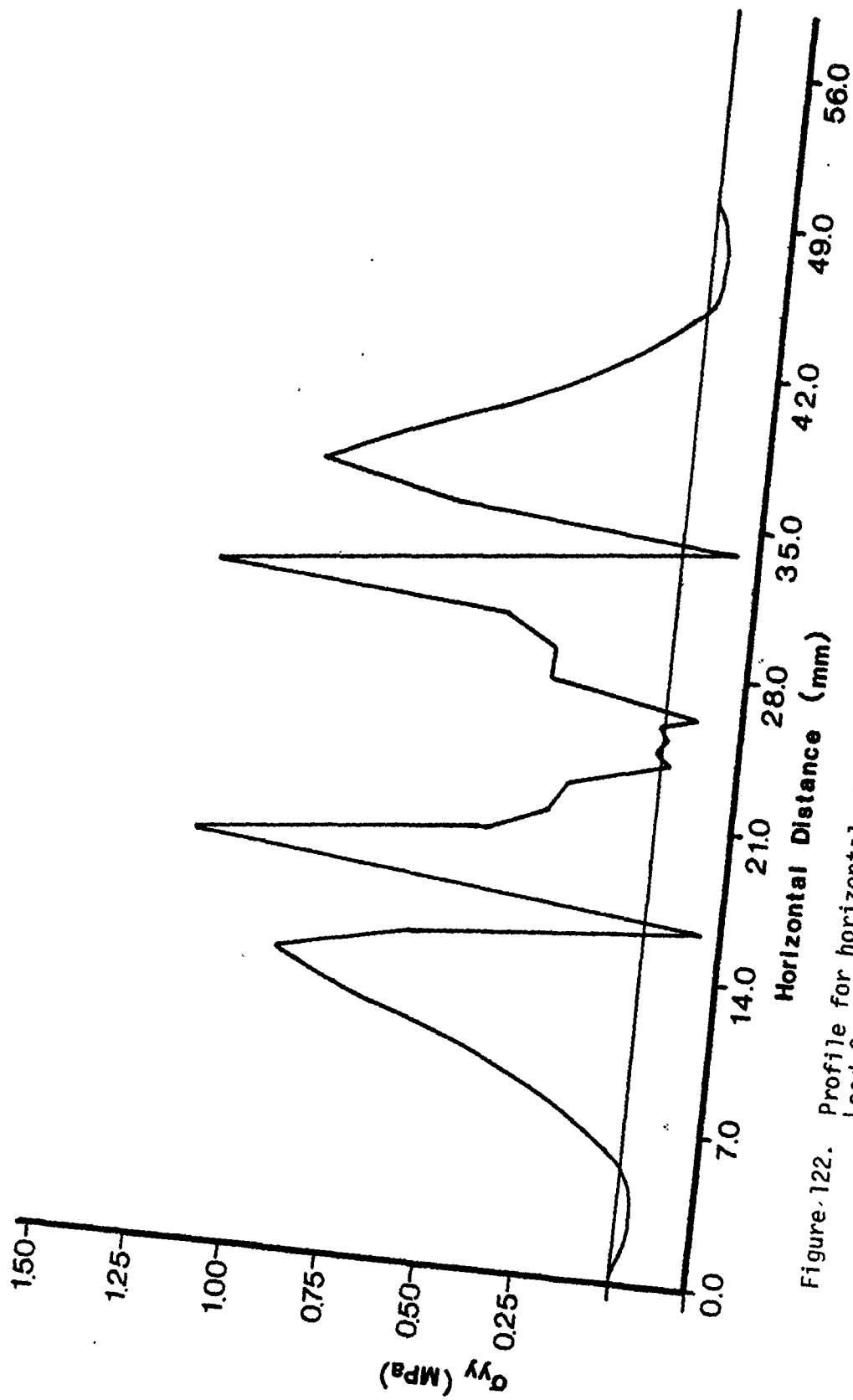


Figure 122. Profile for horizontal stress along the horizontal diameter, Load Case 3, nonlinear analysis,  $t = 30.5 \mu\text{sec}$ .

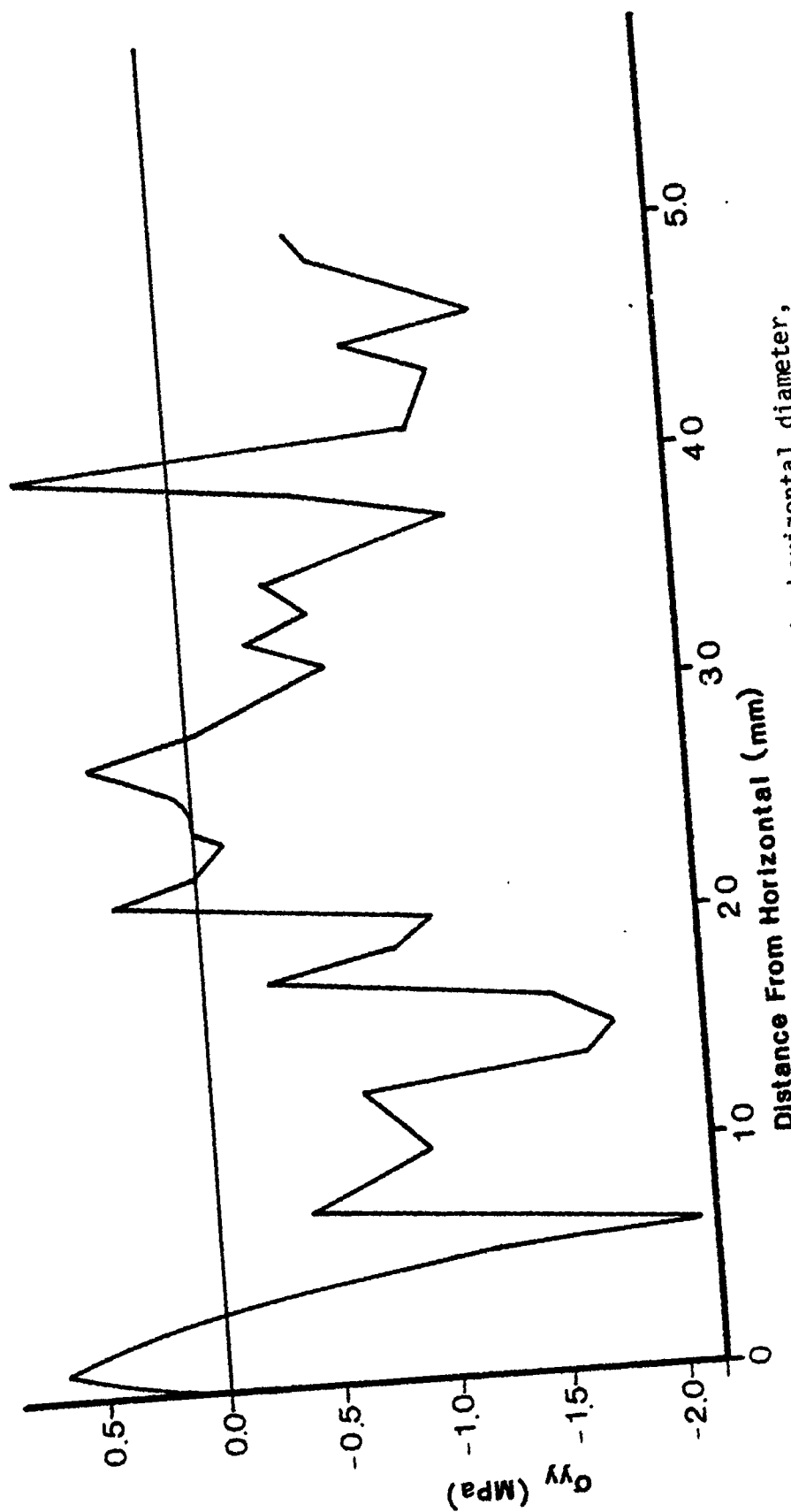


Figure 123. Profile for horizontal stress along the horizontal diameter, Load Case 3, nonlinear analysis,  $t = 35.0 \mu\text{sec}$ .

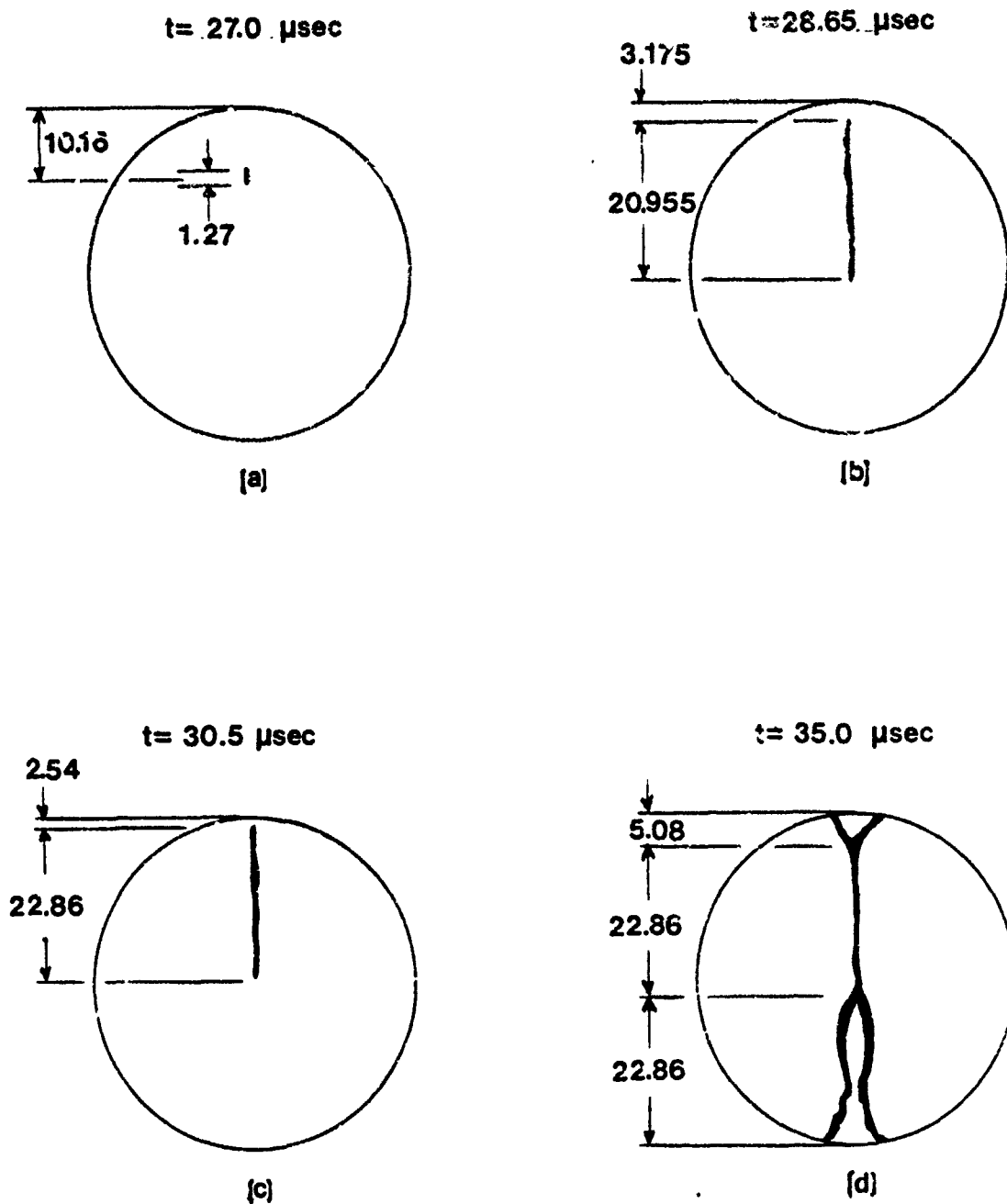


Figure 124. Failure pattern for splitting-tensile specimen, Load Case 3, nonlinear analysis.

## SECTION III

### DIRECT TENSION TESTS

#### A. INTRODUCTION

The direct tension test has seldom been used to evaluate the tensile strength of concrete. This is because of the difficulties of holding the specimens to achieve axial tension and the uncertainties of secondary stresses induced by the holding devices. Recently, however, direct tension tests using a Split Hopkinson Pressure Bar (SHPB) have been successfully conducted (Reference 24). Two types of tensile specimens were tested, a square notch specimen (Figure 125a) and a saddle notch specimen (Figure 125b). All specimens were cemented to the ends of the SHPB with a nonepoxy concrete cement. The bar surfaces and specimen surfaces were cleaned in a manner similar to that used for surface cleaning before the placement of foil-resistant strain gages.

The principles of operation of the compressive SHPB (Figure 126) are detailed in Reference 25, and these same principles apply to the direct tension SHPB. The configuration of the SHPB arrangement employed in the direct tension study reported in Reference 24 is also illustrated in Figure 126. The tensile loading mechanism consists of a hollow cylindrical striker bar sliding on the compressive transmitter bar (Bar 2) of the SHPB. The striker bar impacts a tup threaded into the end of what becomes the tensile incident bar (Bar 2). A tensile stress wave then propagates toward the specimen, cemented between the two bars.

The strain gage signals for a square notch and a saddle notch specimen are presented in Figures 127 and 128, respectively. Knowing that the transmitted and reflected signals are coincident in time, then the peak of the transmitted signal is observed to occur during the rise time of the reflected pulse. Moreover, test data accumulated from a recent direct tension study (Reference 26) indicates that failure may occur in the rise time of the loading pulse.

To ascertain the stress condition in the material specimens at failure, a comprehensive finite element method (FEM) study was conducted on several SHPB direct tension tests. Both linear and nonlinear analyses were performed. From the results of the numerical analyses, the dynamic states of stress occurring in the direct tension specimens before failure, the modes of failure, and the times of failure were revealed.

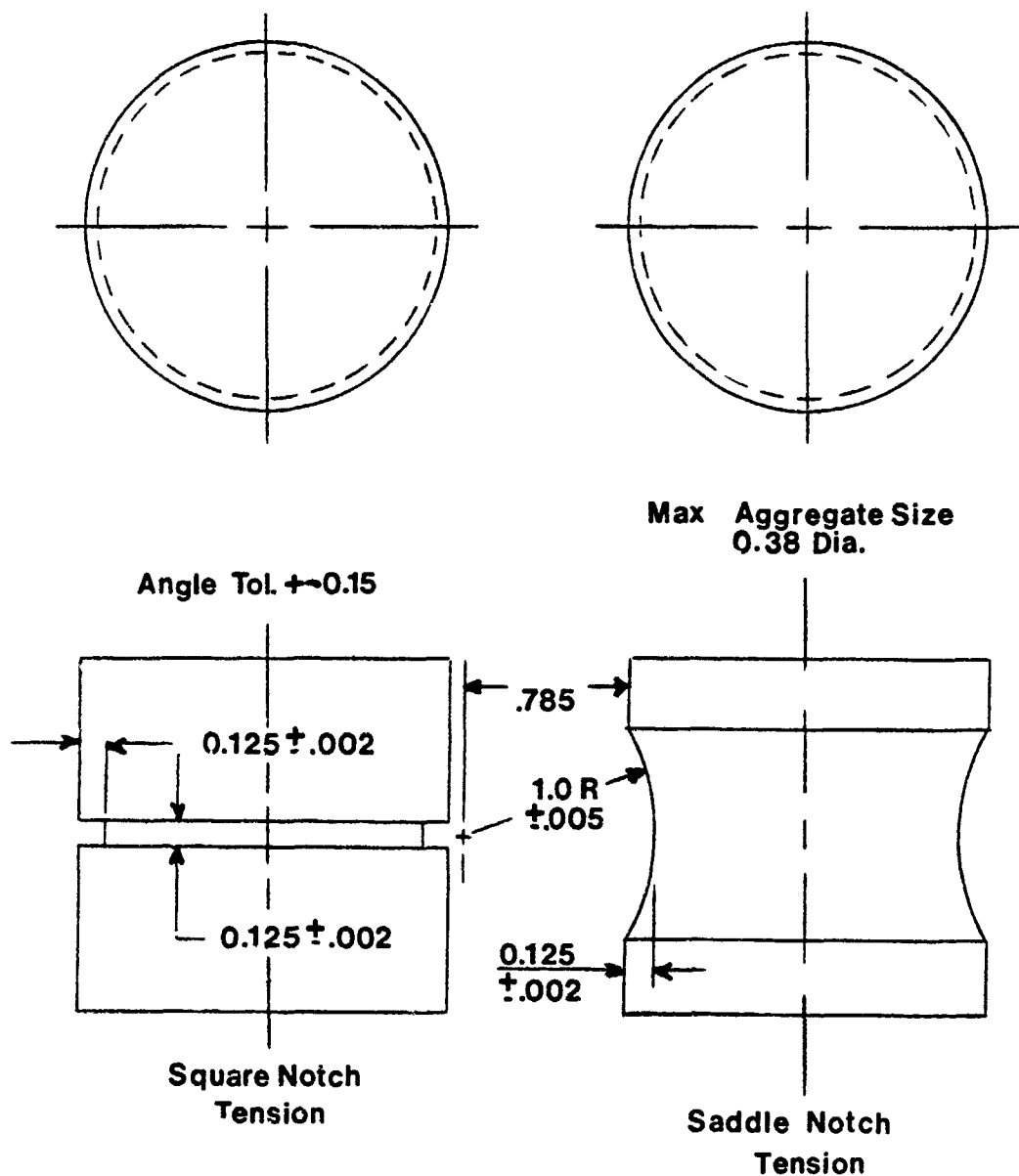


Figure 125. Direct tension specimens: (a) square notch, (b) saddle notch.

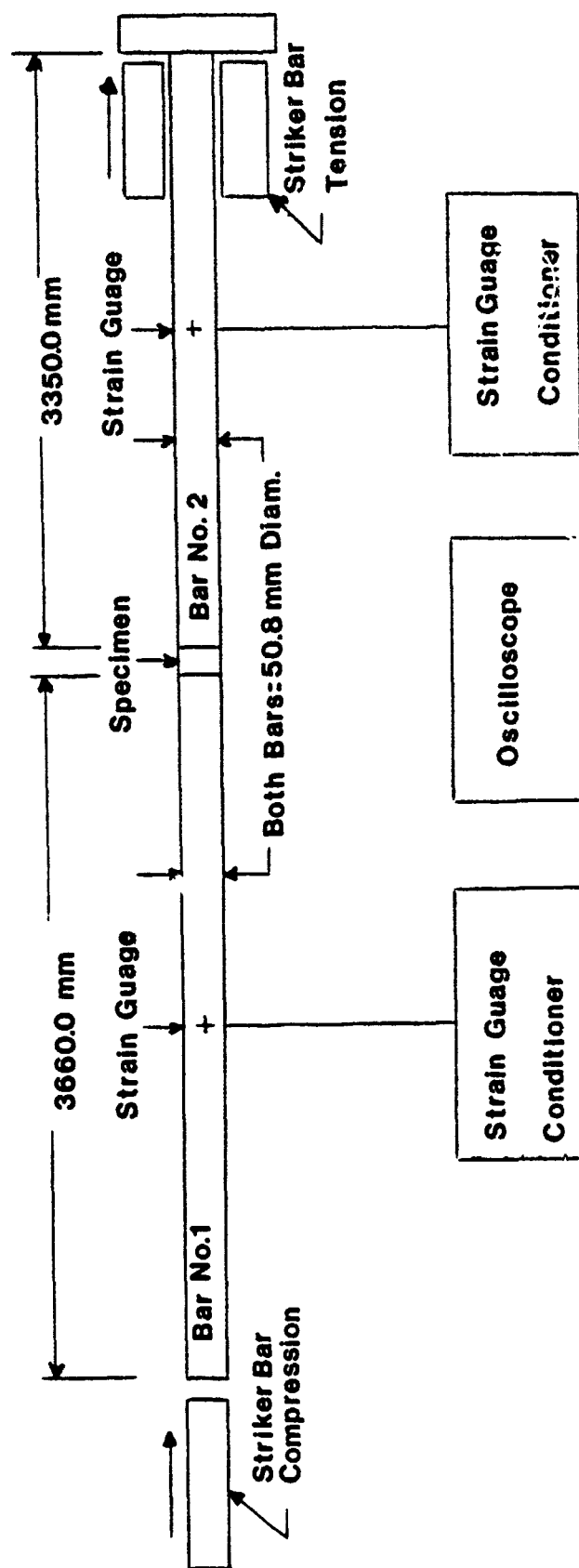


Figure 126. Schematic of Direct Tension SHPB.



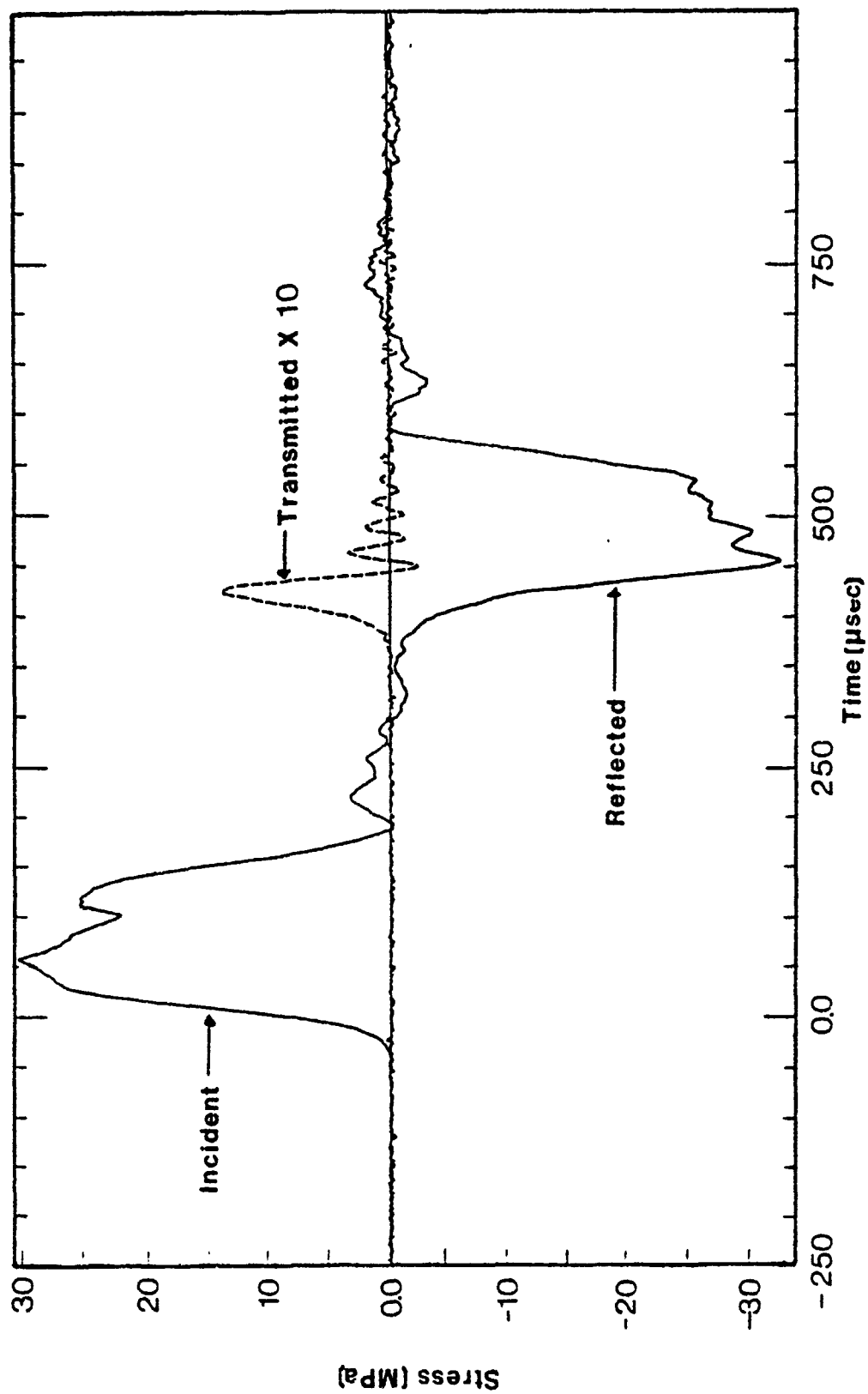


Figure 127. Square Notch Test Data Trace

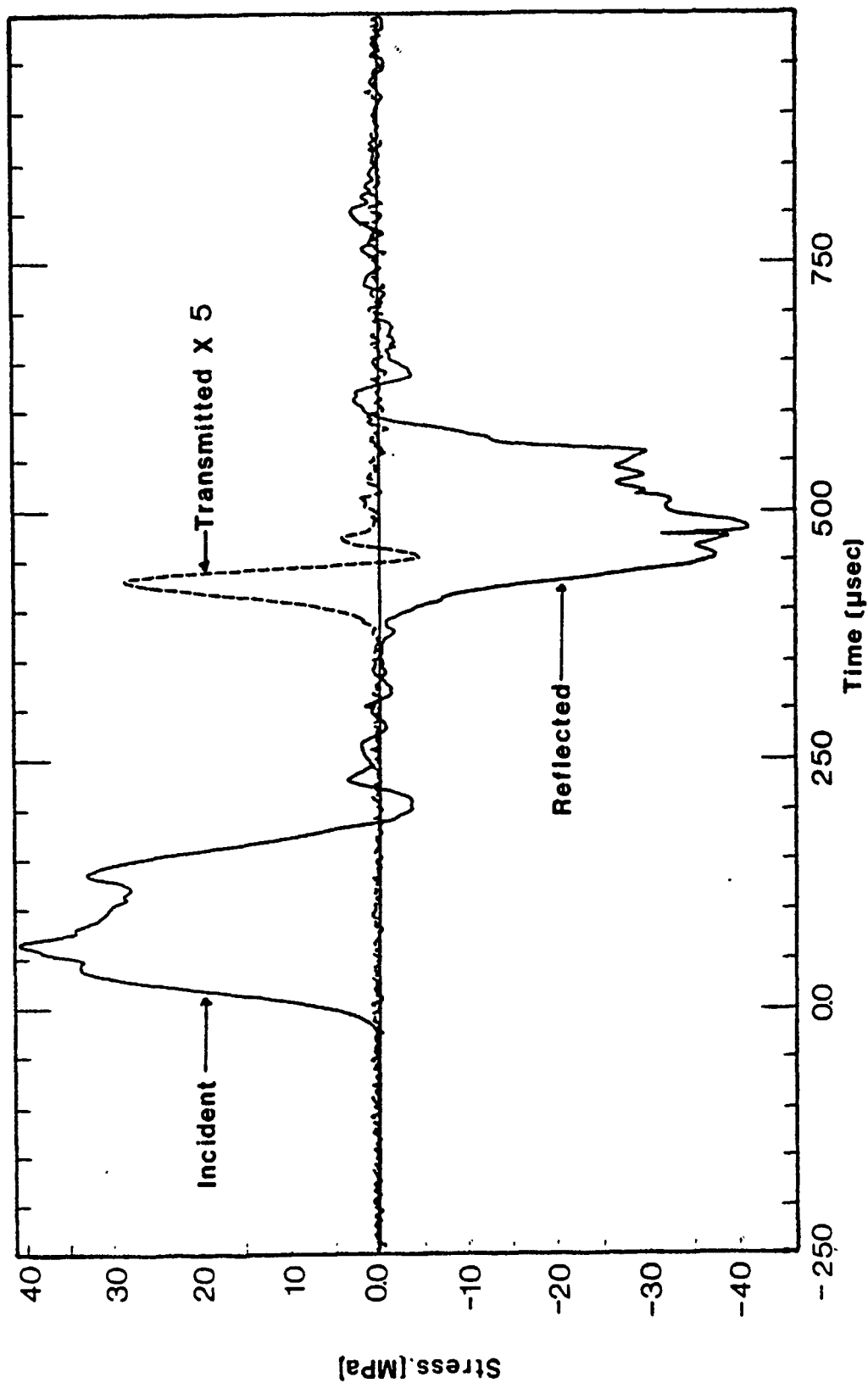


Figure 128. Saddle Notch Test Data Trace

## B. LINEAR ANALYSIS

### 1. The FEM Model

To provide an accurate numerical simulation of the SHPB direct tension tests, a detailed FEM model of the specimens and portions of the incident and transmitter bars was constructed. An illustration of the FEM model for the incident bar is presented in Figure 129. A 52-inch (1321 mm) segment of the incident bar was modeled with 1594 eight-node axisymmetric elements. A similar representation of the transmitter bar is presented in Figure 130. The FEM model of the square notch specimen is presented in Figure 131. It is comprised of 348 eight-node, axisymmetric elements. The FEM model of the saddle notch specimen is illustrated in Figure 132. It is comprised of 408 eight-node, axisymmetric elements. For each analysis, the incident and transmitter bars were joined with the appropriate specimen to provide a continuous FEM model. The longitudinal axis of the model is the z-axis, and the transverse axis is the y-axis.

### 2. Calibration of FEM Model

To verify the accuracy of the FEM model in simulating wave propagation, the transmitter bar portion of the model was subjected to a simple square-wave impulse. The intensity of the input wave was 1000 psi (6.9 MPa) and the duration was 50  $\mu$ sec. Time histories for the longitudinal stress,  $\sigma_z$ , at four locations along the length of the bar ( $z = 1$  inch (25.4 mm),  $z = 12$  inches (305 mm),  $z = 26$  inches (660 mm), and  $z = 51$  inches (1295 mm); where the origin is assumed at the input end of the incident bar) are presented in Figures 133 through 136. The results predicted by the numerical simulation correspond closely with experimentally recorded stress wave traces.

### 3. Square Notch Test

The loading condition for the square notch test was determined from the stress signal presented in Figure 127. The load function employed was a modified ramp loading, depicted in Figure 137. The peak pressure is  $P_0 = 5000$  psi (34.5 MPa), the rise time  $t_r = 47$   $\mu$ sec, the time of duration for uniform load  $t_d = 153$   $\mu$ sec, and the total load duration  $t_t = 200$   $\mu$ sec.

Time histories for the longitudinal stress,  $\sigma_z$ , at four locations along the longitudinal centerline of the specimen are presented in Figure 138. Time histories for the longitudinal stress at the notch roots are presented in

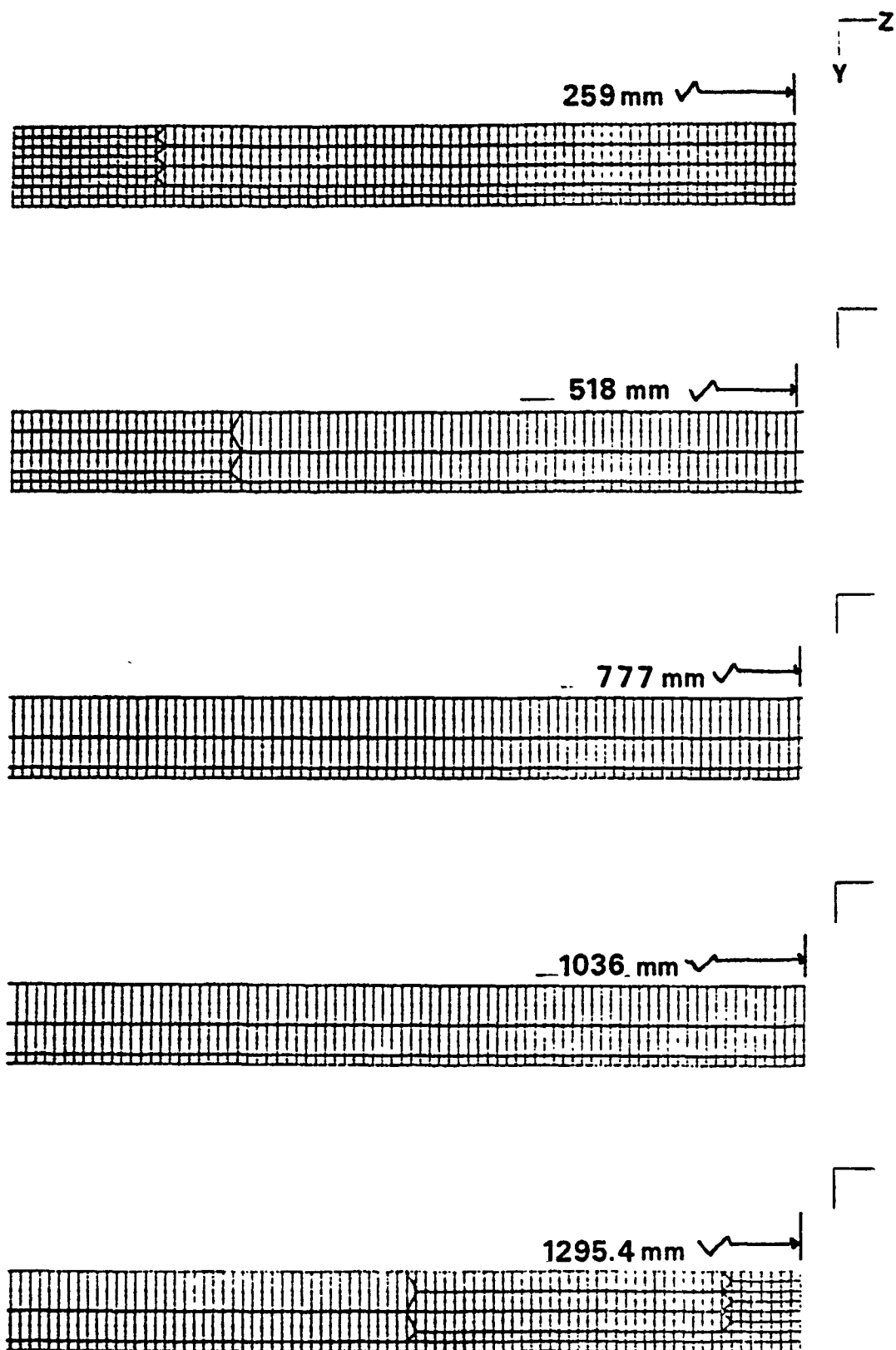


Figure 129. FEM Model of Incident Bar

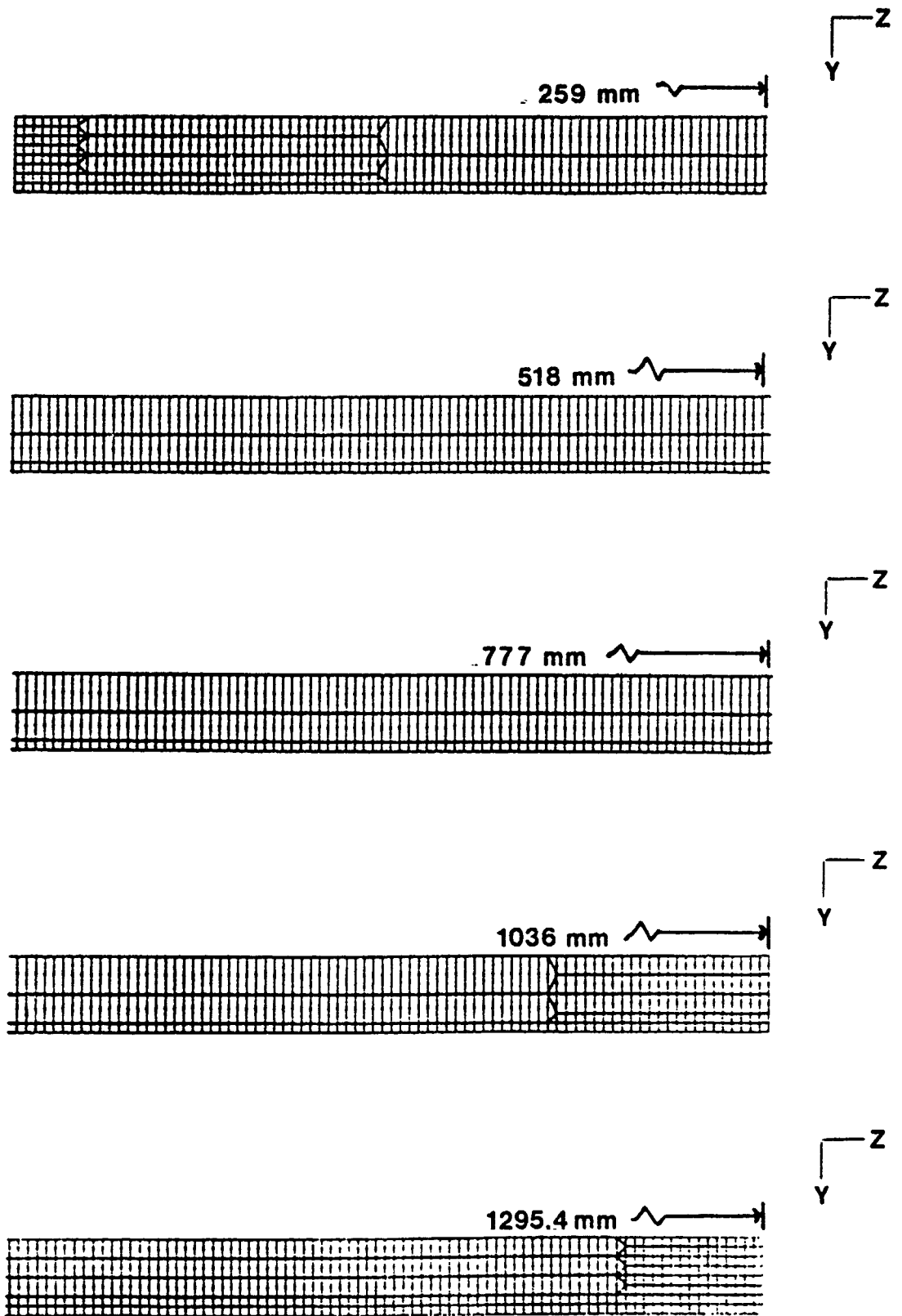


Figure 130. FEM Model of Transmitter Bar

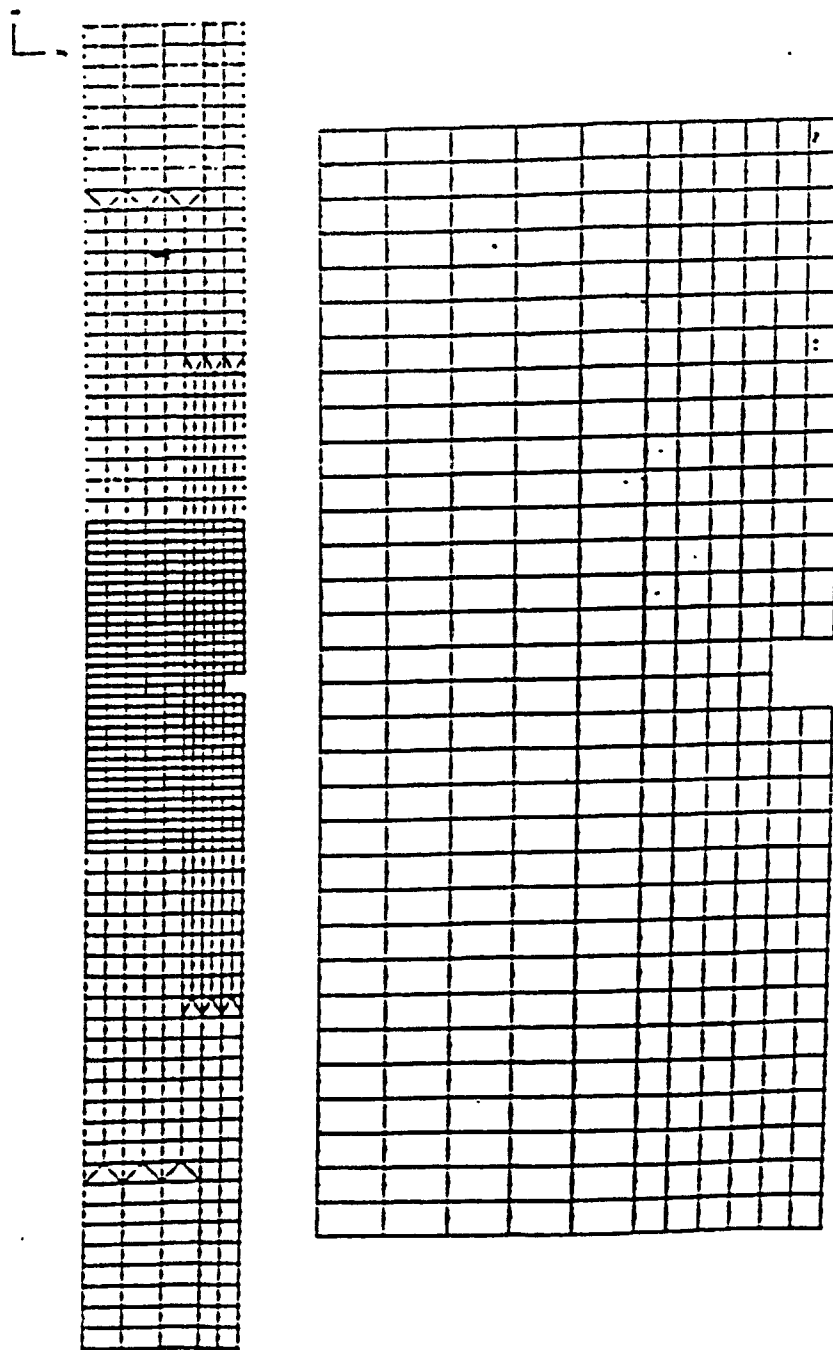


Figure 131. FEM Model of Square Notch Specimen

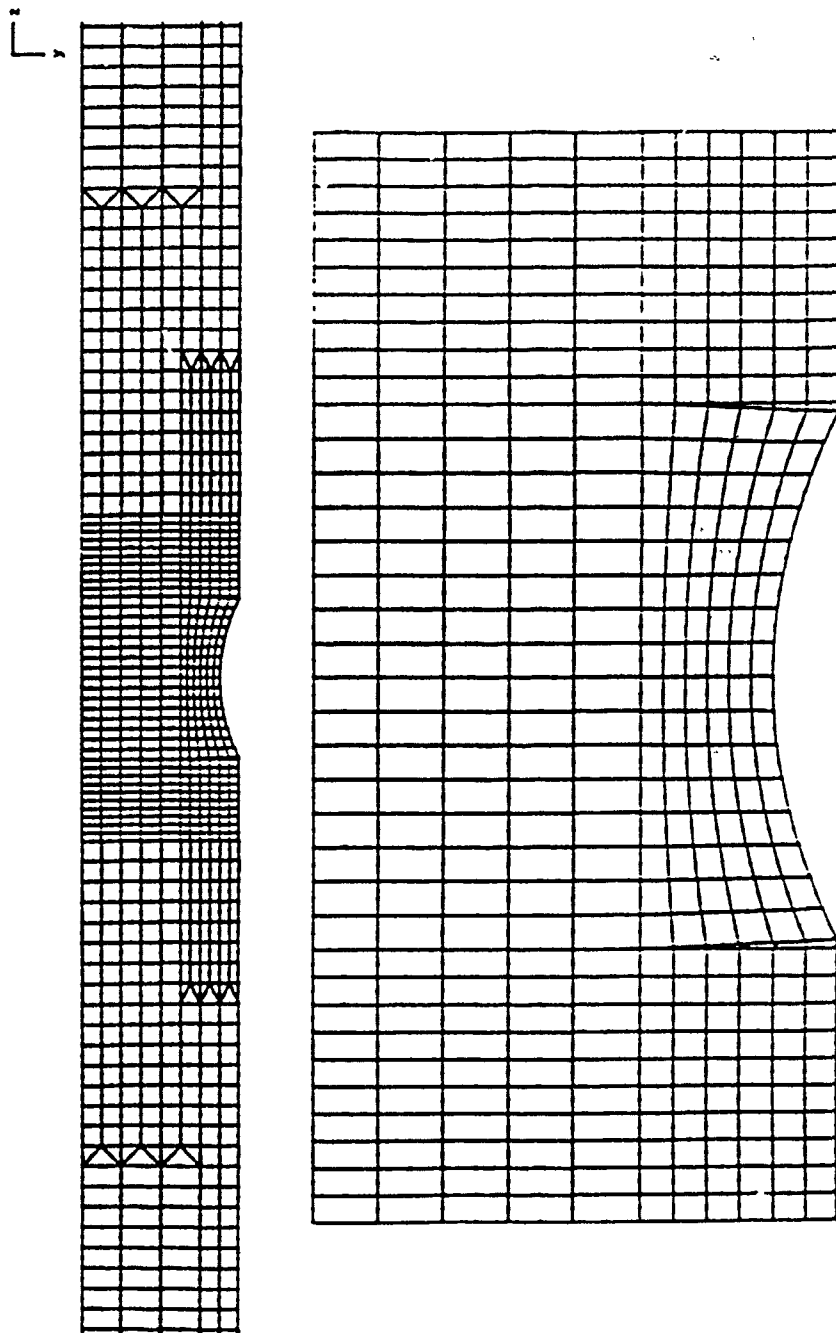


Figure 132. FEM Model of Square Notch Specimen

Surface Wave 25.4 mm From Input 1295.4 mm From Specimen

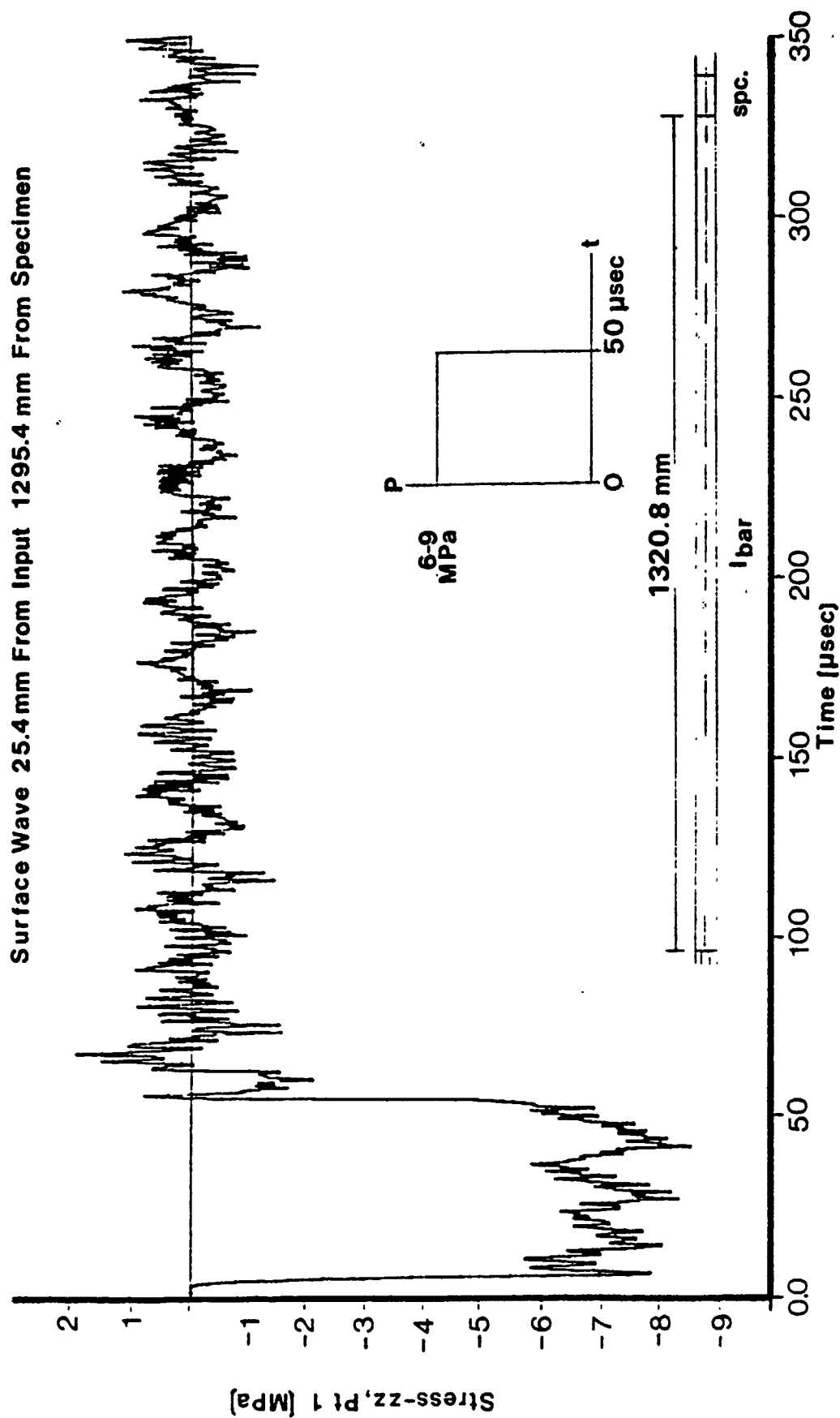


Figure 133. Time History for Longitudinal Stress at  $z = 1.0$  in.



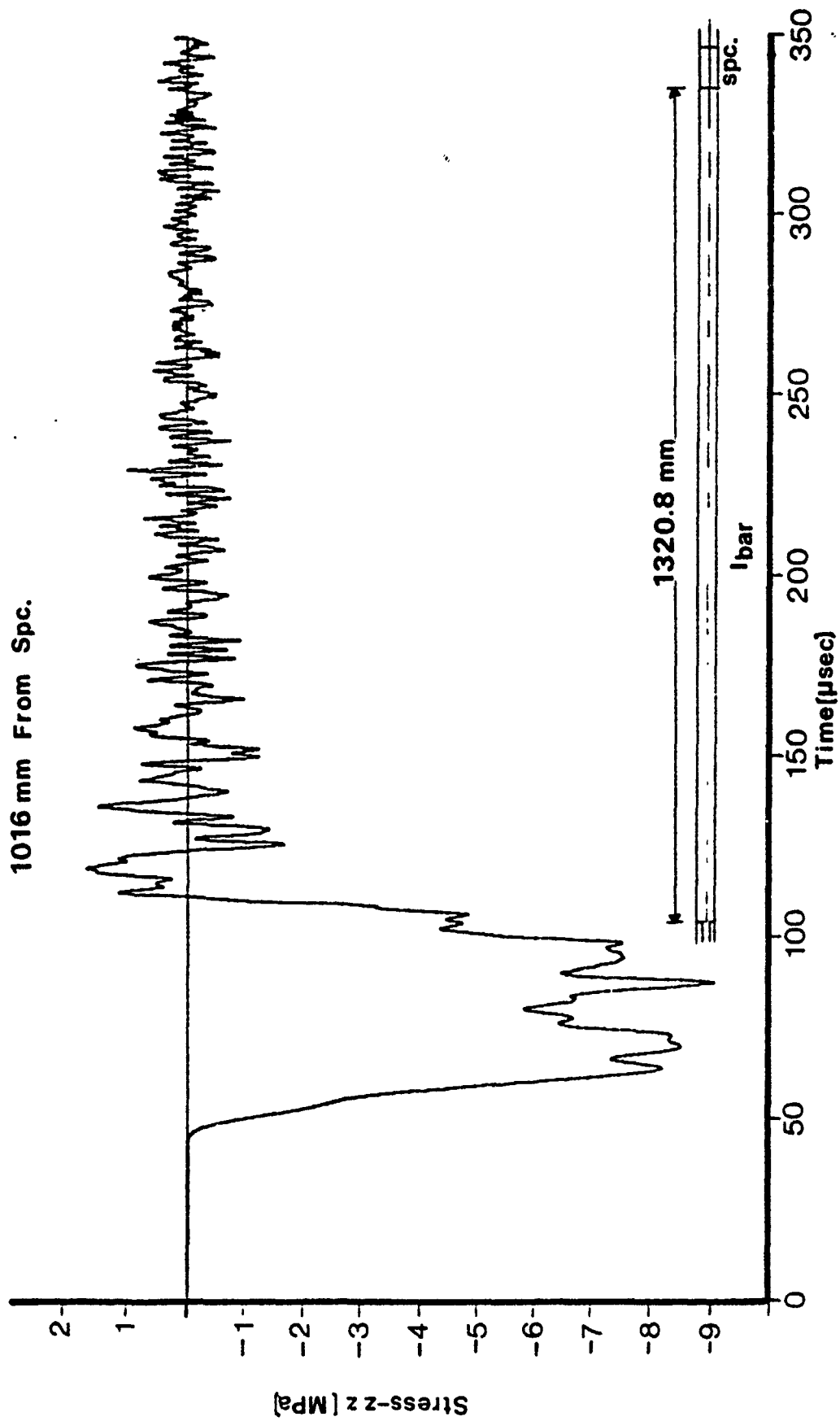


Figure 134. Time History for Longitudinal Stress at  $z = 12.0$  in.

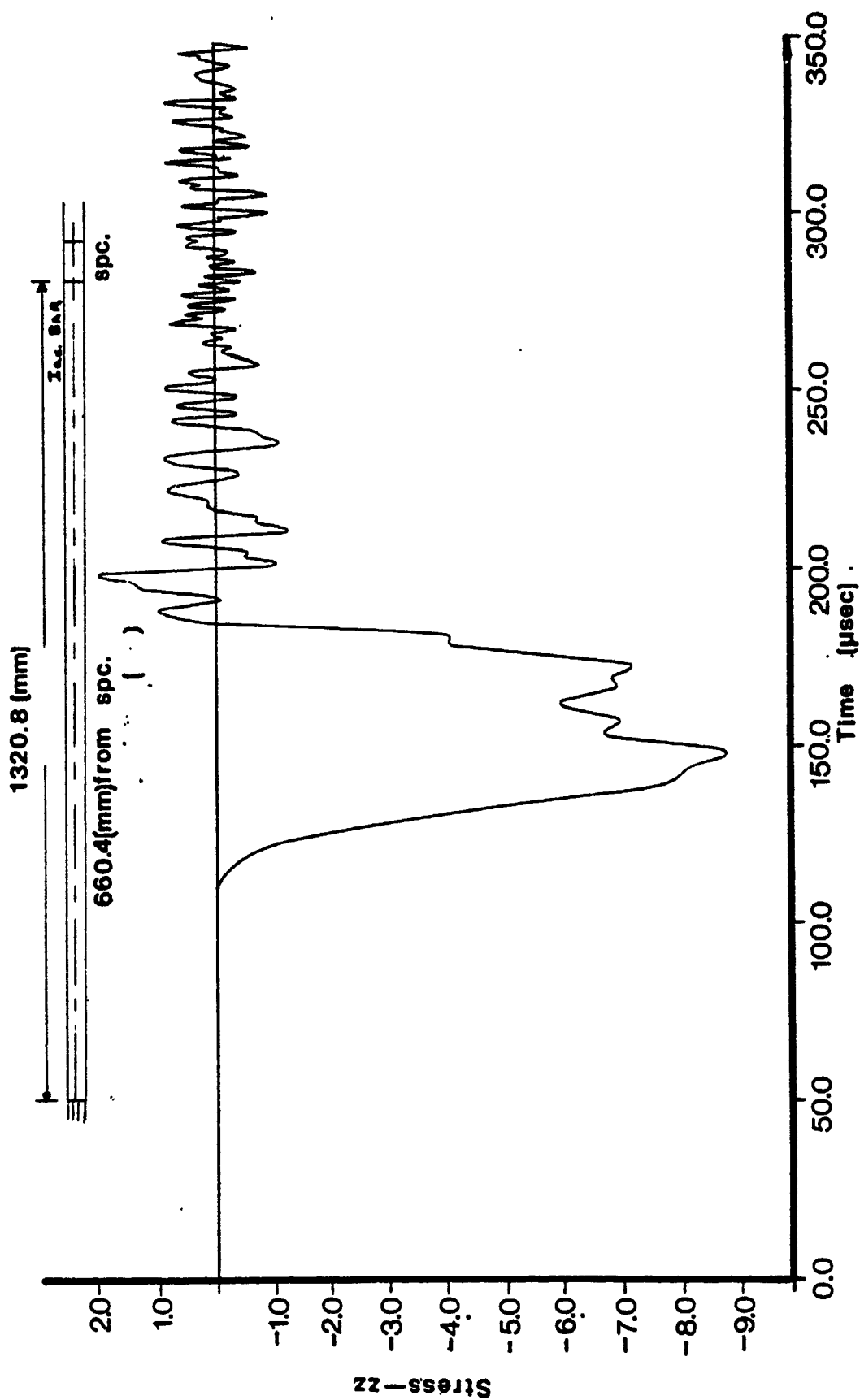


Figure 135. Time History for Longitudinal Stress, @  $z = 26.0$  in.

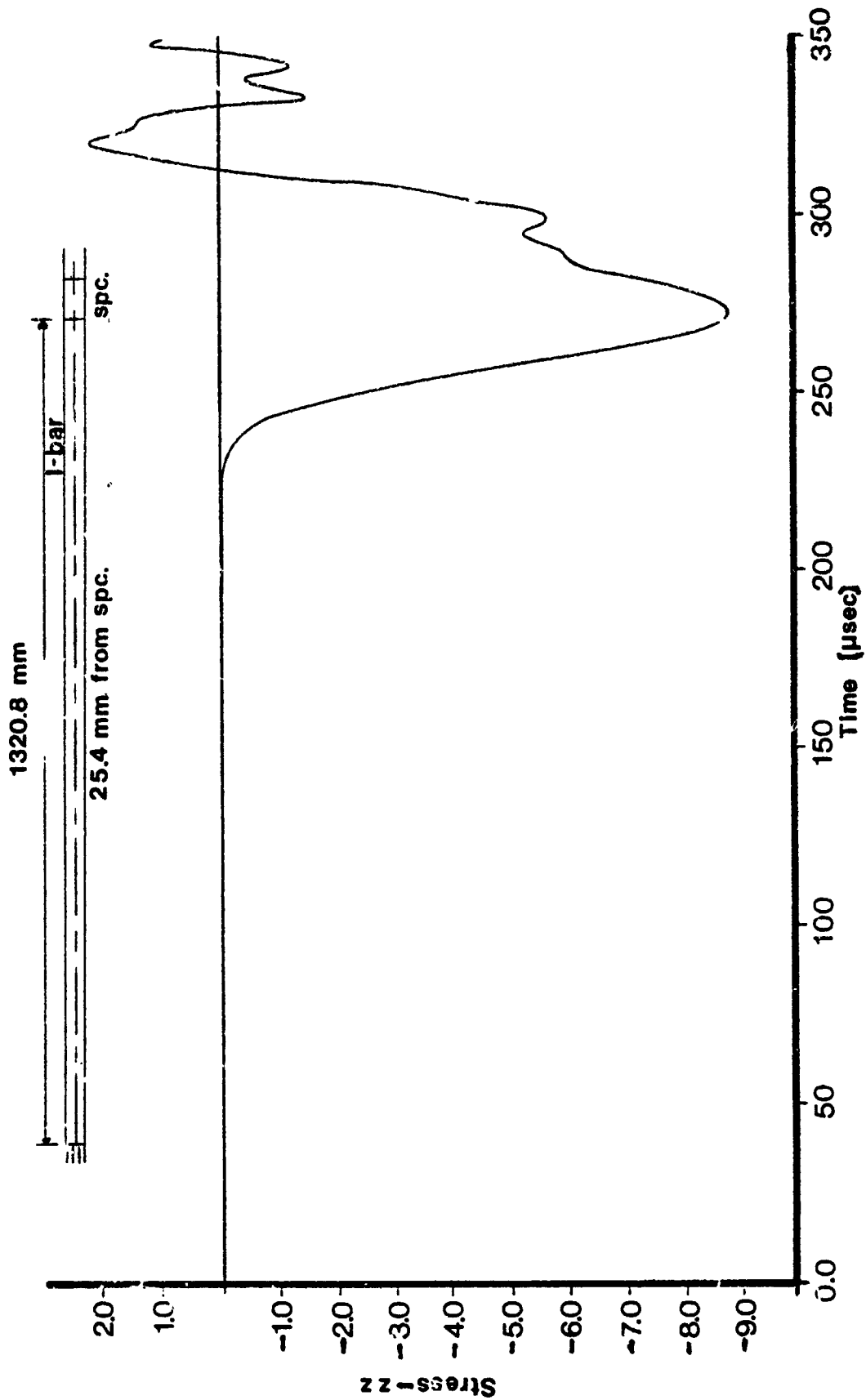


Figure 136. Time History for Longitudinal Stress @  $z = 51$  in.

Pressure

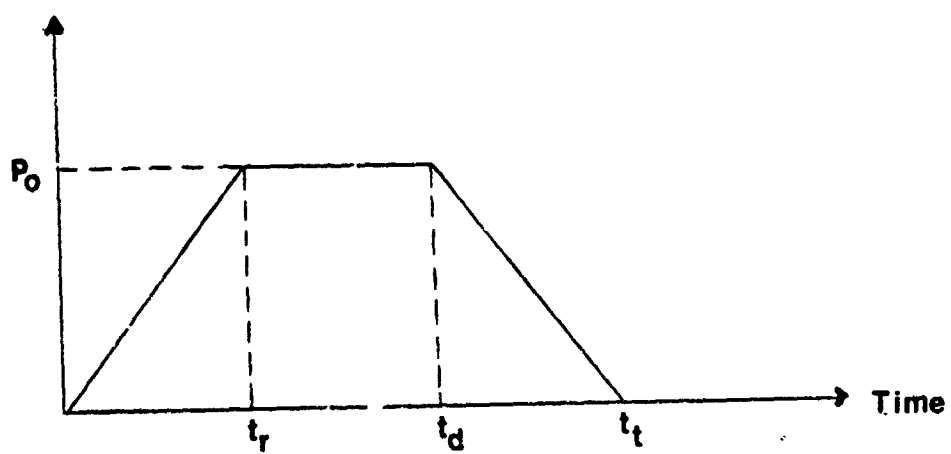


Figure 137. Modified ramp loading function used in FEM Analysis.

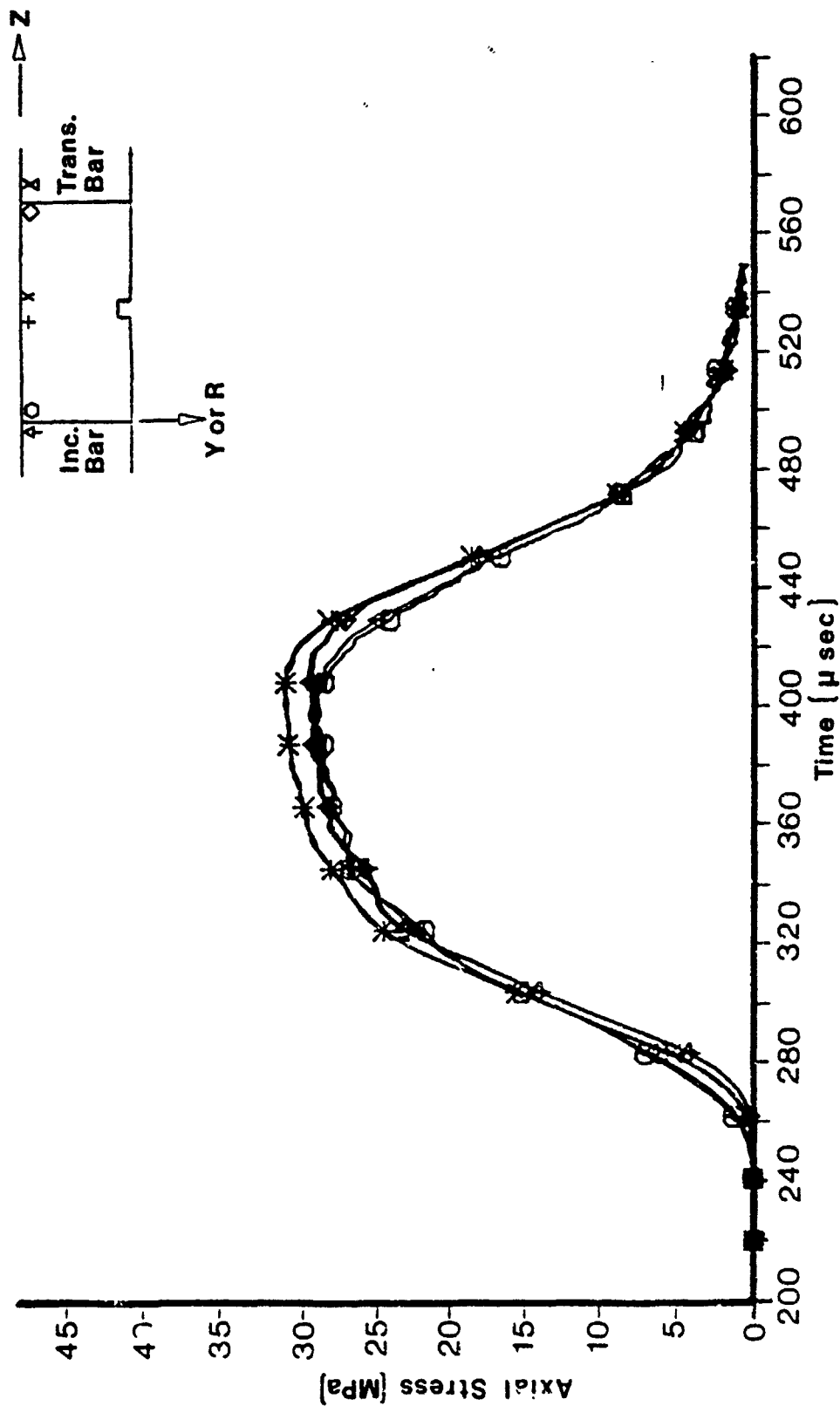


Figure 138. Time history for longitudinal stress along longitudinal centerline, square notch test.

Figure 139. Examination of these time histories suggests a stress concentrating factor of approximately 1.4 at the notch roots.

Profiles of the longitudinal stress,  $\sigma_z$ , along a transverse section passing through the notch roots are illustrated in Figures 140 and 141 for three selected time intervals ( $t = 270 \mu\text{sec}$ ,  $t = 300 \mu\text{sec}$ , and  $t = 420 \mu\text{sec}$ ). These profiles provide confirming evidence of the stress concentration at the notch roots.

#### 4. Saddle Notch Test

The saddle notch specimen was subjected to the same loading conditions as the square notch specimen. Time histories for the longitudinal stress,  $\sigma_z$ , at four locations along the longitudinal centerline of the specimen are presented in Figure 142. Time histories for the longitudinal stress at four locations along the outer surface of the specimen are illustrated in Figure 143. Examination of these time histories suggests a stress concentration factor of approximately 1.6 at the apex of the notch.

Profiles of the longitudinal stress,  $\sigma_z$ , along a transverse section passing through the center of the specimen are illustrated in Figure 144 for three selected time intervals ( $t = 260 \mu\text{sec}$ ,  $t = 290 \mu\text{sec}$ , and  $t = 350 \mu\text{sec}$ ). These profiles provide confirmation of stress concentration at the apex of the notch.

### C. NONLINEAR ANALYSIS

#### 1. Introduction

The concrete material model employed in the nonlinear analysis is a hypoelastic model based upon the uniaxial stress-strain relation depicted in Figure 48. The tension failure envelope illustrated in Figure 49 was incorporated in the concrete model. The pertinent material parameters for the failure envelope and the uniaxial stress-strain relation are summarized in Table 6.

#### 2. Square Notch Test

Time histories for the longitudinal stress,  $\sigma_z$ , and the longitudinal strain,  $\epsilon_z$ , for three longitudinal locations along the exterior surfaces of the specimen are illustrated in Figures 145, 146, and 147, for  $z = 0$ ,  $z = L/2$ , and  $z = L$ , respectively (where  $L$  is the length of the specimen and  $z$  is measured from the face of the incident bar). Time histories for  $\sigma_z$  and  $\epsilon_z$  at the same locations along the longitudinal axis of symmetry are presented in Figures 148,

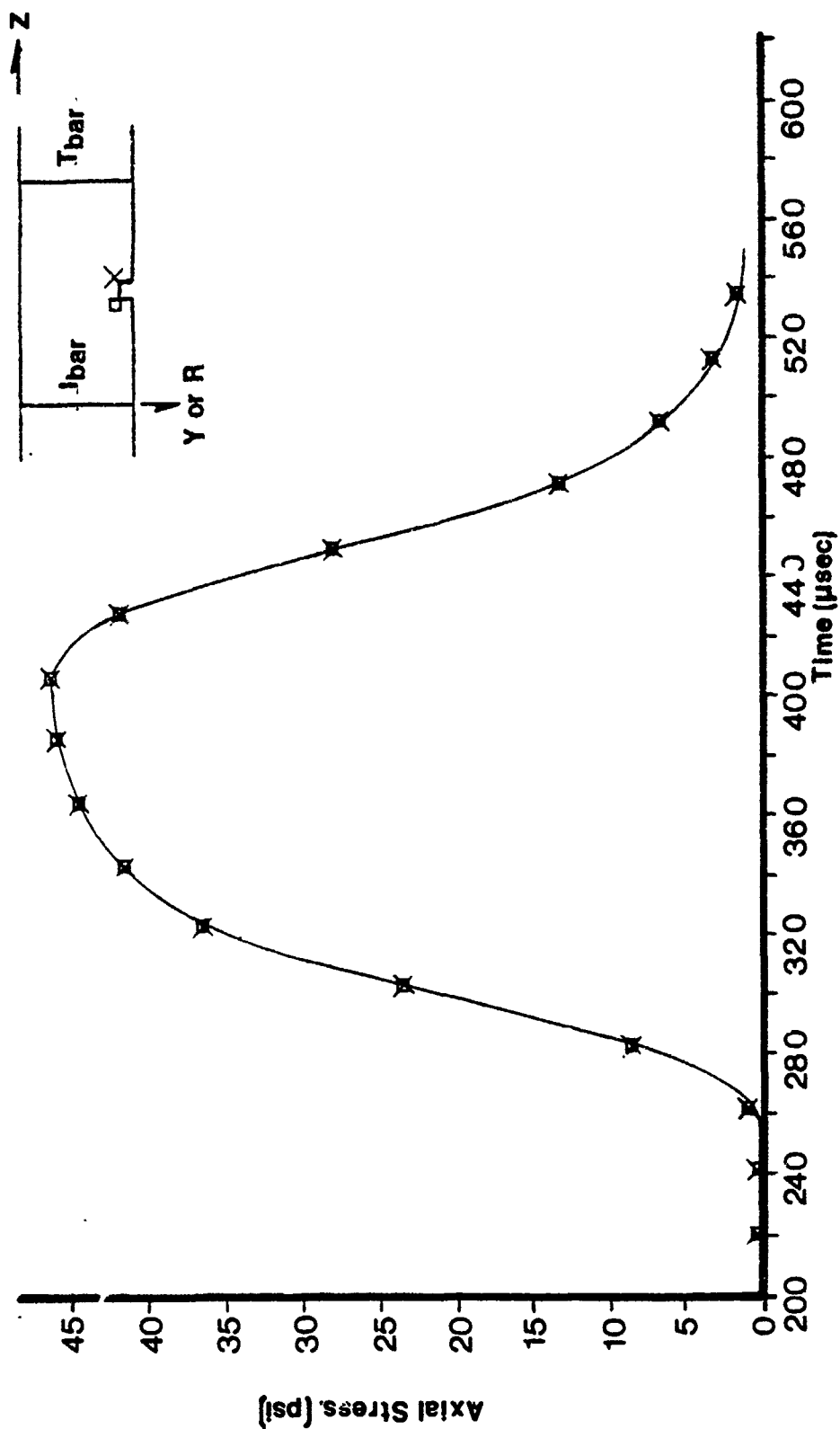


Figure 139. Time histories for longitudinal stress at the notch roots, square notch test.

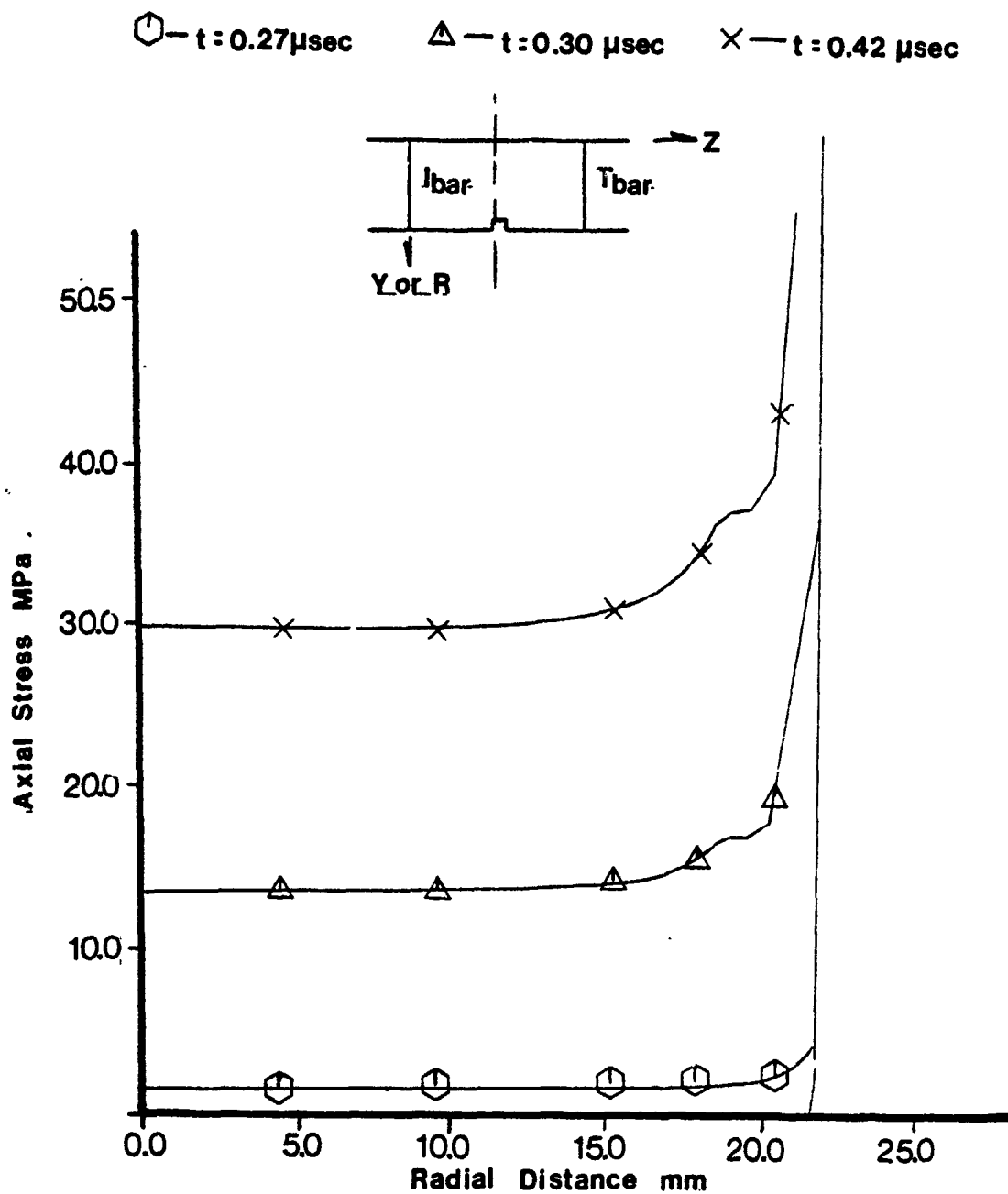


Figure 140. Profiles of longitudinal stress along a transverse plane through the notch root.



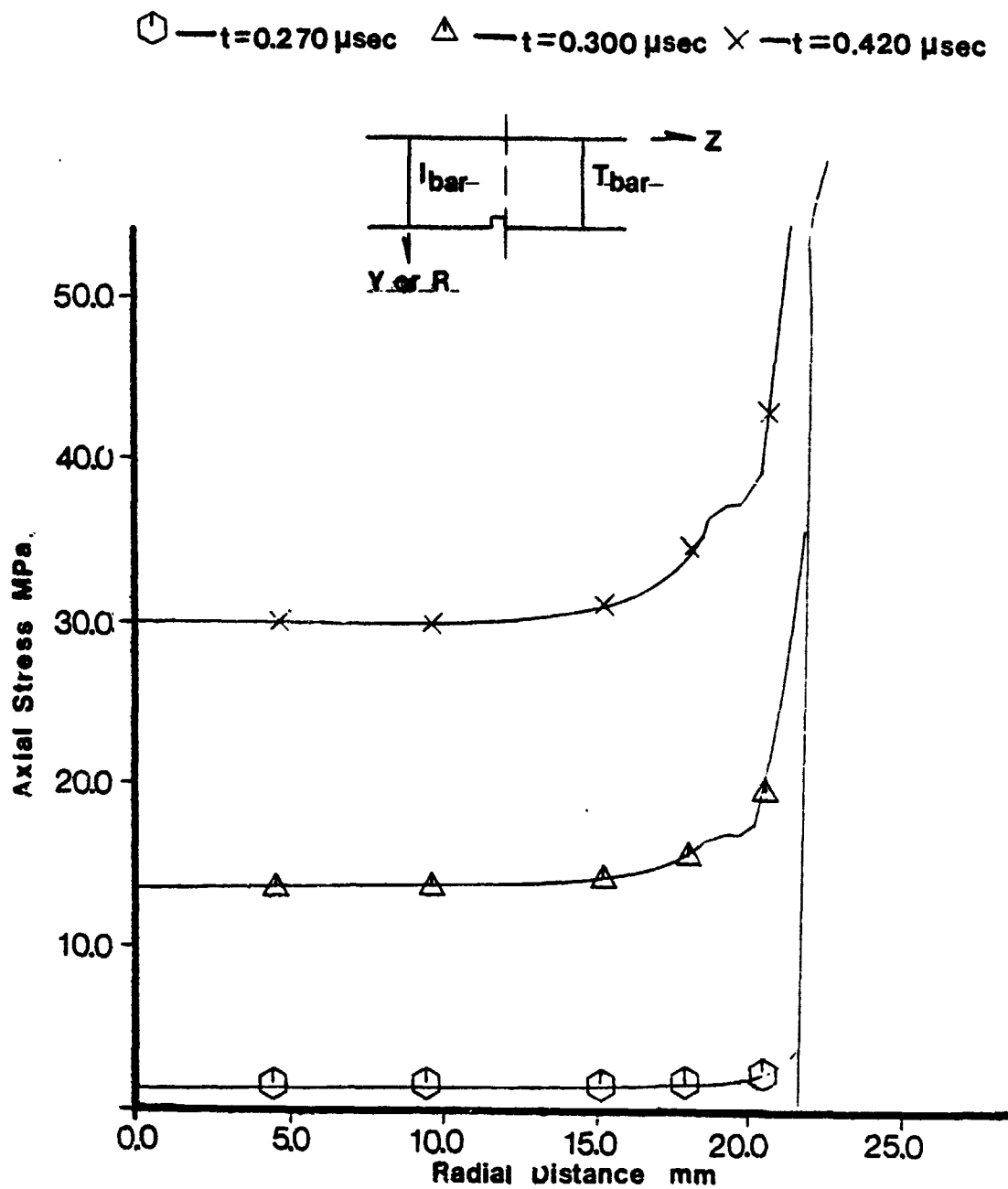


Figure 141. Profiles of longitudinal stress along a transverse plane through the notch root.

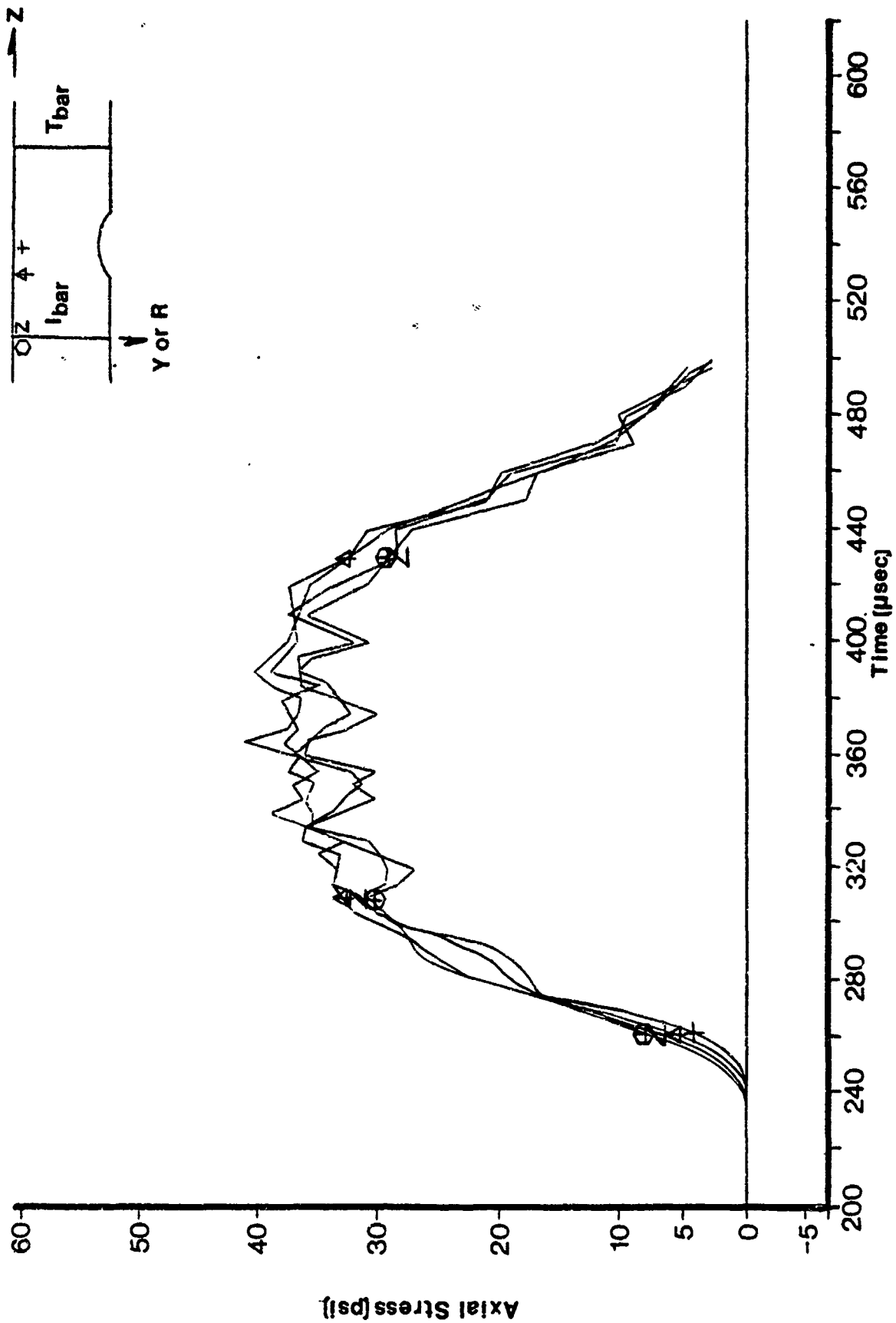


Figure 142. Time histories for longitudinal stress along the longitudinal centerline, saddle notch test.

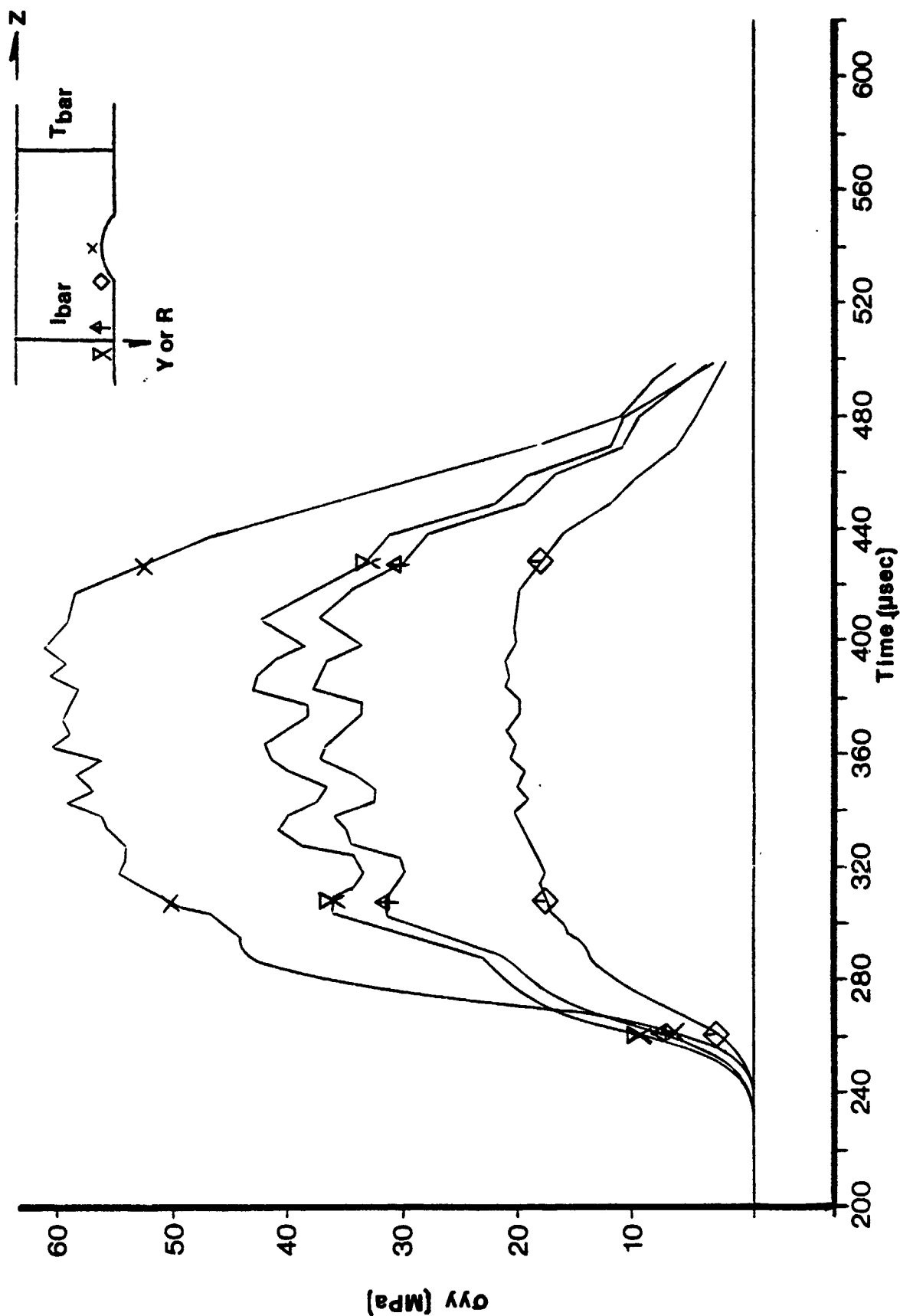


Figure 143. Time histories for longitudinal stress in the vicinity of the notch, saddle notch test.

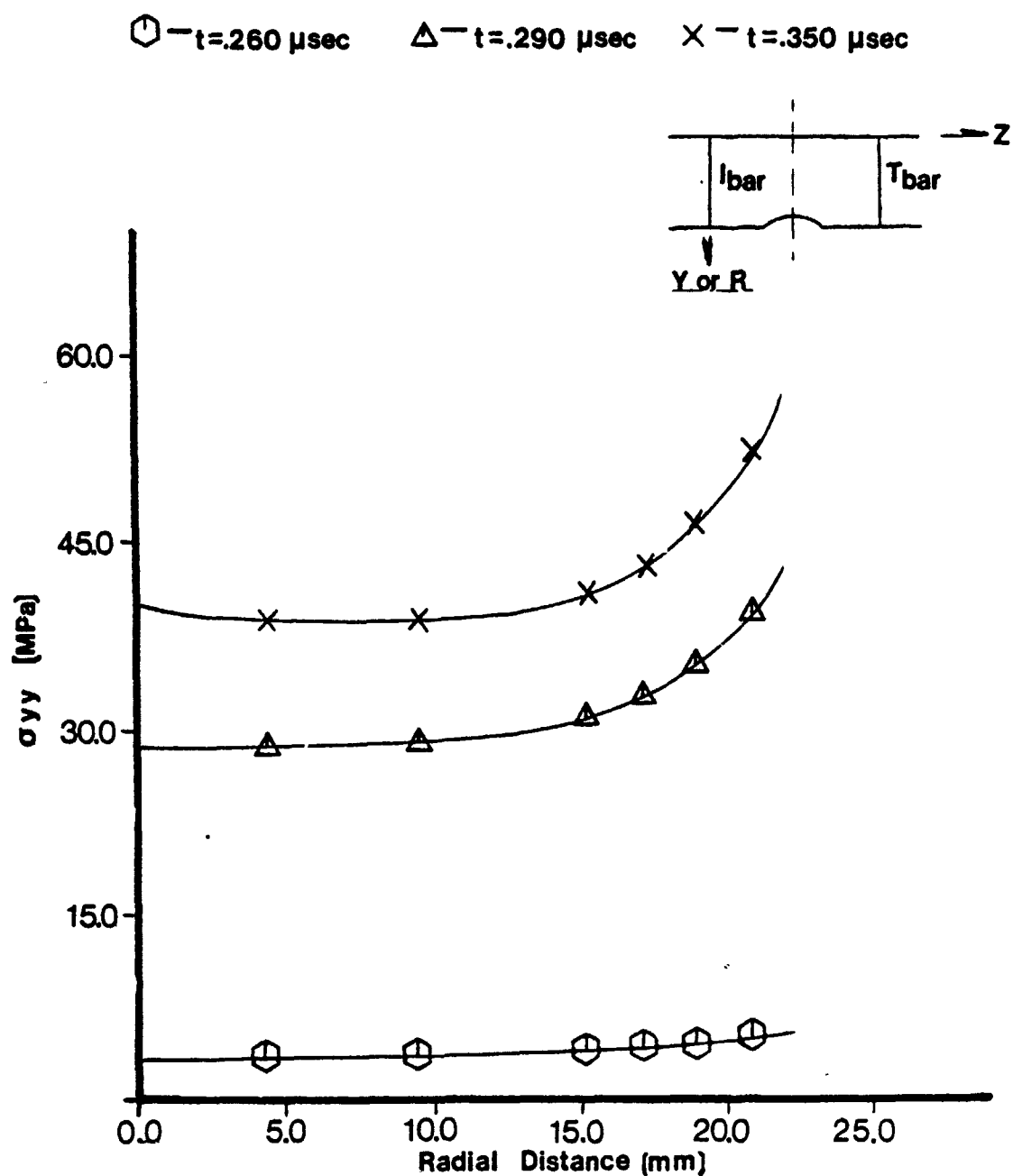


Figure 144. Profiles of the longitudinal stress along a transverse plane through the notch.

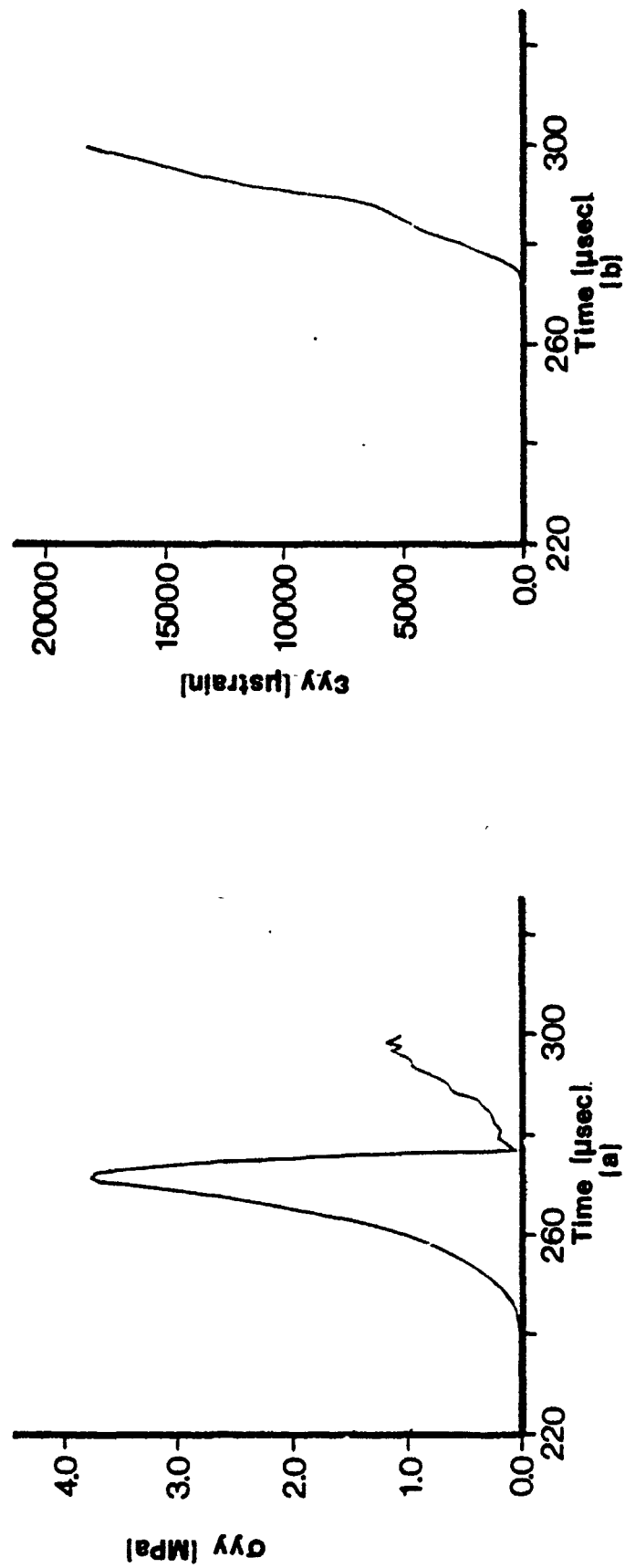


Figure 145. Time histories for (a) longitudinal stress and (b) longitudinal strain along the exterior surface, nonlinear analysis, square notch,  $z = 0$ .

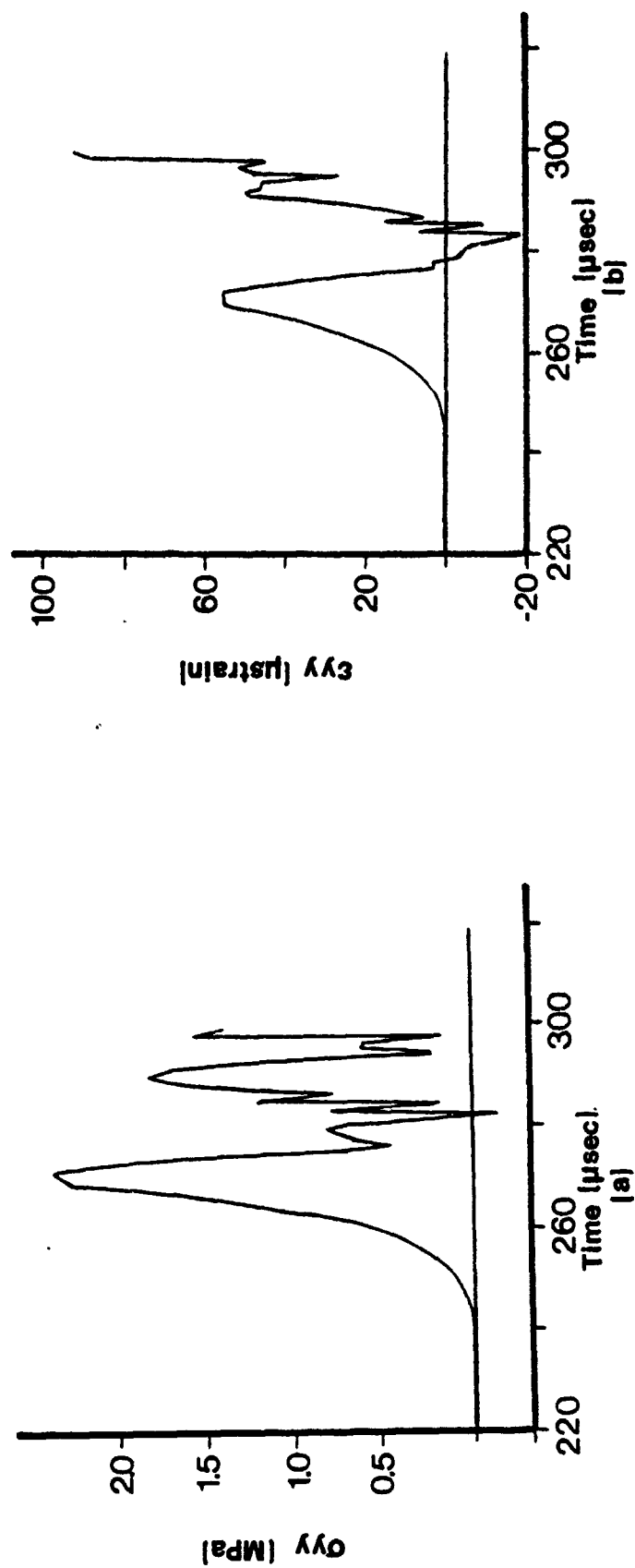
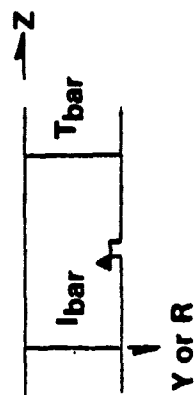


Figure 146. Time histories for (a) longitudinal stress and (b) longitudinal strain along the exterior surface, nonlinear analysis, square notch,  $z = L/2$ .

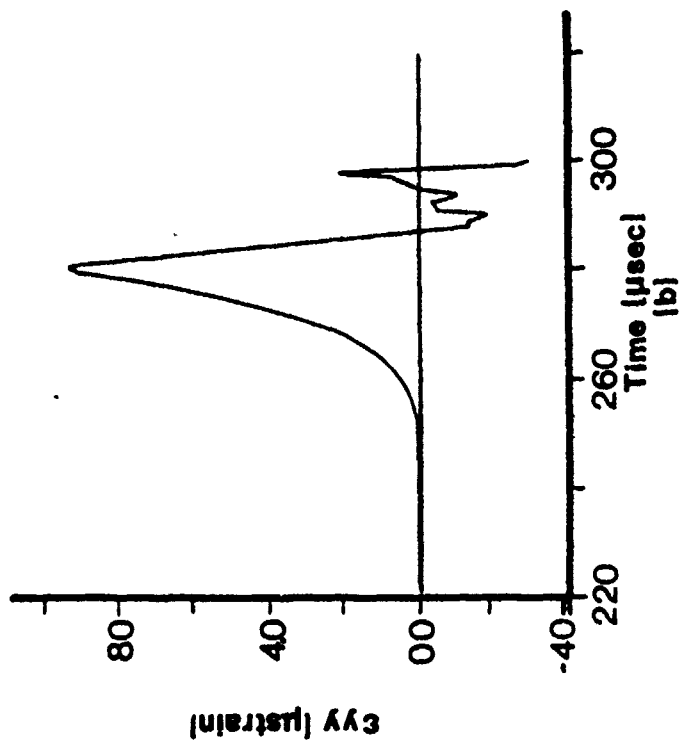
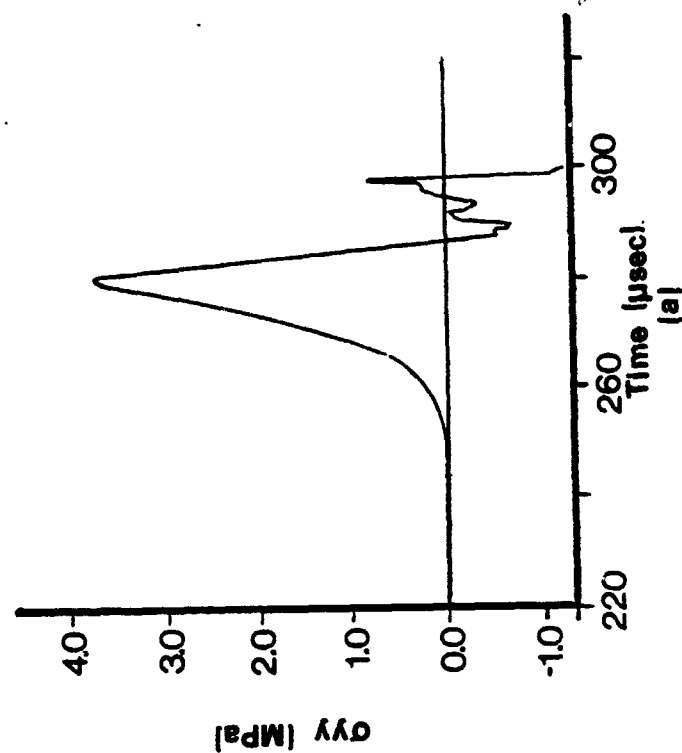
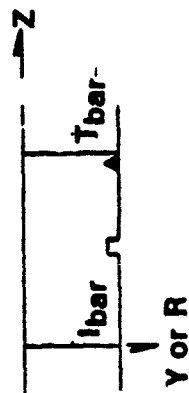


Figure 147. Time histories for (a) longitudinal stress and (b) longitudinal strain along the exterior surface, nonlinear analysis, square notch,  $z = L$ .

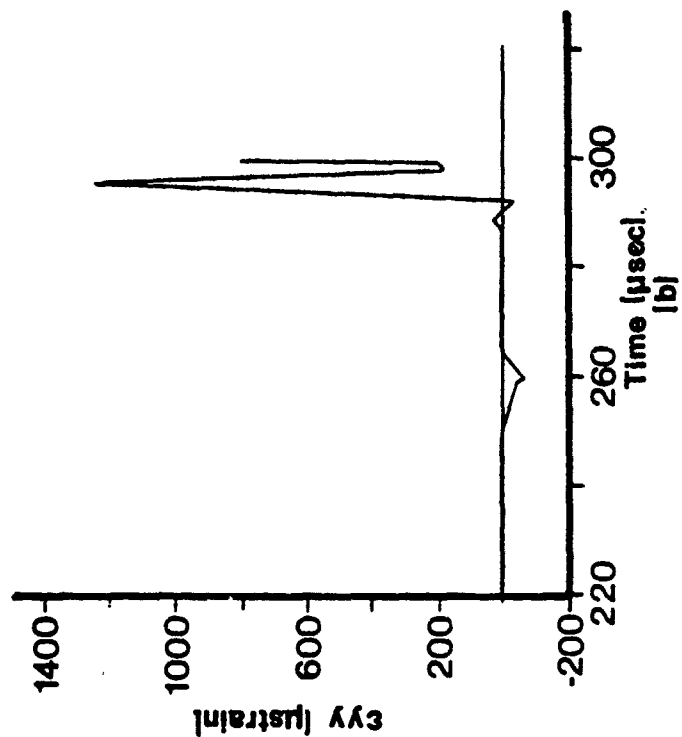
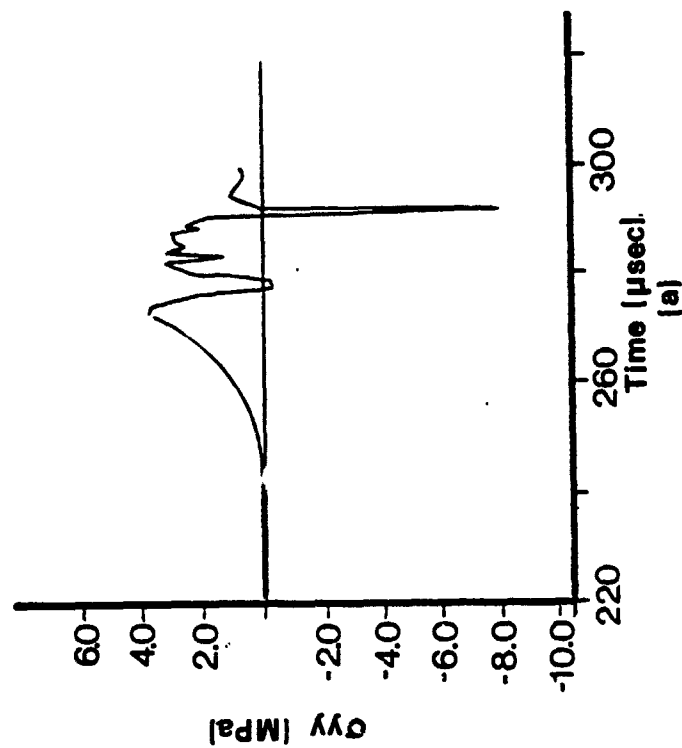
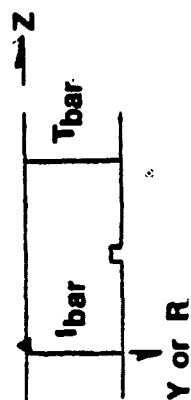


Figure 148. Time histories for (a) longitudinal stress and (b) longitudinal strain along the axis of symmetry, nonlinear analysis, square notch,  $z = 0$ .



149, and 150, respectively. The maximum stresses and strain rates predicted at each of these locations are summarized in Table 9.

TABLE 9. MAXIMUM STRESSES AND STRAIN RATES  
AT SELECTED LOCATIONS  
(SQUARE NOTCH TEST)

Location	$(\sigma_z)_{\max}$ psi (MPa)	$\dot{\epsilon}_z$ ( $\text{sec}^{-1}$ )
$y = \frac{D}{2}, z = 0$	546 (3.77)	5.35
$y = \frac{D}{2}, z = \frac{L}{2}$	348 (2.40)	4.14
$y = \frac{D}{2}, z = L$	535 (3.69)	6.12
$y = 0, z = 0$	542 (3.74)	4.49
$y = 0, z = \frac{L}{2}$	555 (3.83)	3.2
$y = 0, z = L$	535 (3.69)	4.98
Transmitter Bar	589 (4.06)	2.57

Profiles of the longitudinal stress,  $\sigma_z$ , for three selected times at three locations transverse to the longitudinal axis ( $z = 0$ ,  $z = L/2$ , and  $z = L$ ) are illustrated in Figures 151, 152, and 153, respectively. Cracking in the specimen at the root of the notch and at the specimen incident bar interface is evidenced in Figures 152 and 151, respectively.

The cracking sequence simulated by the numerical analysis, from initiation of the first crack until failure, is illustrated in Figures 154, 155, and 156. The first cracking in the specimen occurs at the roots of the notch at time  $t = 270 \mu\text{sec}$  (Figure 154). This is consistent with the stress

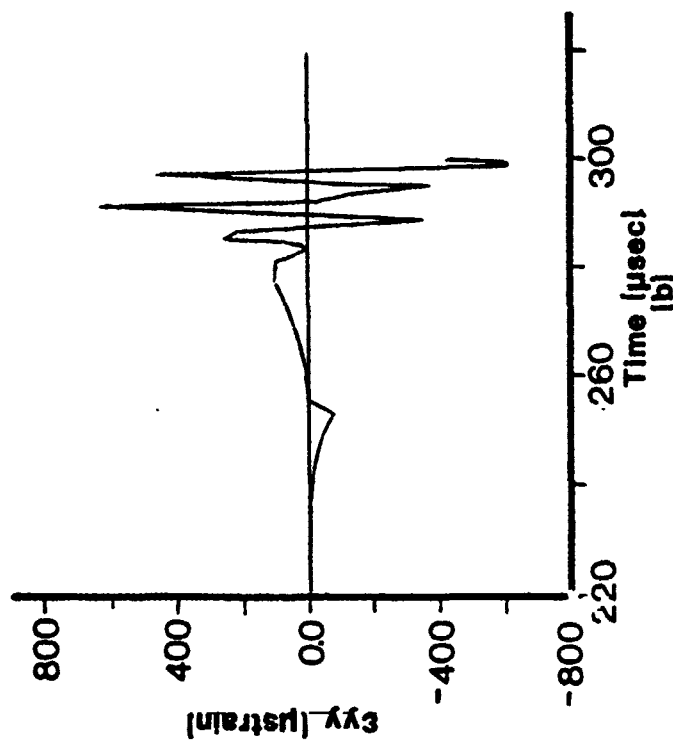
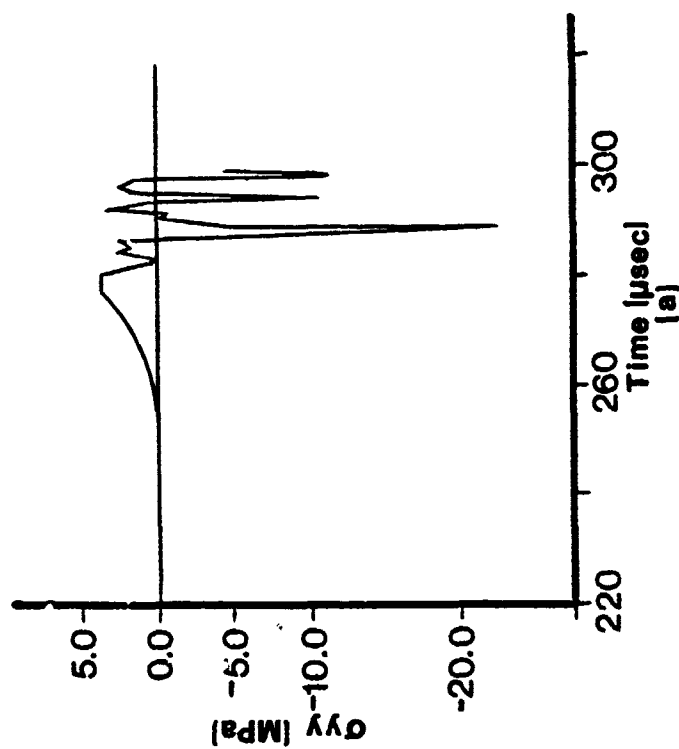
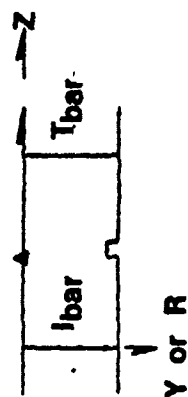


Figure 149. Time histories for (a) longitudinal stress and (b) longitudinal strain along the axis of symmetry, nonlinear analysis, square notch,  $z = L/2$ .

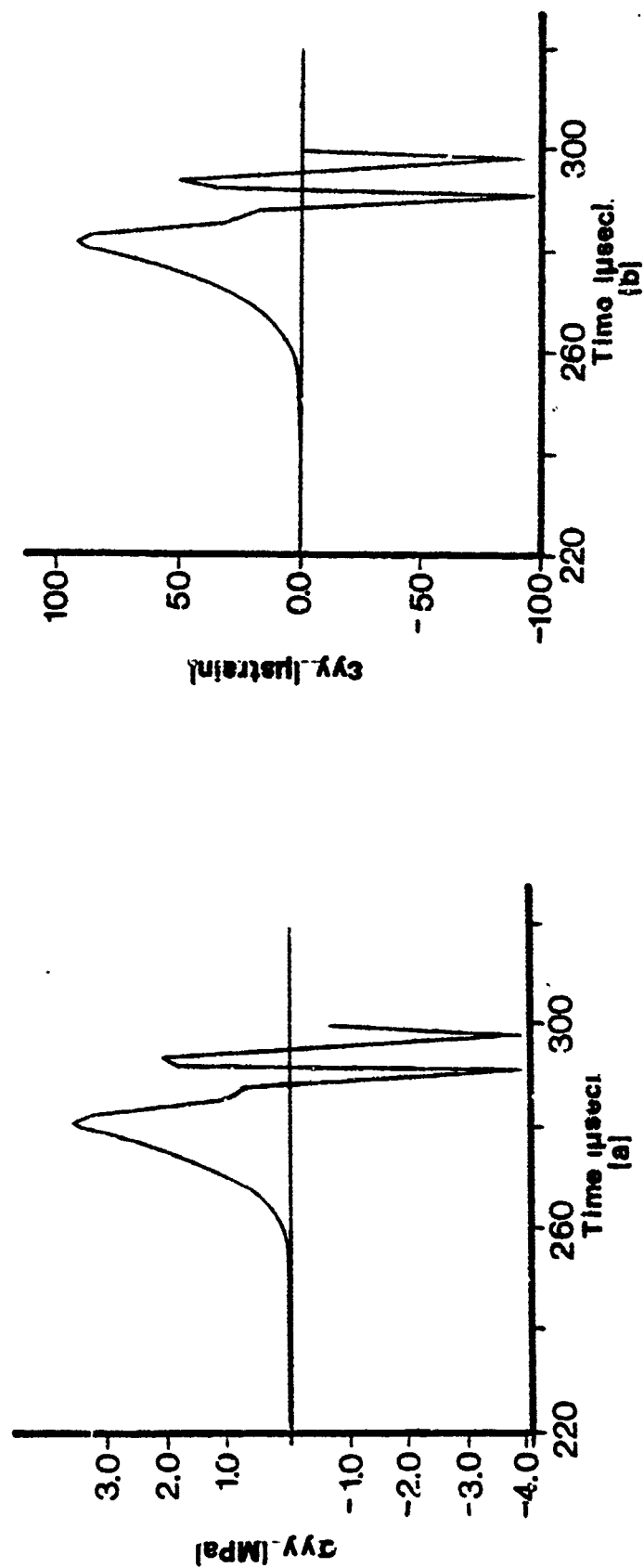


Figure 150. Time histories for (a) longitudinal stress and (b) longitudinal strain along the axis of symmetry, nonlinear analysis, square notch,  $z = L$ .

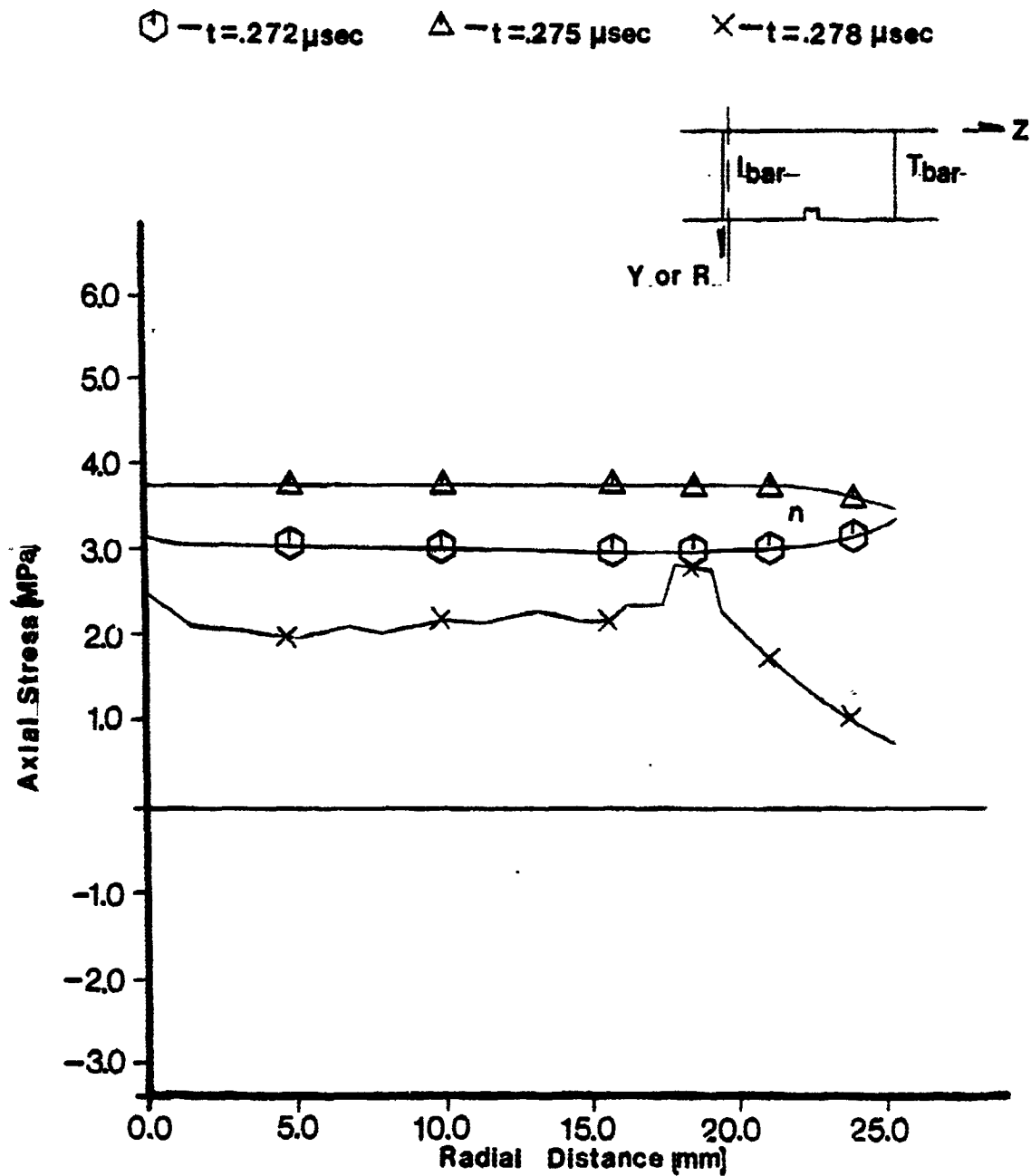


Figure 151. Profiles for longitudinal stress transverse to the longitudinal axis, nonlinear analysis, square notch,  $z = 0$ .

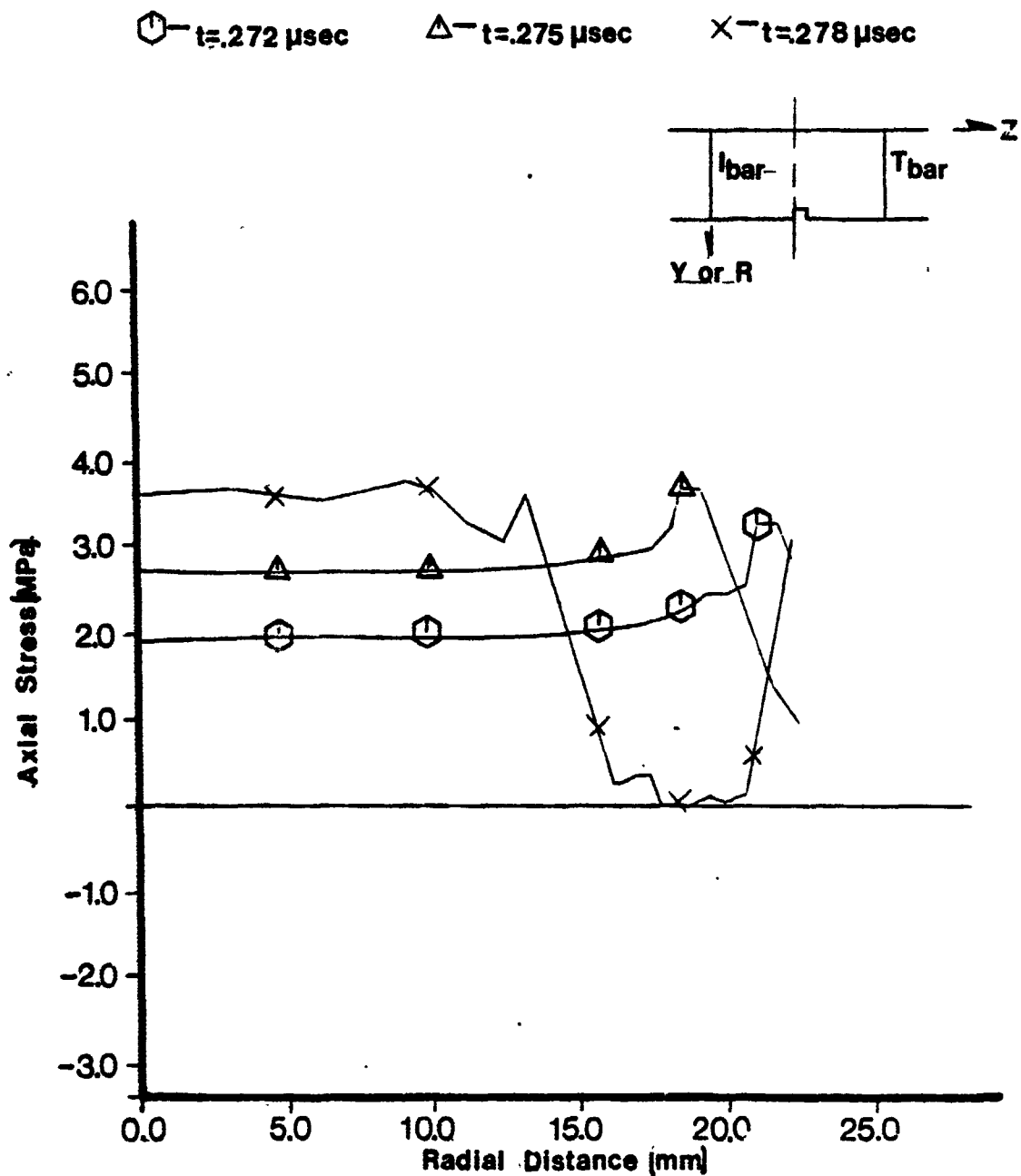


Figure 152. Profiles for longitudinal stress transverse to the longitudinal axis, nonlinear analysis, square notch,  $z = L/2$ .

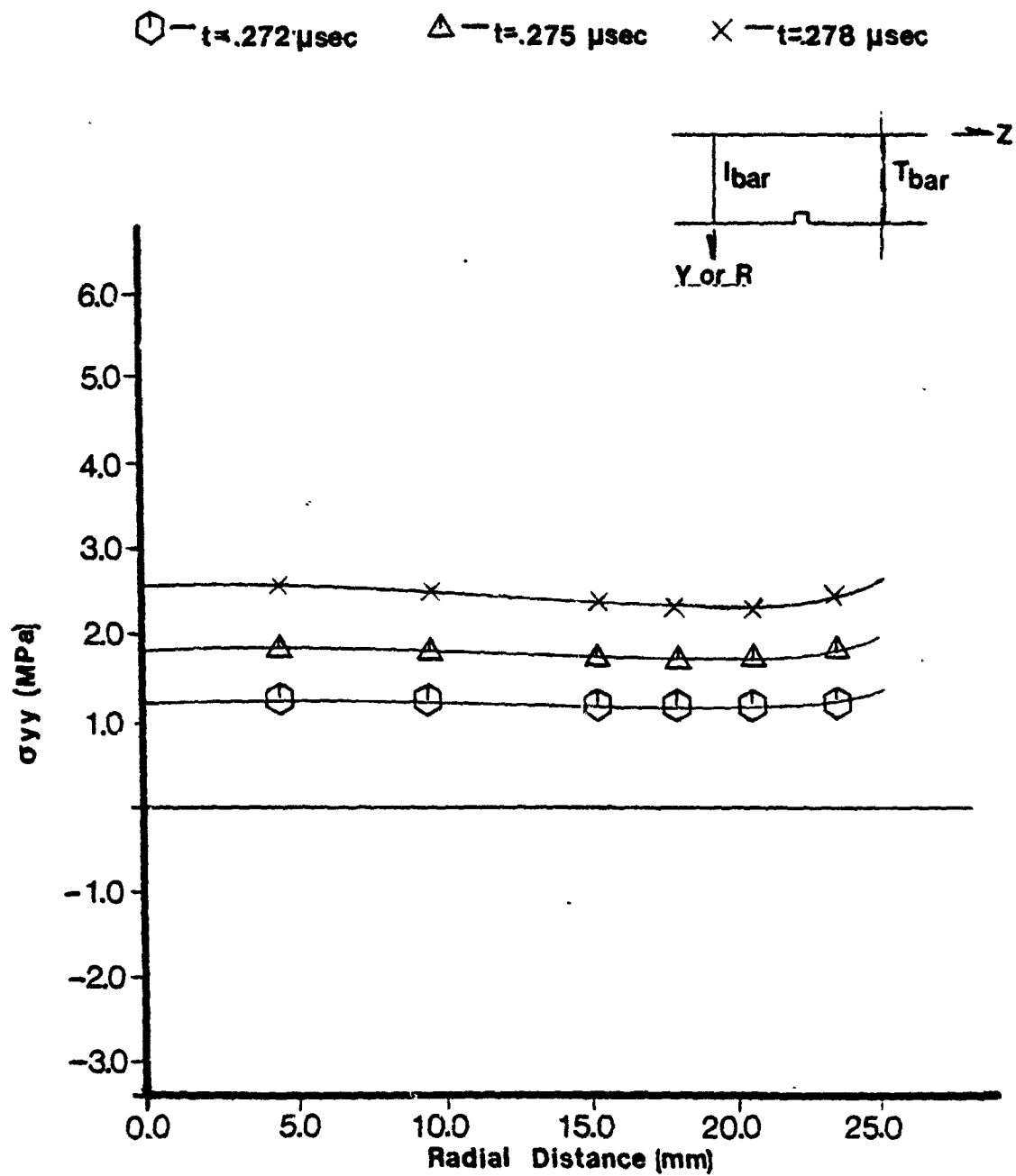


Figure 153. Profiles for longitudinal stress transverse to the longitudinal axis, nonlinear analysis, square notch,  $z = L$ .

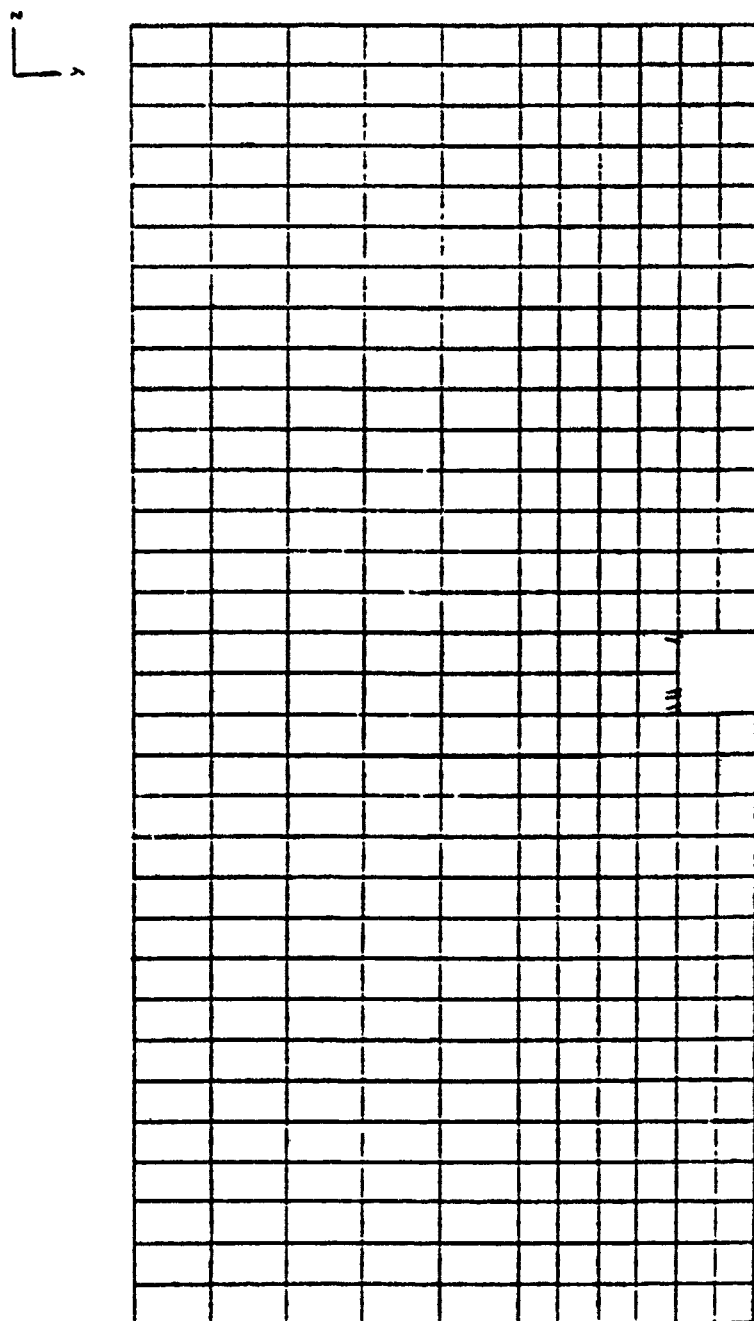


Figure 154. Cracking in square notch specimen at time  $t = 270.0 \mu\text{sec}$ .

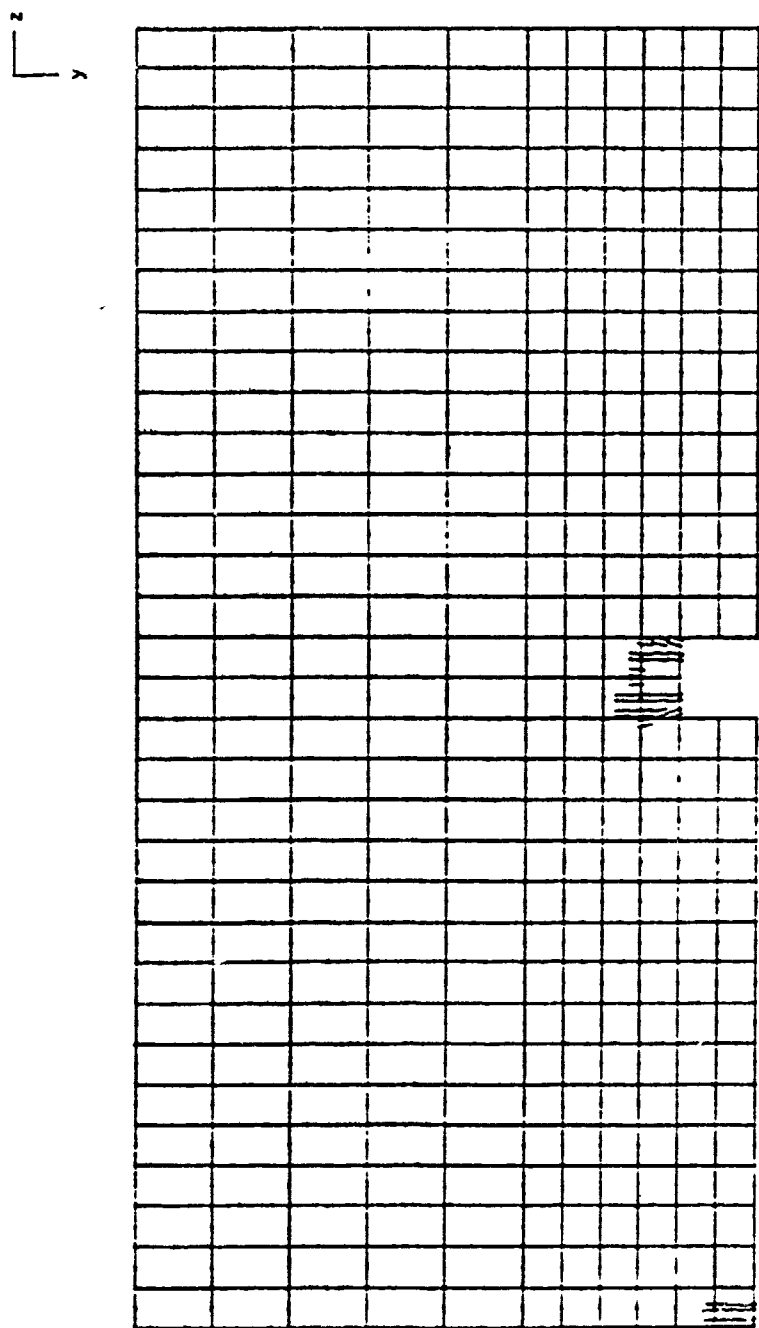


Figure 155. Cracking in square notch specimen at time  $t = 274.0 \mu\text{sec}$ .



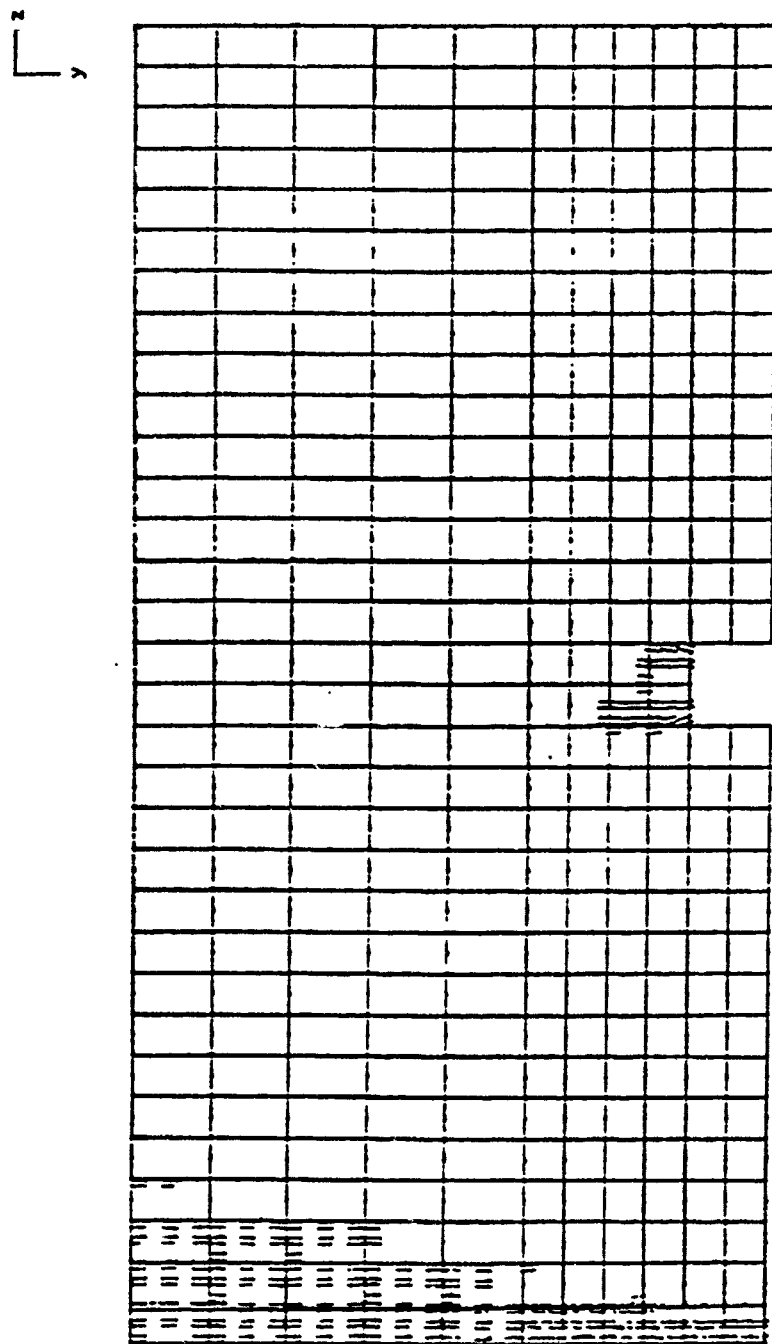


Figure 156. Cracking in square notch specimen at time  $t = 275.0 \mu\text{sec}$ .

concentration predictions from the linear analysis. However, at time  $t = 274 \mu\text{sec}$ , cracks develop at the outside surface of the specimen next to the incident bar at  $t = 274 \mu\text{sec}$  (Figure 155). Failure occurs along a transverse plane at the end of the specimen adjacent to the incident bar at time  $t = 275 \mu\text{sec}$  (Figure 156). This failure pattern is not evidenced in the linear analysis.

### 3. Saddle Notch Test

Time histories for the longitudinal stress,  $\sigma_z$ , and the longitudinal strain,  $\epsilon_z$ , for three longitudinal locations along the exterior surface of the specimen are illustrated in Figures 157, 158, and 159, for  $z = 0$ ,  $z = L/2$ , and  $z = L$ , respectively (where  $L$  is the length of the specimen and  $z$  is measured from the face of the incident bar). Time histories for  $\sigma_z$  and  $\epsilon_z$  at the same locations along the longitudinal axis of symmetry are presented in Figures 160, 161, and 162, respectively. The maximum stresses and strain rates produced at each of these locations are summarized in Table 10.

Profiles of the longitudinal stress,  $\sigma_z$ , for three selected times at three locations transverse to the longitudinal axis ( $z = 0$ ,  $z = L/2$ , and  $z = L$ ) are illustrated in Figures 163, 164, and 165, respectively. Cracking in the specimen at the apex of the notch and at the specimen-incident bar interface is evidenced in Figures 164 and 163, respectively.

The cracking sequence simulated by the numerical analysis, from initiation of the first crack until failure, is illustrated in Figures 166, 167, and 168. The first cracking in the specimen occurs at a transverse section in the specimen, adjacent to the face of the incident bar, at a time  $t = 265 \mu\text{sec}$  (Figure 160). This observation is contradictory to the anticipated failure location predicted by the linear analysis. At time  $t = 257 \mu\text{sec}$ , significant crack growth along this same plane is indicated (Figure 164). Finally, failure occurs along this plane at time  $t = 258 \mu\text{sec}$  (Figure 168). It is not until time  $t = 258 \mu\text{sec}$  that cracks develop in the notch, contemporaneous with failure at another location. This failure pattern is not supported by the results of the linear analysis.

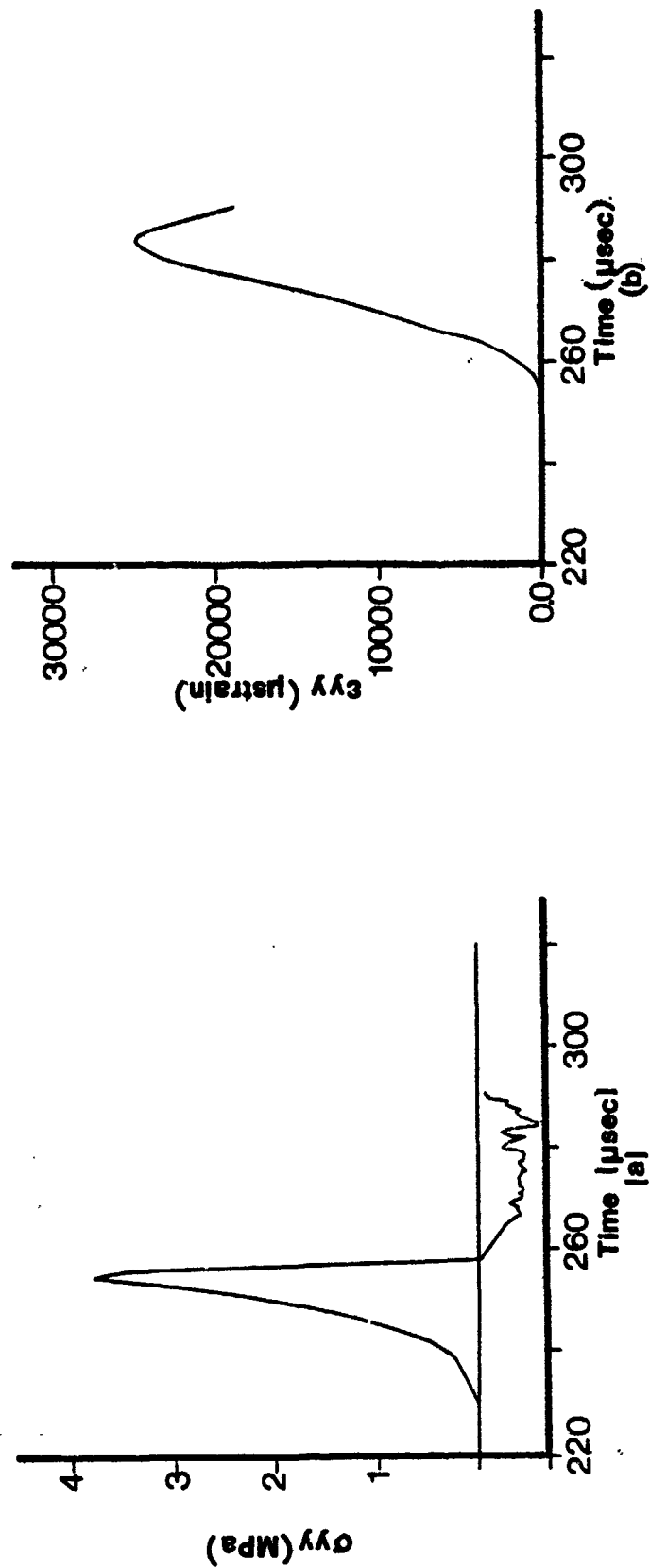
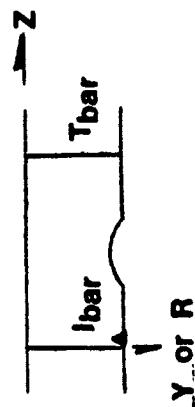


Figure 157. Time histories for (a) longitudinal stress and (b) longitudinal strain along the exterior surface, nonlinear analysis, saddle notch,  $z = 0$ .

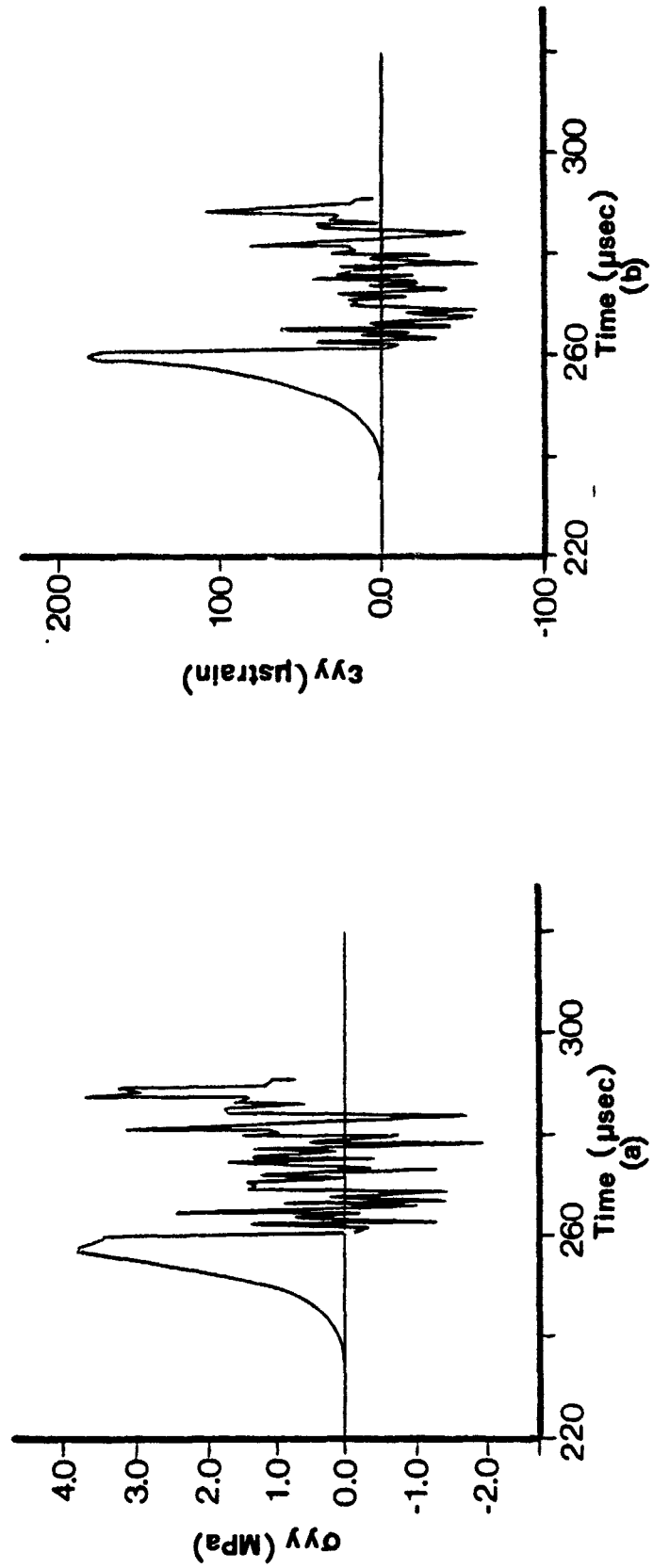


Figure 158. Time histories for (a) longitudinal stress and (b) longitudinal strain along the exterior surface, nonlinear analysis, saddle notch,  $z = L/2$ .

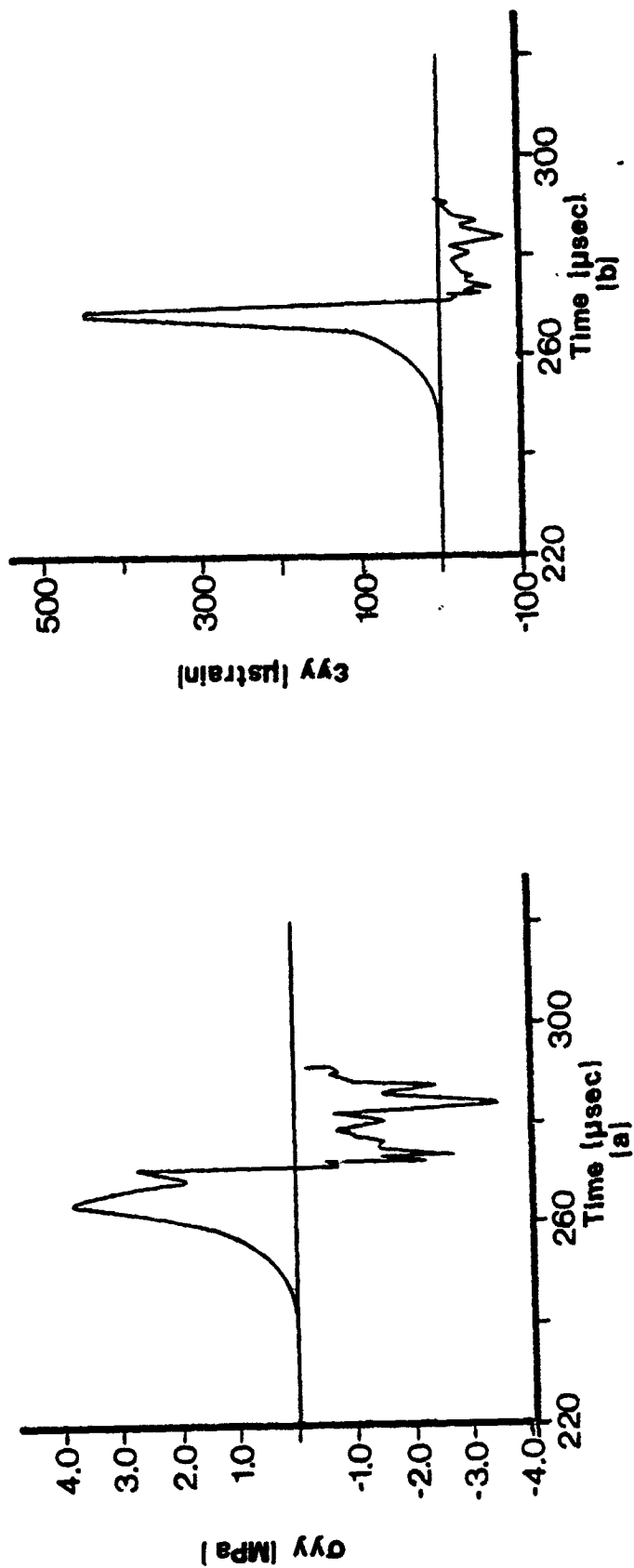
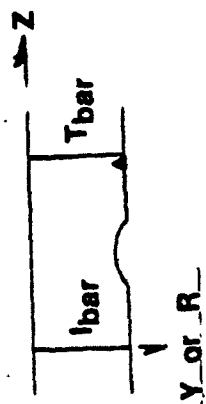


Figure 159. Time histories for (a) longitudinal stress and (b) longitudinal strain along the exterior surface, nonlinear analysis, saddle notch,  $z = L$ .

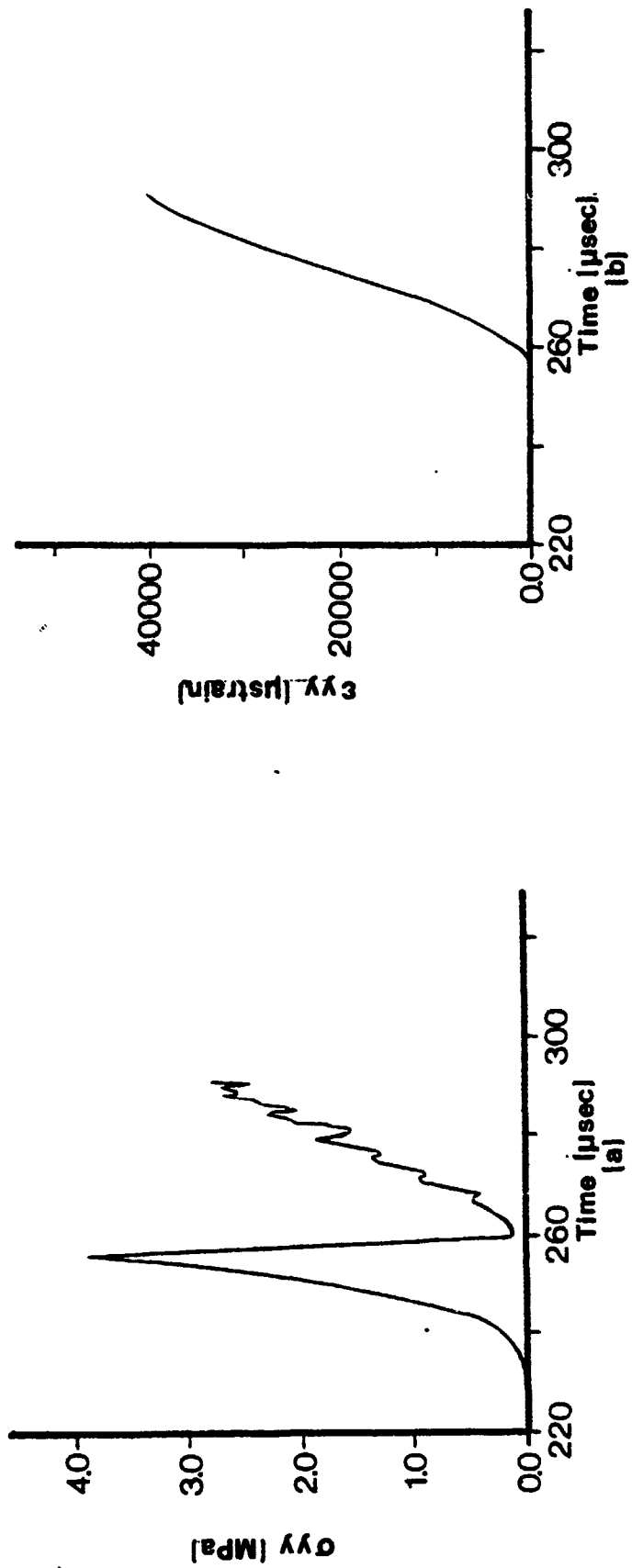


Figure 160. Time histories for (a) longitudinal stress and (b) longitudinal strain along the axis of symmetry, nonlinear analysis, saddle notch,  $z = 0$ .

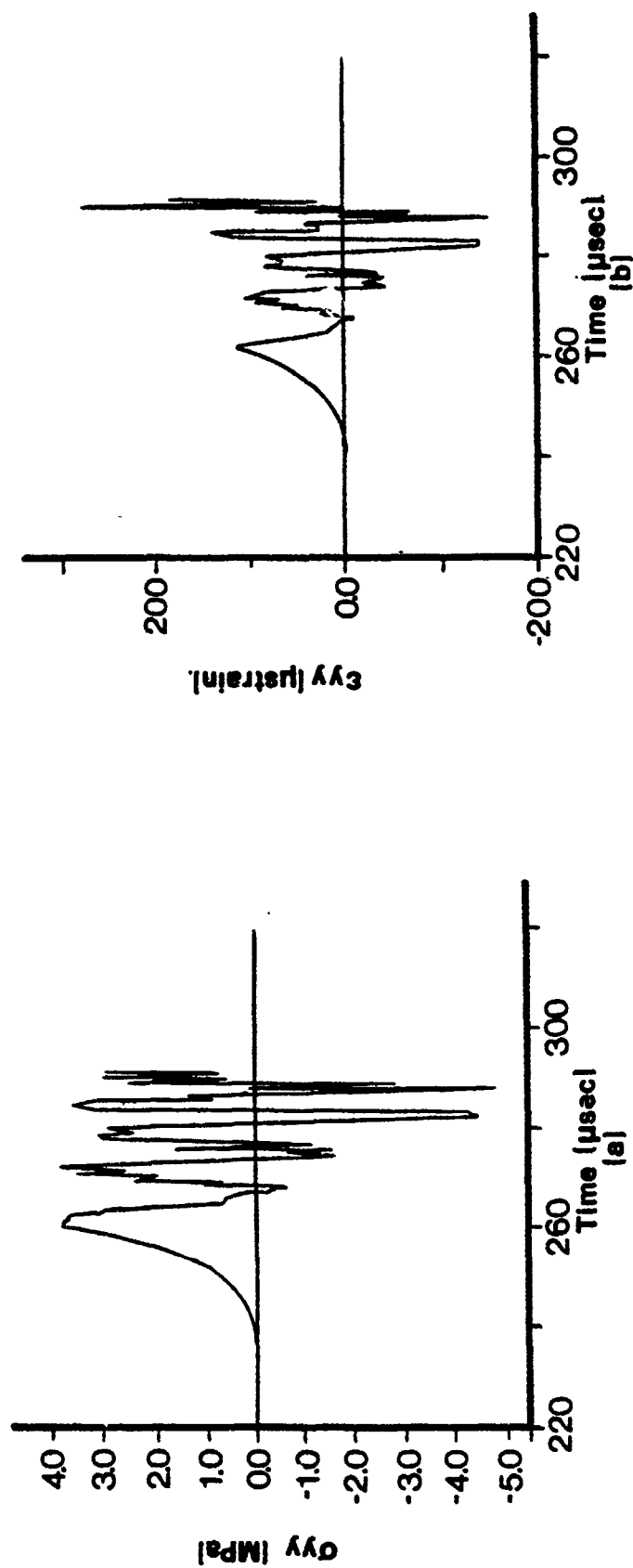
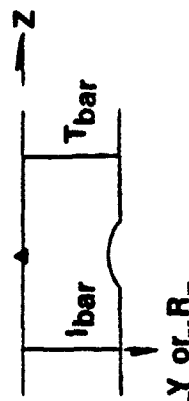


Figure 161. Time histories for (a) longitudinal stress and (b) longitudinal strain along the axis of symmetry, nonlinear analysis, saddle notch,  $z = L/2$ .

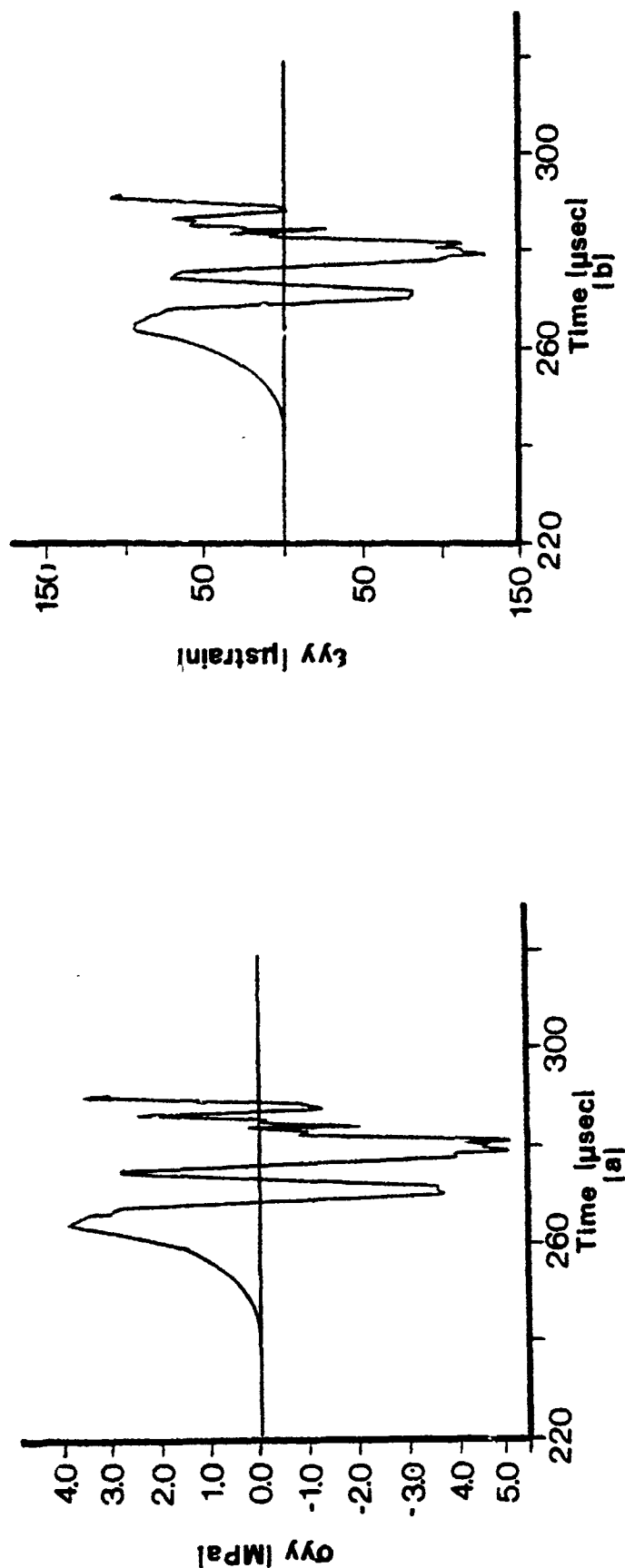
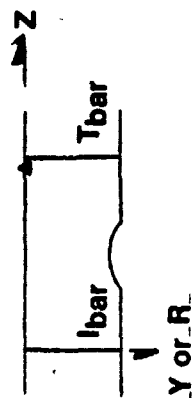


Figure 162. Time histories for (a) longitudinal stress and (b) longitudinal strain along the axis of symmetry, nonlinear analysis, saddle notch,  $z = L$ .



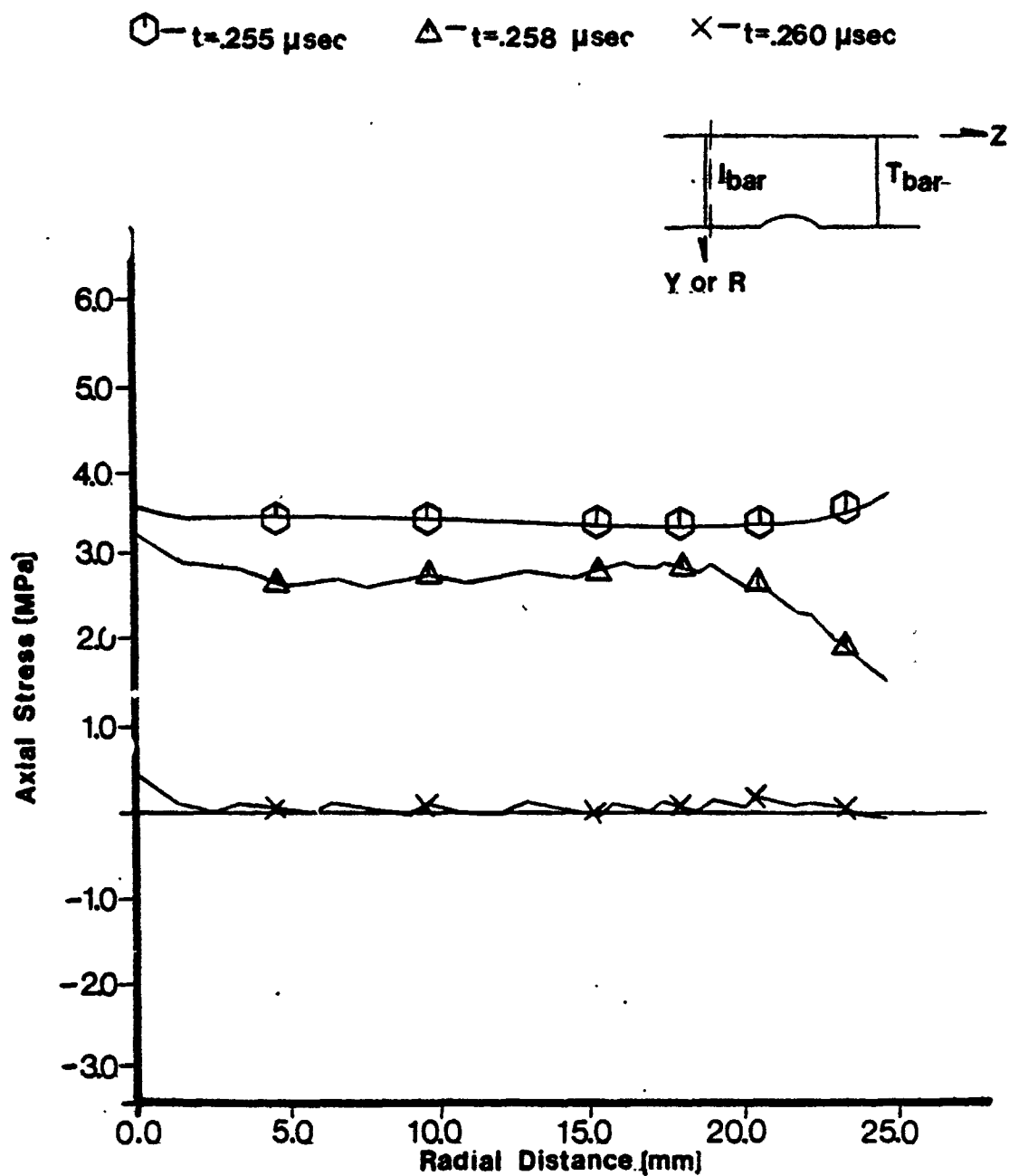


Figure 163. Profiles for longitudinal stress transverse to the longitudinal axis, nonlinear analysis, saddle notch,  $z = 0$ .

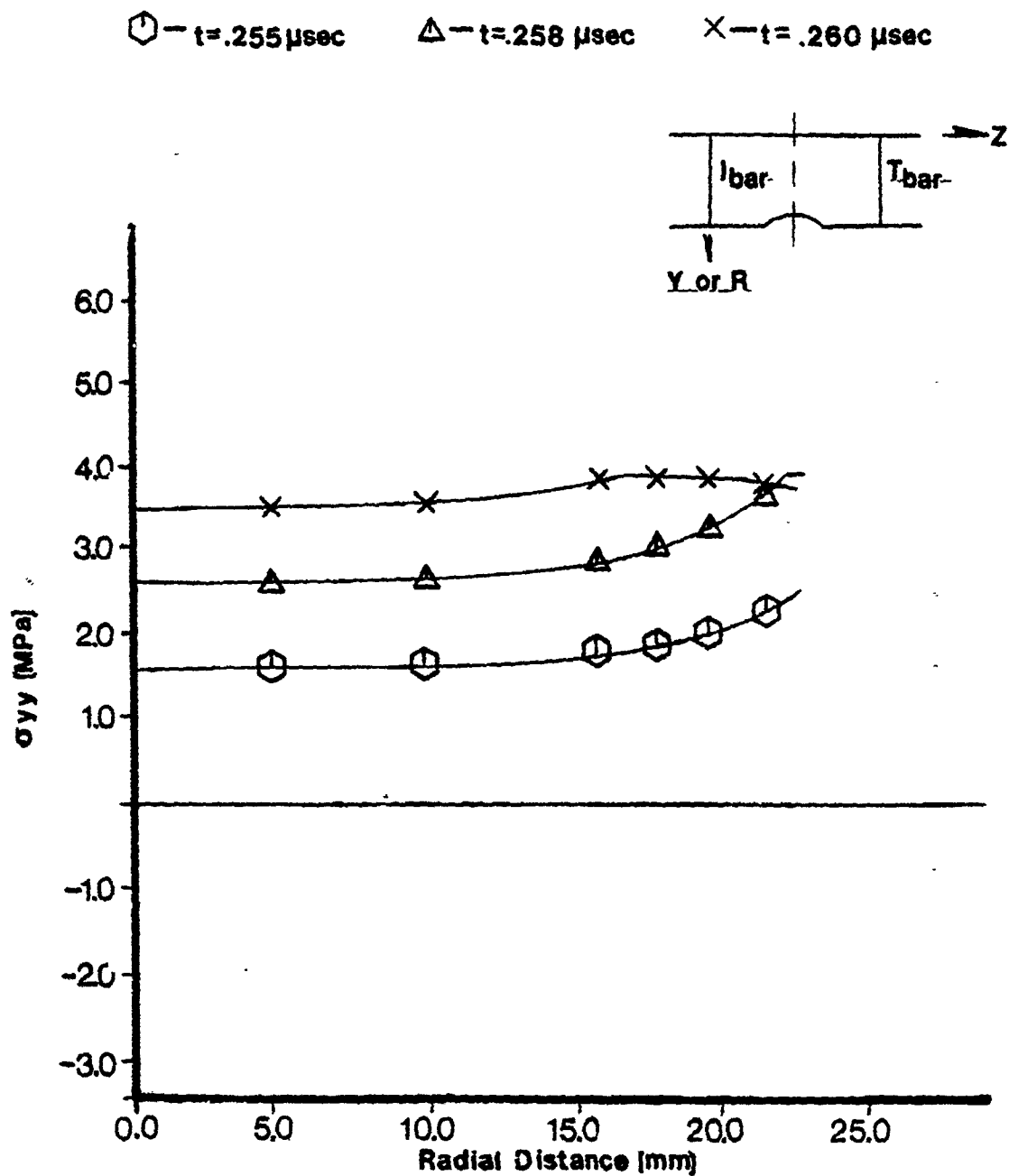


Figure 164. Profiles for longitudinal stress transverse to the longitudinal axis, nonlinear analysis, saddle notch,  $z = L/2$ .

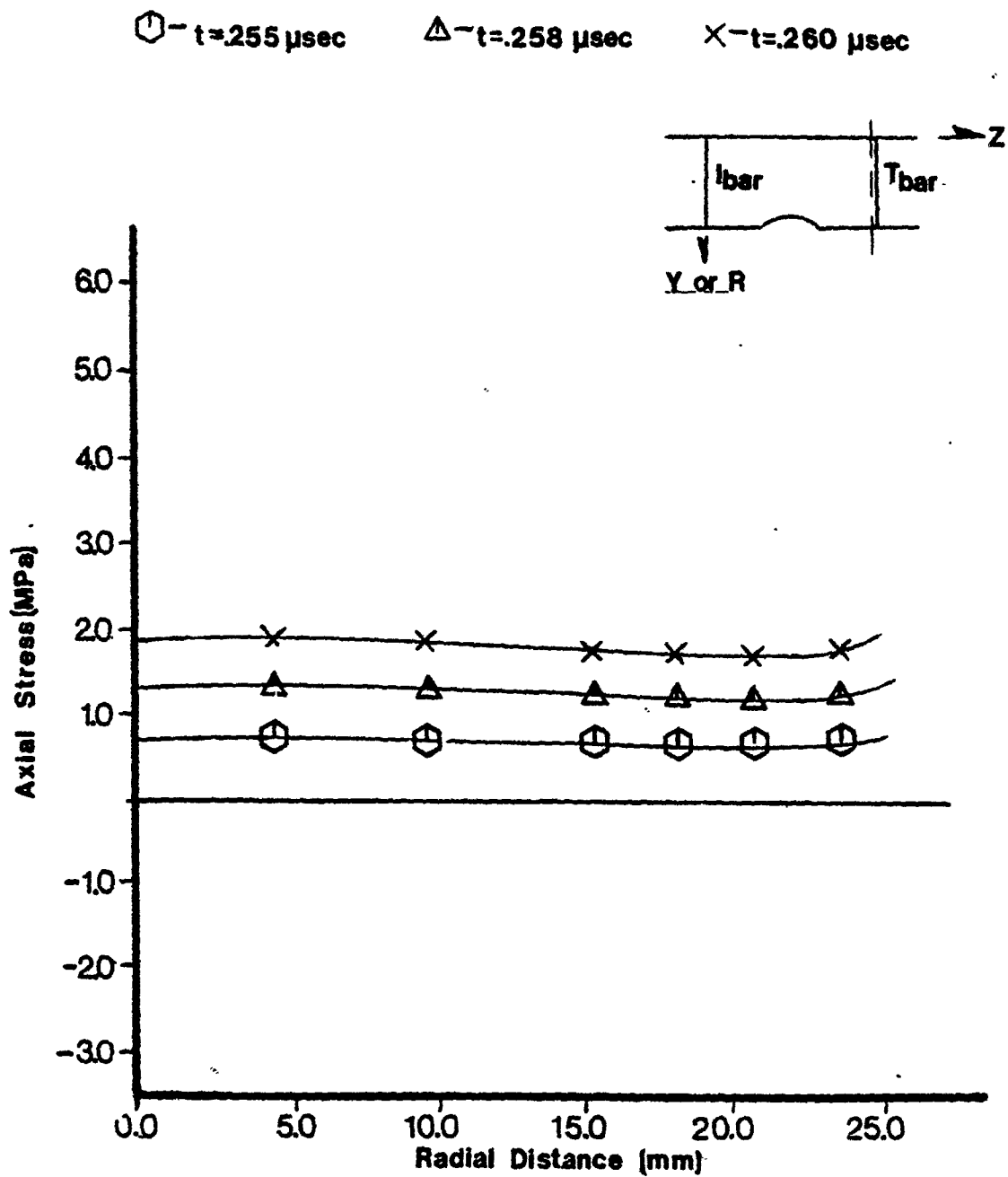


Figure 165. Profiles for longitudinal stress transverse to the longitudinal axis, nonlinear analysis, saddle notch,  $z = L$ .

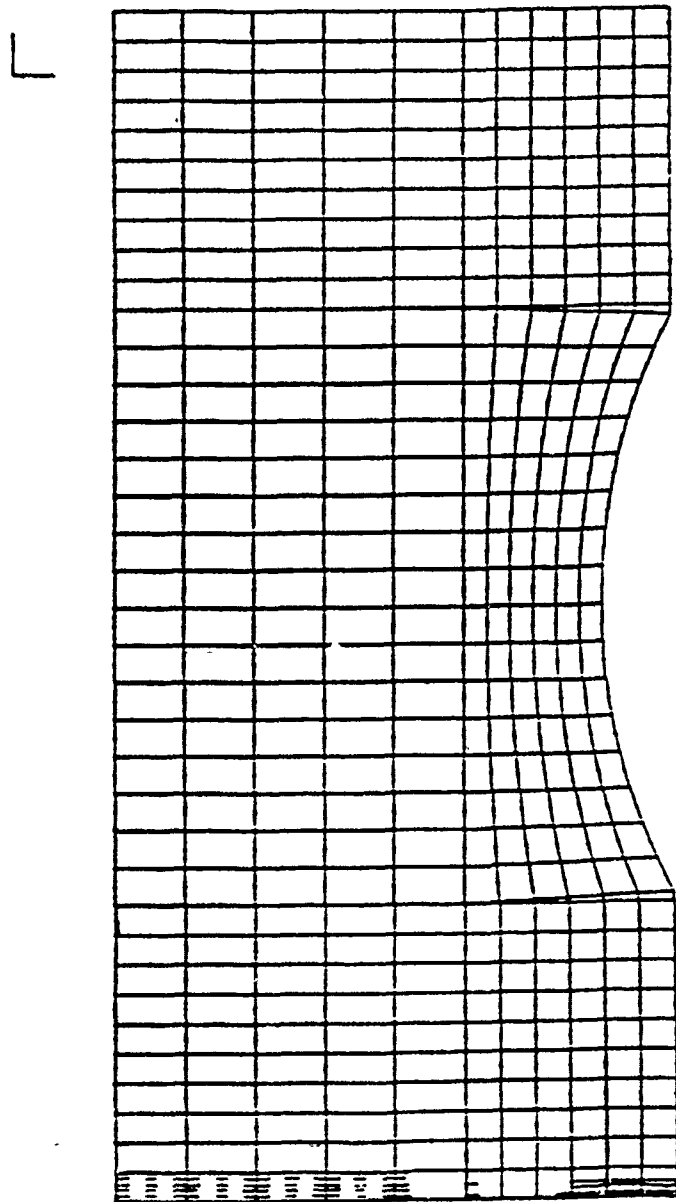


Figure 166. Cracking in saddle notch specimen at time  $t = 256.0 \mu\text{sec}$ .

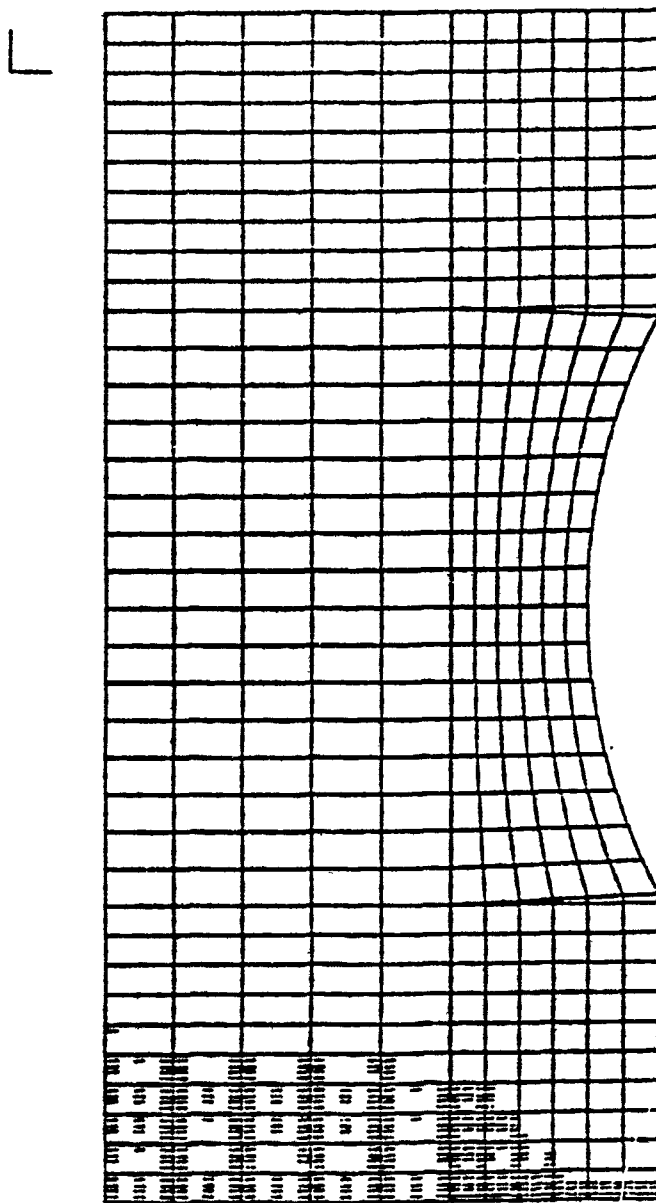


Figure 167. Cracking in saddle notch specimen at time  $t = 257.0 \mu\text{sec}$ .

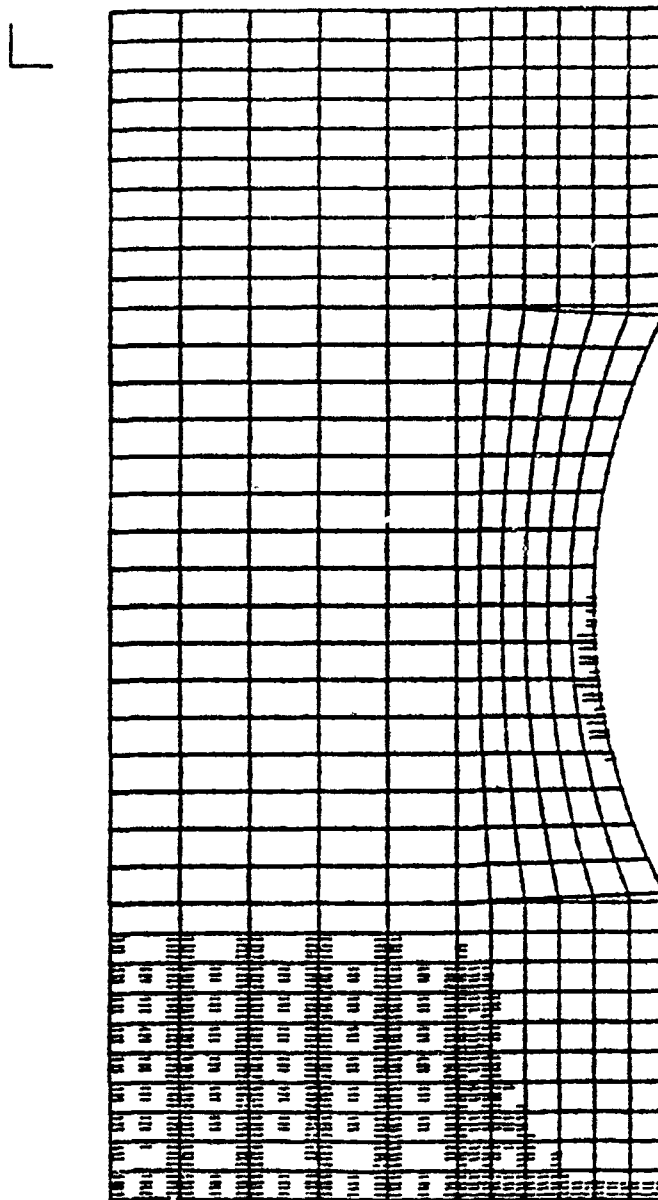


Figure 168. Cracking in saddle notch specimen at time  $t = 258.0 \mu\text{sec}$ .

TABLE 10. MAXIMUM STRESSES AND STRAIN  
RATES AT SELECTED LOCATIONS  
(SADDLE NOTCH TEST)

Location	$(\sigma_z)_{\max}$ psi (MPa)	$\dot{\epsilon}_z$ (sec <sup>-1</sup> )
$y = \frac{D}{2}, z = 0$	552 (3.81)	9.62
$y = \frac{D}{2}, z = \frac{L}{2}$	558 (3.85)	21.8
$y = \frac{D}{2}, z = L$	554 (3.82)	90.4
$y = 0, z = 0$	557 (3.84)	8.88
$y = 0, z = \frac{L}{2}$	556 (3.84)	8.80
$y = 0, z = L$	559 (3.86)	9.84
Transmitter Bar	538 (3.71)	2.36

## SECTION IV

### DISCUSSION OF RESULTS

#### A. SPLITTING-CYLINDER ANALYSIS

##### 1. Linear Analysis

The results of the linear analyses indicate that the dynamic stress distribution in the cylinder behind the initial stress wave is identical to that exhibited in the static analysis. This fact is particularly noticeable in the figures illustrating the profiles for the horizontal stress,  $\sigma_y$ , along both the vertical and horizontal diameters (Figures 36 through 47). This observation suggests that a dynamic failure would closely resemble the static failure. However, the results of the nonlinear analyses dispell this assumption.

Another interesting observation pertains to the development of the maximum horizontal stress at the center of the cylinder. Again, this is consistent with the results of the static analysis. This fact can be shown from the aforementioned profiles of the horizontal stress,  $\sigma_y$ , and from the time histories of  $\sigma_y$  at selected locations along the vertical diameter presented in Figures 18 through 32. Based upon these results, one could conclude that the cylinder would fail from the center, outward to the exterior boundaries of the vertical diameter.

##### 2. Nonlinear Analysis

The mode of failure predicted by the nonlinear analysis differs from that suggested by the results of the linear analysis. In all three load cases, the initiation of first cracking is not at the center of the cylinder (as the results of the linear analysis indicate), but at an approximate distance of 0.2D from the top of the cylinder. The failure sequence for Load Cases 1, 2, and 3 are illustrated in Figures 78, 104, and 124, respectively. The sequence of failure for all load cases is essentially the same: initiation of first cracking at location 0.2D from the top, and subsequent propagation of the cracks in both directions along the vertical centerline of the cylinder toward the top and bottom surfaces.

The deviation of the failure pattern predicted by the nonlinear analysis from that predicted by the results of the linear analysis can be attributed to the tension failure envelope employed in the analysis. The



tension failure envelope is depicted in Figure 49. To identify material failure, the principal stresses are used to locate the current stress state in the failure envelope. The tensile strength of a material in a principal direction does not change with the introduction of tensile stresses in other principal directions, however, the compressive stresses in other principal directions alter the tensile stress. Since the compressive stresses in the vicinity of the top of the cylinder are high in comparison to those at the center of the cylinder, initiation of first cracking will be at that location.

Another interesting idiosyncrasy of the mode of failure is revealed in the illustrations of the failure sequences presented in Figures 78, 104, and 124. The failure pattern for Load Case 1 (Figure 78) reveals no bifurcation in the primary crack pattern. For Load Case 2 (Figure 104), however, several bifurcations in the primary crack pattern are observed. And for Load Case 3 (Figure 124), an exaggerated bifurcation pattern is observed. It can be concluded that the presence and extent of the bifurcations in the failure pattern are related to the load rate. Load Case 1 represents a relatively low load rate, while Load Cases 2 and 3 represent successively high load rates. Therefore, it is concluded that the load rate affects the mode of failure.

The patterns of cracking predicted by the numerical analysis is consistent with those observed in the SHPB experiments (Reference 24). Preliminary results of high speed photography (10,000 frames/second) taken at AFESC of high load rate SHPB tests indicate the development of cracks similar to the pattern illustrated in Figures 104 and 124, along the vertical diameter prior to the appearance of the bifurcated cracks at the top and bottom of the cylinder. Moreover, the SHPB specimens have exhibited evidence of crack bifurcation occurring just below the center of the cylinder, similar to that illustrated in Figure 124d. This is substantiated by the observation from high-speed photography of a lens-shaped piece of fractured concrete being expelled from the flat surface of the specimen. It should be noted that all material fractures are predicated upon the failure envelope presented in Figure 49. No fracture mechanics parameters are used to describe the fracture process.

The results of the splitting-cylinder analyses may be used to correlate the dynamic tensile strength of the concrete to load rate when viewed in conjunction with experimental strength versus strain rate data associated with the appropriate loading rates.

## B. DIRECT TENSION TESTS

### 1. Linear Analysis

The results of the linear analysis indicate the development of high stress concentrations at the root of the notch (1.4) for the square notch specimen, and at the apex of the notch (1.6) for the saddle notch specimen. These concentration factors are determined from the time histories for the longitudinal stress,  $\sigma_z$ , illustrated in Figures 138 and 139 for the square notch test, and Figures 142 and 143 for the saddle notch test.

The results of the linear analyses indicate that first cracking will begin at the locations of high stress concentration. It can further be assumed that failure will ultimately occur on vertical planes passing through those points.

### 2. Nonlinear Analysis

The mode of failure predicted by the nonlinear analysis differs from that suggested by the results of the linear analysis. In the square notch specimen, first cracking occurs at the roots of the notch (Figure 154). This is consistent with the stress concentration predictions from the linear analysis. However, eventual failure of the specimen occurs on a vertical plane adjacent to the face of the incident bar (Figures 155 and 156).

In the saddle notch specimen, first cracking occurs at a transverse section in the specimen next to the incident bar (Figure 166). Almost simultaneously, cracks develop in the apex of the notch (Figure 167). Eventual failure is along the transverse section adjacent to the incident bar.

The failure patterns predicted by the nonlinear analysis contradict those suggested by the linear analysis. There are two basic reasons for this discrepancy: (1) the load rate is very high, therefore critical stresses develop at the loaded end of the specimens before significant stresses can develop in the vicinity of the notches; and (2) the notches are relatively shallow, therefore, they do not represent a critical section for such a high rate of loading.

In the experimental procedure, the saddle notch specimen tended to fail at both the bottom of the saddle notch and at the specimen end next to the incident bar for the same load rate used in the numerical analysis. However, for the square notch specimen, the failure was usually at the notch for the

loading used in the numerical analysis. At higher load rates (i.e., higher striker impact velocities) the square notch specimen also failed at both the notch and the incident end.

## SECTION V

### CONCLUSIONS AND RECOMMENDATIONS

#### A. CONCLUSIONS

##### 1. Splitting-Tensile Tests

The results of the linear analysis indicate that the dynamic stress distribution in the cylinder behind the initial stress wave is identical to that exhibited in the static analysis. The crack patterns and the modes of failure predicted by the nonlinear FEM analysis is consistent with that observed in the SHPB experiments.

In the nonlinear analysis, failure by separation of the cylinders, is predicted at time  $t = 85 \mu\text{sec}$  (Figure 78) for Load Case 1,  $t = 45 \mu\text{sec}$  (Figure 104) for Load Case 2, and  $t = 35 \mu\text{sec}$  (Figure 124) for Load Case 3. In Load Cases 2 and 3, the failure occurs before the maximum load is reached; that is, during the rise time of the load (refer to Table 3). This failure is predicated upon a uniaxial tension cut-off stress equal to the static tensile strength of the material. However, experimental strength vs. strain rate data associated with this loading rate indicates that the concrete tensile strength may be three to four times as great as the static tensile strength. Therefore, using the dynamic tensile strength in the material model would delay the time of failure and possibly bring it into the range of constant load; that is, at a time greater than the rise time. It is anticipated that the higher tensile strength would not affect the overall failure pattern.

It can also be concluded that the nature of the failure mode is directly affected by the rate of loading. For a relatively low load rate, such as Load Case 1, the failure mode manifests itself as a single crack propagating along the vertical centerline of the cylinder (Figure 78). However, for increasingly higher load rates, such as Load Case 2 and Load Case 3, the mode of failure is characterized by several bifurcations in the primary crack pattern (Figures 104 and 124). The higher the load rate, the more pronounced are the bifurcations.

##### 2. Direct Tension Tests

The results of the linear analysis indicate high stress concentrations in the vicinity of the notches. In the square notch test, a stress concentration

factor of 1.4 is indicated at the roots of the notch. In the saddle notch test, a stress concentration factor of 1.6 is indicated at the apex of the notch. These results suggest a failure in a transverse plane passing through the notch.

The nonlinear analysis, however, predicts failure in a transverse plane near the end of the specimen next to the incident bar. The reason for this is that the load rate is so high, that the tensile limit of the material is reached at the end of the specimen (adjacent to the incident bar) before any significant stresses can develop on the transverse plane passing through the notch.

The mode of failure is dominated by the load rate. Moreover, it can be concluded that the specimen fails during the rise time of the load, before multiple reflections can develop within the specimen. However, it is possible that the failure mode could be altered by considering material strain rate effects in the analysis and/or deeper notches in the specimen.

#### B. RECOMMENDATIONS

The failures predicted in both the splitting-tension tests and the direct tension tests are highly sensitive to the rate of loading. Therefore, it is recommended that additional analyses be conducted at a wide range of load rates to quantify the relationship of load rate to mode of failure.

It is also apparent from the results of the analyses that material strain rate effects will delay the time of failure, allowing the specimen to be subjected to a higher load, thus possibly affecting the failure mode. Therefore, it is further recommended that additional numerical analyses be conducted to investigate material strain rate effects on the mode of failure.

Finally, the notches in the direct tension specimens analyzed in this study were relatively shallow. It is recommended that specimens with deeper notches be analyzed, both experimentally and numerically, to quantify the effect of notch depth on the mode of failure.

## REFERENCES

1. Fundamentals of Protective Design for Conventional Weapons, Department of the Army, Waterways Experiment Station, Corps of Engineers, Vicksburg, MS, July 1984.
2. Felice, C. W. and Gaffney, E. S., "Early Time Response of Soil in a Split-Hopkinson Pressure Bar Experiment," Proceedings of the Third Symposium on the Interaction of Non-Nuclear Munitions with Structures, Mannheim, West Germany, March 9-13, 1987, Vol. II, pp. 508-524.
3. A Split Pressure Bar System for Dynamic Materials Testing, Department of Mechanical Sciences, Southwest Research Institute, San Antonio, Texas, April 1966.
4. Ross, C. A., Thompson, P. Y. and Nash, P. T., "Dynamic Testing of Soils Using a Split-Hopkinson Pressure Bar," Proceedings of the Third Symposium on the Interaction of Non-Nuclear Munitions with Structures, Mannheim, West Germany, March 9-13, 1987, Vol. II, pp. 525-537.
5. Gaffney, E. S., Brown, J. A., and Felice, C. W., "Soils as Samples for the Split-Hopkinson Bar," Proceedings of the Second Symposium on the Interaction of Non-Nuclear Munitions with Structures, Panama City Beach, FL, April 15-18, 1985, pp. 397-402.
6. Felice, C. W., Brown, J. A., Gaffney, E. S., and Olsen, J. M., "An Investigation into the High Strain-Rate Behavior of Compacted Sand Using the Split-Hopkinson Pressure Bar Technique," Proceedings of the Second Symposium on the Interaction of Non-Nuclear Munitions with Structures, Panama City Beach, FL, April 15-18, 1985, pp. 391-396.
7. Wilbeck, J. S., Thompson, P. Y., and Ross, C. A., "Laboratory Measurement of Wave Propagation in Soils," Proceedings of the Second Symposium on the Interaction of Non-Nuclear Munitions with Structures, Panama City Beach, FL, April 15-18, 1985, pp. 460-465.
8. Ross, C. A., Nash, P. T., and Friesenhahn, G. J., Pressure Waves in Soils Using a Split-Hopkinson Pressure Bar, ESL-TR-86-29, Air Force Engineering and Services Center, Tyndall AFB, FL, July 1986.
9. Malvern, L. E., Jenkins, D. A., Tianxi, T. and Ross, C. A., "Dynamic Compressive Testing of Concrete," Proceedings of the Second Symposium on

- the Interaction of Non-Nuclear Munitions with Structures, Panama City Beach, FL, April 15-18, 1985, pp. 397-402.
10. Malvern, L. E. and Ross, C. A., Dynamic Response of Concrete and Concrete Structures, First Annual Technical Report, AFOSR, Contract F49620-83-K007, 1984.
  11. Malvern, L. E. and Ross, C. A., Dynamic Response of Concrete and Concrete Structures, Second Annual Technical Report, AFOSR, Contract F49620-83-K007, 1985.
  12. Malvern, L. E. and Ross, C. A., Dynamic Response of Concrete and Concrete Structures, Final Report, AFOSR, Contract F49620-83-K007, May 1986.
  13. Hopkinson, B., "A Method of Measuring the Pressure Produced in the Detonation of High Explosives or by the Impact of Bullets," Philosophical Transactions of the Royal Society of London, Series A, Vol. 213, 1914, pp. 433-456.
  14. Davies, R. M., "A Critical Study of the Hopkinson Pressure Bar," Philosophical Transactions of the Royal Society of London, Series A, Vol. 240, 1948, pp. 375-457.
  15. Kolsky, H., "An Investigation of the Mechanical Properties of Materials at Very High Strain Rates of Loading," Proceedings of the Physical Society, Section B, Vol. 62, 1949, pp. 676-700.
  16. Follansbee, P. S. and Franz, C., "Wave Propagation in the Split Hopkinson Pressure Bar," Journal of Engineering Materials and Technology, Vol. 105, January 1963, pp. 61-66.
  17. ADINA, A Finite Element Computer Program for Automatic Dynamic Incremental Nonlinear Analysis, Report ARD 84-1, ADINA R&D, Inc., Watertown, MA, December 1984.
  18. ADINA, "Theory and Modeling Guide," Report ARD 84-4, ADINA R&D, Inc., Watertown, MA, December 1984.
  19. Nilson, A. H. and Winter, G., Design of Concrete Structures, McGraw-Hill, 1986, p. 40.
  20. Neville, A. M., Properties of Concrete, Pitman Publishing Co., London, UK, 1982, pp. 549-552.

21. Bathe, K. J., Finite Element Procedures in Engineering Analysis, Prentice Hall, Inc., Englewood Cliffs, NJ, 1982, pp. 511-512.
22. Tedesco, J. W., Stress Wave Propagation in Layered Media, Final Report, AFOSR, Contract F49620-85-C-0013, August 1988.